

Synthesis, Structure, and Magnetic Properties of Extended 2-D Triangular Lattices

by

Bart M. Bartlett

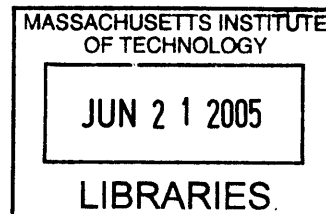
A.B. Summa Cum Laude Chemistry
Washington University in St. Louis, 2000

SUBMITTED TO THE DEPARTMENT OF CHEMISTRY IN PARTIAL
FULFILLMENT OF THE REQUIREMENTS FOR THE DEGREE OF

DOCTOR OF PHILOSOPHY
AT THE
MASSACHUSETTS INSTITUTE OF TECHNOLOGY

June 2005

© 2005 Massachusetts Institute of Technology
All Rights Reserved



Signature of Author: _____

Handwritten signature of Bart M. Bartlett in black ink.

Department of Chemistry
May 18, 2005

Certified by: _____

Handwritten signature of Daniel G. Nocera in black ink.

Daniel G. Nocera
W. M. Keck Professor of Energy and Professor of Chemistry
Thesis Supervisor

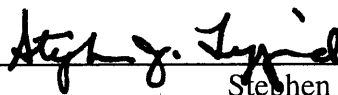
Accepted by: _____

Handwritten signature of Robert W. Field in black ink.

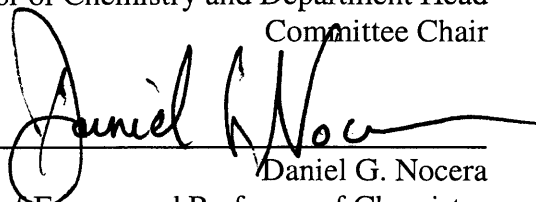
Robert W. Field
Haslam and Dewey Professor of Chemistry
Chairman, Departmental Committee on Graduate Students

ARCHIVES

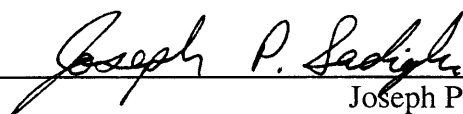
This doctoral thesis has been examined by a Committee of the Department of Chemistry as follows:



Stephen J. Lippard
Arthur Amos Noyes Professor of Chemistry and Department Head
Committee Chair



Daniel G. Nocera
W. M. Keck Professor of Energy and Professor of Chemistry
Thesis Supervisor



Joseph P. Sadighi
Assistant Professor of Chemistry

Synthesis, Structure, and Magnetic Properties of Extended 2-D Triangular Lattices

by

Bart M. Bartlett

Submitted to the Department of Chemistry
on May 18, 2005 in Partial Fulfillment of the
Requirements for the Degree of Doctor of Philosophy in
Chemistry

Abstract

A series of pure iron jarosites (formula $AFe_3(OH)_6(TO_4)_2$) possessing the paradigmatic kagomé lattice has been prepared stoichiometrically pure through the use of a redox-based hydrothermal synthetic strategy. This synthetic method allows us grow single crystals from which we fully characterize the structure and magnetic properties. Iron jarosites show signature spin frustrated behavior, indicated by a large Curie-Weiss constant, $\Theta \approx -800$ K, with a transition temperature, T_N narrowly ranging from 56 – 65 K. Long-range antiferromagnetic order is due to a canted spin structure developed from the Dzyaloshinsky-Moriya (DM) interaction. Although the DM interaction energy is only 1.2 cm^{-1} , this is large enough to give rise to a 3-D magnetic structure, precluding the ability to study the ground state physics of a purely 2-D frustrated spin system.

Copper hydroxy-bridged triangular species have been prepared and characterized both structurally and magnetically. Overall, the nearest-neighbor exchange interaction is found to be antiferromagnetic in each compound, with Θ ranging from -18 to -300 K, although the 1-D material lindgrenite, $Cu_3(OH)_2(MoO_4)_2$, and the kagomé-lattice-containing material clinoatacamite, $Cu_2(OH)_3Cl$, show 3-D long-range ferromagnetic order. The compound zinc paratacamite presents the hallmark of an $S = \frac{1}{2}$ Cu^{2+} compound possessing the kagomé lattice. This compound has magnetically isolated layers, and we find no evidence for magnetic ordering to temperatures down to 2 K, despite strong nearest-neighbor antiferromagnetic coupling, indicated by $\Theta \approx -300$ K.

Thesis Supervisor: Daniel G. Nocera

Title: W. M. Keck Professor of Energy and Professor of Chemistry

To my loving parents, who have been a guiding inspiration and have always encouraged me to imagine, to achieve, and to dream

Acknowledgments

I start by giving all glory, honor, and thanks to the Lord, through whom all things are possible. I thank Him for giving me the gifts and enthusiasm to do this science. I thank Him for faithfulness as I persevere through graduate school, and for the many friends I've made.

Next, I'd like to thank those who have worked closely on the magnetism project with me. When I visited MIT as an undergrad, Daniel Grohol spent much of the weekend telling me all about the wonder of these compounds called jarosites. He then taught me much about them—how to make them and the magic of growing big crystals once I arrived and got started. Then, Dimitris Papoutaskis took time out of his schedule to teach me how to do magnetic measurements using the SQUID, all-the-while finding a job in the last month of his post-doc. Emily Nytko now carries the torch, and I wish her well in her efforts. I also acknowledge the great collaboration this project has brought from Professor Young S. Lee in the MIT Department of Physics. In particular, Kit Matan and Joel Helton in the group for helped to interpret high field magnetization data, and for explained neutron experiments and results to a silly chemist.

Although, Professor F. Matthew P. Shores is best described as a second-rate guy, I'm grateful for the countless scientific discussions, assistance with crystallography, but more for the laughs and the friendship. With Matt, I learned what it truly means to work together with someone—not doing surreptitious experiments to keep the other person in the dark, and even admitting when results are purely serendipitous, and not planned. Matt, and his wife, Amy (one of the best softball pitchers I know), are two of the greatest friends I've made here, and I'm sure the stories will continue for years to come.

I'd like to thank the rest of my labmates who were there making discoveries alongside me. The class below me is affectionately known as J-Crew. Joel (Big Jr.) blasted Sports Radio 66, the Fan, WFAN New York next to me everyday for more than three years. Jenny (JYY), a newly found Red Sox fan, finally found the right spot in lab to get radio reception of WEEL, radio home of the Sox. Julien (a Swiss man in Cambridge) gave the greatest group meetings with

photos described as “questionable-at-best.” Justin (Kiwi) threw the best house parties, complete with an ample supply of Saran-wrap. Also, I thank Arthur and all of the wonderful staff at the B-Side Lounge (especially Claudia and Gizelle) for always being willing to relax and grab a cold frosty one after a hard, sometimes frustrating day of work. Streece, and his fiancée, Linda, taught me the importance of keeping relationships with people the priority, especially when playing spades. Now to all the younger students—G-Len, Kate, Becky, Emily, and Liz, I wish you the best as you progress through your graduate work.

That reminds me—there are a few key people who made this place very fun and exciting. N i e ls Damrauer (and Nelly) ensured that there was more meat for me at the group summer BBQ. Bradford J. Pistorio taught me that it’s totally ok to relax and have fun here, and that everything will work out tot perf. Alex (AK-47) made laser tag at the Good Time a fond memory. Tom Gray made *a-n-y*-thing fun. Erin MacLachlan had the most fun wedding reception ever in Vancouver, CA-NA-DA, complete with periodic table cake. Adam Veige gave me new perspective on the plight of Canadians in the United States. Speaking of our fine neighbor to the north, hanging out at the Ritz in Montréal with the Dave’s (Krodel, Lahr, and Manke), highlights the best weekend in grad school. Chris and Michelle Chang, along with Bob and Em Hefty, provided some of the best nights ‘queing it up with countless hours of MNF, playoff basketball, movies, video games, a summer carnival, Newcastle Brown Ale, chili, and three cool dogs—Jasper, Rookie, and Ginger. Gretchen keeps the group afloat financially, operationally, as well as socially—Topsfield Fair, anyone? I must also thank Josh (Bihe) Figueroa for being the first friend (and one of the best friends) I made in grad school (*JACS*—Athena cluster—’nough said).

There are two fellow grad students who add to the luxury of the group, a fine BMW you might say. My lab/class/roommate David Manke has been the easiest person to live due in large part to the fact that most meals contain potato break and Kraft singles. We agree to disagree on many subjects, and it hasn’t once hindered our friendship. Aetna Wun (AI Steak Sauce) has the “no ‘tudes” mind-set when it comes to work, so she’s been a great officemate. Plus, she has the

best San Francisco homerun call I've ever heard, and since we'll both be in the Bay area, I hope to catch a few games together.

Outside of MIT, I'd like to thank my many friends at Cambridgeport Baptist Church, especially those people in the Tuesday night small group for their prayers, fellowship, and being able to grow to know one another closely. I'll miss you guys a lot and wish you all the best.

I thank my high school and college friends who have encouraged me through the rigors of grad school. In particular, Gina Gebhart was always willing to hit up the beach and usually a really nice restaurant afterwards. And I'll never forget Halloween in Salem—now that's scary. Here, I have to give a special shout out to my boy Brian Haggemiller (Beef) and his family for welcoming into their *Who Wants to Be a Millionaire* home every Thanksgiving I was here in grad school. I appreciate being made part of the family—right down to getting slippers from Macy's from the Friday crack-of-dawn sale. Now, I'll have to make more trips to Miami to see Beef, Damaris, and the fun on South Beach more often.

My parents have shown all the love and support that a son could ever envision during my time in grad school. I miss being close to them, but am so thankful that they have always been in my corner when it comes to getting an education. Mom's the glue that holds the family together. Dad's my biggest hero; he's certainly no shuck and jive dude. After instilling the idea that actions speak louder than words, he practiced what he preached, and got his college degree after forty years of hard work in steel manufacturing.

Last, but most assuredly not least, I thank my research advisor, Dan Nocera, for giving me the opportunity and resources to work in his lab, and for challenging me to think critically about science. I appreciate his perspective and candor. Dan keeps it real, but also supplies a nurturing environment and a great cast of characters with whom to work. I like the fact that he also presents himself as a real person. While he may be just a guy trying to get by, his guidance and thought provoking approach to problems has undoubtedly made me a better scientist. As I've come to know well, he works very hard to provide an atmosphere of learning, and it's been my pleasure to show dedicated reciprocity through this thesis work.

Table of Contents

Abstract	3
Dedication	4
Acknowledgments	5
Table of Contents	8
List of Tables	11
List of Figures	14
List of Charts	21
List of Schemes	21
Chapter 1. Spin Frustration in the Kagomé Lattice	
1.1 Introduction	23
1.2 Spin Frustration	24
1.3 Long Range Order	27
1.4 Resonance Valence Bond (RVB) Theory	30
1.5 Synthetic Targets in Solid-State Chemistry	32
1.6 Outline and Scope of this Thesis	34
1.7 References	36
Chapter 2. Preparation and Characterization of Jarosites, the First Family of Compounds to Contain a Pure Kagomé Lattice	
2.1 Introduction	41
2.2 Experimental	42
2.2.1 General Procedures	42
2.2.2 Synthesis of $\text{Pb}_{0.5}\text{Fe}_3(\text{OH})_6(\text{SO}_4)_2$	42
2.2.3 Synthesis of $\text{AgFe}_3(\text{OH})_6(\text{SO}_4)_2$ and $\text{TlFe}_3(\text{OH})_6(\text{SO}_4)_2$	43
2.2.4 Synthesis of $\text{KFe}_3(\text{OH})_6(\text{SeO}_4)_2$ and $\text{RbFe}_3(\text{OH})_6(\text{SeO}_4)_2$	44
2.2.5 X-Ray Diffraction	44
2.2.6 Physical Methods	45
2.3 Results	46
2.3.1 Redox-based Synthesis	46
2.3.2 Structural Chemistry	50
2.3.3 Magnetism	55
2.3.4 EPR and Mössbauer Spectroscopies	58
2.4 Discussion	60
2.4.1 Intralayer Magnetic Exchange	60
2.4.2 Anisotropy Within the FeO_6 Octahedron	62

2.5	Conclusions	63
2.6	References	63
Chapter 3. Long-Range Order in Pure Jarosites: the Dzyaloshinsky-Moriya Interaction (Iron) and Metamagnetism (Vanadium)		
3.1	Introduction	68
3.2	Experimental	69
3.3	Results	70
	3.3.1 Single Crystal Susceptibility	70
	3.3.2 The Critical Field H_c , and the Spin Canting Angle, η	71
3.4	Discussion	76
	3.4.1 The DM Parameters, D_{ij} and D_z	76
	3.4.2 Interlayer Exchange, J_z , and Long-Range Correlation	78
	3.4.3 Ordering Pathways in Iron Jarosites	79
	3.4.4 Spin Canting and LRO in Jarosites	82
	3.4.5 Metamagnetism in Vanadium Jarosites	84
3.5	Conclusions	87
3.6	References	88
Chapter 4. Toward an $S = \frac{1}{2}$ Kagome Lattice with Copper-Based Materials		
4.1	Introduction	92
4.2	Experimental	96
	4.2.1 General Procedures	96
	4.2.2 Synthesis of (pip)Cu ₃ (OH) ₂ (MoO ₄) ₂	96
	4.2.3 Synthesis of (4,4'-bipy)Cu ₃ (OH) ₂ (MoO ₄) ₂	96
	4.2.4 Synthesis of Clinoatacamite, Cu ₂ (OH)3Cl	97
	4.2.5 Synthesis of Zinc Paratacamite, ZnCu ₃ (OH) ₆ Cl ₂	98
	4.2.6 X-ray Diffraction	99
	4.2.7 Physical Methods	99
4.3	Results	100
	4.3.1 Synthetic Methodology	100
	4.3.2 Structural Chemistry	102
	4.3.3 Magnetic Properties	107
4.4	Discussion	111
4.5	Conclusions	113
4.6	References	113
Chapter 5. Searching for the Resonating Valence Bond (RVB) State		

5.1	Introduction	117
5.2	Experimental	119
	5.2.1 General Procedures	119
	5.2.2 Synthesis of $\text{KFe}_{3-x}\text{V}_x(\text{OH})_6(\text{SO}_4)_2$ ($x \approx 0.8$)	119
	5.2.3 Synthesis of Barbosalite, $\text{Fe}^{2+}\text{Fe}_2^{3+}(\text{OH})_2(\text{PO}_4)_2$	120
	5.2.4 Physical Methods	120
5.3	Results and Discussion	121
	5.3.1 Mixed-metal Jarosite,	121
	5.3.2 Mixed-valency in Barbosalite	124
	5.3.3 Reaction Chemistry of $\text{ZnCu}_3(\text{OH})_6\text{Cl}_2$	129
	5.3.4 ^{60}Co γ -irradiation	130
5.4	Conclusions	132
5.5	References	132
	Appendix A.	136
	Appendix B.	182
	Biographical Sketch	198
	Curriculum Vitae	199

List of Tables

Table 2.1.	Magnetic properties of jarosites prepared by precipitation methods.	42
Table 2.2.	Selected bond distances (Å) and bond angles (°) for jarosites.	53
Table 2.3.	Magnetic data for pure jarosites.	57
Table 3.1.	Fitting parameters for $M(H)$ data at 5 K for $P_1 B_J(x) + P_2 H + P_3$	79
Table 4.1.	Structural comparison of clinoatacamite and zinc paratacamite.	106
Table A.1.	Crystal data and structure refinement for $Pb_{0.5}Fe_3(OH)_6(SO_4)_2$.	138
Table A.2.	Atomic coordinates ($\times 10^4$) and equivalent isotropic displacement parameters ($\text{Å}^2 \times 10^3$) for $Pb_{0.5}Fe_3(OH)_6(SO_4)_2$. $U(eq)$ is defined as one third of the trace of the orthogonalized U_{ij} tensor.	139
Table A.3.	Anisotropic displacement parameters ($\text{Å}^2 \times 10^3$) for $Pb_{0.5}Fe_3(OH)_6(SO_4)_2$. The anisotropic displacement factor exponent takes the form: $-2\pi^2 [h^2a^{*2}U_{11} + \dots + 2hka^*b^*U_{12}]$.	139
Table A.4.	Hydrogen coordinates ($\times 10^4$) and isotropic displacement parameters ($\text{Å}^2 \times 10^3$) for $Pb_{0.5}Fe_3(OH)_6(SO_4)_2$.	139
Table A.5.	Bragg reflections and Miller indices of pXRD pattern for $Pb_{0.5}Fe_3(OH)_6(SO_4)_2$.	140
Table A.6.	Crystal data and structure refinement for $AgFe_3(OH)_6(SO_4)_2$.	142
Table A.7.	Atomic coordinates ($\times 10^4$) and equivalent isotropic displacement parameters ($\text{Å}^2 \times 10^3$) for $AgFe_3(OH)_6(SO_4)_2$. $U(eq)$ is defined as one third of the trace of the orthogonalized U_{ij} tensor.	143
Table A.8.	Anisotropic displacement parameters ($\text{Å}^2 \times 10^3$) for $AgFe_3(OH)_6(SO_4)_2$. The anisotropic displacement factor exponent takes the form: $-2\pi^2 [h^2a^{*2}U_{11} + \dots + 2hka^*b^*U_{12}]$.	143
Table A.9.	Hydrogen coordinates ($\times 10^4$) and isotropic displacement parameters ($\text{Å}^2 \times 10^3$) for $AgFe_3(OH)_6(SO_4)_2$.	143
Table A.10.	Bragg reflections and Miller indices of pXRD pattern for $AgFe_3(OH)_6(SO_4)_2$.	144
Table A.11.	Crystal data and structure refinement for $TlFe_3(OH)_6(SO_4)_2$.	146
Table A.12.	Atomic coordinates ($\times 10^4$) and equivalent isotropic displacement parameters ($\text{Å}^2 \times 10^3$) for $TlFe_3(OH)_6(SO_4)_2$. $U(eq)$ is defined as one third of the trace of the orthogonalized U_{ij} tensor.	147
Table A.13.	Anisotropic displacement parameters ($\text{Å}^2 \times 10^3$) for $TlFe_3(OH)_6(SO_4)_2$. The anisotropic displacement factor exponent takes the form: $-2\pi^2 [h^2a^{*2}U_{11} + \dots + 2hka^*b^*U_{12}]$.	147
Table A.14.	Hydrogen coordinates ($\times 10^4$) and isotropic displacement parameters ($\text{Å}^2 \times 10^3$) for $TlFe_3(OH)_6(SO_4)_2$.	147

Table A.15.	Bragg reflections and Miller indices of pXRD pattern for $\text{TlFe}_3(\text{OH})_6(\text{SO}_4)_2$.	148
Table A.16.	Crystal data and structure refinement for $\text{KFe}_3(\text{OH})_6(\text{SeO}_4)_2$.	150
Table A.17.	Atomic coordinates ($\times 10^4$) and equivalent isotropic displacement parameters ($\text{\AA}^2 \times 10^3$) for $\text{KFe}_3(\text{OH})_6(\text{SeO}_4)_2$. $U(\text{eq})$ is defined as one third of the trace of the orthogonalized U_{ij} tensor.	151
Table A.18.	Anisotropic displacement parameters ($\text{\AA}^2 \times 10^3$) for $\text{KFe}_3(\text{OH})_6(\text{SeO}_4)_2$. The anisotropic displacement factor exponent takes the form: $-2\pi^2 [h^2 a^{*2} U_{11} + \dots + 2hka^* b^* U_{12}]$.	151
Table A.19.	Hydrogen coordinates ($\times 10^4$) and isotropic displacement parameters ($\text{\AA}^2 \times 10^3$) for $\text{KFe}_3(\text{OH})_6(\text{SeO}_4)_2$.	151
Table A.20.	Bragg reflections and Miller indices of pXRD pattern for $\text{KFe}_3(\text{OH})_6(\text{SeO}_4)_2$.	152
Table A.21.	Crystal data and structure refinement for $\text{RbFe}_3(\text{OH})_6(\text{SeO}_4)_2$.	154
Table A.22.	Atomic coordinates ($\times 10^4$) and equivalent isotropic displacement parameters ($\text{\AA}^2 \times 10^3$) for $\text{RbFe}_3(\text{OH})_6(\text{SeO}_4)_2$. $U(\text{eq})$ is defined as one third of the trace of the orthogonalized U_{ij} tensor.	155
Table A.23.	Anisotropic displacement parameters ($\text{\AA}^2 \times 10^3$) for $\text{RbFe}_3(\text{OH})_6(\text{SeO}_4)_2$. The anisotropic displacement factor exponent takes the form: $-2\pi^2 [h^2 a^{*2} U_{11} + \dots + 2hka^* b^* U_{12}]$.	155
Table A.24.	Hydrogen coordinates ($\times 10^4$) and isotropic displacement parameters ($\text{\AA}^2 \times 10^3$) for $\text{RbFe}_3(\text{OH})_6(\text{SeO}_4)_2$.	155
Table A.25.	Bragg reflections and Miller indices of pXRD pattern for $\text{RbFe}_3(\text{OH})_6(\text{SeO}_4)_2$.	156
Table A.26.	Crystal data and structure refinement for $(\text{pip})\text{Cu}_3(\text{OH})_2(\text{MoO}_4)_2$.	158
Table A.27.	Atomic coordinates ($\times 10^4$) and equivalent isotropic displacement parameters ($\text{\AA}^2 \times 10^3$) for $(\text{pip})\text{Cu}_3(\text{OH})_2(\text{MoO}_4)_2$. $U(\text{eq})$ is defined as one third of the trace of the orthogonalized U_{ij} tensor.	159
Table A.28.	Bond lengths (\AA) for $(\text{pip})\text{Cu}_3(\text{OH})_2(\text{MoO}_4)_2$.	159
Table A.29.	Bond angles ($^\circ$) for $(\text{pip})\text{Cu}_3(\text{OH})_2(\text{MoO}_4)_2$.	160
Table A.30.	Anisotropic displacement parameters ($\text{\AA}^2 \times 10^3$) for $(\text{pip})\text{Cu}_3(\text{OH})_2(\text{MoO}_4)_2$. The anisotropic displacement factor exponent takes the form: $-2\pi^2 [(ha^*)^2 U_{11} + \dots + 2hka^* b^* U_{12}]$.	161
Table A.31.	Hydrogen coordinates ($\times 10^4$) and isotropic displacement parameters ($\text{\AA}^2 \times 10^3$) for $(\text{pip})\text{Cu}_3(\text{OH})_2(\text{MoO}_4)_2$.	161
Table A.32.	Crystal data and structure refinement for $(\text{bipy})\text{Cu}_3(\text{OH})_2(\text{MoO}_4)_2$.	163

Table A.33.	Atomic coordinates ($\times 10^4$) and equivalent isotropic displacement parameters ($\text{\AA}^2 \times 10^3$) for $(\text{bipy})\text{Cu}_3(\text{OH})_2(\text{MoO}_4)_2$. $U(\text{eq})$ is defined as one third of the trace of the orthogonalized U_{ij} tensor.	164
Table A.34.	Bond lengths (\AA) for $(\text{bipy})\text{Cu}_3(\text{OH})_2(\text{MoO}_4)_2$.	165
Table A.35.	Bond angles ($^\circ$) for $(\text{bipy})\text{Cu}_3(\text{OH})_2(\text{MoO}_4)_2$.	166
Table A.36.	Anisotropic displacement parameters ($\text{\AA}^2 \times 10^3$) for $(\text{bipy})\text{Cu}_3(\text{OH})_2(\text{MoO}_4)_2$. The anisotropic displacement factor exponent takes the form: $-2\pi^2[(\text{ha}^*)^2U_{11} + \dots + 2\text{hka}^*\text{b}^*U_{12}]$.	167
Table A.37.	Hydrogen coordinates ($\times 10^4$) and isotropic displacement parameters ($\text{\AA}^2 \times 10^3$) for $(\text{bipy})\text{Cu}_3(\text{OH})_2(\text{MoO}_4)_2$.	168
Table A.38.	Crystal data and structure refinement for $\text{Cu}_2(\text{OH})_3\text{Cl}$.	170
Table A.39.	Atomic coordinates ($\times 10^4$) and equivalent isotropic displacement parameters ($\text{\AA}^2 \times 10^3$) for $\text{Cu}_2(\text{OH})_3\text{Cl}$. $U(\text{eq})$ is defined as one third of the trace of the orthogonalized U_{ij} tensor.	171
Table A.40.	Anisotropic displacement parameters ($\text{\AA}^2 \times 10^3$) for $\text{Cu}_2(\text{OH})_3\text{Cl}$. The anisotropic displacement factor exponent takes the form: $-2\pi^2[h^2\text{a}^*U_{11} + \dots + 2\text{hka}^*\text{b}^*U_{12}]$.	171
Table A.41.	Hydrogen coordinates ($\times 10^4$) and isotropic displacement parameters ($\text{\AA}^2 \times 10^3$) for $\text{Cu}_2(\text{OH})_3\text{Cl}$.	171
Table A.42.	Bragg peaks and Miller indices for $\text{Cu}_2(\text{OH})_3\text{Cl}$.	172
Table A.43.	Crystal data and structure refinement for $\text{ZnCu}_3(\text{OH})_6\text{Cl}_2$.	174
Table A.44.	Atomic coordinates ($\times 10^4$) and equivalent isotropic displacement parameters ($\text{\AA}^2 \times 10^3$) for $\text{ZnCu}_3(\text{OH})_6\text{Cl}_2$. $U(\text{eq})$ is defined as one third of the trace of the orthogonalized U_{ij} tensor.	175
Table A.45.	Anisotropic displacement parameters ($\text{\AA}^2 \times 10^3$) for $\text{ZnCu}_3(\text{OH})_6\text{Cl}_2$. The anisotropic displacement factor exponent takes the form: $-2\pi^2[h^2\text{a}^*U_{11} + \dots + 2\text{hka}^*\text{b}^*U_{12}]$.	175
Table A.46.	Hydrogen coordinates ($\times 10^4$) and isotropic displacement parameters ($\text{\AA}^2 \times 10^3$) for $\text{ZnCu}_3(\text{OH})_6\text{Cl}_2$.	175
Table A.47.	Bragg peaks and Miller indices for $\text{ZnCu}_3(\text{OH})_6\text{Cl}_2$.	176
Table A.48.	Bragg peaks and Miller indices for $\text{KFe}_3(\text{OH})_6(\text{CrO}_4)_2$.	178
Table A.49.	Bragg peaks and Miller indices for $\text{KFe}_{3-x}\text{V}_x(\text{OH})_6(\text{CrO}_4)_2$.	179
Table A.50.	Bragg peaks and Miller indices for $\text{Fe}^{2+}\text{Fe}_2^{3+}(\text{OH})_2(\text{PO}_4)_2$.	181

List of Figures

Figure 1.1.	Types of magnetic coupling on a one-dimensional wire: a) ferromagnetism; b) antiferromagnetism; c) ferrimagnetism.	24
Figure 1.2.	Frustration emerging from the spin glass state in doped cuprates.	25
Figure 1.3.	Geometric spin frustration on a triangle. Two antiferromagnetically coupled spins can couple pairwise antiparallel, but a third cannot.	26
Figure 1.4.	Dimensionality and ordering in the Ising model.	28
Figure 1.5.	One energy minimum in the 2-D triangular Ising net studied by Wannier. Note that each triangle has two antiferromagnetic and one ferromagnetic interaction. Since the rows of spins alternate in this arrangement, no long-range order is possible.	28
Figure 1.6.	Two compromised 120° ground state structures of the kagomé antiferromagnet: a) the $q = 0$ and b) the $q = \sqrt{3} \times \sqrt{3}$ spin arrangements.	30
Figure 1.7.	Parallels between the square lattice of high T_c cuprate superconductors and the kagomé lattice of Heisenberg antiferromagnets.	31
Figure 1.8.	Magnetic lattice of SCGO garnets. Kagomé planes of Cr^{3+} ions (\bullet) are separated by triangular planes of Cr^{3+} (\circ).	33
Figure 2.1.	FTIR spectra of the (a) sulfate-capped iron jarosites, $\text{Pb}_{0.5}\text{Fe}_3(\text{OH})_6(\text{SO}_4)_2$ (top) $\text{AgFe}_3(\text{OH})_6(\text{SO}_4)_2$ (middle), and $\text{TlFe}_3(\text{OH})_6(\text{SO}_4)_2$ (bottom) and (b) selenate-capped iron jarosite analogs $\text{KFe}_3(\text{OH})_6(\text{SO}_4)_2$ (top) and $\text{RbFe}_3(\text{OH})_6(\text{SO}_4)_2$ (bottom).	48
Figure 2.2.	Powder X-ray diffraction patterns of a) $\text{Pb}_{0.5}\text{Fe}_3(\text{OH})_6(\text{SO}_4)_2$, b) $\text{AgFe}_3(\text{OH})_6(\text{SO}_4)_2$ c) $\text{TlFe}_3(\text{OH})_6(\text{SO}_4)_2$, d) $\text{KFe}_3(\text{OH})_6(\text{SeO}_4)_2$, and e) $\text{RbFe}_3(\text{OH})_6(\text{SO}_4)_2$. Note that for $\text{Pb}_{0.5}\text{Fe}_3(\text{OH})_6(\text{SO}_4)_2$, the (003) reflection occurs at $15.85^\circ 2\theta$.	50
Figure 2.3.	Basic structural unit of $\text{AgFe}_3(\text{OH})_6(\text{SO}_4)_2$, highlighting the intralayer structure and local structure about the Fe^{3+} center. Ellipsoids are shown at 50% probability.	51
Figure 2.4.	Packing diagram of jarosite, viewed along [110]. Note that all Fe atoms within a kagomé layer lie within a plane normal to the c axis. Note that the FeO_6 elongated octahedron is tilted approximately 17° from the crystallographic c axis. One elongated, tilted FeO_6 octahedron is highlighted.	54
Figure 2.5.	(a) FC and ZFC susceptibilities for $\text{AgFe}_3(\text{OH})_6(\text{SO}_4)_2$. Both measurements were performed under a 100 Oe measuring field. For the FC measurement, the cooling field was also 100 Oe. (b) Temperature dependence on the ac susceptibility of	

- AgFe₃(OH)₆(SO₄)₂ measured under an ac field, $H_{ac} = H_0 \sin(2\pi ft)$ for $H_0 = 3$ Oe and $f = 2$ Hz (\circ), 20 Hz (Δ), and 200 Hz (\square). 56
- Figure 2.6.** ZFC susceptibilities for the jarosite compounds prepared in this study: Pb_{0.5}Fe₃(OH)₆(SO₄)₂ (\circ), AgFe₃(OH)₆(SO₄)₂ (Δ), TlFe₃(OH)₆(SO₄)₂ (\square), KFe₃(OH)₆(SeO₄)₂ (\times), and RbFe₃(OH)₆(SeO₄)₂ (\diamond). The maximum in T_N ranges from 56.4 - 66.5 K. Plots are offset for clarity. 56
- Figure 2.7.** X-band EPR spectrum of a) NaFe₃(OH)₆(SO₄)₂ recorded at 10 K and b) AgFe₃(OH)₆(SO₄)₂ recorded at 100 K. 58
- Figure 2.8.** Mössbauer spectrum of Pb_{0.5}Fe₃(OH)₆(SO₄)₂ recorded at a) 150 K and b) 4.2 K. Note that only one quadrupole doublet is observed above T_N , which is split into a six-line pattern due to the ordered magnetism below T_N . 59
- Figure 2.9.** Antiferromagnetic spin arrangement in molecular dimers and trimers of iron. The antiferromagnetic coupling is easily achieved in dimers by the antiparallel pairing of spins on the individual iron centers. The ground state magnetic structure of trimers cannot be satisfied by antiparallel spin pairing; the frustrated spin is indicated by the double-headed arrow. 61
- Figure 3.1.** Single crystal susceptibility of KFe₃(OH)₆(SO₄)₂. When H is applied perpendicular to the kagomé layers, the transition is sharp, but when applied parallel to the layers, only a broad signal is observed. 70
- Figure 3.2.** Magnetization curve of (a) powdered RbFe₃(OH)₆(SO₄)₂ at 54 K (\circ), 57 K (\square), and 60 K (Δ) and of (b) powdered Pb_{0.5}Fe₃(OH)₆(SO₄)₂ at 40 K (\circ), 46.5 K (\square), and 51 K (Δ). The solid line shows linear behavior of $M(H)$ above T_N . The labeled arrows represent the abscissa of the critical field, defined as the maximum of $(dM/dH)|_T$, which is determined from the maximum in the plots of Figure B.16. 71
- Figure 3.3.** Temperature dependence of the critical field and magnetization difference in RbFe₃(OH)₆(SO₄)₂ and Pb_{0.5}Fe₃(OH)₆(SO₄)₂. The data are fit to a power law function to extrapolate H_c and ΔM values at $T = 0$. 72
- Figure 3.4.** Magnetization curve for argentojarosite powder at 5 K measured upon increasing (\bullet) and decreasing (\circ) applied field with fits of the linearly behaved regions. The inset shows the first derivative, (dM/dH) , from which we define the critical field, H_c . 73
- Figure 3.5.** (a) Temperature-dependence of the induced magnetization shown at $T = 5$ K (\circ), 45 K (Δ), and 54 K (\square). (b) Temperature-dependence of the average critical field, H_c , from 5 - 60 K. 74

- Figure 3.6.** Temperature-dependence of the deviation in the magnetization from the spin-only value $5.92 \mu_B$. Δm saturates at $0.0535 \mu_B$ below $T = 40$ K. 75
- Figure 3.7.** The kagomé lattice with spins in one possible ground state configuration. Note that the spins on a hexagon can be rotated out of the plane about the dotted ellipse without changing the energy, thus giving rise to an infinite number of degenerate ground states. 77
- Figure 3.8.** Interlayer exchange through Fe d_{z^2} and the closed-shell interlayer cation of A_1 symmetry. 80
- Figure 3.9.** Ordering temperature v. interlayer spacing (d_{003}) in iron jarosites. 80
- Figure 3.10.** Magnetostructural trends in iron jarosites. Plotted are the ordering temperature, T_N v. a) O(1)···H distance and b) O(1)···H—O(3) angle. 81
- Figure 3.11.** Field-dependent behavior of antiferromagnetically-coupled layers of canted spins by the application of a strong critical field, H_c . Below H_c (left), only antiferromagnetism is observed. Above H_c (right), ferromagnetic ordering results from the alignment of the spins with the applied field. 83
- Figure 3.12.** a) π -symmetry pathway involving overlap of d_{xz} , d_{yz} of V^{3+} with the sp^3 lone pair of the bridging hydroxy group. b) σ -symmetry pathway involving overlap of $d_{x^2-y^2}$ of Fe^{3+} with the sp^3 hybrid orbitals forming the Fe—O bonds. 85
- Figure 3.13.** (Left) Magnetic unit cell of $NaV_3(OD)_6(SO_4)_2$. A metamagnet, having ferromagnetic layers with alternating net moments pointing in opposite directions, results in a magnetic cell that is double the crystallographic cell. (Right) Ordering temperature v interlayer spacing, d_{003} , for vanadium jarosites with different interlayer cations. 86
- Figure 4.1.** Magnetoelectronic correlation in jarosites emphasizing the need to go to late metals for nearest-neighbor antiferromagnetic coupling. 93
- Figure 4.2.** Magnetic Jahn-Teller distortions prevalent in molecular triangles relieve spin frustration by providing a 2 (coupled) + 1 (uncoupled) ground state. 94
- Figure 4.3.** Structure of a) lindgrenite, $Cu_3(OH)_2(MoO_4)_2$, and the layer-expanded versions b) (pip) $Cu_3(OH)_2(MoO_4)_2$ and c) (4,4'-bipy) $Cu_3(OH)_2(MoO_4)_2$. Light blue spheres are Cu, green spheres are Mo, red spheres are O, dark blue spheres are N, gray spheres are C, and white spheres are H. The bottom panel shows the alternating corner- and edge-sharing connectivity of the triangles within 1-D chains. 103

- Figure 4.4.** Powder X-ray diffraction patterns of a) clinoatacamite and b) zinc paratacamite. Although the structures are similar, the most distinguishing feature is found at $\approx 40^\circ 2\theta$, which occurs as multiple peaks in a), but a single peak in b) due to the difference in symmetry. 104
- Figure 4.5.** X-ray crystal structure of clinoatacamite, $\text{Cu}_2(\text{OH})_3\text{Cl}$, showing distorted kagomé layers (left) that come about due to Jahn-Teller distorted Cu^{2+} ions between the layers (right). 104
- Figure 4.6.** X-ray crystal structure of zinc paratacamite, $\text{ZnCu}_3(\text{OH})_6\text{Cl}_2$, showing perfect rhombohedral symmetry with no kagomé lattice distortions. 105
- Figure 4.7.** Atom labeling scheme for triangles of clinoatacamite and Zn-paratacamite. 106
- Figure 4.8.** (a) ZFC (\circ) and FC (\square) susceptibility of $\text{Cu}_3(\text{OH})_2(\text{MoO}_4)_2$. (b) Magnetization of $\text{Cu}_3(\text{OH})_2(\text{MoO}_4)_2$ showing hysteresis at 5 K (\circ), but not above the ordering temperature at 20 K (\square). 107
- Figure 4.9.** (a) ZFC (\circ) and FC (\square) susceptibility and (b) magnetization versus field of $(4,4'\text{-bipy})\text{Cu}_3(\text{OH})_2(\text{MoO}_4)_2$. 108
- Figure 4.10.** ZFC (\circ) and FC (\square) molar susceptibility in clinoatacamite, showing a sharp transition to a ferromagnetically ordered state at 6.5 K. 109
- Figure 4.11.** Evidence for ferromagnetic ordering in $\text{Cu}_2(\text{OH})_3\text{Cl}$ given by (a) hysteresis in the magnetization with a coercive field of $H_{\text{coercive}} \approx 1100$ Oe, and b) a frequency independent maximum in the ac susceptibility. 109
- Figure 4.12.** ZFC (\circ) and FC (\square) molar susceptibility in zinc paratacamite, showing no transition to LRO. The black line on the plot is the expected molar susceptibility of a simple Cu^{2+} paramagnet, following the Curie law. The inset shows that to temperatures down to 2 K, the susceptibility does not reach a maximum and no discontinuities in $\chi(T)$ are observed. 110
- Figure 4.13.** Comparison of the ZFC susceptibility measured for clinoatacamite (\square) which orders ferromagnetically at 6.5 K, and zinc paratacamite (\circ) which shows no ordering transition to temperatures down to 2 K. 110
- Figure 5.1.** Tetragonal unit cell of La_2CuO_4 . Green circles are La, black circles are Cu, and white circles are O. 118
- Figure 5.2.** Spin frustration in transport of a hole in a square lattice. Nearest-neighbor exchange results in frustration in mechanism (a), but transport through a singlet pair of spins in the RVB liquid state shown in (b) does not create frustration. 118

Figure 5.3.	X-ray powder pattern of $\text{KFe}_{3-x}\text{V}_x(\text{OH})_6(\text{SO}_4)_2$.	122
Figure 5.4.	ZFC (\circ) and FC (\square) susceptibility of mixed-metal $\text{KFe}_{3-x}\text{V}_x(\text{OH})_6(\text{SO}_4)_2$, showing no features of pure $\text{KFe}_3(\text{OH})_6(\text{SO}_4)_2$ or $\text{KV}_3(\text{OH})_6(\text{SO}_4)_2$.	123
Figure 5.5.	IR spectrum of $\text{KFe}_{3-x}\text{V}_x(\text{OH})_6(\text{SO}_4)_2$, emphasizing the presence of an H—O—H bending mode at 1630 cm^{-1} .	123
Figure 5.6.	pXRD pattern of $\text{Fe}^{2+}\text{Fe}_2^{3+}(\text{OH})_2(\text{PO}_4)_2$.	125
Figure 5.7.	ZFC (\diamond) and FC (100 Oe, \square ; 2000 Oe, \circ) d.c. susceptibility of $\text{Fe}^{2+}\text{Fe}_2^{3+}(\text{OH})_2(\text{PO}_4)_2$.	126
Figure 5.8.	(a) Hysteresis loop for $\text{Fe}^{2+}\text{Fe}_2^{3+}(\text{OH})_2(\text{PO}_4)_2$, with $H_{\text{coercive}} \approx 0.6$ T. (b) Remanent magnetization at $H_{\text{cooling}} = 2000$ Oe, measured in zero field.	126
Figure 5.9.	Mössbauer spectrum of $\text{Fe}^{2+}\text{Fe}_2^{3+}(\text{OH})_2(\text{PO}_4)_2$, providing evidence for mixed-valency.	127
Figure 5.10.	IR spectrum of $\text{Fe}^{2+}\text{Fe}_2^{3+}(\text{OH})_2(\text{PO}_4)_2$ showing no H—O—H bending mode.	127
Figure 5.11.	ZFC dc susceptibility of $\text{NaFe}_3(\text{OH})_6(\text{SO}_4)_2$ recorded before γ -irradiation (\circ) and after 96 h of irradiation (\square).	131
Figure 5.12.	Comparison of $\text{ZnCu}_3(\text{OH})_6\text{Cl}_2$ before (\circ) and after (\square) γ -irradiation.	131
Figure A.1.	Thermal ellipsoid plot for $\text{Pb}_{0.5}\text{Fe}_3(\text{OH})_6(\text{SO}_4)_2$. Ellipsoids shown at 50% probability.	137
Figure A.2.	Recorded (top) and simulated (bottom) pXRD pattern of $\text{Pb}_{0.5}\text{Fe}_3(\text{OH})_6(\text{SO}_4)_2$.	137
Figure A.3.	Thermal ellipsoid plot for $\text{AgFe}_3(\text{OH})_6(\text{SO}_4)_2$. Ellipsoids shown at 50% probability.	141
Figure A.4.	Recorded (top) and simulated (bottom) pXRD pattern of $\text{AgFe}_3(\text{OH})_6(\text{SO}_4)_2$.	141
Figure A.5.	Thermal ellipsoid plot for $\text{TlFe}_3(\text{OH})_6(\text{SO}_4)_2$. Ellipsoids shown at 50% probability.	145
Figure A.6.	Recorded (top) and simulated (bottom) pXRD pattern of $\text{TlFe}_3(\text{OH})_6(\text{SO}_4)_2$.	145
Figure A.7.	Thermal ellipsoid plot for $\text{KFe}_3(\text{OH})_6(\text{SeO}_4)_2$. Ellipsoids shown at 50% probability.	149
Figure A.8.	Recorded (top) and simulated (bottom) pXRD pattern of $\text{KFe}_3(\text{OH})_6(\text{SeO}_4)_2$.	149
Figure A.9.	Thermal ellipsoid plot for $\text{RbFe}_3(\text{OH})_6(\text{SeO}_4)_2$. Ellipsoids shown at 50% probability.	153

Figure A.10.	Recorded (top) and simulated (bottom) pXRD pattern of $\text{RbFe}_3(\text{OH})_6(\text{SeO}_4)_2$.	153
Figure A.11.	A portion of the crystal structure of $(\text{pip})\text{Cu}_3(\text{OH})_2(\text{MoO}_4)_2$, rendered with 40% thermal ellipsoids. One inversion center is located at the center of the piperazine ring, the other is located on Cu(2). Atoms labeled with letters correspond to symmetry equivalent atoms as found in Tables A.28 and A.29. Hydrogen atoms are not labeled.	157
Figure A.12.	A portion of the crystal structure of $(\text{bipy})\text{Cu}_3(\text{OH})_2(\text{MoO}_4)_2$, rendered with 40% thermal ellipsoids. Inversion centers are located between C(5) and C(6) (symmetry equivalent atoms) and on Cu(2). Only one orientation of the bipyridine ligand is shown for clarity. Atoms labeled with letters correspond to symmetry equivalent atoms as found in Tables A.34 and A.35. Hydrogen atoms are not labeled.	162
Figure A.13.	Thermal ellipsoid plot for $\text{Cu}_2(\text{OH})_3\text{Cl}$. Ellipsoids shown at 50% probability.	169
Figure A.14.	Recorded (top) and simulated (bottom) pXRD pattern of $\text{Cu}_2(\text{OH})_3\text{Cl}$.	169
Figure A.15.	Thermal ellipsoid plot for $\text{ZnCu}_3(\text{OH})_6\text{Cl}_2$. Ellipsoids shown at 50% probability.	173
Figure A.16.	Recorded (top) and simulated (bottom) pXRD pattern of $\text{ZnCu}_3(\text{OH})_6\text{Cl}_2$.	173
Figure A.17.	X-ray powder pattern of $\text{KFe}_3(\text{OH})_6(\text{CrO}_4)_2$.	177
Figure A.18.	X-ray powder pattern of $\text{KFe}_{3-x}\text{V}_x(\text{OH})_6(\text{SO}_4)_2$.	177
Figure A.19.	X-ray powder pattern of $\text{Fe}^{2+}\text{Fe}_2^{3+}(\text{OH})_2(\text{PO}_4)_2$.	180
Figure B.1.	ZFC and FC molar susceptibility for $\text{Pb}_{0.5}\text{Fe}_3(\text{OH})_6(\text{SO}_4)_2$.	183
Figure B.2.	AC susceptibility of $\text{PbFe}_3(\text{OH})_6(\text{SO}_4)_2$ measured under various frequencies.	183
Figure B.3.	Curie-Weiss plot for $\text{Pb}_{0.5}\text{Fe}_3(\text{OH})_6(\text{SO}_4)_2$.	184
Figure B.4.	ZFC and FC molar susceptibility for $\text{AgFe}_3(\text{OH})_6(\text{SO}_4)_2$.	185
Figure B.5.	AC susceptibility of $\text{AgFe}_3(\text{OH})_6(\text{SO}_4)_2$ measured under various frequencies.	185
Figure B.6.	Curie-Weiss plot for $\text{AgFe}_3(\text{OH})_6(\text{SO}_4)_2$.	186
Figure B.7.	ZFC and FC molar susceptibility for $\text{TlFe}_3(\text{OH})_6(\text{SO}_4)_2$.	187
Figure B.8.	AC susceptibility of $\text{TlFe}_3(\text{OH})_6(\text{SO}_4)_2$ measured under various frequencies.	187
Figure B.9.	Curie-Weiss plot for $\text{TlFe}_3(\text{OH})_6(\text{SO}_4)_2$.	188

Figure B.10.	ZFC and FC molar susceptibility for $\text{KFe}_3(\text{OH})_6(\text{SeO}_4)_2$.	189
Figure B.11.	AC Susceptibility of $\text{KFe}_3(\text{OH})_6(\text{SeO}_4)_2$ measured under various frequencies.	189
Figure B.12.	Curie-Weiss plot for $\text{KFe}_3(\text{OH})_6(\text{SeO}_4)_2$.	190
Figure B.13.	ZFC and FC molar susceptibility for $\text{RbFe}_3(\text{OH})_6(\text{SeO}_4)_2$.	191
Figure B.14.	AC susceptibility of $\text{RbFe}_3(\text{OH})_6(\text{SeO}_4)_2$ measured under various frequencies.	191
Figure B.15.	Curie-Weiss plot for $\text{RbFe}_3(\text{OH})_6(\text{SeO}_4)_2$.	192
Figure B.16.	First derivative plots of the magnetization with applied field at a given temperature for (a) $\text{RbFe}_3(\text{OH})_6(\text{SO}_4)_2$ and (b) $\text{Pb}_{0.5}\text{Fe}_3(\text{OH})_6(\text{SO}_4)_2$. The maximum gives the critical field for the ferromagnetic alignment of canted spins between layers.	193
Figure B.17.	Curie-Weiss plot for $\text{Cu}_3(\text{OH})_2(\text{MoO}_4)_2$.	194
Figure B.18.	Curie-Weiss plot for $(4,4'\text{-bipy})\text{Cu}_3(\text{OH})_2(\text{MoO}_4)_2$.	194
Figure B.19.	Curie-Weiss plot for $\text{Cu}_2(\text{OH})_3\text{Cl}$.	195
Figure B.20.	Curie-Weiss plot for $\text{ZnCu}_3(\text{OH})_6\text{Cl}_2$.	195
Figure B.21.	AC susceptibility of $\text{KFe}_{3-x}\text{V}_x(\text{OH})_6(\text{SO}_4)_2$ measured under various frequencies.	196
Figure B.22.	Curie-Weiss plot for $\text{KFe}_{3-x}\text{V}_x(\text{OH})_6(\text{SO}_4)_2$.	196
Figure B.23.	Curie-Weiss plot for $\text{Fe}^{2+}\text{Fe}_3^{3+}(\text{OH})_2(\text{PO}_4)_2$.	197

List of Charts

Chart 2.1	60
------------------	-----------

List of Schemes

Scheme 5.1	128
Scheme 5.2	129

Chapter 1. Spin Frustration and the Kagomé Lattice

1.1 Introduction

A challenging area of research in modern science is the study of cooperative phenomena in systems that have different spatial orientation and sign of interaction, and show local anisotropy of the fundamental interacting unit. One archetype for such a study is magnetic spin in ordered structures. David Jiles, in his book, *Introduction to Magnetism and Magnetic Materials*, poses the key question, “What types of ordered magnetic structures exist and how do they differ?”¹ This question long predates modern science. In Allan Morrish’s classic text, *The Physical Principles of Magnetism*, the author points out that the discovery that lodestone somehow magically attracts iron dates the human knowledge of magnetism to at least 600 B.C.²

Today, the ground states of many magnetic systems, including lodestone, are well understood. However, understanding the magnetic ground states in systems that cannot achieve known configurations due to limitations imposed by conflicting interactions remains an unsolved mystery in modern magnetism. The particular restraint of interest to this work is that of antiferromagnetic coupling of spins on a triangular-based lattice, leading to the physical phenomenon known as *spin frustration*. The overall goal of this thesis research is to prepare pure materials containing the paradigmatic kagomé lattice to probe the magnetic ground states in a spin frustrated system. While this particular problem may seem poised to absorb the curiosity only of condensed matter physicists, this thesis will show that the actual challenge is centered on the inorganic chemist’s ability to prepare spin frustrated compounds in pure forms. With the preparation of pure, spin frustrated systems, the thesis will turn to the search for the experimentally elusive quantum spin liquid state that links the magnetic properties of spin frustration to the resonance valence bond (RVB) theory of high- T_c superconductivity.

The remainder of this chapter will highlight basic concepts of magnetic ordering and present the specific problem of spin frustration. Then, the broader impact of this research will be unveiled by linking spin frustration and the RVB theory of high T_c superconductivity. Finally,

we will review lattice types in which spin frustration has been studied to understand the essential role of synthetic inorganic chemistry to the magnetism problem.

1.2 Spin Frustration

Returning to the question posed by Jiles in the previous section, we now know much about ordered magnetism, from the perspectives of both theory and experiment. As an example, consider the coupling between magnetic spins on a one-dimensional wire. If we impose the restraint that a given spin will be influenced only by its nearest-neighbors (the mean-field approximation),¹ then materials in which all spins are aligned in the same direction are ferromagnetic. By contrast, antiferromagnetism occurs when nearest-neighbors are aligned in an antiparallel manner. When the magnetic moments are antiferromagnetically coupled, but do not have the same magnitude, ferrimagnetism results. Figure 1.1 illustrates these varieties of magnetic coupling.

Using the definition in the foregoing paragraph, a problem arises when competing interactions on a lattice prevent these coupling interactions from being satisfied simultaneously. The term *frustration* first appears in the literature to describe the magnetic interactions in spin glasses made of materials in which ferromagnetic spins are doped into an otherwise non-frustrated lattice of antiferromagnetically coupled spins.³ A spin glass “freezes” into a given

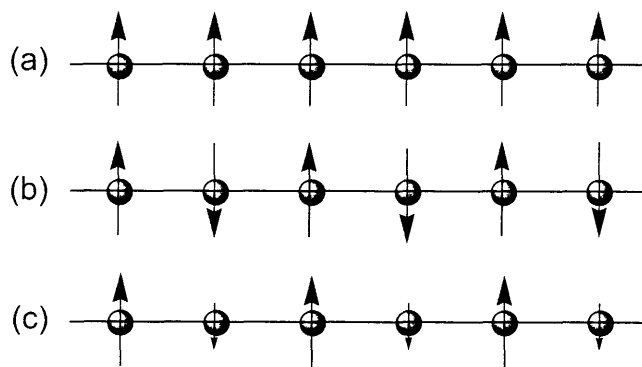


Figure 1.1. Types of magnetic coupling on a one-dimensional wire: a) ferromagnetism; b) antiferromagnetism; c) ferrimagnetism.

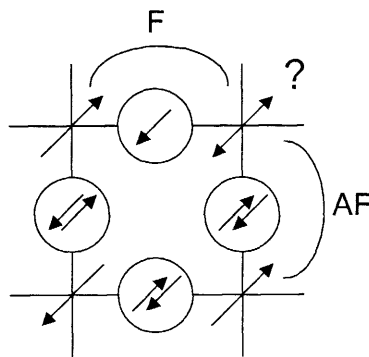


Figure 1.2. Frustration emerging from the spin glass state in doped cuprates.

configuration once the coupling energy between spins is greater than the thermal energy, $k_B T$, to form the ground state. But, as the word *glass* suggests, the spins introduced by doping order randomly with respect to each other, thus there is no true ordered state. An example of a spin glass that will be relevant to the broader impact of this thesis work is $\text{La}_{2-x}(\text{Sr,Ba})_x\text{CuO}_4$, studied extensively here at MIT.⁴ The parent compound La_2CuO_4 has a square lattice of antiferromagnetically coupled Cu^{2+} spins in the ordered state as Figure 1.1b can be extended in two dimensions without competing spin interactions. For $x = 0.04$, a spin glass state emerges as holes are doped into the lattice by removing an electron from one of the oxo bridging ligands⁵ to add ferromagnetic coupling, shown in Figure 1.2.⁶ Cu^{2+} ions are located on the vertices of the square with the oxo ligands illustrated as circles. Magnetic exchange between Cu^{2+} ions occurs via the oxo bridging ligand. By virtue of hole formation, the pair of spins illustrated on the top of the square couple ferromagnetically through the singly occupied orbital of the oxo bridge. But, the pair on the right side of the square wish to couple antiferromagnetically through the pair of electrons bridging these two Cu^{2+} centers. This results in spin frustration.

Although spin glasses represent the first studied examples of frustration, the central problem of this thesis becomes clear when we attempt to couple spins antiferromagnetically on a triangular based lattice. Immediately a problem arises when applying the definitions presented in the beginning of this section. While two spins are allowed to couple in a pairwise antiparallel fashion, an added third spin cannot be simultaneously paired in an antiparallel arrangement to the

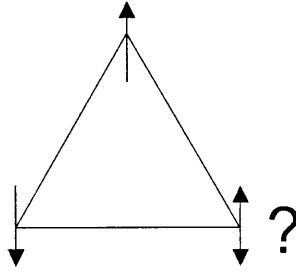


Figure 1.3. Geometric spin frustration on a triangle. Two antiferromagnetically-coupled spins can couple pairwise antiparallel, but a third cannot.

other two, illustrated in Figure 1.3. Unlike the spin glass problem, where doping leads to frustration, this problem arises purely from the spatial orientation of the interacting spins even in a structurally perfect compound, and is referred to as *geometric spin frustration*.

Spin frustrated magnetic materials are readily identified by experimentally probing their bulk magnetic properties. Maxima in the specific heat or in the magnetic susceptibility provide evidence for a transition to a three-dimensional long-range ordered state. Fitting the high temperature magnetic susceptibility to the Curie-Weiss Law,

$$\chi = \frac{C}{T - \Theta} \quad (1.1)$$

we get two parameters, the Curie constant, C , and the Weiss constant, Θ . Relying on a mean-field theory treatment of the Heisenberg-van Vleck-Dirac spin Hamiltonian ($\hat{H} = -2J S_i \cdot S_j$),^{7,8} C gives a measure of the magnetic moment (S), and Θ is indicative of the exchange constant (J). The mean-field equations used to obtain these values are

$$C = N \mu_{\text{eff}}^2 / 3k_B \quad (1.2)$$

$$\Theta = z J S(S+1) / 3k_B \quad (1.3)$$

Where N is Avogadro's number, μ_{eff} is the effective magnetic moment, and z is the number of nearest neighbor spins. The effective moment is determined by the number of unpaired spins, given by $\mu_{\text{eff}} = g\sqrt{S(S+1)}$ in the spin only limit, where g is the gyromagnetic ratio for the electron.

In a non-frustrated antiferromagnet, a fit of the inverse susceptibility vs. temperature gives an extrapolated Θ that is on the same order as the observed transition temperature, T_N . That is, the material would be expected to order at $T = \Theta$ as thermal fluctuations become smaller than the exchange energy and the ground state configuration is achieved. In a spin frustrated system, however, the observed T_N is significantly smaller relative to Θ because the ground state is highly degenerate and fluctuations among states suppress the transition to long-range order. Ramirez has proposed an empirical frustration parameter,

$$f = \frac{|\Theta|}{T_N} \quad (1.4)$$

that allows for simple classification of materials, where $f > 10$ represents highly frustrated materials for which mean-field theory does not adequately describe the magnetic properties of the system.⁹

In order for spin frustration to be manifest in a system, a high degree of symmetry in the interacting spins must be present to give rise to a large number of degenerate ground states. No real materials behave as perfect frustrated systems. They show transitions to a long-range ordered state, but with transition temperatures well below Θ . Nevertheless, Schiffer and Ramirez point out three principal requirements for identifying strong geometric frustration in magnetic real materials:¹⁰

1. The material must be an antiferromagnet ($\Theta < 0$).
2. The material cannot show a transition to long-range order down to temperatures well below Θ (i.e.— f is large)
3. $\chi^{-1}(T)$ must be linear for $T \ll \Theta$ (in order to use a Curie-Weiss analysis)

1.3 Long Range Order (LRO)

Turning now to the issue of long-range magnetic order in low-dimensional systems, theory shows that no model which is infinite in only one dimension can have any transition.^{11,12} These studies are based on the Ising model, in which individual spins have no directionality beyond “spin up” and “spin down.” No transition to a long-range ordered state can occur because

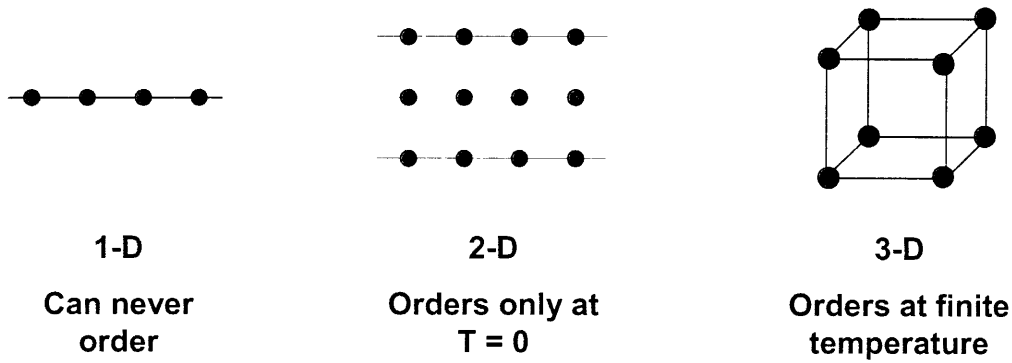


Figure 1.4. Dimensionality and ordering in the Ising model.

the entropy required is larger than the average internal spin energy per lattice point at any temperature. Onsager extended this original work to include two-dimensional ferromagnetic systems.¹³ In this case, order-disorder transitions are observed provided the crystal size is large with respect to the ordered domain size. Wannier later showed that the transition to long-range order in a two-dimensional antiferromagnetic lattice is thermodynamically unfavorable, although there is a finite entropy at absolute zero.¹⁴ Figure 1.4 presents a summary of LRO considering the lattice dimensionality. Turning our attention to a triangular net, Wannier demonstrated that ferromagnetic 2-D systems have a zero-point internal energy $U(0) = -\frac{3}{2} J$ with a Curie ordering temperature, $T_c \approx 1.8 J$. Similar antiferromagnetic systems have $U(0) = -\frac{1}{2} J$ with no observed

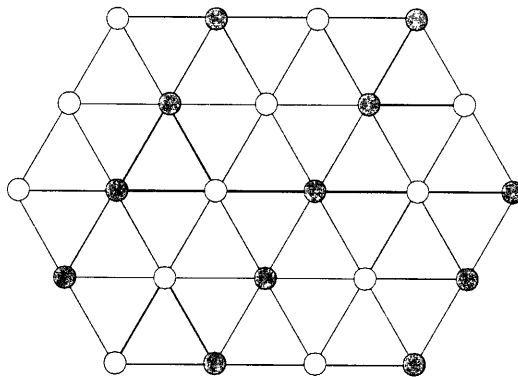


Figure 1.5. One energy minimum in the 2-D triangular Ising net studied by Wannier. Note that each triangle has two antiferromagnetic and one ferromagnetic interaction. Since the rows of spins alternate in this arrangement, no long-range order is possible.

ordering. In the simplest ground state energy minimum, one pair of spins must interact ferromagnetically with alternating rows of up spins and down spins, as drawn in Figure 1.5. Note that neighboring triangles have different local environments (2 up + 1 down or 2 down + 1 up). Therefore, the difference in internal energy and lack of long-range order is easily understood since in a scalar model of antiferromagnetically coupled spins on a triangular array, no spin arrangement in which each triangle has the same ground state configuration is compatible with the lattice.

While the Ising model easily identifies the problem of order on a frustrated lattice, the spins in real magnetic systems are not confined simply to the directions up or down. The Ising model is used because it gives a phase transition with a pure mathematical solution.^{15,16} Real classical spins have directionality with respect to the lattice, and discovering the true ground states in spin frustrated lattices can be better understood by considering either an *XY* model, where the spins are allowed to point in any direction confined to a 2-D plane, or a Heisenberg model, where the spins can point in any direction. The kagomé lattice, comprised of corner-sharing triangles in two-dimensions, is the ideal architecture in which to study spin frustration because all lattice points are symmetrically equivalent. Even in the Heisenberg model, there is still no arrangement that satisfies the pairwise antiferromagnetic arrangement of all three spins.^{9,17} However, unusual ground states are possible in the kagomé antiferromagnet, and their explanation is predicated on careful scrutiny of the definition of antiferromagnetism.¹⁸ In the 1-D wire example of § 1.1, we see that in an antiferromagnet, each pair of spins that makes up the repeat unit results in a net sum of zero. Now, suppose the three spins of a triangle are aligned such that the vector sum of the spins is zero. This results in a 120° arrangement that globally satisfies this consequence of antiferromagnetism. Two such compromised spin arrangements are the so-called $q = 0$ and $q = \sqrt{3} \times \sqrt{3}$ ground states shown on the kagomé lattice in Figure 1.6. Still, phase transitions to a long-range ordered state should not be observed since any spin configuration in which each individual triangle in the lattice is at an energy minimum is a ground state by definition. This gives rise to an enormous number of degenerate ground states. In

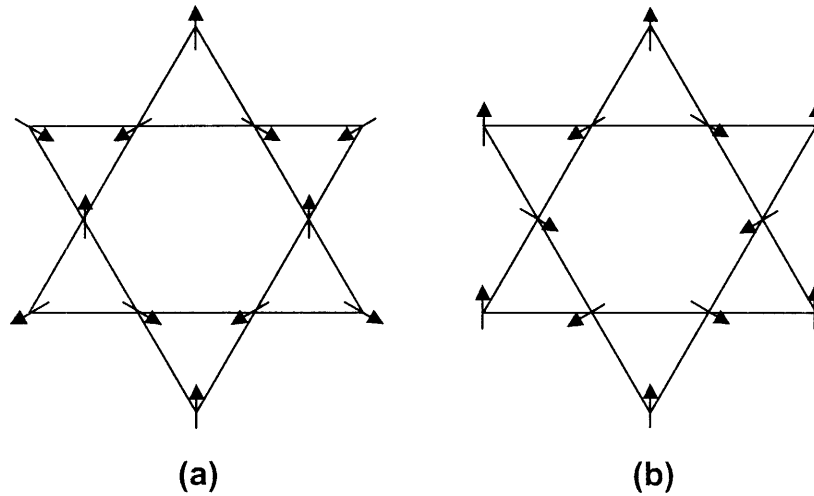


Figure 1.6. Two compromised 120° ground state structures of the kagome antiferromagnet: a) the $q = 0$ and b) the $q = \sqrt{3} \times \sqrt{3}$ spin arrangements.

classical systems, thermal, quantum, or spacial fluctuations among spin configurations of the same energy are sufficient to suppress conventional long-range order, leading to novel spin physics. For quantum spins, where each different spin configuration comprises an eigenstate of different energy, the situation is even more complex, and various theoretical treatments predict a ground state that remains quantum disordered at zero temperature.¹⁸⁻²¹

1.4 Resonating Valence Bond (RVB) Theory

The impetus for studying ordering in the magnetic ground states of spin frustrated systems lies in the relationship between magnetism and high T_c superconductivity. The resonating liquid state, consisting of spin-singlet bonds, has been proposed to explain the scatterless hole transport in high T_c superconductors²²⁻²⁴ and properties of other strongly correlated systems.^{25,26} In this resonating valence bond (RVB) model, spins spontaneously pair into singlet bonds, which fluctuate (hence the name *liquid*) between many different configurations. This leads to a highly degenerate ground state owing to an exceptionally large number of different spin configurations at the same energy.^{9,27-30} Fluctuations resulting from the resonating pair leads to a quantum spin liquid which should show a signature singlet-to-triplet

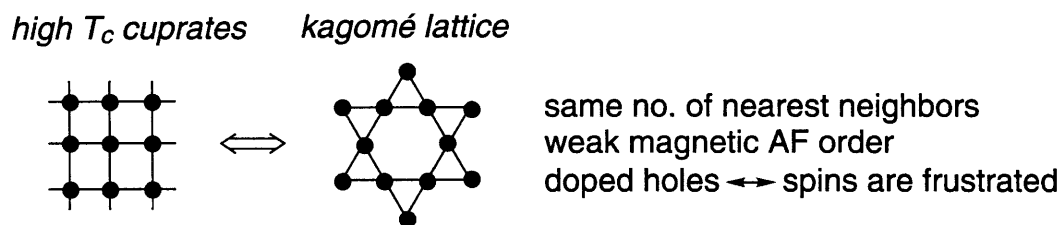


Figure 1.7. Parallels between the square lattice of high T_c cuprate superconductors and the kagomé lattice of Heisenberg antiferromagnets.

spin gap.^{21,31-34} Thus, high degeneracy in the ground state of a kagomé antiferromagnet leaves open the possibility that quantum spin fluctuations are large enough in these systems to suppress long-range order and therefore permit RVB to be established.^{21,32}

In the high T_c superconducting cuprates, the role of spin correlation is essential to understanding the mechanism of superconductivity. Returning to the $\text{La}_{2-x}(\text{Sr,Ba})_x\text{CuO}_4$ compounds introduced as spin glasses in § 1.2, once $x = 0.15$, the material undergoes a superconducting transition at $T_c \approx 37$ K.^{24,35} The parent copper oxide material is a pure insulator with a 2-D square lattice of antiferromagnetically coupled spins that show a transition to 3-D LRO at $T_N \approx 300$ K. The relationship between the short-range antiferromagnetic interactions associated with the ordered state at zero doping and the formation of singlet pairs in the superconducting state remains unclear. It is thought that the quantum spin liquid phase resulting from RVB is most likely to be found for magnetically frustrated spins on a low dimensional lattice.³³ Of the various lattices that can support the RVB state, a Heisenberg antiferromagnet on a pure kagomé lattice emerges prominently.^{36,37} Therefore, one would ideally study the frustration associated with the RVB state in material that cannot show LRO at any temperature. This thesis work will produce materials that are poised to undertake such studies, and Figure 1.7 illustrates the similarities in the square lattice cuprate superconductors and the kagomé antiferromagnet. In both cases, there are four nearest-neighbor spins contributing to the system and there is antiferromagnetic ordering in the parent materials. However, the key difference is the spin glass vs. geometric frustration issue discussed in § 1.2. The kagomé lattice can

unambiguously reveal the ground state physics of frustration without structural disorder.

1.5 Synthetic Targets in Solid-State Chemistry

Several lattice types present geometric spin frustration. In two dimensions, the edge-sharing triangular lattice (triangular) and the corner-sharing triangular lattice (kagomé) show frustration, as has been illustrated in § 1.3. Their three-dimensional analogs, the face-centered-cubic and pyrochlore lattices, respectively, also demonstrate spin frustration.

Spin frustration in the triangular lattice has been studied at length in several extended-lattice systems. The simplest example of a frustrated 2-D system is the binary solid VCl_2 , which shows an antiferromagnetically ordered ground state below $T = 36$ K.³⁸ Here, two hexagonal layers of V^{2+} ions are separated by two Cl^- layers in the CdI_2 structure. The ternary solids NaTiO_2 ,³⁹ and LiCrO_2 ⁴⁰ have also been studied. The lattice is made up of hexagonal layers of transition metal ions with three hexagonal layers (O^{2-} , Na^+ or Li^+ , O^{2-}) in between. Here, non-magnetic ions keep the layers of magnetic transition-metal ions well separated. LiCrO_2 orders antiferromagnetically at 15 K. VCl_2 and LiCrO_2 show classical Néel ordering with spins parallel to the c axis of the hexagonal cell.^{38,40} Here, two opposite ferromagnetic mean-field sublattices fully describe the system, and no new spin physics emerges. The compound NaTiO_2 once generated much interest as a strongly frustrated magnet because the $S = \frac{1}{2}$ spin of Ti^{3+} should show pronounced quantum spin effects at low temperature.³⁹ Original magnetic studies showed no transition to a long-range ordered state in susceptibility measurements down to 1.4 K, although high temperature susceptibility measurements give a Weiss constant $\Theta = 1000$ K, fitting Ramirez's definition of strong frustration. However, this compound is extremely unstable and decomposes over the course of several hours. Moreover, crystallographic studies show that even pure samples undergo a second-order Jahn-Teller distortion.⁴¹ Above 250 K, the structure has hexagonal symmetry, but the compound adopts a monoclinic structure as confirmed by neutron studies at 5 K. In the monoclinic phase, isosceles triangles (two distinct $\text{Ti}\cdots\text{Ti}$ distances) result, thus structural deformation in NaTiO_2 inhibits its use for studying spin frustration.

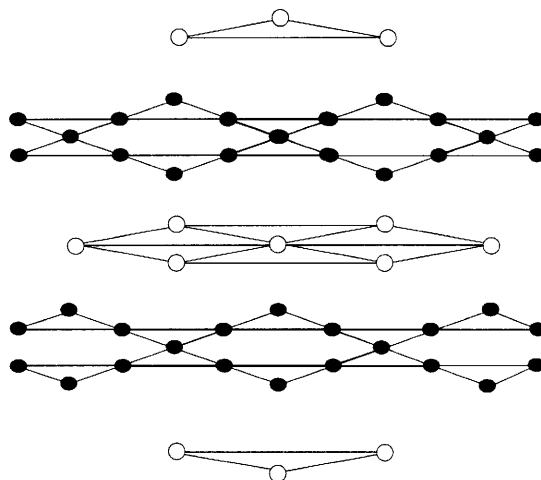


Figure 1.8. Magnetic lattice of SCGO garnets. Kagomé planes of Cr^{3+} ions (\bullet) are separated by triangular planes of Cr^{3-} (\circ).

The layered garnet $\text{SrCr}_{9x}\text{Ga}_{12-9x}\text{O}_{19}$ (SCGO) has been intensely studied since $\frac{2}{3}$ of the magnetic Cr^{3+} sites are contained within corner-sharing kagomé layers, as shown in Figure 1.8.⁴²⁻⁴⁶ It was once considered the ideal compound for spin frustration studies because for $x = 0.89$, no transition to LRO was observed, despite the strong antiferromagnetic coupling of nearest-neighbor ions (indicated by $\Theta \approx -500$ K).⁴⁷ However, alternating layers of edge-sharing triangles and corner-sharing kagomé triangles in SCGO compounds complicate the interpretation of their magnetic properties. These two types of sites engender different coupling constants, thus making it difficult to understand all of the ground-state interactions. The short correlation length in the neutron scattering indicates that SCGO is a spin glass, again meaning that the frustration comes not from the inherent geometry of the lattice, rather from site disorder. Although it is postulated that the kagomé layers order antiferromagnetically, site disorder in the triangular layers gives rise to the observed spin glass behavior, again rendering the material unsuitable for studying the physics of spin frustration.

Of the various known compounds comprised exclusively of kagomé layers, the jarosite family of minerals has long been regarded as a principal model for studying spin frustration.^{9,17,18,27,48-51} This alunite family subgroup, based on the $\text{KFe}_3(\text{OH})_6(\text{SO}_4)_2$ parent, is

composed of kagomé layers formed from $\text{Fe}^{\text{III}}_3(\mu\text{-OH})_3$ triangles.⁵² The alternate faces of neighboring triangles are capped by the sulfate dianion, with the potassium cation sitting in an icosahedral site opposite the sulfate caps. Jarosite is a naturally occurring mineral, and Na^+ , Rb^+ , Ag^+ , and $\frac{1}{2} \text{Pb}^{2+}$ can replace the monovalent K^+ cation in nature. Although promising due to their crystallographic regularity, jarosites have been far less studied than SCGO materials because they have been notoriously difficult to prepare in stoichiometrically pure form. Magnetically, jarosites show a transition to LRO with T_N varying from 18 - 65 K.^{50,53} This discrepancy in reported ordering temperature is thought to be due to impurities. Thus, the starting point of this thesis work is to explore chemical methods to prepare pure jarosites for the study of spin frustrated magnetism.

In the copper mineral literature, the compound volborthite, $\text{Cu}_3\text{V}_2\text{O}_7(\text{OH})_2 \cdot 2\text{H}_2\text{O}$,⁵⁴ is comprised of a 2-D kagomé-like network, although the compound contains isosceles triangles since it crystallizes in a monoclinic space group. In this compound, no evidence for LRO has been observed at temperatures down to 1.8 K, and the layers are magnetically isolated, with a 7 Å interlayer separation. There are also minerals of the atacamite family, with the parent compound having the formula $\text{Cu}_2(\text{OH})_2\text{Cl}$.⁵⁵⁻⁵⁹ The magnetic properties of these materials remains unexplored, and this thesis work will develop the magnetism of these $S = \frac{1}{2}$ kagomé materials.

1.6 Outline and Scope of this Thesis

This thesis is structured about the synthesis, structure, and magnetism of two kagomé materials—the iron-based materials called jarosites (Chapters 2 and 3) and copper-based materials called atacamites (Chapter 4). The interplay between synthesis, structure, and magnetism is an important theme in this research, and it only makes sense to present them together for a given set of compounds. After characterizing the ground states of pure frustrated systems, Chapter 5 then presents attempts to further our studies by doping electrons or holes into

both of these kagomé lattices in order to examine transport properties with the objective of experimentally probing the connection between RVB theory and spin frustration.

In Chapter 2, we start, by looking at the power of synthesis to prepare a pure kagomé lattice and thus enable a complete and reliable characterization of the ground state magnetism of iron jarosites. A full description of the crystal structure is presented, highlighting the structural homology among members of this family of minerals. The similarity in structure reveals that the magnetic properties are intrinsic to the geometry of the lattice and are fully contained within the basic magnetic unit, the intralayer $\text{Fe}_3(\mu\text{-OH})_3$ triangle. Pure iron jarosites display a sharp antiferromagnetic ordering at $T_N = 61.4 \pm 5$ K, in contrast to the widely varying results of the past.

Chapter 3 focuses on the origin of LRO in iron jarosites, where we find that the Dzyaloshinsky-Moriya (DM) interaction is responsible for the canted spin structure. Field-dependent magnetization experiments reveal that LRO arises from antiferromagnetic stacking of an out-of-plane moment developed from spin canting within the kagomé layers. We determine the spin canting angle as well as the DM interaction energy using magnetization and single crystal neutron studies. We discover that the DM interaction energy, D , is tiny with respect to the overall nearest-neighbor exchange coupling, and that interlayer exchange is negligible. Consequently, canted spins with long correlation lengths within an isolated kagomé layer give rise to the sizable observed ordering temperature. The chapter ends by distinguishing between LRO in iron jarosites and LRO in vanadium jarosite analogs studied in the group.

Chapter 4 highlights the need to prepare $S = \frac{1}{2}$ materials with the goal of diminishing the strength of the DM interaction by lowering the total spin of the system in order to study short-range correlations. Two closely related materials, clinoatacamite, $\text{Cu}_2(\text{OH})_3\text{Cl}$ and zinc paratacamite, $\text{ZnCu}_3(\text{OH})_6\text{Cl}_2$, provide the keystone compounds for this study. We find that for zinc paratacamite, a pure 2-D $S = \frac{1}{2}$ kagomé lattice, no magnetic ordering is observed down to 2 K, although the nearest-neighbor exchange is strongly antiferromagnetic, as indicated by a Weiss

constant ($\Theta \approx -300$ K). Thus, this is the most highly frustrated system to date, and provides the best model closely representing the known high T_c superconductors.

Chapter 5 presents experiments designed to dope electrons and holes into the fully characterized kagomé lattice. Although these efforts have to date been unsuccessful, we have discovered a new synthetic route to a mixed-valent iron mineral, barbosalite, and we understand more about the reactivity of hydroxy-bridged copper species. We present the magnetic properties of barbosalite and discuss the reactivity of zinc paratacamite.

Following the chapters, there are two appendices containing raw data that, while important to other experts and perhaps to posterity, would make the chapters cumbersome to read. Appendix A contains details of structural acquisition for all of the compounds presented in this thesis, as well as the tables of atomic coordinates and thermal parameters. Appendix B contains all of the full magnetic data for the new iron jarosites prepared in this study, as well as the Curie-Weiss plots from which Θ is determined for all compounds.

1.7 References

1. Jiles, D. *Introduction to Magnetism and Magnetic Materials*. 2nd ed.; Chapman & Hall: New York, 1998; p 228.
2. Morrish, A. H. *The Physical Principles of Magnetism*. ed.; IEEE Press: Piscataway, NJ, 2001; p 1.
3. Toulouse, G. *Commun. Phys. (London)* **1977**, *2*, 115-119.
4. Aharony, A.; Birgeneau, R. J.; Coniglio, A.; Kastner, M. A.; Stanley, H. E. *Phys. Rev. Lett.* **1988**, *60*, 1330-1333.
5. Tranquada, J. M.; Heald, S. M.; Moodenbaugh, A. R. *Phys. Rev. B* **1987**, *36*, 5263-5274.
6. Birgeneau, R. J.; Aharony, A.; Belk, N. R.; Chou, F. C.; Endoh, Y.; Greven, M.; Hosoya, S.; Kastner, M. A.; Lee, C. H.; Lee, Y. S.; Shirane, G.; Wakimoto, S.; Wells, B. O.; Yamada, K. *J. Phys. Chem. Solids* **1995**, *56*, 1913-1919.
7. Heisenberg, W. Z. *Phys.* **1928**, *49*, 619-636.
8. Dirac, P. A. M. *Proc. Roy. Soc. (London)* **1929**, *A123*, 714-733.
9. Ramirez, A. P. *Annu. Rev. Mater. Sci.* **1994**, *24*, 453-480.

Chapter 1

10. Schiffer, P.; Ramirez, A. P. *Comments Condens. Matter Phys.* **1996**, *18*, 21-50.
11. Herzfeld, K. F.; Goepfert-Mayer, M. J. *Chem. Phys.* **1934**, *2*, 38-45.
12. Montroll, E. W. *J. Chem. Phys.* **1941**, *2*, 38-45.
13. Onsager, L. *Phys. Rev.* **1944**, *65*, 117-149.
14. Wannier, G. H. *Phys. Rev.* **1950**, *79*, 357-364.
15. Ising, E. Z. *Phys.* **1925**, *31*, 253-258.
16. Baxter, R. J.; Wu, F. Y. *Phys. Rev. Lett.* **1973**, *31*, 1294-1297.
17. Greedan, J. E. *J. Mater. Chem.* **2001**, *11*, 37-53.
18. Harris, A. B.; Kallin, C.; Berlinsky, A. J. *Phys. Rev. B* **1992**, *45*, 2899-2919.
19. Chalker, J. T.; Eastmond, J. F. G. *Phys. Rev. B* **1992**, *26*, 14201-14204.
20. Sindzingre, P.; Misguich, G.; Lhuillier, C.; Bernu, B.; Pierre, L.; Waldtmann, C.; Everts, H. U. *Phys. Rev. Lett.* **2000**, *84*, 2953-2956.
21. Koretsune, T.; Ogata, M. *Phys. Rev. Lett.* **2002**, *89*, 116401/1-4.
22. Anderson, P. W. *Mater. Res. Bull.* **1973**, *8*, 153-160.
23. Anderson, P. W. *Science* **1987**, *235*, 1196-1198.
24. Anderson, P. W.; Baskaran, G.; Zou, Z.; Hsu, T. *Phys. Rev. Lett.* **1987**, *58*, 2790-2793.
25. Baskaran, G.; Zou, Z.; Anderson, P. W. *Solid State Commun.* **1987**, *63*, 973-976.
26. Ueda, K.; Kontani, H.; Sigrist, M.; Lee, P. A. *Phys. Rev. Lett.* **1996**, *76*, 1932-1935.
27. Chalker, J. T.; Holdsworth, P. C. W.; Shender, E. F. *Phys. Rev. Lett.* **1992**, *68*, 855-858.
28. Reimers, J. N.; Berlinsky, A. J. *Phys. Rev. B* **1993**, *48*, 9539-9554.
29. Shender, E. F.; Holdsworth, P. C. W. Order by Disorder and Topology in Frustrated Magnetic Systems. In *Fluctuations and Order*, Millonas, M., Ed. Springer-Verlag: Berlin, 1995; pp 259-279.
30. Lhuillier, C.; Misguich, G. *Lect. Notes Phys.* **2001**, *595*, 161-190.
31. Lauchli, A.; Poilblanc, D. *Phys. Rev. Lett.* **2004**, *92*, 236404/1-4.
32. Coldea, R.; Tennant, D. A.; Tyliczynski, Z. *Phys. Rev. B* **2003**, *68*, 134424/1-16.
33. Wen, X.-G. *Phys. Rev. B* **2002**, *65*, 165113/1-37.

Chapter 1

34. Santos, L.; Baranov, M. A.; Cirac, J. I.; Everts, H. U.; Fehrmann, H.; Lewenstein, M. *Phys. Rev. Lett.* **2004**, *93*, 030601/1-4.
35. Goodenough, J. B.; Zhou, J. S.; Chan, J. *Phys. Rev. B* **1993**, *47*, 5275-5286.
36. Hastings, M. B. *Phys. Rev. B* **2001**, *63*, 014413/1-16.
37. Waldtmann, C.; Everts, H. U.; Bernu, B.; Lhuillier, C.; Sindzingre, P.; Lecheminant, P.; Pierre, L. *Eur. Phys. J. B* **1998**, *2*, 501-507.
38. Hirakawa, K.; Ikeda, H.; Kadowaki, H.; Ubukoshi, K. *J. Phys. Soc. Jpn.* **1983**, *52*, 2882-2887.
39. Hirakawa, K.; Kadowaki, H.; Ubukoshi, K. *J. Phys. Soc. Jpn.* **1985**, *54*, 3526-3536.
40. Tauber, A.; Moller, W. M.; Banks, E. *J. Solid State Chem.* **1972**, *4*, 138-152.
41. Clarke, S. J.; Fowkes, A. J.; Harrison, A.; Ibberson, R. M.; Rosseinsky, M. J. *Chem. Mater.* **1998**, *10*, 372-384.
42. Lee, S. H.; Broholm, C.; Aeppli, G.; Perring, T. G.; Hesse, B.; Taylor, A. *Phys. Rev. Lett.* **1996**, *76*, 4424-4427.
43. Broholm, C.; Aeppli, G.; Espinosa, G. P.; Cooper, A. S. *Phys. Rev. Lett.* **1990**, *65*, 3173-3176.
44. Ramirez, A. P.; Espinosa, G. P.; Cooper, A. S. *Phys. Rev. Lett.* **1990**, *64*, 2070-2073.
45. Keren, A.; Mendels, P.; Horvatic, M.; Ferrer, F.; Uemura, Y. J.; Mekata, M.; Asano, T. *Phys. Rev. B* **1998**, *57*, 10745-10749.
46. Keren, A.; Uemura, Y. J.; Luke, G.; Mendels, P.; Mekata, M.; Asano, T. *Phys. Rev. Lett.* **2000**, *84*, 3450-3453.
47. Obradors, X.; Labarta, A.; Isalgue, A.; Tejada, J.; Rodriguez, J.; Pernet, M. *Solid State Commun.* **1988**, *65*, 189-192.
48. Sachdev, S. *Phys. Rev. B* **1992**, *45*, 12377-12396.
49. Ritchey, I.; Chandra, P.; Coleman, P. *Phys. Rev. B* **1993**, *47*, 15342-15345.
50. Wills, A. S.; Harrison, A. *J. Chem. Soc., Faraday Trans.* **1996**, *92*, 2161-2166.
51. Ramirez, A. P. In *Handbook on Magnetic Materials*; Busch, K. J. H., Ed. Elsevier Science: Amsterdam, 2001; *13*, pp 423-520.
52. Jambor, J. L. *Can. Mineral.* **1999**, *37*, 1323-1341.
53. Inami, T.; Nishiyama, M.; Maegawa, S.; Oka, Y. *Phys. Rev. B* **2000**, *61*, 12181-12186.

Chapter 1

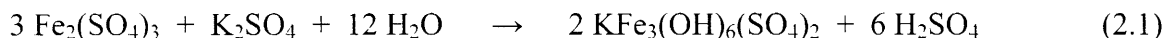
54. Hiroi, Z.; Hanawa, M.; Kobayashi, N.; Nohara, M.; Takagi, H.; Kato, Y.; Takigawa, M. *J. Phys. Soc. Jpn.* **2001**, *70*, 3377-3384.
55. Oswald, H. R.; Guenter, J. R. *Journal of Applied Crystallography* **1971**, *4*, 530-531.
56. Parise, J. B.; Hyde, B. G. *Acta Crystallogr., Sect. C* **1986**, *C42*, 1277-1280.
57. Jambor, J. L.; Dutrizac, J. E.; Roberts, A. C.; Grice, J. D.; Szymanski, J. T. *Can. Mineral.* **1996**, *34*, 61-72.
58. Grice, J. D.; Szymanski, J. T.; Jambor, J. L. *Can. Mineral.* **1996**, *34*, 73-78.
59. Braithwaite, R. S. W.; Mereiter, K.; Paar, W. H.; Clark, A. M. *Mineral. Mag.* **2004**, *68*, 527-539.

Chapter 2. Preparation and Characterization of Jarosites, the First Family of Compounds to Contain a Pure Kagomé Lattice

2.1 Introduction

Of the synthetic targets highlighted in Chapter 1, jarosites emerge as the prime candidates for the study of spin frustration since all magnetic ions reside within the 2-D kagomé layers. Jarosite was first discovered in the Barranco Jaroso mine in southern Spain in 1852,¹ and has since been found on every continent except Antarctica.² Experimental investigation of iron jarosites as model systems for the problem of spin frustration began with Takano's report of the magnetic susceptibility in 1968.^{3,4}

Historically, jarosites have been prepared in the laboratory by precipitation from hydrolyzed ferric sulfate in aqueous acidic solutions heated from 100 – 200° under hydrothermal conditions^{5,6} by the overall reaction



Materials prepared in this manner are subject to compositional variation. Under the reaction conditions, the monovalent K^+ cation is replaced by hydronium, and/ or the Fe^{3+} site occupancy within the lattice is only 70 – 94%. Consequently, the magnetic properties of these materials are highly sample-dependent. While iron jarosites show long-range antiferromagnetic order, noted by a maximum in the susceptibility, the ordering temperature differs widely from study to study.^{3,4,7-10} In some cases, a secondary maximum is observed. The hydronium congener, $(\text{H}_3\text{O})\text{Fe}_3(\text{OH})_6(\text{SO}_4)_2$, is the only outlier in that a spin glass transition is observed at 15 K in both the ac magnetic susceptibility and in neutron studies. Interestingly, this is the only compound that has been prepared with near complete occupancy (97%).¹¹ As emphasized in § 1.2, however, spin glass behavior implies that site disorder is also prevalent this particular analog.^{10,12,13} As would be expected, evidence of spin glass behavior is accentuated upon doping of diamagnetic Ga^{3+} ¹⁴ and Al^{3+} ^{15,16} into the lattice. Table 2.1 highlights this variation in magnetic properties with chemical composition.

In addition to the issue of magnetic lattice site occupancy, only microcrystalline powders result from these reactions, and single crystal X-ray diffraction studies are difficult.¹⁷⁻¹⁹ With the

Table 2.1. Magnetic properties of jarosites prepared by precipitation methods.

Chemical Formula	T_N (K)	Θ (K)	Reference
$\text{KFe}_3(\text{OH})_6(\text{SO}_4)_2$	65	-700	8
$\text{Na}_{0.59}\text{Fe}_{2.86}(\text{OH},\text{H}_2\text{O})_{6.55}(\text{SO}_4)_2$	62, 42	-667(5)	9
$\text{Ag}_{0.31}\text{Fe}_{2.68}(\text{OH},\text{H}_2\text{O})_{7.01}(\text{SO}_4)_2$	51	-677(4)	9
$\text{Rb}_{0.57}\text{Fe}_{2.62}(\text{OH},\text{H}_2\text{O})_{6.81}(\text{SO}_4)_2$	47	-688(5)	9
$\text{KFe}_{2.85}\text{Al}_y(\text{OD})_6(\text{SO}_4)_2$	64.5, 57.0	-663(2)	16
$\text{KFe}_{2.76}\text{Al}_y(\text{OD})_6(\text{SO}_4)_2$	60.5, 45.5	-630(5)	16
$\text{KFe}_{2.61}\text{Al}_y(\text{OD})_6(\text{SO}_4)_2$	53.5, 41.5	-430(19)	16

goal of using jarosites to investigate the ground state magnetic properties of the kagomé lattice, the work presented in this Chapter develops a redox-based synthetic method for the preparation of pure and highly crystalline iron jarosites. With pure materials in hand, we describe the structure, present the bulk magnetic properties, and spectroscopically probe the local structure about Fe^{3+} .

2.2 Experimental

2.2.1 General Procedures

All chemicals of reagent or analytical grade were obtained from Aldrich or Strem, and they were used without purification. Hydrothermal reactions were carried out in Teflon-lined pressure vessels, which were purchased from Parr Instruments. A Fisher Isotemp programmable oven with forced-air circulation was used to obtain the desired temperature profiles for hydrothermal reactions. Chemical analyses were conducted by the H. Kolbe Mikroanalytisches Laboratorium.

2.2.2 Synthesis of $\text{Pb}_{0.5}\text{Fe}_3(\text{OH})_6(\text{SO}_4)_2$

A 23-mL Teflon liner was charged with 0.168 g of 2.0 mm iron wire (3.00 mmol). In a separate, small beaker, 0.199 g of $\text{Pb}(\text{NO}_3)_2$ (0.600 mmol) was dissolved in 10 mL of deionized water. Into this solution, 0.50 mL of concentrated sulfuric acid (9.0 mmol) was added via Mohr pipet. PbSO_4 was observed to precipitate after which 0.58 mL of concentrated HNO_3 (9.0 mmol)

was added to the mixture via Mohr pipet; the resulting mixture was stirred for 15 min. The beaker mixture was poured into the Teflon liner, including several backwashings to transfer all of the lead sulfate precipitate. The liner was sealed and placed into a steel hydrothermal bomb in an Aldrich Atmosbag under an atmosphere of oxygen. The tightened bomb was heated at a rate of 5 °C/min to 210 °C, which was maintained for 72 h. The oven was cooled to room temperature at a rate of 0.1 °C/min. A yellow-orange crystalline powder was isolated from the bottom of the liner; it was washed with deionized water and then 150 mL of a 1:1 HNO₃:H₂O mixture which was heated to 100 °C in order to remove the residual lead sulfate byproduct. The powder was then washed a second time with deionized water, and dried in air. Yield: 0.302 g (53.4% based on starting iron). The product was determined to be plumbojarosite, Pb_{0.5}Fe₃(OH)₆(SO₄)₂, by powder X-ray diffraction. Anal. Calcd. for H₆Pb_{0.5}Fe₃S₂O₁₄: H, 1.07; Pb, 18.33; Fe, 29.64; S 11.34. Found: H, 1.12; Pb, 18.26; Fe, 29.72; S, 11.41.

2.2.3 Synthesis of AgFe₃(OH)₆(SO₄)₂ and TlFe₃(OH)₆(SO₄)₂

A 125-mL Teflon liner was charged with 0.563 g of 2.0 mm iron wire (10.1 mmol). In a separate beaker, the nitrate salt of the interlayer cation (1.711 g of silver nitrate (10.07 mmol), 2.662 g of thallium nitrate (9.99 mmol)) was dissolved in 50 mL of deionized water. Into this solution, 2.2 mL of concentrated sulfuric acid (40 mmol) was added via Mohr pipet, and the resulting solution was allowed to stir for 15 min. The beaker solution was poured into the Teflon liner, which was then capped and placed into a steel hydrothermal bomb under an atmosphere of oxygen using an Aldrich Atmosbag. The tightened bomb was heated at a rate of 5 °C/min to 210 °C, which was maintained for 72 h. The oven was then cooled to room temperature at a rate of 0.1 °C/min. A yellow-orange crystalline powder was isolated from the walls and the bottom of the Teflon liner, and the product was washed with deionized water and dried in air. The powder was identified by powder X-ray diffraction. Yield: 1.697 g of AgFe₃(OH)₆(SO₄)₂ (88.5% based on starting Fe) and 1.466 g of TlFe₃(OH)₆(SO₄)₂ (66.1% based on starting Fe). Anal. Calcd. for H₆AgFe₃S₂O₁₄: H, 1.06; Ag, 18.94; Fe, 29.41; S, 11.26. Found: H, 1.12; Ag, 18.82; Fe 29.50; S,

11.35. Anal. Calcd. for $H_6TlFe_3S_2O_{14}$: H, 0.91; Tl, 30.68; Fe, 25.15; S, 9.63. Found: H, 0.92; Tl, 30.44; Fe 25.17; S, 9.65.

2.2.4 Synthesis of $KFe_3(OH)_6(SeO_4)_2$ and $RbFe_3(OH)_6(SeO_4)_2$

A 23-mL Teflon liner was charged with 0.168 g of 2.0 mm iron wire (3.00 mmol). In a separate, small beaker, the interlayer cation salt (0.660 g of potassium selenate (2.98 mmol), 0.299 g rubidium nitrate (2.03 mmol)) was dissolved in 10 mL of deionized water. Into this solution, 0.37 mL of selenic acid (6.0 mmol) and 0.58 mL of concentrated nitric acid (9.0 mmol) were added via Mohr pipet for the potassium analog, and 0.19 mL of selenic acid and 0.26 mL of concentrated nitric acid (4.0 mmol) were added for the rubidium analog. The resulting solution was allowed to stir for 15 min. The beaker solution was poured into the Teflon liner, which was then capped and placed into a steel hydrothermal bomb under an atmosphere of oxygen in an Aldrich Atmosbag. The tightened bomb was heated at a rate of 5 °C/min to 210 °C, which was maintained for 72 h. The oven was then cooled to room temperature at a rate of 0.1 °C/min. This reaction is limited by the passivation of the iron wire, which was physically removed from complete reaction mixtures. A yellow-orange crystalline powder was isolated from the walls and bottom of the Teflon liner, and the product was washed with deionized water and dried in air. The powder was identified by powder X-ray diffraction. Yield: 0.327 g of $KFe_3(OH)_6(SeO_4)_2$ (55.2% based on starting Fe) and 0.112 g of $RbFe_3(OH)_6(SeO_4)_2$ (17.5% based on starting Fe). Anal. Calcd. for $H_6KFe_3Se_2O_{14}$: H, 1.02; K, 6.58; Fe, 28.18; Se, 26.56. Found: H, 0.98; K, 6.48; Fe 28.24; Se, 26.50. Anal. Calcd. for $H_6RbFe_3Se_2O_{14}$: H, 0.94; Rb, 13.33; Fe, 26.14; Se, 24.64. Found: H, 0.92; Rb, 13.25; Fe 26.24; Se, 24.71.

2.2.5 X-ray Diffraction

Powder X-ray diffraction patterns were measured using a Rigaku RU300 rotating anode X-ray diffractometer with Cu $K\alpha$ radiation ($\lambda = 1.5405 \text{ \AA}$), which was wavelength-selected with a single-crystal graphite monochromator. Samples were spread onto a glass slide fixed with

double-sided Scotch tape. Samples were rotated through $2\theta/\theta$ space and intensity was recorded as a function of 2θ from $10 - 60^\circ$. Patterns were indexed with MDI Jade software version 7.0 and referenced using the JCPDS powder diffraction database.

X-ray diffraction data were collected using a Siemens three-circle single crystal diffractometer on a SMART platform equipped with a CCD area or APEX detector. Data were acquired at -90°C using Mo $K\alpha$ radiation ($\lambda = 0.71073 \text{ \AA}$), which was wavelength-selected with a single-crystal graphite monochromator. For each crystal, at least four data sets of 40-s frames were collected over a hemisphere of reciprocal space using ω scans and a -0.3° scan width. The data frames were integrated to hkl /intensity, and final unit cells were calculated using the SAINT program. Space group assignments were based on systematic absences, E statistics, and successful refinement of the structures. Structures were solved by the Patterson methods with the aid of successive difference Fourier maps and were refined against all data using version 6.1 of the Brüker SHELXTL suite of programs. Thermal parameters for all heavy atoms were refined anisotropically.

2.2.6 Physical Methods

IR spectra were recorded in KBr pellets on a Nicolet Magna-IR 860 spectrometer equipped with a KBr beam splitter and a DTGS detector. For each spectrum, 32 scans were acquired with 4 cm^{-1} resolution over an energy range of $4000 - 400 \text{ cm}^{-1}$.

Magnetic susceptibilities were determined on powdered samples contained in gelatin capsules using a Quantum Design MPMSR2 Susceptometer over a $5 - 300 \text{ K}$ temperature range at field strengths varying from $0 - 50 \text{ kOe}$. For each dc susceptibility data point, the average of three measurements of 32 scans over a 4 cm scan length was acquired. Data were corrected for core diamagnetism using Pascal's constants.²⁰ Ac susceptibilities were recorded for each compound under an ac field, $H_{ac} = H_0 \sin(2\pi ft)$ for $H_0 = 3 \text{ Oe}$ and $f = 2, 20, \text{ and } 200 \text{ Hz}$.

Zero-field cooled (ZFC) susceptibilities were measured by first cooling the samples from 300 K to 5 K under zero field. Dc susceptibility was then measured in a field $H_m = 100 \text{ Oe}$ as a

function of temperature as the sample was warmed from 5 – 300 K. Field-cooled (FC) susceptibilities were measured in a similar fashion, except the cooling and measuring fields were both 100 Oe. Curie-Weiss analysis was done on the inverse susceptibility of ZFC samples under $H_m = 2000$ Oe over the temperature range 150 – 300 K. Plots are printed in Appendix B.

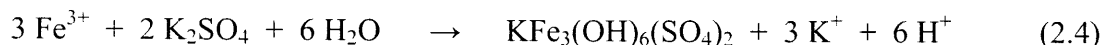
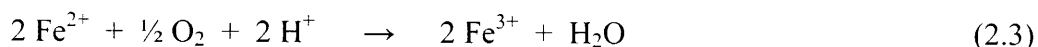
Mössbauer spectra were recorded on a MS1 spectrometer (WEB Research Co. Model W200 instrument) with a ^{57}Co source in a Rh matrix kept at room temperature. The samples were cooled with liquid He to obtain 4.2 K at 150 K data. The high temperature spectra were fit to Lorentzian line shapes by using the WMOSS software package, and isomer shifts were referenced to a room temperature iron foil calibration. The solid samples were prepared by suspending powdered material (≈ 50 mg) in Apiezon N grease and placing the mixture into a nylon sample holder.

X-band EPR spectra were recorded on a Brüker EMX spectrometer fitted with an Oxford Instruments liquid helium cryostat. Solid samples were prepared by mixing ≈ 10 mg of jarosite powder with diamagnetic sodium bicarbonate, which was introduced into a quartz EPR tube in an acetone slurry, which provides a frozen matrix for low temperature measurements. Data were fit using the Brüker WINEPR suite of programs.

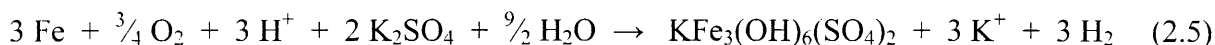
2.3 Results

2.3.1 Redox-based Synthesis

The hurdles to obtaining magnetically pure materials mentioned in § 2.1 have been overcome with the development of redox-based hydrothermal methods for synthesis.²¹⁻²³ Control over the precipitation of the jarosite is achieved by inserting two oxidation-reduction steps prior to jarosite precipitation,

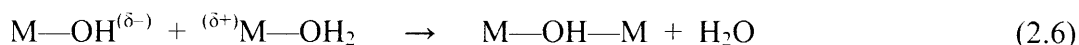


The overall reaction is therefore,



The redox steps of equations 2.2 and 2.3 proceed with a driving force of $E^\circ = 0.97 \text{ V}$.

The kagomé lattice is assembled through ololation of Fe^{3+} ions, which are slowly generated throughout the course of the hydrothermal process via controlled redox reactions.²⁴ Ololation is the condensation reaction that proceeds via dissociative nucleophilic substitution with M—OH as the nucleophile and H_2O leaving group, resulting in the formation of a metal hydroxy bridged species. This reaction occurs with aquo-hydroxy and aquo precursors,



The condensation shown in equation 2.6 is very sensitive to pH, as the formation of the reactant and product species depends on the $\text{p}K_a$ of the formed hydroxy-bridged species. If the solution is too acidic, the starting nucleophile is unable to form; if it is too basic, the product undergoes further deprotonation to yield give the oxo-bridged species. In the redox-based hydrothermal method of jarosite synthesis, the pH of the reaction stays relatively constant at around 0.5, unlike the rapid decrease in pH during a single-step precipitation reaction. This moderation in pH is an important factor in obtaining crystalline material.

The reaction presented above is general, and with simple modifications in the ions used, we have prepared several iron jarosite analogs. The monovalent alkali K^+ ion and can be replaced by Na^+ or Rb^+ by using their respective sulfate salts.²² Substituting the non-alkali metal cations Ag^+ and Tl^+ have been made by starting with their nitrate salts. Nitrate salts are necessary here due to the low solubility products of Ag_2SO_4 , Tl_2SO_4 . Nitrate does not interfere with the synthetic method outlined, and no sulfate impurities are found in the products. In a similar manner, divalent $\frac{1}{2} \text{ Pb}^{2+}$ can replace the K^+ ion, however, the reaction is less clean in that the cloudy PbSO_4 precipitate is observed immediately upon addition of H_2SO_4 ($K_{\text{sp}} = 2.5 \times 10^{-8}$ at 25 °C). Nonetheless, the remaining PbSO_4 can be cleanly removed after the reaction by washing the product mixture with hot nitric acid solution. The synthesis outlined above also affords substitution of the SO_4^{2-} anion. In this manner, SeO_4^{2-} derivatives of jarosites have been prepared

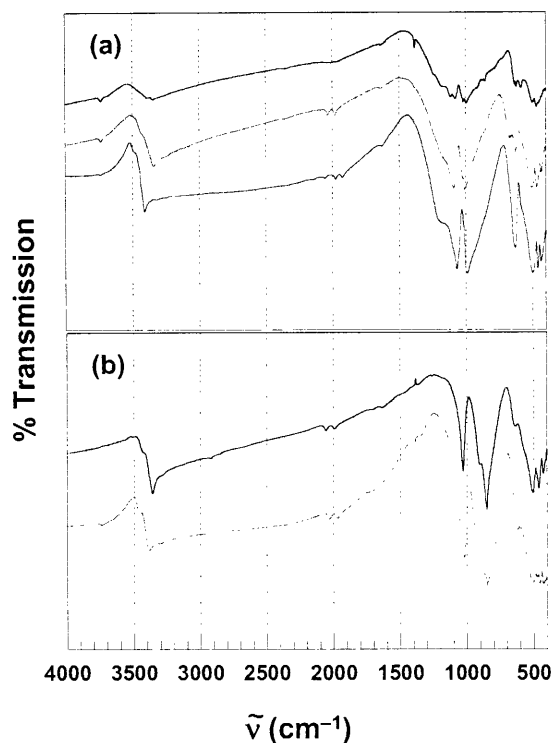


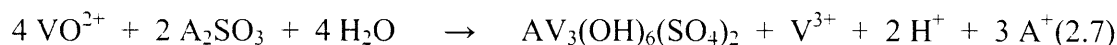
Figure 2.1. FTIR spectra of the (a) sulfate-capped iron jarosites, $\text{Pb}_{0.5}\text{Fe}_3(\text{OH})_6(\text{SO}_4)_2$ (top) $\text{AgFe}_3(\text{OH})_6(\text{SO}_4)_2$ (middle), and $\text{TlFe}_3(\text{OH})_6(\text{SO}_4)_2$ (bottom) and (b) selenate-capped iron jarosite analogs $\text{KFe}_3(\text{OH})_6(\text{SO}_4)_2$ (top) and $\text{RbFe}_3(\text{OH})_6(\text{SO}_4)_2$ (bottom).

for K^+ and Rb^+ as the monovalent cations. Attempts to incorporate Na^+ into the selenate reaction result in the formation of $\text{Fe}_2(\text{SeO}_3)_3 \cdot 3\text{H}_2\text{O}$ powder, as determined by powder X-ray diffraction. We have also prepared a chromate derivative of jarosite, $\text{KFe}_3(\text{OH})_6(\text{CrO}_4)_2$, starting from Fe metal and chromic acid, H_2CrO_4 , under ambient room atmosphere. Although the powder X-ray diffraction pattern shows only the jarosite analog product (Appendix A), magnetic studies reveal the presence of CrO_2 impurities, as one may expect starting from Fe^0 and Cr^{6+} . Hydrothermal reactions done in this manner failed to produce any solid product.

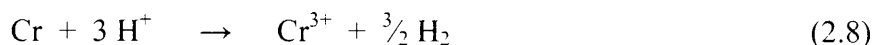
Chemical analysis of all pure jarosite samples used in this study gave an Fe^{3+} content of $100.0 \pm 0.3\%$ and an A^+ content of $99.5 \pm 0.5\%$. Additionally, IR spectroscopy (Figure 2.1) shows no significant absorption feature at 1630 cm^{-1} , which is indicative of an H—O—H bending mode of water.^{7,21,25} This observation speaks directly to a jarosite lattice with completely

occupied Fe^{3+} sites. As we have previously discussed, protonation of OH^- by H^+ to form H_2O prevents the accrual of negative charge on kagomé layers possessing M^{3+} site vacancies. In stoichiometrically pure jarosites, as is the case reported here, water is absent in the lattice and consequently this absorption should not be observed.

In addition to iron compounds, vanadium and chromium jarosites have been studied extensively in our group. Reactions with vanadium or chromium also proceed by redox methods, although the reactions giving pure materials proceed slightly differently. In the case of vanadium, a reductive method starting from VOCl_2 gives rise to the largest crystals,²¹



For chromium, the Cr^{2+} oxidation state is not accessible starting from Cr^0 metal, thus the reaction proceeds directly from the oxidation by protons,²³



Lattice assembly then proceeds in a manner similar to equation 2.4 listed above for iron.

Given the modular nature of our synthetic route, we also attempted to use redox-based hydrothermal methods to prepare hybrid inorganic-organic materials with phosphonate (RPO_3^{2-}) anions, noting that the phosphonate cap should have the same structural binding motif as the sulfate group, as we will see in the next section. Although kagomé-lattice-containing materials with a $\text{CH}_3\text{PO}_3^{2-}$ capping group are known for d^0 V^{5+} ,²⁶ Mo^{6+} ,^{27,28} and W^{6+} ²⁹ ions comprising the kagomé layers, no paramagnetic analogs are known. In contrast to the jarosites, these diamagnetic materials are made under basic conditions with added tetraethylammonium hydroxide. Under the oxidizing acidic hydrothermal conditions of equation 2.5, we find cleavage of the C—P bond in the phosphonate group to give phosphate materials. Realizing that phosphate can also cap the triangles of the jarosite lattice, we also tried to prepare iron jarosites with phosphate anions that are charge-balanced by lanthanide of the proposed formula $\text{LnFe}_3(\text{OH})_6(\text{PO}_4)_2$. In order to keep the pH at ≈ 0.5 , we added nitric acid, knowing that the nitrate anion does not interfere with jarosite synthesis from our reactions with Ag, Tl, and Pb. Despite taking clues from the synthetic scheme outlined above, reactions with lanthanides

(starting from their nitrate salts) result in the formation of thermodynamically stable lanthanide phosphates, as determined by powder X-ray diffraction.

2.3.2 Structural Chemistry

Figure 2.2 shows the X-ray powder diffraction pattern for each of the iron jarosites prepared in this study, with full data, Miller indices, and comparison with simulated patterns based on single crystal structures given in Appendix A. All jarosites crystallize in the $R\bar{3}m$ space group, and details regarding the refined data and cell parameters are provided in Appendix A. The connectivity of the heavy atoms in the asymmetric unit is illustrated in Figure 2.3 for the $\text{AgFe}_3(\text{OH})_6(\text{SO}_4)_2$ exemplar. The asymmetric unit consists of the iron atom, the oxygen of the hydroxide bridge, the central atom (sulfur or selenium) of the capping group and two of its oxygens (the unique apical oxygen and one oxygen of the pyramidal base of the capping group,

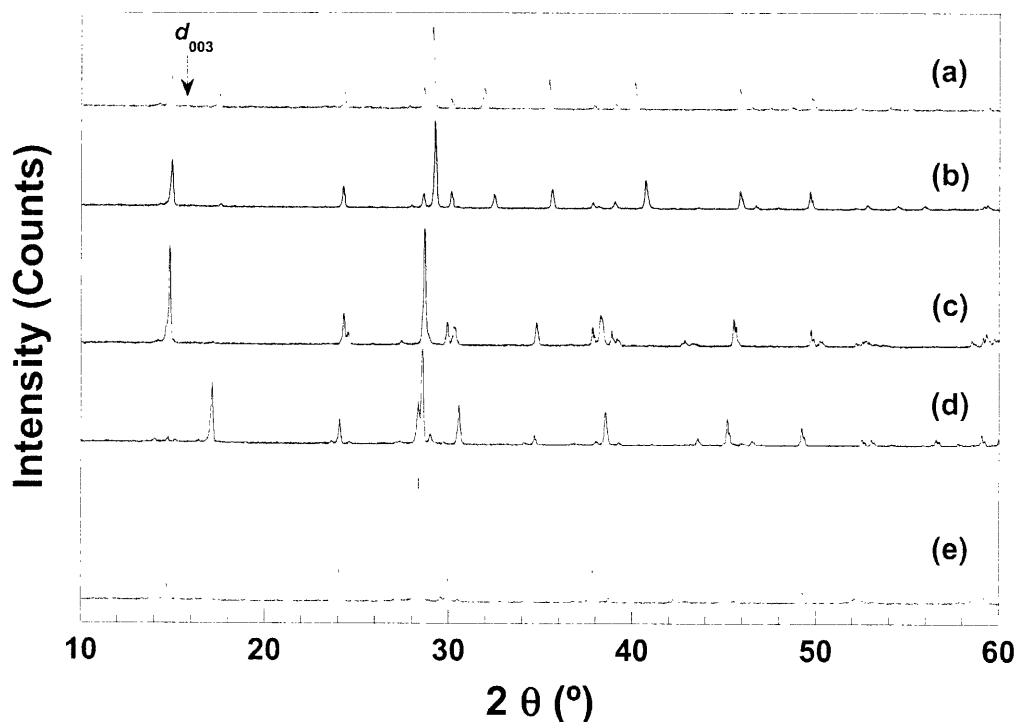


Figure 2.2. Powder X-ray diffraction patterns of a) $\text{Pb}_{0.5}\text{Fe}_3(\text{OH})_6(\text{SO}_4)_2$, b) $\text{AgFe}_3(\text{OH})_6(\text{SO}_4)_2$, c) $\text{TlFe}_3(\text{OH})_6(\text{SO}_4)_2$, d) $\text{KFe}_3(\text{OH})_6(\text{SeO}_4)_2$, and e) $\text{RbFe}_3(\text{OH})_6(\text{SO}_4)_2$. Note that for $\text{Pb}_{0.5}\text{Fe}_3(\text{OH})_6(\text{SO}_4)_2$, the (003) reflection occurs at $15.85^\circ 2\theta$.

as projected over the 3-fold axis). The consistency of the asymmetric unit is an especially noteworthy observation for $\text{Pb}_{0.5}\text{Fe}_3(\text{OH})_6(\text{SO}_4)_2$, whose structure was first predicted to display Pb^{2+} residency in alternating interlayers in order to maintain charge neutrality.³⁰ Such a distribution of Pb^{2+} cations should exhibit a c axis doubled superstructure on the unit cell, which has been observed ($c = 34 \text{ \AA}$) for mined samples of $\text{Pb}_{0.5}\text{Fe}_3(\text{OH})_6(\text{SO}_4)_2$.³¹ Notwithstanding, we find a c axis dimension of $16.795(6) \text{ \AA}$ for the stoichiometrically pure sample of $\text{Pb}_{0.5}\text{Fe}_3(\text{OH})_6(\text{SO}_4)_2$, consistent with the known structures of all other pure jarosite compounds. The Pb^{2+} occupancy is $\frac{1}{2}$ that of a monovalent interlayer cation, and Pb^{2+} is disordered along the three-fold inversion axis. In further support of these single crystal results, the first observed reflection in the powder diffraction pattern of $\text{Pb}_{0.5}\text{Fe}_3(\text{OH})_6(\text{SO}_4)_2$ appears at $2\theta = 15.852^\circ$, corresponding to a d_{003} spacing of 5.586 \AA , which is typical for the single interlayer distance of jarosites; there is no diffraction feature at 11 \AA corresponding to a c -axis doubled superstructure. The calculated cell constants from powder data yield an a axis of 7.310 \AA and a c axis of 16.737 \AA , in excellent agreement with single crystal data.

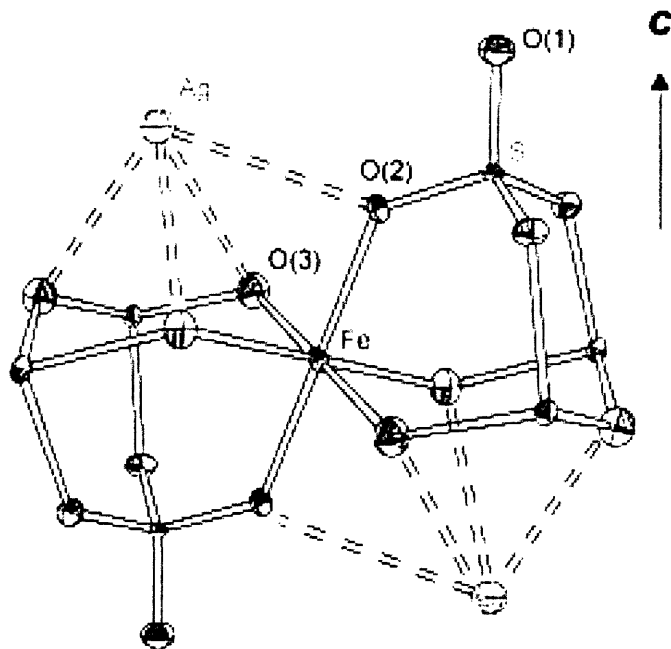


Figure 2.3. Basic structural unit of $\text{AgFe}_3(\text{OH})_6(\text{SO}_4)_2$, highlighting the intralayer structure and local structure about the Fe^{3+} center. Ellipsoids are shown at 50% probability.

As highlighted by the bond distances and angles shown in Table 2.2, the structure of the jarosite intralayer is remarkably similar regardless of the identity of the interlayer cation or capping group. Only slight structural disparities in jarosite intralayers arise as a result of differing SO_4^{2-} and SeO_4^{2-} anions, which cap the Fe_3 triangular unit of the kagomé lattice with the basal plane of the TO_4^{2-} tetrahedron. The surface area of the basal plane for SO_4^{2-} is 3.28 \AA^2 vs 3.69 \AA^2 for SeO_4^{2-} . The larger surface area of the latter capping anion arises from the longer T—O bond length ($d_{\text{avg}}(\text{S—O}) = 1.46 \text{ \AA}$, $d_{\text{avg}}(\text{Se—O}) = 1.64 \text{ \AA}$). The expanded SeO_4^{2-} polyhedron is conveyed to the $\text{Fe}_3(\mu\text{-OH})_3$ triangle that it caps, though not as much as might be expected owing to a constricted Fe—O(2)—Se bond angle ($\angle\text{Fe—O(2)—Se} = 130.4$ vs $\angle\text{Fe—O(2)—S} = 126.3$). The Fe \cdots Fe distance of the selenate jarosites is slightly elongated, producing an expanded Fe—O(3)—Fe angle (134.2° for sulfate vs 137.1° for selenate). The pyramidal base of the TO_4^{2-} cap is also manifested in the metric of the FeO_6 pseudo-octahedra, which is highlighted in Figure 2.4 by the red outline. All Fe atoms of a triangle in the same kagomé plane must be normal to the c axis as crystallographically imposed by the unique Fe atom in the $R\bar{3}m$ space group. As shown in Figure 2.4, however, the FeO_6 pseudo-octahedra tilt to produce corrugated kagomé layers. The angle of the Fe—O(2) bond from the c axis provides a convenient marker of the tilt angle, which we define as $\{90^\circ - [\text{Fe}\cdots\text{Fe—O(2)}]\}$. The tilt angle of $\approx 17^\circ$ for sulfate-capped jarosites is slightly larger than the $\approx 14^\circ$ tilt angle observed in selenate-capped jarosites.

Outside of the minor structural differences arising from the different capping groups, the rigidity of the jarosite structure is noteworthy, especially for the Pb^{2+} compound. Kintoreite, $\text{PbFe}_3(\text{OH},\text{H}_2\text{O})_6(\text{PO}_4)_2$, a structural analog to $\text{Pb}_{0.5}\text{Fe}_3(\text{OH})_6(\text{SO}_4)_2$, has distorted PbO_{12} icosahedra that are ascribed to the inert s -pair effect.³² The Pb—O(2) distances in kintoreite range from 2.6 – 3.3 \AA and the Pb—O(3) distances range from 2.6 – 3.0 \AA . We observe no such distortion in jarosites, and observe single-valued Pb—O(2) and Pb—O(3) distances of 2.97 and 2.78 \AA respectively; these values are consistent with those observed for jarosite with interlayer

Table 2.2. Selected bond distances (Å) and bond angles (°) for jarosites.

Bond	Bond distance (Å)									
	Na/S ^{a,b}	K/S ^b	Rb/S ^b	Pb/S	Ag/S	Tl/S	K/Se	Rb/Se	Bond angle (°)	
A—O(2)	2.961(4)	2.971(4)	2.999(5)	2.968	2.962	3.005	2.884(7)	2.906(2)		
A—O(3)	2.727(4)	2.826(4)	2.902(5)	2.770	2.714	2.916	2.913(7)	2.985(2)		
T—O(1)	1.462(7)	1.460(7)	1.452(10)	1.453(7)	1.463(8)	1.450(11)	1.611(11)	1.621(3)		
T—O(2)	1.483(4)	1.481(4)	1.481(5)	1.483(4)	1.477(5)	1.486(6)	1.643(7)	1.645(2)		
Fe—O(2)	2.061(4)	2.066(4)	2.070(5)	2.051(4)	2.041(5)	2.058(6)	2.056(6)	2.061(2)		
Fe—O(3)	1.994(2)	1.9865(16)	1.984(2)	1.9882(17)	1.9881(19)	1.985(3)	1.987(3)	1.9855(8)		
Fe...Fe distance	3.671	3.652	3.657	3.664	3.665	3.661	3.695	3.707		
Angle	Bond angle (°)									
O(1)—T—O(2)	109.35(15)	109.8(17)	110.1(2)	109.72(16)	109.5(2)	109.9(3)	110.1(2)	110.16(7)		
O(2)—T—O(2)	109.59(15)	109.15(17)	108.8(2)	109.22(17)	109.4(2)	109.0(3)	108.8(2)	108.77(7)		
O(2)—Fe—O(2)	180	180	179.999(1)	180	179.999(1)	179.999(1)	179.999(1)	180.0		
O(2)—Fe—O(3)	91.84(13)	91.77(13)	91.04(17)	91.39(14)	91.44(16)	90.9(2)	92.5(2)	91.75(7)		
O(2)—Fe—O(3)	88.16(13)	88.23(13)	88.96(17)	88.61(14)	88.56(16)	89.1(2)	87.5(2)	88.25(7)		
O(3)—Fe—O(3)	180	180	179.999(1)	180	179.999(1)	179.999(1)	179.999(1)	180.0		
O(3)—Fe—O(3)	91.8(3)	90.5(2)	90.1(3)	91.1(2)	92.0(3)	90.4(4)	90.8(4)	90.07(12)		
O(3)—Fe—O(3)	88.2(3)	89.5(2)	89.9(3)	88.9(2)	88.0(3)	89.6(4)	89.2(4)	89.93(12)		
Fe—O(3)—Fe	134.0(2)	133.6(2)	134.4(3)	134.3(2)	134.4(3)	134.5(3)	136.8(4)	137.51(11)		
Fe—O(2)—T	129.8(2)	130.0(2)	130.5(3)	130.3(2)	130.3(3)	130.3(4)	126.8(4)	126.88(11)		
FeO ₆ tilt angle ^c	17.7	17.4	17.5	17.7	17.9	17.6	14.5	14.4		

^a Na/S = NaFe₃(OH)₆(SO₄)₂, etc. ^b Data taken from Reference 21. ^cTilt angle defined as {90° - (Fe...Fe-O(2))}.

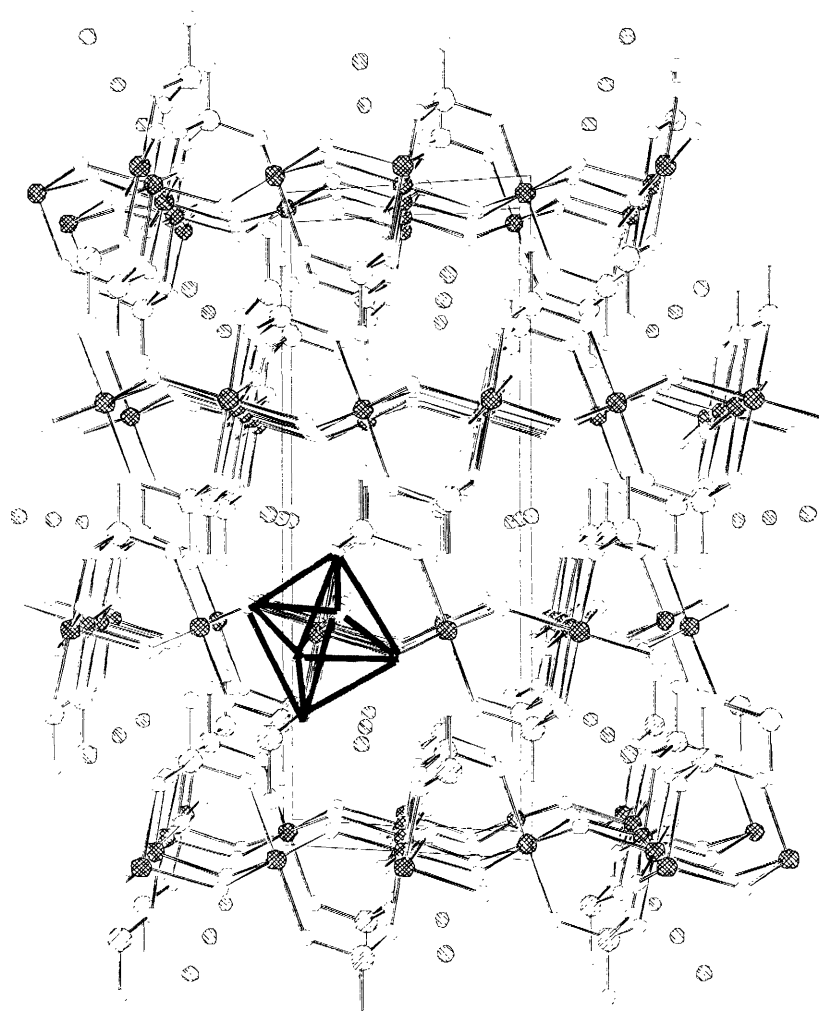


Figure 2.4. Packing diagram of jarosite, viewed along [110]. Note that all Fe atoms within a kagomé layer lie within a plane normal to the c axis. Note that the FeO_6 elongated octahedron is tilted approximately 17° from the crystallographic c axis. One elongated, tilted FeO_6 octahedron is highlighted.

alkali metal A^+ cations. Furthermore, we see no evidence of an inert s -pair effect in the structure of Tl^+ analog, which also exhibits $Tl-O$ distances that are in line with jarosite layers occupied by alkali metal cations. Of course, one significant structural difference among the jarosites is the c dimension of the unit cell, which monotonically tracks the size of the intralayer cation.

2.3.3 Magnetism

The temperature and field dependence of the dc and ac susceptibility of iron jarosites was examined. Figure 2.5(a) displays the temperature dependence of the zero field-cooled (ZFC) and field-cooled (FC) molar susceptibilities for $AgFe_3(OH)_6(SO_4)_2$, which is representative of the other jarosites examined in this study, shown in Figure 2.6. Measurements were performed under an applied measuring field, $H_m = 100$ Oe. We observe a maximum in χ_m at T_N ; Table 2.3 lists T_N values for the various jarosite derivatives. The single, frequency-independent maximum in the ac susceptibility shown for $AgFe_3(OH)_6(SO_4)_2$ in Figure 2.6(b) confirms that T_N is indeed a primary ordering event and precludes spin-glass behavior. Full data for all of the jarosites presented in this study are presented in Appendix B.

The susceptibility follows the Curie-Weiss law $\chi = C/(T - \Theta)$ at high temperatures. A fit of the measured susceptibilities between $150 \text{ K} < T < 300 \text{ K}$ yields Weiss temperatures and Curie constants listed in Table 2.3. For completeness, Θ and C are also presented for the previously prepared jarosites possessing alkali metal cations. Extraction of the effective moment, μ_{eff} , and the nearest-neighbor exchange coupling, J , from these values is problematic in the case of jarosites because $T_N \ll \Theta$. Harris et al. have addressed this issue by taking a high temperature expansion of the susceptibility for antiferromagnetically coupled spins in a kagomé lattice.³³ The analysis corrects the Curie and Weiss constants obtained from the result of standard mean-field theory outlined in § 1.2 by factors of $9/8$ and $3/2$, respectively,

$$C = (9/8)[N\mu_{\text{eff}}^2/3k_B] \quad (2.9)$$

$$\Theta = (3/2)[zJS(S+1)/3k_B] \quad (2.10)$$

where N is Avogadro's number and z is the number of nearest-neighbor spins. Applying these correction factors yields the values of μ_{eff} and J shown in Table 2.3 for the complete series of pure jarosites. The μ_{eff} are close to the spin-only value of $5.92 \mu_{\text{B}}$ for Fe^{3+} .

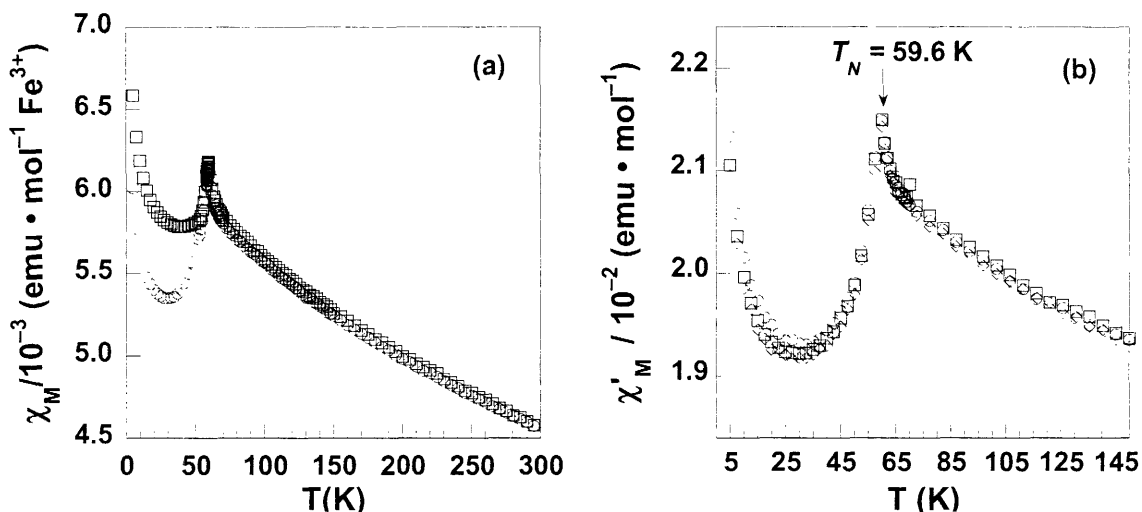


Figure 2.5. (a) FC and ZFC susceptibilities for $\text{AgFe}_3(\text{OH})_6(\text{SO}_4)_2$. Both measurements were performed under a 100 Oe measuring field. For the FC measurement, the cooling field was also 100 Oe. (b) Temperature dependence on the ac susceptibility of $\text{AgFe}_3(\text{OH})_6(\text{SO}_4)_2$ measured under an ac field, $H_{\text{ac}} = H_0 \sin(2\pi ft)$ for $H_0 = 3$ Oe and $f = 2$ Hz (\circ), 20 Hz (Δ), and 200 Hz (\square).

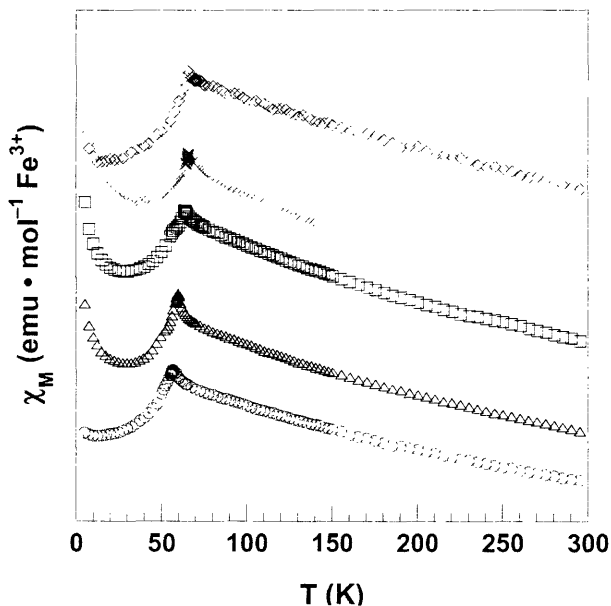


Figure 2.6. ZFC susceptibilities for the jarosite compounds prepared in this study: $\text{Pb}_{0.5}\text{Fe}_3(\text{OH})_6(\text{SO}_4)_2$ (\circ), $\text{AgFe}_3(\text{OH})_6(\text{SO}_4)_2$ (Δ), $\text{TlFe}_3(\text{OH})_6(\text{SO}_4)_2$ (\square), $\text{KFe}_3(\text{OH})_6(\text{SeO}_4)_2$ (\times), and $\text{RbFe}_3(\text{OH})_6(\text{SeO}_4)_2$ (\diamond). The maximum in T_N ranges from 56.4 – 66.5 K. Plots are offset for clarity.

Table 2.3. Magnetic data for pure jarosites.

	T_N (K)	Θ_{CW} (K) ^a	f^b	C_m (emu·K·mol ⁻¹)	μ_{eff} (BM)	J^c (cm ⁻¹)	d_{003} (Å)	Fe–O–Fe (°)	tilt angle (°)
NaFe ₃ (OH) ₆ (SO ₄) ₂ ^d	61.7	– 825	13.5	5.91	6.49	32.8	5.535(10)	134.0(2)	17.6(3)
KFe ₃ (OH) ₆ (SO ₄) ₂ ^d	65.4	– 828	12.7	5.77	6.41	32.9	5.728(2)	133.6(2)	17.4(3)
RbFe ₃ (OH) ₆ (SO ₄) ₂ ^d	64.4	– 829	12.9	5.82	6.44	32.9	5.856(3)	134.4(3)	17.5(3)
TlFe ₃ (OH) ₆ (SO ₄) ₂	63.4	– 813	12.8	6.03	6.55	32.3	5.870(2)	134.4(4)	17.6(4)
AgFe ₃ (OH) ₆ (SO ₄) ₂	59.7	– 803	13.5	5.06	6.00	31.9	5.498(3)	134.0(3)	17.9(3)
Pb _{0.5} Fe ₃ (OH) ₆ (SO ₄) ₂	56.4	– 839	14.9	4.65	5.75	33.3	5.598(6)	134.1(3)	17.7(3)
KFe ₃ (OH) ₆ (SeO ₄) ₂	66.5	– 820	12.3	5.85	6.45	32.6	5.832(3)	130.5(3)	14.5(3)
RbFe ₃ (OH) ₆ (SeO ₄) ₂	65.1	– 845	13.0	5.44	6.21	33.6	5.934(5)	137.51(11)	14.4(11)

^a Θ found from Curie-Weiss fit. ^b frustration parameter defined as $f = |\Theta|/T_N$. ^c μ_{eff} and J corrected by high-temperature expansion method as described in ref. 32. ^d Data taken from ref. 21.

2.3.4 EPR and Mössbauer Spectroscopy

We have also examined the local structure about the FeO_6 octahedron by examining the EPR and Mössbauer spectroscopies of iron jarosites. The low temperature X-band EPR spectrum of the $\text{NaFe}_3(\text{OH})_6(\text{SO}_4)_2$ example in Figure 2.7(a) shows evidence of both axial and rhombic splittings with two resonances at $g_{\parallel} = 2.1$ and $g_{\perp} = 4.3$. In the stoichiometrically pure material, the signals are quite broad (≈ 320 G for the g_{\perp} line and ≈ 1650 G for the g_{\parallel} line) due to both exchange coupling and magnetic ordering. We desired to analyze the spectrum of a pure material rather than using an impure material with diamagnetic ion doped into the lattice. Above the magnetic ordering temperature, the spectrum shows just one broad resonance with an isotropic g -

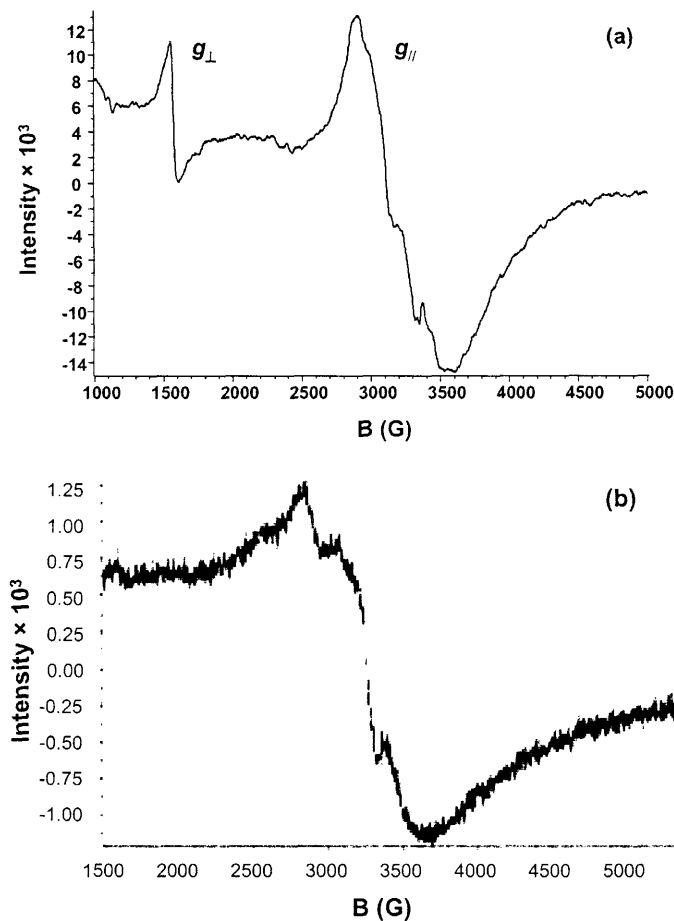


Figure 2.7. X-band EPR spectrum of a) $\text{NaFe}_3(\text{OH})_6(\text{SO}_4)_2$ recorded at 10 K and b) $\text{AgFe}_3(\text{OH})_6(\text{SO}_4)_2$ recorded at 100 K.

value of 2.0 (Figure 2.7(b)). Thus, further interpretation to find the zero field splitting and hyperfine structure parameters in pure jarosites is difficult.

The Mössbauer spectrum of jarosite confirms that our redox-based synthesis takes all of the starting Fe metal to an Fe^{3+} product. This is particularly relevant for characterizing $\text{Pb}_{0.5}\text{Fe}_3(\text{OH})_6(\text{SO}_4)_2$, as it confirms the site occupancies and oxidation state assignment based on the X-ray crystal structure. One could imagine that more Pb^{2+} is incorporated into the structure with a mixed valent $\text{Fe}^{2+}/\text{Fe}^{3+}$ kagomé lattice. However, Figure 2.8(a) shows that only Fe^{3+} is present, evidenced by a single quadrupole doublet having an isomer shift of $\delta = 0.35$ mm/s, and quadrupole splitting $\Delta E_Q = 0.83$ mm/s. Below the ordering temperature (Figure 2.8(b)), a typical six-line pattern emerges, as expected for a compound with a magnetic hyperfine interaction.

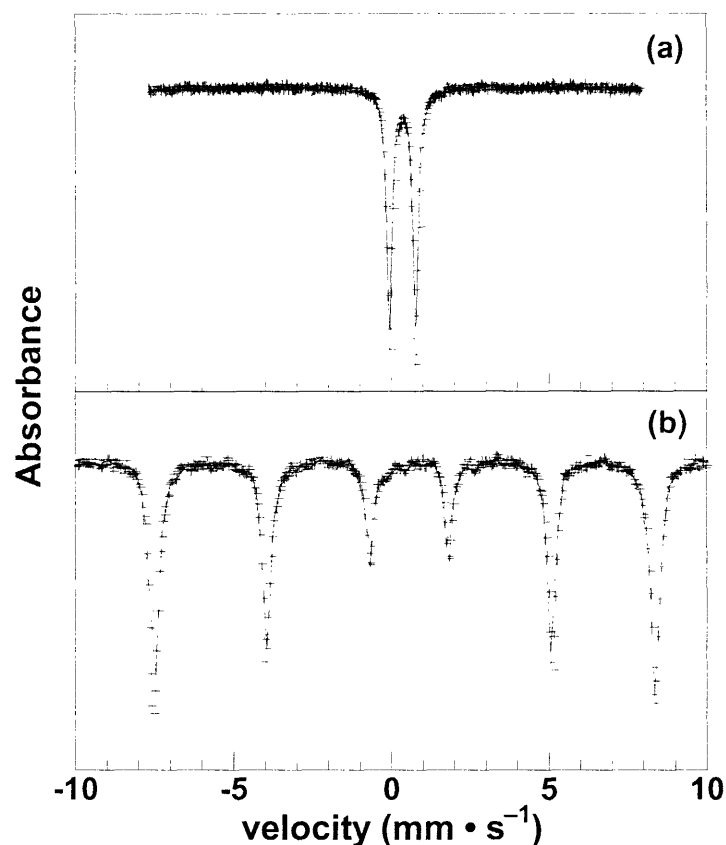


Figure 2.8. Mössbauer spectrum of $\text{Pb}_{0.5}\text{Fe}_3(\text{OH})_6(\text{SO}_4)_2$ recorded at a) 150 K and b) 4.2 K. Note that only one quadrupole doublet is observed above T_N , which is split into a six-line pattern due to the ordered magnetism below T_N .

2.4 Discussion

2.4.1 Intralayer Magnetic Exchange

The basic magnetic element composing the spin frustrated lattice of jarosite is the $\text{Fe}^{\text{III}}_3(\mu\text{-OH})_3$ triangle. The primary magnetic interaction occurs between nearest-neighbor Fe^{3+} ions via a bridging hydroxide. Chart 2.1 summarizes this exchange interaction for 6 high spin $\text{Fe}^{\text{III}}(\mu\text{-OH})\text{Fe}^{\text{III}}$ binuclear species³⁴ and 32 high spin $\text{Fe}^{\text{III}}(\mu\text{-O})\text{Fe}^{\text{III}}$ binuclear species.³⁵ All stereoelectronic models,²⁰ including the original orbital treatments of Goodenough³⁶ and Kanamori,³⁷ identify the predominant superexchange pathway to be comprised of metal $d_{x^2-y^2}$ orbitals and the p orbitals of the bridging oxide or hydroxide. Accordingly, J depends on the Fe—O distances r_1 and r_2 as well as on the Fe—O—Fe bridging angle, φ .^{38,39} Jarosites possess values of (r_1, r_2) and φ that are mid-range to those of $\text{Fe}^{\text{III}}(\mu\text{-OH})\text{Fe}^{\text{III}}$ and of $\text{Fe}^{\text{III}}(\mu\text{-O})\text{Fe}^{\text{III}}$, respectively. In accordance with this intermediate structural behavior, the observed $J \approx -30 \text{ cm}^{-1}$ for jarosites is greater than that observed for $\mu\text{-OH}$ bimetallic compounds (-5 to -11 cm^{-1}) but smaller than $\mu\text{-O}$ di-iron compounds (-160 to -265 cm^{-1}). As shown in Figure 2.9, whereas an ordered antiferromagnetic state is easily achieved for the dimers of Chart 2.1, an antiparallel spin arrangement is frustrated by the geometry imposed by a triangle. The addition of a third spin to the dimer structure gives rise to the complicating situation that only two of the three antiferromagnetic spin pairings can be simultaneously satisfied.

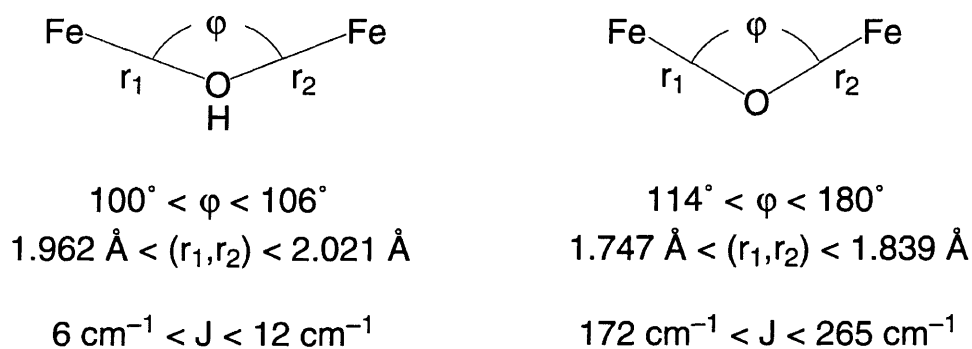


Chart 2.1

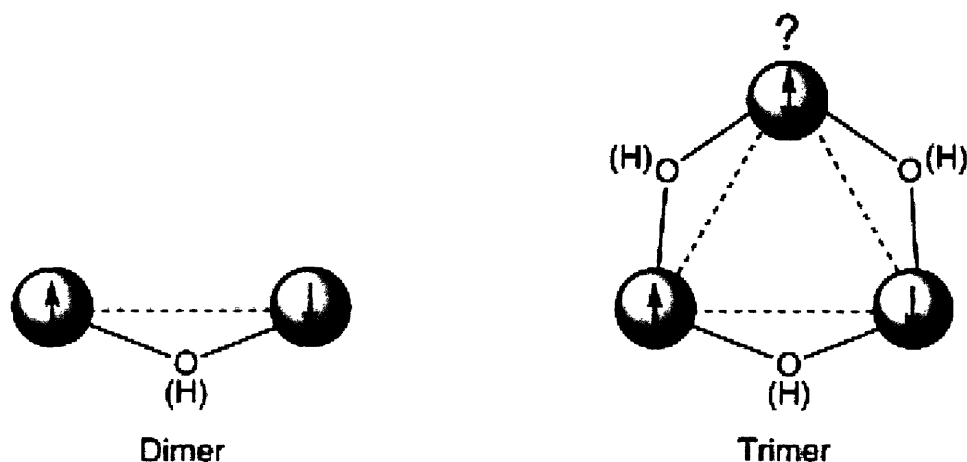


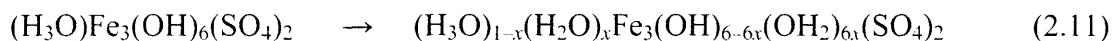
Figure 2.9. Antiferromagnetic spin arrangement in molecular dimers and trimers of iron. The antiferromagnetic coupling is easily achieved in dimers by the antiparallel pairing of spins on the individual iron centers. The ground state magnetic structure of trimers cannot be satisfied by antiparallel spin pairing; the frustrated spin is indicated by the double-headed arrow.

The presence of spin frustration has been sought at the molecular level in trimers of copper,⁴⁰⁻⁵¹ iron⁵²⁻⁵⁸ and chromium.⁵⁹⁻⁶¹ However, magnetism characteristic of spin frustration is not typically obtained. Geometric distortion of the antiferromagnetic ground state eradicates spin frustration by allowing a 2 (antiferromagnetic) + 1 (unpaired) spin system to be achieved.^{62,63} Even when the triangles exhibit perfect three-fold symmetry at room temperature, as is the case for the Fe₃ cluster mineral α -metavoltine,⁶⁴ and molecular triangles of iron^{53,54,57,58,62} and copper,^{40,62,65} low symmetry distortions prevail at low temperature and spin frustration is alleviated.

Such magnetic Jahn-Teller distortions are minimized when triangles are catenated into the extended plaquette of a kagomé lattice. The X-ray crystal data reproduced in Table 2.2 shows the AFe₃(OH)₆(TO₄)₂ jarosites to possess an undistorted triangular lattice. The spin frustration within this perfect triangular lattice is evident from the difference between the observed transition temperature, T_N , and the expected ordering temperature, given by Θ . Because frustration inhibits the tendency for spins to order, T_N will be suppressed relative to Θ . Ramirez has provided a measure for spin frustration by defining $f = \Theta/T_N$, with values of $f > 10$ signifying

a strong effect.⁶⁶ As is evident from the values of f in Table 2.3, jarosites exceed this criterion for strong spin frustration.

Intralayer exchange pathway analysis also allows us to address the anomalous absence of LRO in the hydronium congener. Prior studies undertaken in the group show that disorder results from acid/base chemistry, namely proton transfer from the hydronium cation to the hydroxy group in the kagomé layer,²²



From equation 2.11, we see that the site disorder that gives rise to spin glass behavior results from having both hydroxy and aquo bridging ligands, thus altering the σ superexchange pathway.^{7,21}

2.4.2 Anisotropy Within the FeO_6 Octahedron

Inami ascribes the presence of LRO in jarosites to single ion anisotropy within the FeO_6 pseudoocathedron.⁸ However, we note that the high spin Fe^{3+} ion is totally symmetric, with a ${}^6A_{1g}$ ground term in pseudo- D_{4h} symmetry, and should have no anisotropy associated with it. We therefore sought to study and describe the local electronic properties of the FeO_6 distorted octahedron in iron jarosites. The X-band EPR spectrum shown in Figure 2.7 is somewhat unusual in that evidence of both axial and rhombic symmetry is observed below the ordering temperature, compared to features found in inorganic complexes.⁶⁷ Note that in the solid-state, EPR samples are usually prepared by dilution within a diamagnetic host of the same structure. In the case of studying geometric spin frustration, however, this brings us back to the problem of doping observed at the beginning of this Chapter. Doping in diamagnetic ions results in a lattice in which spin frustration is relieved, and the ordering temperature varies with Fe^{3+} occupancy. The observed features are extremely broad (on the order of $10^2 - 10^3$ G) because we prepared pure jarosite samples and grinded them into an inert diamagnetic matrix. Such line broadening due to magnetic interactions has been studied in corundum-hematite ($\alpha\text{Al}_2\text{O}_3-\alpha\text{Fe}_2\text{O}_3$) solid-solutions, where line widths of up to 1250 G are typical for a hematite mole fraction of 12.5.⁶⁸

Additionally, the low temperature Mössbauer spectrum of jarosite (Figure 2.8) shows a six-line pattern as expected for the hyperfine splitting in a magnetically ordered system under zero applied field. Therefore, electronically isolating the crystal field splitting parameters of the FeO_6 octahedron from the magnetically ordered state of jarosite is spectroscopically difficult.

2.5 Conclusions

We have used synthetic Inorg. Chem. to prepare pure jarosite compounds, and we have characterized them structurally, magnetically, and spectroscopically. Redox steps in the hydrothermal reaction slow seed nucleation relative to crystal growth, allowing us to obtain highly crystalline materials. All of the jarosites have a rigid kagomé structure, comprised of $\text{Fe}^{\text{III}}_3(\mu\text{-OH})_3$ triangles which are the same size regardless of capping group or interlayer cation. Also, the kagomé layers of jarosite do not undergo low-temperature distortions. Accordingly, we find exemplary spin frustrated magnetic behavior in iron jarosites, with ordering temperatures on the order of 60 K, much suppressed relative to the Weiss constant on the order of -800 K. However, the subtle differences in ordering temperatures among iron jarosites elude standard spectroscopic probes that focus on the FeO_6 pseudooctahedron. Thus, probing the magnetism more deeply is required to understand the origin of long-range antiferromagnetic order.

2.6 References

1. Dana, J. D.; Gaines, R. V.; Skinner, H. C. W.; Foord, E. E.; Mason, B.; Rosenzweig, A. *Dana's New Mineralogy*. 8th ed.; John Wiley & Sons, Inc.: New York, 1997; p 629-636.
2. The Mineralogy Database. <http://www.mindat.org>.
3. Takano, M.; Shinjo, T.; Kiyama, M.; Takada, T. *J. Phys. Soc. Jpn.* **1968**, *25*, 902.
4. Takano, M.; Shinjo, T.; Takada, T. *J. Phys. Soc. Jpn.* **1971**, *30*, 1049-1053.
5. Dutrizac, J. E.; Kaiman, S. *Can. Mineral.* **1976**, *14*, 151-158.
6. Dutrizac, J. E. *Metall. Trans. B* **1983**, *14B*, 531-539.
7. Powers, D. A.; Rossman, G. R.; Schugar, H. J.; Gray, H. B. *J. Solid State Chem.* **1975**, *13*, 1-13.

Chapter 2

8. Inami, T.; Nishiyama, M.; Maegawa, S.; Oka, Y. *Phys. Rev. B* **2000**, *61*, 12181-12186.
9. Wills, A. S.; Harrison, A.; Ritter, C.; Smith, R. I. *Phys. Rev. B* **2000**, *61*, 6156-6169.
10. Wills, A. S.; Dupuis, V.; Vincent, E.; Hammann, J.; Calemczuk, R. *Phys. Rev. B* **2000**, *62*, R9264-R9267.
11. Wills, A. S.; Harrison, A. *J. Chem. Soc., Faraday Trans.* **1996**, *92*, 2161-2166.
12. Harrison, A.; Kojima, K. M.; Wills, A. S.; Fudamoto, Y.; Larkin, M. I.; Luke, G. M.; Nachumi, B.; Uemura, Y. J.; Visser, D.; Lord, J. S. *Physica B* **2000**, *289&290*, 217-220.
13. Dupuis, V.; Vincent, E.; Hammann, J.; Greedan, J. E.; Wills, A. S. *J. Appl. Phys.* **2002**, *91*, 8384-8386.
14. Earle, S. A.; Ramirez, A. P.; Cava, R. J. *Physica B* **1999**, *262*, 199-204.
15. Harrison, A.; Wills, A. S.; Ritter, C. *Physica B* **1998**, *241-243*, 722-723.
16. Frunzke, J.; Hansen, T.; Harrison, A.; Lord, J. S.; Oakley, G. S.; Visser, D.; Wills, A. S. *J. Mater. Chem.* **2001**, *11*, 179-185.
17. Kubisz, J. *Mineral. Pol.* **1970**, *1*, 47-59.
18. Kubisz, J. *Mineral. Pol.* **1971**, *2*, 51-60.
19. Dutrizac, J. E.; Chen, T. T. *Can. Mineral.* **2003**, *41*, 479-488.
20. Kahn, O. *Molecular Magnetism*; VCH: New York, 1993; p. 3-4.
21. Grohol, D.; Nocera, D. G. *J. Am. Chem. Soc.* **2002**, *124*, 2640-2646.
22. Grohol, D.; Nocera, D. G.; Papoutsakis, D. *Phys. Rev. B* **2003**, *67*, 064401/1-13.
23. Nocera, D. G.; Bartlett, B. M.; Grohol, D.; Papoutsakis, D.; Shores, M. P. *Chem. Eur. J.* **2004**, *10*, 3850-3859.
24. Jolivet, J.-P. *Metal Oxide Chemistry and Synthesis: From Solution to Solid State*. ed.; John Wiley & Sons, Ltd.: New York, 2000; pp 53-92.
25. Kubisz, J. *Mineral. Pol.* **1972**, *3*, 23-37.
26. Harrison, W. T. A.; Dussack, L. L.; Jacobson, A. J. *Inorg. Chem.* **1996**, *35*, 1461-1467.
27. Harrison, W. T. A.; Dussack, L. L.; Jacobson, A. J. *Inorg. Chem.* **1995**, *34*, 4774-4779.
28. Harrison, W. T. A.; Dussack, L. L.; Jacobson, A. J. *J. Solid State Chem.* **1998**, *138*, 365-368.

Chapter 2

29. Harrison, W. T. A.; Dussack, L. L.; Vaughey, J. T.; Vogt, T.; Jacobson, A. J. *J. Mater. Chem.* **1996**, *6*, 81-87.
30. Hendricks, S. B. *Amer. Mineral.* **1937**, *22*, 774-784.
31. Szymanski, J. T. *Can. Mineral.* **1985**, *23*, 659-668.
32. Kharisun; Taylor, M. R.; Bevan, D. J. M. *Mineral. Mag.* **1997**, *61*, 123-129.
33. Harris, A. B.; Kallin, C.; Berlinsky, A. J. *Phys. Rev. B* **1992**, *45*, 2899-2919.
34. Weihe, H.; Gudel, H. U. *J. Am. Chem. Soc.* **1997**, *119*, 6539-6543.
35. Werner, R.; Ostrovsky, S.; Griesar, K.; Haase, W. *Inorg. Chim. Acta* **2001**, *326*, 78-88.
36. Goodenough, J. B. *J. Phys. Chem. Solids* **1958**, *6*, 287-297.
37. Kanamori, J. *J. Phys. Chem. Solids* **1959**, *10*, 87-98.
38. Atanasov, M.; Angelov, S. *Chem. Phys.* **1991**, *150*, 383-93.
39. Weihe, H.; Guedel, H. U. *J. Am. Chem. Soc.* **1998**, *120*, 2870-2879.
40. Yoon, J.; Mirica, L. M.; Stack, T. D. P.; Solomon, E. I. *J. Am. Chem. Soc.* **2004**, *126*, 12586-12595.
41. Padilla, J.; Gatteschi, D.; Chaudhuri, P. *Inorg. Chim. Acta* **1997**, *260*, 217-220.
42. Beckett, R.; Colton, R.; Hoskins, B. F.; Martin, R. L.; Vince, D. G. *Aust. J. Chem.* **1969**, *22*, 2527-2533.
43. Butcher, R. J.; O'Connor, C. J.; Sinn, E. *Inorg. Chem.* **1981**, *20*, 537-545.
44. Kwiatkowski, M.; Kwiatkowski, E.; Olechnowicz, A.; Ho, D. M.; Deutsch, E. *Inorg. Chim. Acta* **1988**, *150*, 65-73.
45. Chaudhuri, P.; Karpenstein, I.; Winter, M.; Butzlaff, C.; Bill, E.; Trautwein, A. X.; Floerke, U.; Haupt, H. J. *J. Chem. Soc., Chem. Commun.* **1992**, 321-322.
46. Colacio, E.; Dominguez-Vera, J. M.; Escuer, A.; Klinga, M.; Kivekas, R.; Romerosa, A. *J. Chem. Soc., Dalton Trans.* **1995**, 343-348.
47. Ferrer, S.; Haasnoot, J. G.; Reedijk, J.; Mueller, E.; Cingi, M. B.; Lanfranchi, M.; Lanfredi, A. M. M.; Ribas, J. *Inorg. Chem.* **2000**, *39*, 1859-1867.
48. Clérac, R.; Cotton, F. A.; Dunbar, K. R.; Hillard, E. A.; Petrukhina, M. A.; Smucker, B. W. *Comptes Rendus Ser. IIc* **2001**, *4*, 315-319.
49. Ferrer, S.; Lloret, F.; Bertomeu, I.; Alzuet, G.; Borrás, J.; Garcia-Granda, S.; Liu-Gonzalez, M.; Haasnoot, J. G. *Inorg. Chem.* **2002**, *41*, 5821-5830.

Chapter 2

50. Cage, B.; Cotton, F. A.; Dalal, N. S.; Hillard, E. A.; Rakvin, B.; Ramsey, C. M. *J. Am. Chem. Soc.* **2003**, *125*, 5270-5271.
51. Liu, X.; de Miranda Marcelo, P.; McInnes Eric, J. L.; Kilner Colin, A.; Halcrow Malcolm, A. *Dalton Trans* **2004**, 59-64.
52. Rakitin, Y. V.; Yablokov, Y. V.; Zelentsov, V. V. *J. Magn. Reson.* **1981**, *43*, 288-301.
53. Blake, A. B.; Fraser, L. R. *J. Chem. Soc., Dalton Trans.* **1975**, 193-197.
54. Cannon, R. D.; Jayasooriya, U. A.; Wu, R.; arapKoske, S. K.; Stride, J. A.; Nielsen, O. F.; White, R. P.; Kearley, G. J.; Summerfield, D. *J. Am. Chem. Soc.* **1994**, *116*, 11869-11874.
55. Zheng, H.; Zang, Y.; Dong, Y.; Young, V. G., Jr.; Que, L., Jr. *J. Am. Chem. Soc.* **1999**, *121*, 2226-2235.
56. Raptopoulou, C. P.; Tangoulis, V.; Psycharis, V. *Inorg. Chem.* **2000**, *39*, 4452-4459.
57. Sowrey, F. E.; Tilford, C.; Wocadlo, S.; Anson, C. E.; Powell, A. K.; Bennington, S. M.; Montfrooij, W.; Jayasooriya, U. A.; Cannon, R. D. *J. Chem. Soc., Dalton Trans.* **2001**, 862-866.
58. Hibbs, W.; Van Koningsbruggen, P. J.; Arif, A. M.; Shum, W. W.; Miller, J. S. *Inorg. Chem.* **2003**, *42*, 5645-5653.
59. Wucher, J.; Gijsman, H. M. *Physica* **1954**, *20*, 361-366.
60. Nishimura, H.; Date, M. *J. Phys. Soc. Jpn.* **1985**, *54*, 395-399.
61. Cannon, R. D.; Jayasooriya, U. A.; Sowrey, F. E.; Tilford, C.; Little, A.; Bourke, J. P.; Rogers, R. D.; Vincent, J. B.; Kearley, G. J. *Inorg. Chem.* **1998**, *37*, 5675-5677.
62. Cannon, R. D.; White, R. P. *Prog. Inorg. Chem.* **1988**, *36*, 195-298.
63. Murao, T. *Phys. Lett. A* **1974**, *49A*, 33-35.
64. Furrer, A.; Guedel, H. U. *Helv. Phys. Acta* **1977**, *50*, 439-446.
65. Belinsky, M. I. *Inorg. Chem.* **2004**, *43*, 739-746.
66. Ramirez, A. P. *Annu. Rev. Mater. Sci.* **1994**, *24*, 453-480.
67. Bencini, A.; Gatteschi, D., Electron Paramagnetic Resonance Spectroscopy. In *Inorganic Electronic Structure and Spectroscopy*; Solomon, E. I.; Lever, A. B. P., Eds. John Wiley & Sons, Inc.: New York, 1999; I, pp 93-159.
68. Gesmundo, F.; De Asmundis, C. *J. Phys. Chem. Solids* **1972**, *33*, 1861-1872.

Chapter 3. Long-Range Order in Pure Jarosites: the Dzyaloshinsky-Moriya Interaction (Iron) and Metamagnetism (Vanadium)

3.1 Introduction

The presence of a transition to an antiferromagnetically ordered state in stoichiometrically pure jarosites implies the existence of some intrinsic mechanism for 3-D LRO in the kagomé lattice. Spin frustration confines the localized magnetic moments on the Fe^{3+} ions comprising the kagomé lattice to a 2-D plane.¹⁻³ In Chapter 1, we learned that in systems displaying magnetic dimensionality that is less than 3, long-range ordering (LRO) should not be observed;⁴⁻⁷ yet jarosites clearly exhibit a LRO that occurs without symmetry lowering of the lattice.

Theory predicts that LRO in jarosites may arise from spin anisotropy developed by the Dzyaloshinsky-Moriya (DM) interaction,⁸ which induces a moment by canting spins slightly out of the plane. The DM interaction is a perturbation on the Heisenberg-van Vleck-Dirac (HvVD) symmetric exchange spin Hamiltonian. It accounts for weak ferromagnetism in mainly antiferromagnetic compounds by adding an antisymmetric spin-spin interaction.^{9,10} The DM interaction has been well documented by experimentally probing the magnetization and EPR spectra in spin frustrated perovskite cuprates,¹¹⁻¹⁸ the pyrochlore antiferromagnet Cu_4O_3 ,¹⁹ and molecule-based magnets.²⁰⁻²⁴ Also, the DM interaction has been theoretically investigated in iron jarosites.^{8,25,26} DM interactions may be present whenever there is no inversion symmetry within the crystal lattice. The FeO_6 octahedron in jarosite is tilted $14 - 17^\circ$ from the crystallographic c axis, drawn in Figure 2.4, and there no inversion center is present. The functional form of the DM interaction is given by

$$\bar{\mathbf{D}}_{ij} (\bar{\mathbf{S}}_i \times \bar{\mathbf{S}}_j) \quad (3.1)$$

where \mathbf{D}_{ij} is a vector with magnitude of the antisymmetric spin-spin interaction of nearest-neighbor spins \mathbf{S}_i and \mathbf{S}_j and the direction gives the easy axis for the observed weak ferromagnetism. Application of Moriya's rules^{10,27} to Anderson's superexchange theory²⁸ shows

$$\bar{\mathbf{D}}_{ij} \propto \frac{\lambda t_{ij}^2}{\Delta U} \quad (3.2)$$

where λ is the spin-orbit coupling of the magnetic ion, Fe^{3+} in the case of jarosites, t_{ij} is the intersite hopping integral, Δ is the crystal-field splitting, and U is the on-site Coulomb repulsion. Monte Carlo simulations on jarosite performed by Elhajal and LaCroix show that DM interactions can give rise to LRO even in a single 2-D kagomé layer.^{8,25,26} However, the kagomé layers of jarosite are separated by 5.5 Å, and no experimental evidence for weak ferromagnetism has been well described to date in this system.

Within the chemistry community, the DM interaction has been sought in molecular trimers that possess a spin frustrated antiferromagnetic ground state.²⁹⁻³⁵ However, geometric distortion of the molecular triangle tends to obscure the direct observation of the DM interaction.³⁵ The structural studies done in Chapter 2 show that distortion of the triangles is not prevalent when the triangles are catenated into an extended 2-D kagomé lattice. Here, we find that DM interactions give rise to a canted spin structure, which fully explains LRO.

3.2 Experimental

Single crystal susceptibility measurements were carried out on a 48 mg sample of $\text{KFe}_3(\text{OH})_6(\text{SO}_4)_2$ prepared by Nocera group post-doctoral associate, Daniel Grohol. Field-dependent magnetization measurements on jarosite samples were performed using a Quantum Design PPMS System over a 5 – 65 K temperature range at field strengths varying from 0 – 14 T. Each data point is the average of ten extraction magnetometry scans. Raw magnetization data were corrected for paramagnetic contributions by subtracting the Brillouin function. For $H < H_c$, $M(H)$ data were fit to $M = P_1 B_J(x) + P_2 H + P_3$, where P_n are empirical prefactors, and $B_J(x)$ is the Brillouin function, $\frac{2J+1}{2J} \coth\left(\frac{2J+1}{2J}x\right) - \frac{1}{2J} \coth\frac{x}{2J}$ with $x = \frac{Jg\mu_B H}{k_B T}$ and $J = 5/2$.

3.3 Results

3.3.1 Single crystal susceptibility

Figure 3.1 shows that in the SQUID, application of the magnetic field perpendicular to the kagomé layers of $\text{KFe}_3(\text{OH})_6(\text{SO}_4)_2$ results in a sharp transition at $T_N = 65.4 \text{ K}$. But, when the field is applied parallel to the layers, only a broad signal is observed, hinting that LRO is developed along the crystallographic c axis (i.e.—out-of-plane). Inelastic neutron scattering and spin-wave analysis confirm that the moments within a given kagomé layer are indeed canted out-of-plane.³⁶ Each $\text{Fe}^{\text{III}}_3(\mu\text{-OH})_3$ triangle develops an “umbrella” structure of ferromagnetically aligned moments within the kagomé plane, consistent with the presence of the Dzyaloshinsky-Moriya (DM) interaction. Then, alternating layers have canted spins pointing in opposite directions. This opens the possibility of LRO occurring via the Dzyaloshinsky-Moriya (DM) interaction.

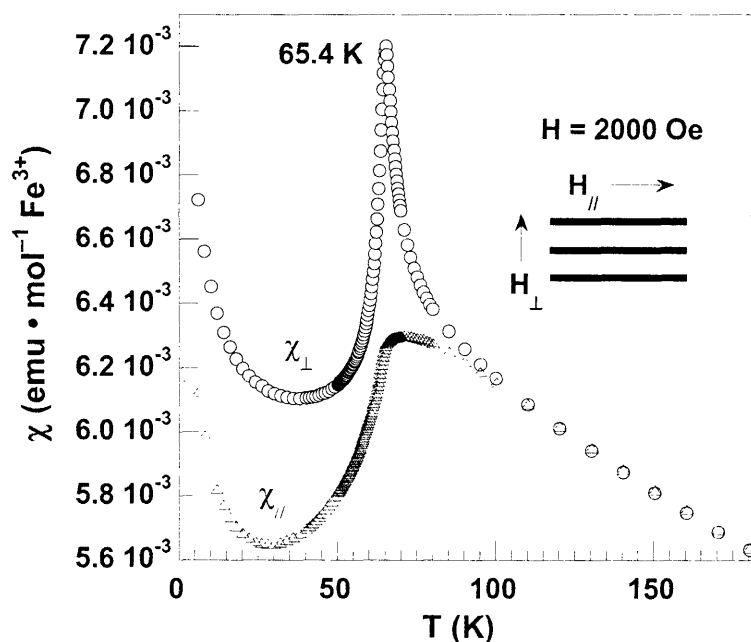


Figure 3.1. Single crystal susceptibility of $\text{KFe}_3(\text{OH})_6(\text{SO}_4)_2$. When H is applied perpendicular to the kagomé layers, the transition is sharp, but when applied parallel to the layers, only a broad signal is observed.

3.3.2 The Critical Field, H_c , and the Spin Canting Angle, η

To further investigate the direction of the developed ordering and the ordering mechanism in jarosites, the field-dependent magnetization was characterized. Figure 3.2 shows the M vs. H plots for our first studies done on rubidium- and plumbojarosites. The magnetization increases linearly when measurements are performed above T_N ; this behavior is consistent with paramagnetism above the ordering temperature. As the temperature is lowered below T_N , the magnetization is observed to abruptly change at a critical field, H_c , which we define as the field at which $(dM/dH)|_T$ is a maximum.³⁷ The critical fields are determined from $(dM/dH)|_T$ plots of Figure B.16 and indicated by the arrows on the plots of Figure 3.2. From the $M(H)$ plot, we determine ΔM , the difference in the y -intercept of the linear fits of $M(H)$ above and below H_c . Figure 3.3 shows the temperature-dependence of H_c and ΔM . Extrapolation of ΔM to $T = 0$ gives a saturation deviation of $0.0743 \mu_B$ for $\text{RbFe}_3(\text{OH})_6(\text{SO}_4)_2$ and $0.0794 \mu_B$ for $\text{Pb}_{0.5}\text{Fe}_3(\text{OH})_6(\text{SO}_4)_2$.

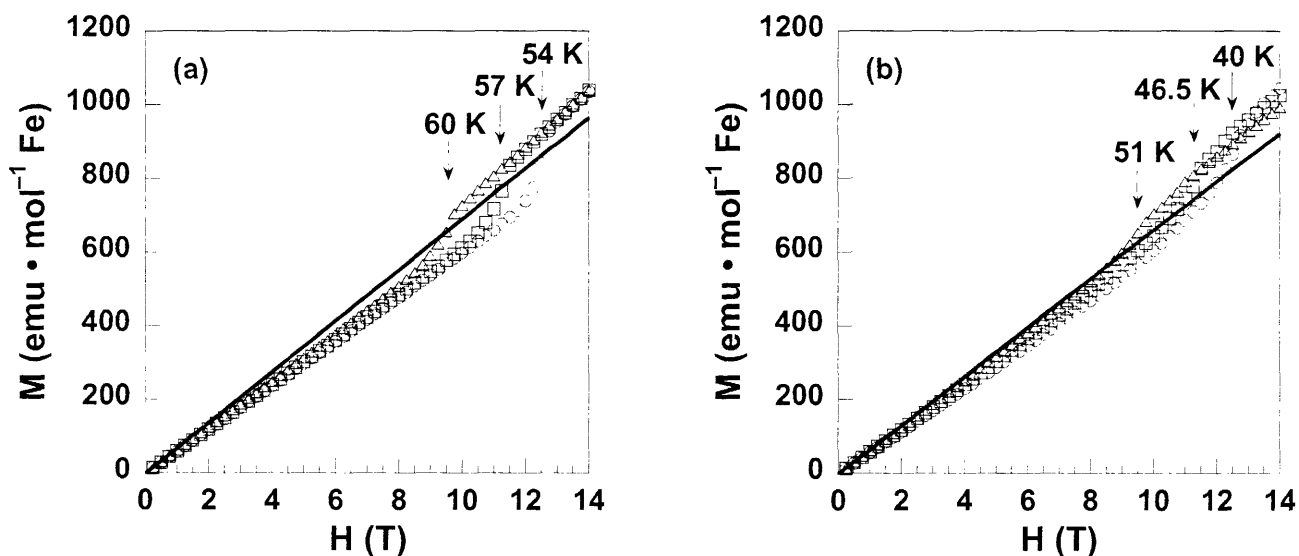


Figure 3.2. Magnetization curve of (a) powdered $\text{RbFe}_3(\text{OH})_6(\text{SO}_4)_2$ at 54 K (\circ), 57 K (\square), and 60 K (Δ) and of (b) powdered $\text{Pb}_{0.5}\text{Fe}_3(\text{OH})_6(\text{SO}_4)_2$ at 40 K (\circ), 46.5 K (\square), and 51 K (Δ). The solid line shows linear behavior of $M(H)$ above T_N . The labeled arrows represent the abscissa of the critical field, defined as the maximum of $(dM/dH)|_T$, which is determined from the maximum in the plots of Figure B.16.

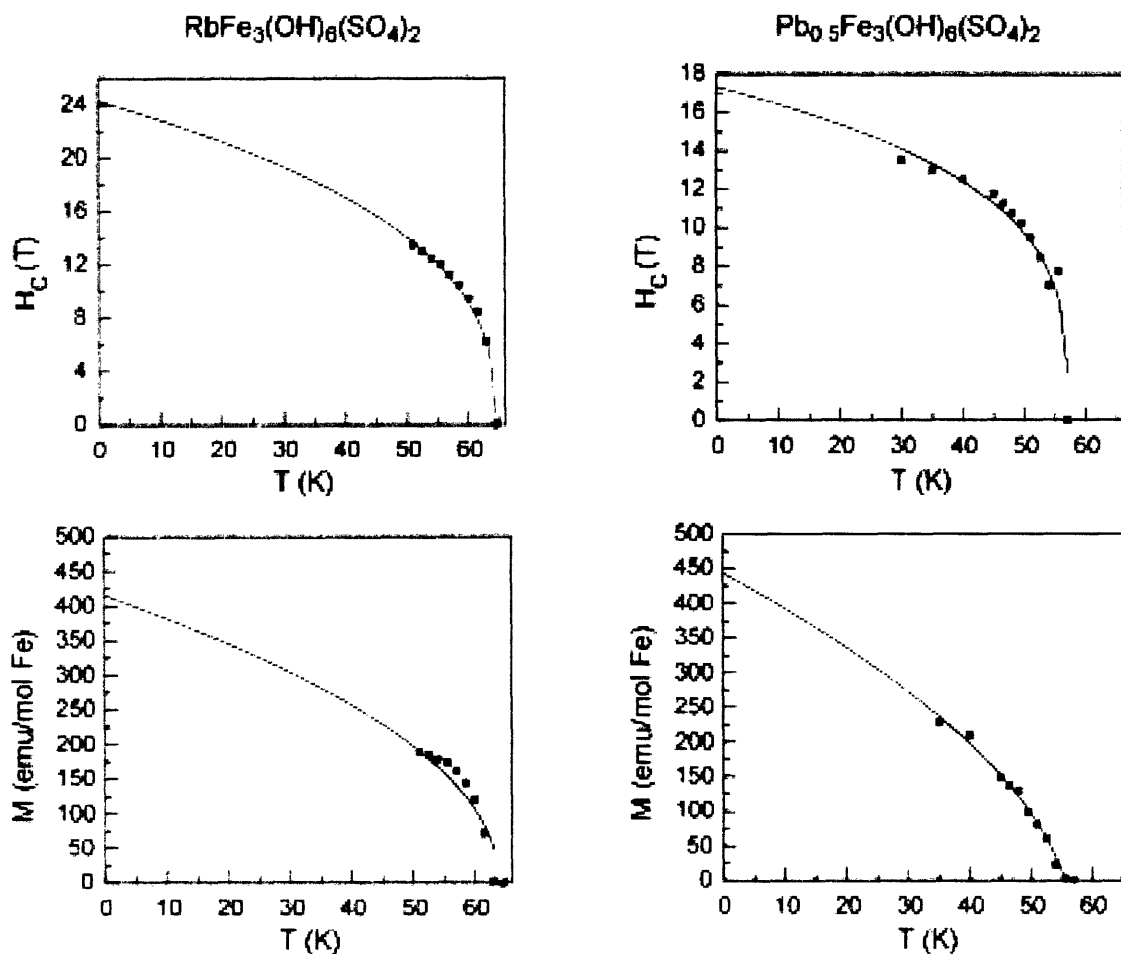


Figure 3.3. Temperature dependence of the critical field and magnetization difference in $\text{RbFe}_3(\text{OH})_6(\text{SO}_4)_2$ and $\text{Pb}_{0.5}\text{Fe}_3(\text{OH})_6(\text{SO}_4)_2$. The data are fit to a power law function to extrapolate H_c and ΔM values at $T = 0$.

The increase in magnetization is consistent with the development of a ferromagnetic moment at H_c . Below $T = 49$ K in $\text{RbFe}_3(\text{OH})_6(\text{SO}_4)_2$ and below $T = 30$ K in $\text{Pb}_{0.5}\text{Fe}_3(\text{OH})_6(\text{SO}_4)_2$, the critical field becomes larger than the instrument limit of 14 T and therefore a saturation H_c cannot be precisely obtained. In the case of argentojarosite, $\text{AgFe}_3(\text{OH})_6(\text{SO}_4)_2$, we fortuitously observe saturation in the magnetization at low temperatures. Thus, this compound allows us to probe the spin structure in detail. Figure 3.4 shows the $M(H)$ magnetization plot for argentojarosite at 5 K. The hysteresis in the bulk magnetization points to a ferromagnetic ordering event. M increases linearly with increasing applied field, H , until $H =$

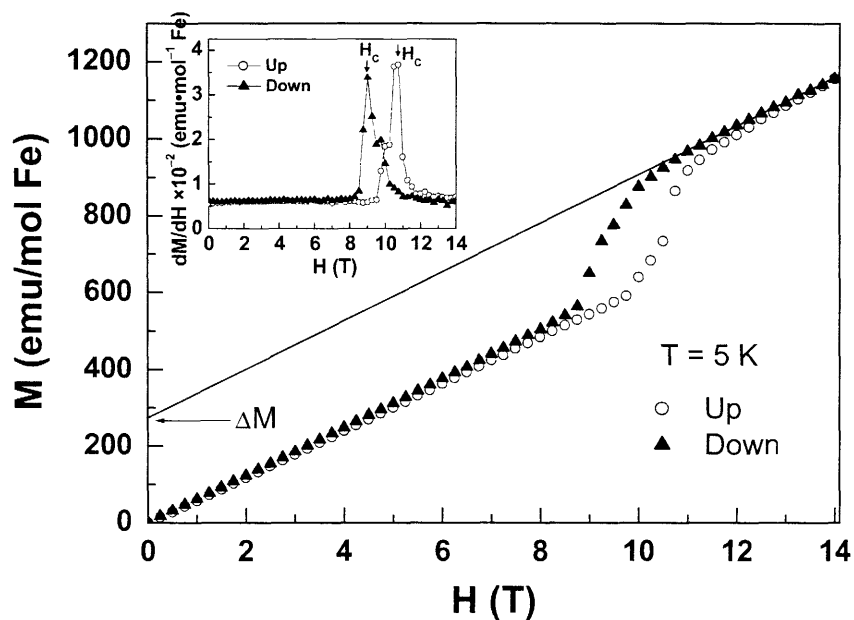


Figure 3.4. Magnetization curve for argentojarosite powder at 5 K measured upon increasing (●) and decreasing (○) applied field with fits of the linearly behaved regions. The inset shows the first derivative, (dM/dH), from which we define the critical field, H_c .

9.75 T. This is followed by a sharp, non-linear response in M from $H = 9.75 - 11.5$ T. For $H > 11.5$ T, a linear response is again observed. Continuing the measurement while decreasing the applied field, M decreases linearly to 10.5 T, then drops sharply between 10.5 – 8.75 T. Again, linear behavior resumes once $H < 8.75$ T. The critical fields are shown in the inset of Figure 3.4. Then, fitting the linear portions of the $M(H)$ curve and noting the difference in y -intercepts, we find ΔM . For the fitting, the average of the slopes was taken to fit each linear component and the y -intercept of the $H > H_c$ line is $\Delta M = 278 \text{ emu} \cdot \text{mol}^{-1} \text{ Fe}$. Hysteresis in the $M(H)$ curve implies spin anisotropy, noted by substantial coercive field of approximately 0.5 T.

Figure 3.5 shows the temperature-dependence of the magnetization and H_c over the range 5 – 65 K. H_c saturates at low temperature to the 5 K value of 9.8 T. Upon heating, H_c decreases and goes to zero as we approach the ordering temperature. The 60 K line on the plot in Figure 3.5(a) shows only linear behavior typical of a paramagnet. Hysteresis below T_N results in two measured critical fields for any given temperature, and we average the two fields in reporting our

data. The critical field measures the magnetic field above which ferromagnetic behavior is observed, and its behavior approaching the ordering temperature should have a well defined order parameter with magnetic field as its thermodynamic conjugate. The fit of the order parameter provided in Figure 3.5(b) is to guide the eye and has the functional form of a

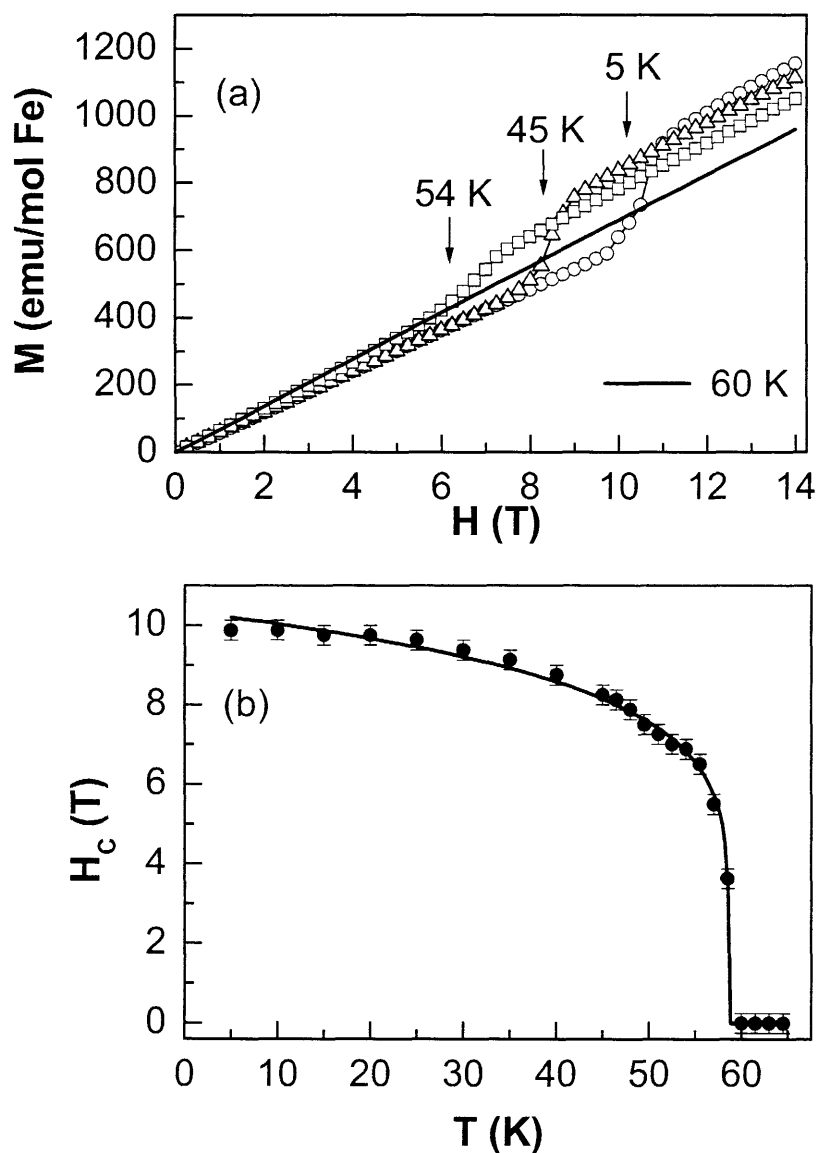


Figure 3.5. (a) Temperature-dependence of the induced magnetization shown at $T = 5$ K (\circ), 45 K (Δ), and 54 K (\square). (b) Temperature-dependence of the average critical field, H_c , from 5 – 60 K.

conventional power law, $a + b |T - T_N|^\beta$. We find that the exponent of the order parameter, β 0.164, lies somewhere between expected values from Landau theory and the Ising model.³⁸ Understanding the thermodynamics of ordering in jarosites is complicated in that the order parameter is described by two interactions—ferromagnetic ordering observed in the critical field measurement, but bulk antiferromagnetism at fields smaller than H_c . Although we study the onset of ferromagnetism by applying the critical field, H_c decreases sharply as we approach T_N , therefore the antiferromagnetic LRO cannot be ignored.

Since the critical field varies with temperature, ΔM must also be a temperature-dependent quantity, and Figure 3.6 shows $\Delta M(T)$ for the entire temperature range, 5 – 60 K. On the plot, the left axis gives ΔM in the cgs unit $\text{emu} \cdot \text{mol}^{-1}$ from the PPMS magnetometer, and the right axis shows the same data, Δm , with a scale in Bohr magnetons, μ_B . Given Δm , we can find the deviation of the spin angular momentum from $m = 5.92 \mu_B$ expected for localized moments of high spin Fe^{3+} . The dashed line on Figure 3.6 shows that below the ordering temperature, Δm

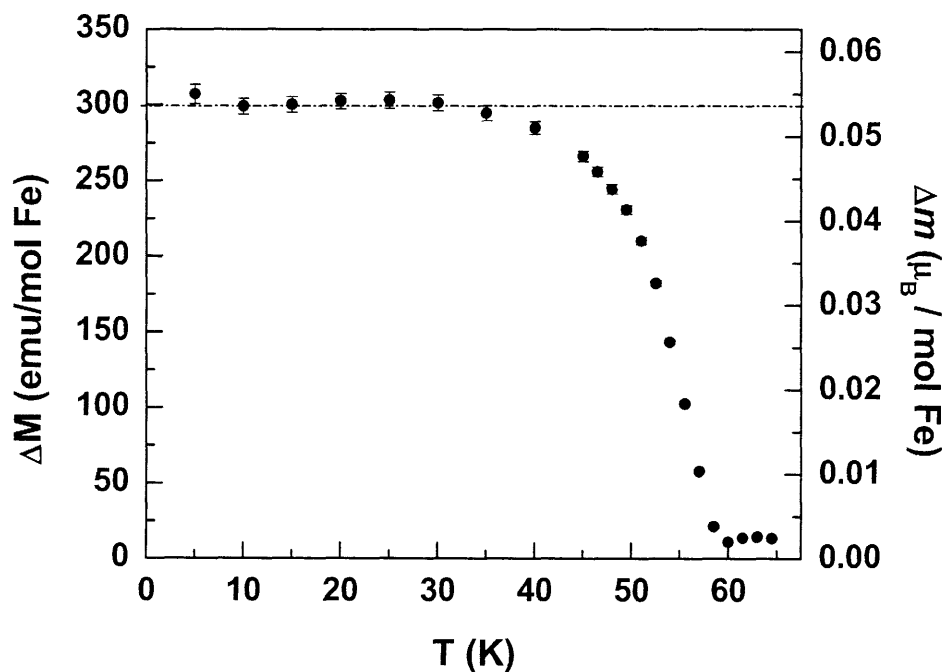


Figure 3.6. Temperature-dependence of the deviation in the magnetization from the spin-only value $5.92 \mu_B$. Δm saturates at $0.0535 \mu_B$ below $T = 40$ K.

saturates at $0.0535 \mu_B$. With the deviation from the expected moment, we proceed to calculate the spin canting angle in $\text{AgFe}_3(\text{OH})_6(\text{SO}_4)_2$ powder. The canting angle, η , is geometrically defined as

$$\eta = \sin^{-1}\left(\frac{\Delta m}{m}\right) = \sin^{-1}\left(\frac{0.0535}{5.92}\right) = 0.517^\circ \quad (3.3)$$

3.4 Discussion

3.4.1 The DM Parameters, D_{ij} and D_z

In order to determine the overall magnitude of \mathbf{D}_{ij} (noted as D throughout this discussion), we start with the canting angle, η , from the critical field measurement. The in-plane component, D_{ij} , can be found by following the methods of Elhajal and LaCroix.

$$\tan(2\eta) = \frac{2 D_{ij}}{\sqrt{3} J + D_z} \quad (3.4)$$

Since the DM interaction is a perturbation on the HvVD Hamiltonian, we can assume that $D_z/J \ll 1$ as $D_z \rightarrow 0$. In this limit, equation 3.4 reduces to

$$D_{ij} = \frac{\sqrt{3}}{2} J \tan(2\eta) \quad (3.5)$$

SQUID and high-field magnetization measurements on $\text{AgFe}_3(\text{OH})_6(\text{SO}_4)_2$ powder give, $J = 3.95$ meV and $\eta = 0.517^\circ$ respectively. Solving equation 3.5 gives $D_{ij} = 0.062$ meV.

In order to determine D_z , we need a second measurement, and therefore rely on single crystal neutron studies done in collaboration with Professor Young S. Lee's group at the MIT department of physics. In order to understand the neutron results, we must first go back to the compromised spin ground states introduced in § 1.3. From these configurations, an allowed global rotation emerges such that two spins move concomitantly in and out of the kagomé plane while keeping the vector sum of spins equal to zero. This is illustrated for the $q = \sqrt{3} \times \sqrt{3}$ lattice in Figure 3.7. Because of spin canting, however, free rotation of these spins is destroyed, and the energy of the non-dispersive zone of the lowest-energy band in the neutron spin-wave spectrum of a single crystal measures that spin rotation energy. From this, we can determine the magnitude

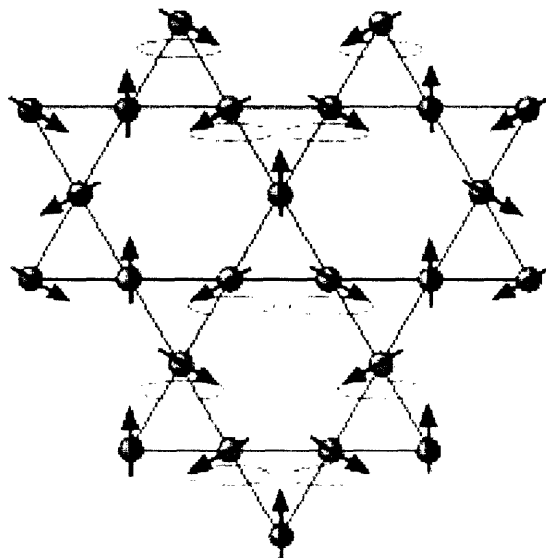


Figure 3.7. The kagomé lattice with spins in one possible ground state configuration. Note that the spins on a hexagon can be rotated out of the plane about the dotted ellipse without changing the energy, thus giving rise to an infinite number of degenerate ground states.

of overall D .²⁶ In $\text{KFe}_3(\text{OH})_6(\text{SO}_4)_2$, the energy at the dispersion zone-center, ε , is 6.73(23) meV.

Given ε and J , D , is given by

$$\varepsilon = \sqrt{6\sqrt{3} D (J + \sqrt{3} D)} \quad (3.6)$$

From neutron studies, we find that $J = 3.9(2)$ meV in $\text{KFe}_3(\text{OH})_6(\text{SO}_4)_2$.³⁹ Again, we point out that the J values for $\text{KFe}_3(\text{OH})_6(\text{SO}_4)_2$ and $\text{AgFe}_3(\text{OH})_6(\text{SO}_4)_2$ (3.9(2) meV cf. 3.95 meV) are the same due to the structural homology of the fundamental interacting unit, the $\text{Fe}^{\text{III}}_3(\mu\text{-OH})_3$ triangle. In $\text{KFe}_3(\text{OH})_6(\text{SO}_4)_2$, we find $D = 0.166$ meV.

Then, we assume that the parameters governing the \mathbf{D}_{ij} vector (equation 3.2) are the same for all iron jarosites due to the rigid intralayer structure. Therefore, we can determine the out-of-plane component simply by deconvoluting the vector \mathbf{D}_{ij} .

$$D = \sqrt{D_{ij}^2 + D_z^2} \quad (3.7)$$

Solving equations 3.4 and 3.7 simultaneously given D from single crystal studies, J from mean-field theory, and η from the critical field measurement, we find $D_z = 0.154$ meV and $D_{ij} = 0.063$ meV. These values are in good agreement with the assumption presented in equation 3.5 above.

3.4.2 Interlayer exchange, J_z and Long-Range Correlation

The non-linear behavior of $M(H)$ allows us to discuss two additional energy considerations in the $\text{AgFe}_3(\text{OH})_6(\text{SO}_4)_2$ spin system. First, finding Δm from the critical field data allows us to find the interlayer exchange constant, J_z , following the methods of Thio and others. The relationship is given by

$$J_z = \frac{m \cdot H_c}{S^2} \quad (3.8)$$

Using the 5 K data for $H_c = 9.75$ T, we find $J_z = 4.83 \times 10^{-3}$ meV. Thus, interlayer coupling is negligible in the absence of a strong field, and any ferromagnetic component observed in low field SQUID measurements is due to spin canting within the layer. That is, the simulations presented by Elhajal and LaCroix appear to be consistent with experimental observation. The three-dimensionality of the spin system arises with negligible interlayer coupling, thus LRO exists within a single kagomé layer. Consequently, the DM interaction may impose LRO on any spin frustrated kagomé system in which the layers are corrugated and no inversion symmetry is present.

Finally, the Brillouin prefactor presented in the experimental section gives a measure of the non-interacting, free spins Fe^{3+} spins in the ordered state. Assuming a spin only system, $S = J = 5/2$ and $L = 0$, where here J is the total angular momentum quantum number, not the Heisenberg symmetric exchange constant,

$$M = NgJ\mu_B B_J(x) \quad (3.9)$$

where $B_J(x)$ is the Brillouin function, N is the number volume of magnetic ions, and g is the Landé splitting factor. This assumption gives the spin-only, free electron Landé g factor, $g = 1 + \frac{J(J+1) + S(S+1) - L(L+1)}{2J(J+1)} = 2$.

Substituting into equation 3.9 gives

$$\frac{M}{N} = 5\mu_B B_J(x) \quad (3.10)$$

Table 3.1 gives the experimental fitting of the Brillouin function for the $M(H)$ data taken at 5 K, as described in the experimental section. If $\text{AgFe}_3(\text{OH})_6(\text{SO}_4)_2$ were a pure paramagnet and all spins were non-interacting, we see from equation 3.10, the Brillouin function prefactor would be $P_I = 5\mu_B$. However, the average of P_I for the measurement upon increasing and decreasing applied field at 5 K is 0.0424 emu, which corresponds to $4.98 \times 10^{-3} \mu_B$. That is, less than 0.1% of the Fe^{3+} spins are non-interacting at 5 K. As we expected, at 5 K (well below the ordering temperature), argentojarosite has virtually no non-interacting moments, and thus a correlation length that approaches infinity. This results because spin frustration and the DM interaction require all spins to exchange couple within a given layer below T_N .

Table 3.1. Fitting parameters for $M(H)$ data at 5 K for $P_1 B_J(x) + P_2 H + P_3$

	5 K Increasing	5 K Decreasing
P_1	0.0438 ± 0.00146	0.04095 ± 0.0013
P_2	$9.3881 \pm 0.0021 \times 10^{-6}$	$9.8204 \pm 0.0020 \times 10^{-6}$
P_3	0 ± 0	0 ± 0
R^2	0.99996	0.99997

3.4.3 Ordering Pathways in Iron Jarosites

In an effort to determine a 3-D ordering pathway in iron jarosites, we first consider plausible mechanisms. Examining interlayer orbital superexchange, Figure 3.8 shows that the simplest pathway involves the overlap of the singly occupied d_{z^2} orbital of Fe^{3+} with the closed shell interlayer cation. In such a case, the ordering temperature would scale inversely to the interlayer separation since the orbital overlap gets smaller as the layers are spread further apart. Plotting T_N vs. d_{003} in iron jarosites (Figure 3.9) leads to no such simple correlation. From this plot, we also conclude that ordering does not occur by a simple dipole-dipole interaction, noting

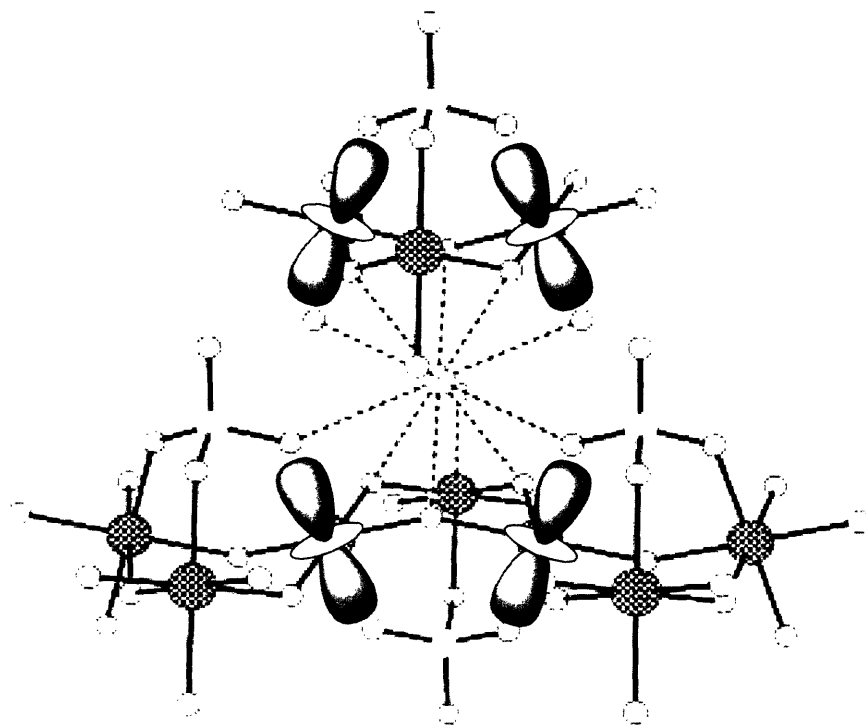


Figure 3.8 Interlayer exchange through Fe d_{z^2} and the closed-shell interlayer cation of A_1 symmetry.

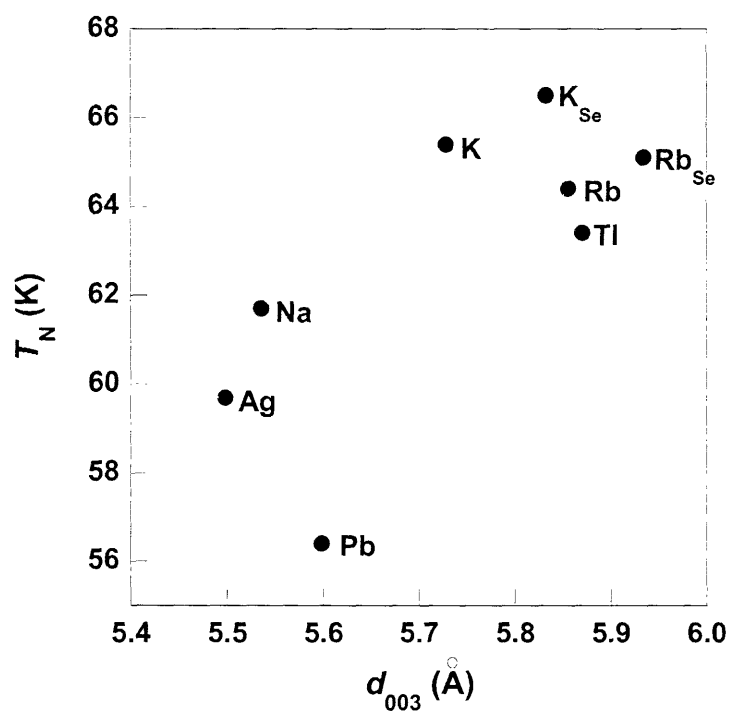


Figure 3.9. Ordering temperature v. interlayer spacing (d_{003}) in iron jarosites.

that if the interlayer coupling of spins occurs by a dipole-dipole interaction, again we would expect T_N to decrease as d_{003} increases since the dipole-dipole interaction has a $1/r^3$ distance dependence. We then sought to examine other possible exchange pathways involving the capping group.

It has long been believed that the sulfate capping group provides an effective interlayer superexchange pathway.⁴⁰ Superexchange involving the capping group requires a six-bond pathway over the span of 5.5 Å since the capping group is terminal and does not directly bond to adjacent layers. Therefore, interlayer superexchange must include one hydrogen bond to make a rather circuitous Fe—O(2)—S—O(1)⋯H—O(3)—Fe pathway (labels from Fig. 2.3) Nonetheless, hydrogen bonds are thought to be important in magnetic exchange in layered materials.⁴¹ As we have shown, the geometry of the capping group is determined directly from the rigid structure of the $\text{Fe}^{\text{III}}_3(\mu\text{-OH})_3$ triangles. If indeed there is superexchange involving the capping group, the O(1)⋯H—O(3) distances and angles are important. The hydrogen atom shows up as the largest unresolved peak after anisotropic refinement of all heavy atoms in the structure. Figure 3.10

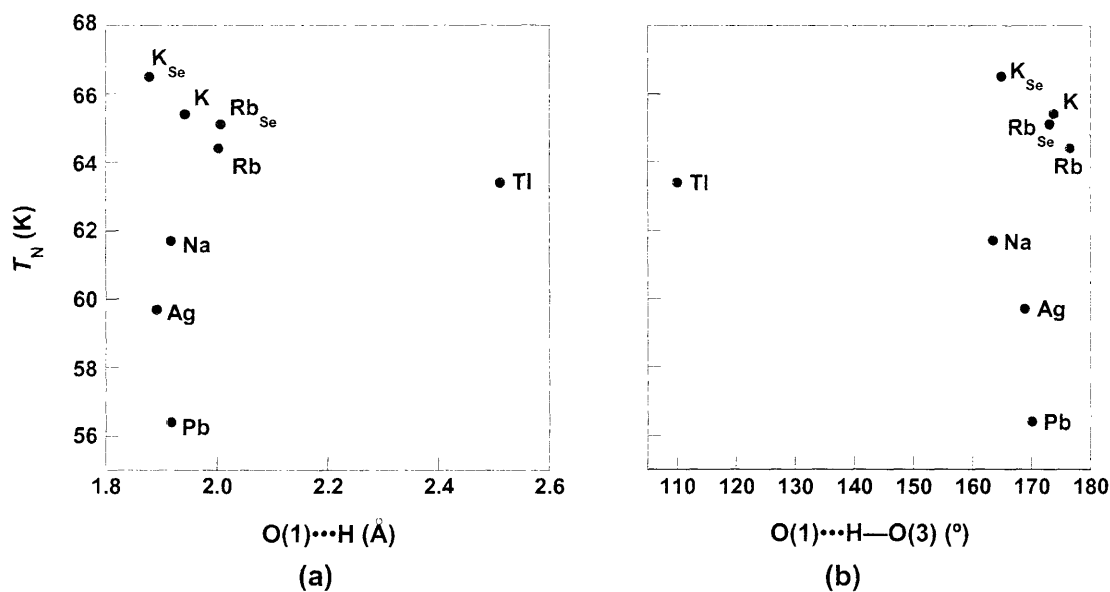


Figure 3.10. Magnetostructural trends in iron jarosites. Plotted are the ordering temperature, T_N v. a) O(1)⋯H distance and b) O(1)⋯H—O(3) angle.

shows plots of T_N versus a) the O(1)···H distance, and b) the O(1)···H—O(3) angle. Of course, these correlations are limited by the certainty in the position of the hydrogen atom. For example, the Tl^+ derivative seems anomalous, but it is most likely due to the large spin-orbit coupling on the fully occupied special position, which makes locating the hydrogen atom difficult. Thus, the O(1)···H bond distance and the O(1)···H—O(3) angle are virtually constant, 1.94(6)Å and 170(6)° respectively. Additionally, there is no clear-cut connection between the spin canting angle estimates obtained from the high-field PPMS measurements from any crystallographic parameters from a fundamental physics standpoint. We conclude by finding no evidence for magnetostructural correlations using simple orbital-based arguments here.

3.4.4 Spin Canting and LRO in Jarosites

The DM interaction results in a weak ferromagnetic component to the overall magnetism of mainly antiferromagnetic compounds. If the HvVD Hamiltonian in § 1.2 fully described all of the spin interactions in jarosite, all of the spins would be confined to the 2-D kagomé plane because of spin frustration. However, jarosites must have some mechanism for which to attribute 3-D ordering. The DM interaction has two components— D_x , which gives Ising-like anisotropy and results in spin canting out of the kagomé plane, and D_z which gives and XY-type anisotropy and selects the spin chirality of the system.³⁹

In a highly frustrated system, the weak ferromagnetism associated with the DM interaction is difficult to observe directly because at low magnetic fields, adjacent layers with canted spins stack antiferromagnetically, and the magnetization of the sample increases linearly. This is the same behavior seen above the ordering temperature, as the susceptibility (M/H) remains constant. Near the critical field, H_c , however, a non-linear increase in the induced magnetization observed. Now, the spins start to align with the applied magnetic field. In this strong field limit, the Zeeman energy is greater than the interlayer coupling energy, and ΔM occurs due to the difference in spin magnetization caused by 180° rotation of all spins on the oppositely canted layer as shown in Figure. 3.11.

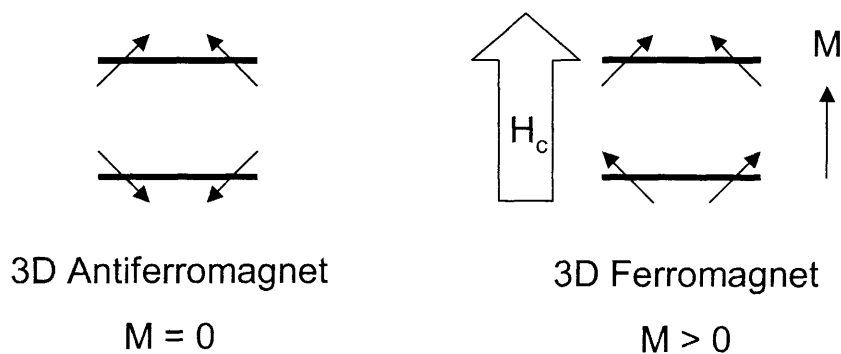


Figure 3.11. Field-dependent behavior of antiferromagnetically-coupled layers of canted spins by the application of a strong critical field, H_c . Below H_c (left), only antiferromagnetism is observed. Above H_c (right), ferromagnetic ordering results from the alignment of the spins with the applied field.

The DM interaction is not a key interaction in other magnetic systems because it is really a second order perturbation after magnetocrystalline single-ion anisotropy. However, we established back in Chapter 2 that Fe^{3+} has a totally symmetric ${}^6A_{1g}$ ground state in the pseudo- D_{4h} point symmetry of the transition metal ion in jarosite. Thus, the DM interaction becomes significant in enforcing LRO on top of the infinite number of degenerate ground states due to spin frustration. In non-frustrated weak trigonal systems such as $\alpha\text{-Fe}_2\text{O}_3$, MnCO_3 , CoCO_3 , CrF_3 , and FeF_3 , originally treated by Moriya¹⁰, LRO is expected. In these compounds, the magnetic ions lie along the [111] crystallographic axis and can couple antiferromagnetically along the linear chains. Then, the DM interaction in these compounds results from the spin substructure of the magnetic unit cell and has a much smaller impact on the bulk magnetism. Observation of the DM interaction in a canted spin structure using high field magnetization experiments finds precedent with La_2CuO_4 .^{42,43} This compound has been intensely studied as the parent compound of high- T_c superconductors, and it has a very small canting angle, $\eta = 0.17^\circ$, within this 2-D system with an ordering temperature $T_N = 300$ K. Here, we demonstrate the ability to elicit the DM interaction energy in jarosites from these experiments.

The disparity between J_z and overall J attests to the high two-dimensional nature of the magnetism in jarosites. Even though J_z is small, it can give rise to sizable T_N when the

correlation length of the canted spins is large. For instance, experimental fitting of the temperature dependence of the in-plane and out-of-plane susceptibility in La_2CuO_4 using modified Landau theory⁴⁴ shows that the T_N of 216 K results from a J_z of only $8 \times 10^{-3} \text{ cm}^{-1}$, but propagated over a large correlation length of $\xi = 768 \text{ \AA}$.⁴⁵ Since the correlation length is exponentially related to the exchange interaction, the large Θ values of jarosites suggest that the small out-of-plane component brought about by the DM interaction is correlated over a long length scale, thus accounting for the appreciable T_N of $\approx 60 \text{ K}$.

Within a framework of a DM interpretation for LRO, the consistency of T_N in jarosites possessing different interlayer cations and capping groups can now be understood. The basic magnetic element from which the DM interaction arises, the $\text{Fe}^{\text{III}}_3(\mu\text{-OH})_3$ triangle, exhibits remarkable structural integrity within the jarosite intralayer, shown in Chapter 2. Chemical modification of the interlayer capping group or interlayer cation does little to perturb the structure of the jarosite intralayer. The inability of the former to affect intralayer structure is particularly surprising. The FeO_6 octahedra of individual triangles tilt inward owing to a mismatch between the areas of the $\text{Fe}^{\text{III}}_3(\mu\text{-OH})_3$ intralayer triangles and basal planes of the TO_4^{2-} capping groups. One might assume that increases in area of the TO_4^{2-} basal plane would be conveyed to the intralayer triangle. However, comparison of the SO_4^{2-} and SeO_4^{2-} structures shows this assumption to be incorrect. The capping group distorts to preserve the structure of the $\text{Fe}^{\text{III}}_3(\mu\text{-OH})_3$ triangles. These results show that it is the Fe–O–Fe linkage that is the primary determinant of the structure of the iron jarosites. With invariant metrics for the bond lengths and angles of the $\text{Fe}^{\text{III}}_3(\mu\text{-OH})_3$ triangles, the DM interaction energy should be similar for the Fe^{3+} jarosites. This contention is supported by the consistency of T_N and J for the jarosites listed in back in Table 2.3.

3.4.5 Metamagnetism in Vanadium Jarosites

Magnetically, vanadium jarosite analogs also show antiferromagnetic LRO, marked by $T_N = 35 \text{ K}$.^{46,47} However, vanadium jarosites show intralayer ferromagnetic coupling that results

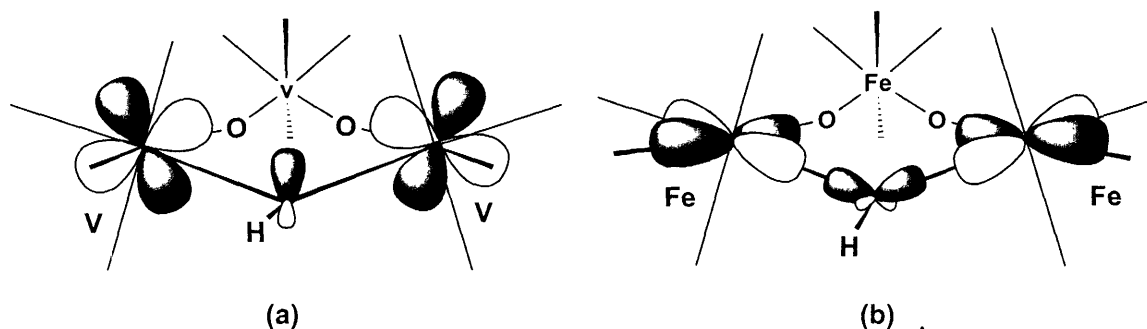


Figure 3.12. a) π -symmetry pathway involving overlap of d_{xz} , d_{yz} of V^{3+} with the sp^3 lone pair of the bridging hydroxy group. b) σ -symmetry pathway involving overlap of $d_{x^2-y^2}$ of Fe^{3+} with the sp^3 hybrid orbitals forming the Fe—O bonds.

from π -symmetry overlap between the V d_{xz} , d_{yz} , and the lone pair hybrid orbital of the bridging OH group. The Weiss constant is much smaller, as would be expected for π vs. σ overlap (shown in Figure 3.12) and is positive ($\Theta = +53$ K). Here, we wish to distinguish between the observation of both ferromagnetic and antiferromagnetic components to the magnetism of vanadium jarosites and iron jarosites. In the case of vanadium, the neutron structure shows that nearest-neighbor ferromagnetically coupled moments are aligned completely within the kagomé plane in the ordered state.⁴⁸ Then, bulk antiferromagnetism results by having alternating layers with moments pointing in opposite directions, known as metamagnetism, and vanadium jarosite analogs show a distinct trend between the interlayer separation (d_{003}) and the observed ordering temperature, as shown in Figure 3.13.⁴⁹ As is the case of the iron jarosites prepared in this study, single-crystal X-ray analysis of the $AV_3(OH)_6(SO_4)_2$ series reveals an isostructural intralayer; only the spacing between layers is varied by A^+ substitution.⁴⁶ The ability to precisely alter the interlayer spacing while preserving the intralayer structure, and consequently ferromagnetic coupling, allows us to examine how the antiferromagnetic coupling of ferromagnetic kagomé layers depends on their separation.

Interlayer coupling is a critical factor for metamagnetism, which typically requires both low dimensionality imposed by a layered structure and anisotropic magnetic properties of the constituent magnetic centers. This is the case for binary halides of Fe^{2+} , Ni^{2+} , and Co^{2+} , in which

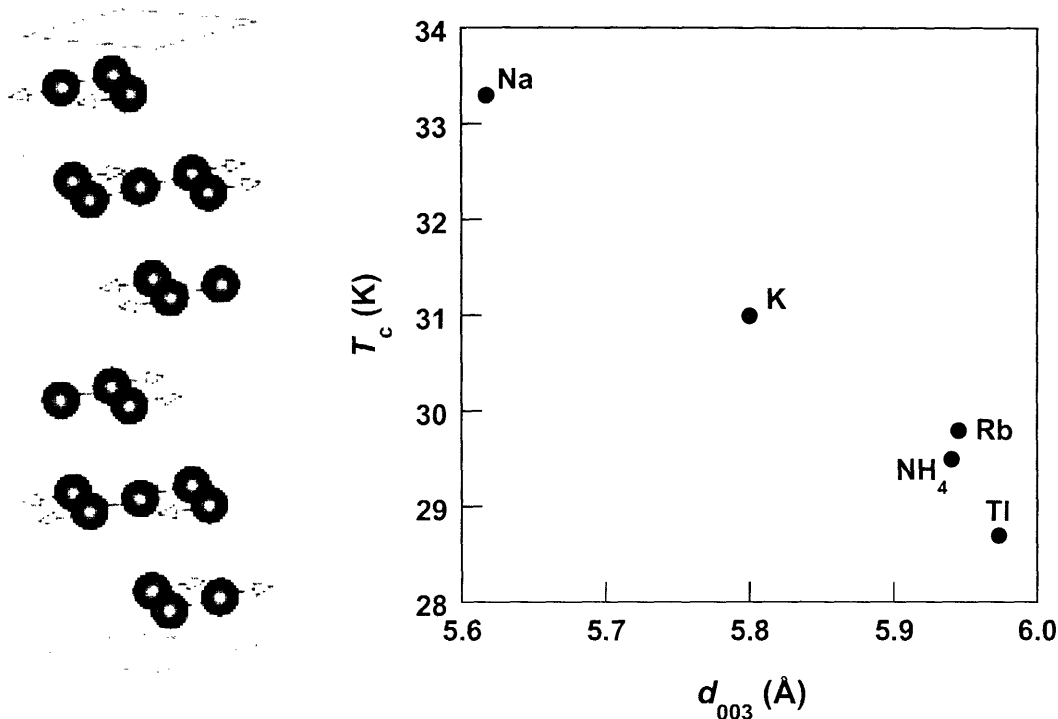


Figure 3.13. (Left) Magnetic unit cell of $\text{NaV}_3(\text{OD})_6(\text{SO}_4)_2$. A metamagnet, having ferromagnetic layers with alternating net moments pointing in opposite directions, results in a magnetic cell that is double the crystallographic cell. (Right) Ordering temperature v interlayer spacing, d_{003} , for vanadium jarosites with different interlayer cations.

original studies of the antiferromagnetic stacking of ferromagnetic sheets were performed.⁵⁰⁻⁵³ We find that vanadium jarosites display strong ferromagnetic interactions that are unprecedented in kagomé layers. The in-plane coupling is invariant with the choice of A^+ cation, and the single-ion anisotropy of the $d^2 V^{3+}$ ion confines the exchange-coupled moments to lie within the kagomé plane with sufficient coupling strengths to prevent saturation of the magnetization when an external field is applied orthogonal to the kagomé plane. Weak interlayer antiferromagnetic coupling of the ferromagnetic kagomé layers becomes dominant below ≈ 30 K, giving rise to overall 3-D metamagnetic behavior observed for the $\text{AV}_3(\text{OH})_6(\text{SO}_4)_2$ jarosites. This interlayer exchange coupling may be overcome by applying a sufficiently strong field, which is estimated to be ≈ 6 kOe.⁴⁹ We have been able to establish the magnetostructural correlation of decreasing antiferromagnetic coupling with increasing interlayer separation for the layered metamagnet

because the bond angles and distances within the kagomé lattice are not perturbed by A^+ substitution.

3.5 Conclusions

The DM interaction appears by the canting spins away from the geometrically frustrated 2-D plane and LRO results. Even when the canting of the spin is small, as measured here for jarosites, a pronounced ordering temperature can be observed owing to long correlation lengths for a spin frustrated kagomé lattice. The DM interaction has been experimentally probed by high field magnetization experiments. Above a strong critical field, ferromagnetic coupling emerges which allows us to calculate the canting angle and the DM interaction energy. D is relatively small compared to the nearest-neighbor exchange constant, J , explaining why it takes such high field measurements to overwhelm the strong antiferromagnetic coupling associated with spin frustration. Although $D < 0.2$ meV, it is sufficiently strong enough to cause LRO in a two-dimensional triangular spin system.

While being able to experimentally probe weak ferromagnetism, determine the spin-canting angle, and thus calculate the interlayer coupling and the DM parameters in jarosites are significant, the consequences of the DM interaction on the study of spin frustrated 2-D systems tell the bigger story. The DM interaction gives each kagomé plane a net ferromagnetic moment by canting the spins slightly out of the plane, and may induce the 3-D magnetically ordered state below T_N . The DM interaction is present whenever there is no inversion center present at the magnetic ion. The results reported in this Chapter show that the DM interaction is responsible for LRO, and it will be difficult to suppress or eliminate by chemical modification of the jarosite lattice owing to the structural rigidity of the $Fe^{III}_3(\mu-OH)_3$ triangles. Previous attempts to reduce the DM interaction through flattening the fundamental triangle structure by changing the anionic capping group have proven futile. All stoichiometrically pure Fe^{3+} jarosite analogues exhibit LRO, and the capping group of jarosite distorts to maintain a rigid intralayer structure. Thus, even in the limit of infinitely separated layers, an out-of-plane component to the overall moment

will exist ($D_{\parallel} > 0$), and long-range antiferromagnetic order should still be observed in jarosites, accompanied by weak ferromagnetism.

3.6 References

1. Schiffer, P.; Ramirez, A. P. *Comments Condens. Matter Phys.* **1996**, *18*, 21-50.
2. Wills, A. S. *Can. J. Phys.* **2001**, *79*, 1501-1510.
3. Harrison, A. *J. Phys.: Condens. Matter* **2004**, *16*, S553-S572.
4. Shender, E. F.; Holdsworth, P. C. W., Order by Disorder and Topology in Frustrated Magnetic Systems. In *Fluctuations and Order*; Millionas, M., Ed. Springer-Verlag: Berlin, 1995; pp 259-279.
5. Chalker, J. T.; Holdsworth, P. C. W.; Shender, E. F. *Phys. Rev. Lett.* **1992**, *68*, 855-858.
6. Greedan, J. E. *J. Mater. Chem.* **2001**, *11*, 37-53.
7. Harris, A. B.; Kallin, C.; Berlinsky, A. J. *Phys. Rev. B* **1992**, *45*, 2899-2919.
8. Elhajal, M.; Canals, B.; Lacroix, C. *Phys. Rev. B* **2002**, *66*, 014422/1-6.
9. Dzyaloshinsky, I. E. *Phys. Chem. Solids* **1958**, *4*, 241-255.
10. Moriya, T. *Phys. Rev.* **1960**, *120*, 91-98.
11. Coffey, D.; Rice, T. M.; Zhang, F. C. *Phys. Rev. B* **1991**, *44*, 10112-10116.
12. Shekhtman, L.; Entin-Wohlman, O.; Aharony, A. *Phys. Rev. Lett.* **1992**, *69*, 836-839.
13. Aharony, A.; Entin-Wohlman, O.; Harris, A. B. *NATO ASI Series, Series E* **1998**, *349*, 281-305.
14. Cepas, O.; Kakurai, K.; Regnault, L. P.; Ziman, T.; Boucher, J. P.; Aso, N.; Nishi, M.; Kageyama, H.; Ueda, Y. *Phys. Rev. Lett.* **2001**, *87*, 167205/1-4.
15. Cepas, O.; Sakai, T.; Ziman, T. *Prog. Theor. Phys. Suppl.* **2002**, *145*, 43-51.
16. Steren, L. B.; Tovar, M.; Oseroff, S. B. *Phys. Rev. B* **1992**, *46*, 2874-2878.
17. Hucker, M.; Kataev, V.; Pommer, J.; Ammerahl, U.; Revcolevschi, A.; Tranquada, J. M.; Buchner, B. *Phys. Rev. B* **2004**, *70*, 214515/1-21.
18. Li, R. K.; Kremer, R.; Maier, J. *J. Solid State Chem.* **1999**, *146*, 488-493.
19. Elhajal, M.; Canals, B.; Lacroix, C. *J. Phys.: Condens. Matter* **2004**, *16*, S917-S922.

Chapter 3

20. Girtu, M. A.; Wynn, C. M.; Fujita, W.; Awaga, K.; Epstein, A. J. *Phys. Rev. B* **2000**, *61*, 4117-4130.
21. Blinc, R.; Pokhodnia, K.; Cevc, P.; Arcon, D.; Omerzu, A.; Mihailovic, D.; Venturini, P.; Golic, L.; Trontelj, Z.; Luznik, J.; Jeglicic, Z.; Pirnat, J. *Phys. Rev. Lett.* **1996**, *76*, 523-526.
22. Wang, Z.; Zhang, B.; Otsuka, T.; Inoue, K.; Kobayashi, H.; Kurmoo, M. *Dalton Trans.* **2004**, 2209-2216.
23. Rawson, J. M.; Alberola, A.; El-Mkami, H.; Smith, G. M. *Journal of Phys. Chem. Solids* **2004**, *65*, 727-731.
24. Joy, P. A.; Vasudevan, S. *J. Chem. Phys.* **1993**, *99*, 4411-4422.
25. Elhajal, M.; Canals, B.; Lacroix, C. *Physica B* **2002**, *312&313*, 716-718.
26. Ballou, R.; Canals, B.; Elhajal, M.; Lacroix, C.; Wills, A. S. *J. Magn. Magn. Mater.* **2003**, *262*, 465-471.
27. Moriya, T. *Phys. Rev. Lett.* **1960**, *4*, 228-230.
28. Anderson, P. W. *Phys. Rev.* **1959**, *115*, 2-13.
29. Tsukerblat, B. S.; Novotortsev, V. M.; Kuyavskaya, B. Y.; Belinsky, M. I.; Ablov, A. V.; Bazhan, A. N.; Kalinnikov, V. T. *Sov. Phys. JETP Lett.* **1974**, *19*, 277-278.
30. Tsukerblat, B. S.; Kuyavskaya, B. Y.; Belinskii, M. I.; Ablov, A. V.; Novotortsev, V. M.; Kalinnikov, V. T. *Theor. Chim. Acta* **1975**, *38*, 131-138.
31. Cannon, R. D.; White, R. P. *Prog. Inorg. Chem.* **1988**, *36*, 195-298.
32. Clemente, J. M.; Palii, A. V.; Tsukerblat, B. S.; Georges, R., In *Molecular Magnetism: From Molecular Assemblies to the Devices*; Coronado, E.; Delhaes, P.; Gatteschi, D.; Miller, J. S., Eds. Kluwer: Dordrecht, 1996; pp 85-104.
33. Padilla, J.; Gatteschi, D.; Chaudhuri, P. *Inorg. Chim. Acta* **1997**, *260*, 217-220.
34. Belinsky, M. I. *Inorg. Chem.* **2004**, *43*, 739-746.
35. Yoon, J.; Mirica, L. M.; Stack, T. D. P.; Solomon, E. I. *J. Am. Chem. Soc.* **2004**, *126*, 12586-12595.
36. Grohol, D. G.; Matan, K.; Lee, Y. S.; Nocera, D. G. in preparation.
37. Thio, T.; Thurston, T. R.; Preyer, N. W.; Picone, P. J.; Kastner, M. A.; Jensen, H. P.; Gabbe, D. R.; Chen, C. Y.; Birgeneau, R. J.; Aharony, A. *Phys. Rev. B* **1988**, *38*, 905-908.
38. Kadanoff, L. P.; Gotze, W.; Hamblen, D.; Hecht, R.; Lewis, E. A. S.; Palciauskas, V. V.; Rayl, M.; Swift, J.; Aspnes, D. E.; Kane, J. *Rev. Mod. Phys.* **1967**, *39*, 395-431.

Chapter 3

39. Grohol, D.; Matan, K.; Cho, J.-H.; Lee, S.-H.; Lynn, J. W.; Nocera, D. G.; Lee, Y. S. *Nature Materials* **2005**, *4*, 323-328.
40. Long, G. J.; Longworth, G.; Battle, P.; Cheetham, A. K.; Thundathil, R. V.; Beveridge, D. *Inorg. Chem.* **1979**, *18*, 624-632.
41. Papoutsakis, D.; Kirby, J. P.; Jackson, J. E.; Nocera, D. G. *Chem. Eur. J.* **1999**, *5*, 1474-1480.
42. Kastner, M. A.; Birgeneau, R. J.; Thurston, T. R.; Picone, P. J.; Jenssen, H. P.; Gabbe, D. R.; Sato, M.; Fukuda, K.; Shamoto, S.; Endoh, Y.; Yamada, K.; Shirane, G. *Phys. Rev. B* **1988**, *38*, 6636-6640.
43. Wells, B. O.; Birgeneau, R. J.; Chou, F. C.; Endoh, Y.; Johnston, D. C.; Kastner, M. A.; Lee, Y. S.; Shirane, G.; Tranquada, J. M.; Yamada, K. *Z. Phys. B: Condens. Matter* **1996**, *100*, 535-545.
44. Morrish, A. H. *The Physical Principles of Magnetism*. ed.; IEEE Press: Piscataway, NJ, 2001.
45. Uchinokura, K.; Ino, T.; Terasaki, I.; Tsukada, I. *Physica B* **1995**, *205*, 234-248.
46. Grohol, D.; Nocera, D. G. *J. Am. Chem. Soc.* **2002**, *124*, 2640-2646.
47. Grohol, D.; Papoutsakis, D.; Nocera, D. G. *Angew. Chem., Int. Ed.* **2001**, *40*, 1519-1521.
48. Grohol, D.; Huang, Q.; Toby, B. H.; Lynn, J. W.; Lee, Y. S.; Nocera, D. G. *Phys. Rev. B* **2003**, *68*, 094404/1-7.
49. Papoutsakis, D.; Grohol, D.; Nocera, D. G. *J. Am. Chem. Soc.* **2002**, *124*, 2647-2656.
50. Lines, M. E. *Phys. Rev.* **1963**, *131*, 546-555.
51. Birgeneau, R. J.; Yelon, W. B.; Cohen, E.; Makovsky, J. *Phys. Rev. B* **1972**, *5*, 2607-2615.
52. Day, P. *Acc. Chem. Res.* **1988**, *21*, 250-254.
53. Katori, H. A.; Katsumata, K.; Katori, M. *Phys. Rev. B* **1996**, *54*, R9620-R9623.

Chapter 4. Toward Spin Frustration in an $S = \frac{1}{2}$ Kagomé Lattice

4.1 Introduction

In Chapter 3, we fully described the magnetic interactions in spin frustrated iron jarosites—both the strong interlayer antiferromagnetism and the spin canting which gives rise to 3-D long-range order. Recall from Chapter 1, however, that in order to probe the relationship between magnetic spin frustration and resonance valence bond theory, we require a purely 2-D system of *quantum* spins that cannot show LRO. Iron jarosites have classical ground states, meaning there is a continuum of degenerate zero-energy rotational modes¹ like the one shown in Figure 3.7. This macroscopic degeneracy scales as the spin quantum number, S , which makes iron jarosites not suitable for the investigation of possible RVB states. For these reasons, we set out to find an $S = 1/2$ kagomé antiferromagnet, where the quantum nature of the system does not allow for such zero-energy modes.²⁻⁵

Previous studies of V^{3+} and Cr^{3+} jarosite analogs, along with the Fe^{3+} jarosites, provide guideposts for the development of an $S = 1/2$ kagomé antiferromagnet. The magnetic M^{3+} ions of jarosites reside in a tetragonally distorted crystal field. Axial elongation of the M^{3+} octahedron lifts the degeneracy of the t_{2g} and e_g orbital sets in a parent octahedral field: the t_{2g} orbital set splits into a lower energy, doubly-degenerate $e_g(d_{xz}, d_{yz})$ orbital set and an empty, singly-degenerate $b_{2g}(d_{xy})$ orbital; the e_g orbital set splits into a lower energy $a_{1g}(d_{z^2})$ orbital and higher energy $b_{1g}(d_{x^2-y^2})$ orbital.

Figure 4.1 presents the magnetic properties of the known first row transition metal jarosites together with the d -electron occupancy of the crystal field energy level diagram. The two d -electrons of V^{3+} jarosite occupy the $e_g(d_{xz}, d_{yz})$ orbital. The positive Θ of V^{3+} jarosite reveals that the π -symmetry pathway, composed of the interaction of the $e_g(d_{xz}, d_{yz})$ orbital set with the p orbital of the bridging hydroxide, leads to a ferromagnetic exchange interaction. Neutron diffraction studies show that the O—H bond is rotated 18° out of the Fe—O—Fe plane. This rotation is apparently sufficiently severe enough to decouple the $d\pi$ orbitals of neighboring V^{3+} metals to lead to a ferromagnetic ground state. This is not so for Cr^{3+} -jarosite; the sign of the

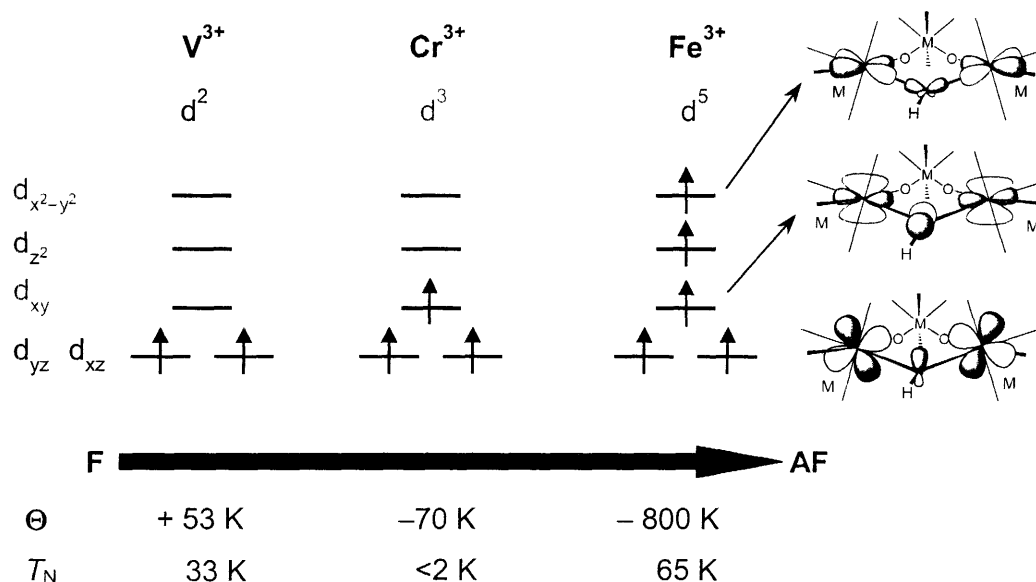


Figure 4.1. Magneto-electronic correlation in jarosites emphasizing the need to go to late metals for nearest-neighbor antiferromagnetic coupling.

nearest-neighbor magnetic coupling changes upon the addition of one more electron to the crystal field diagram. Occupation of the metal d_{xy} orbitals in Cr^{3+} jarosites leads to a dominant antiferromagnetic exchange term via a $d_{xy}(\sigma) - p(\text{O}) - d_{xy}(\sigma)$ pathway that is capable of overwhelming the ferromagnetic contribution of the $d_{xz}(\pi) - p(\text{O}) - d_{xz}(\pi)$ pathway. Placement of two more electrons in the d_{z^2} and $d_{x^2-y^2}$ orbitals of Fe^{3+} jarosite increases this antiferromagnetic exchange interaction within the kagomé lattice by more than an order of magnitude. Inasmuch as the overlap between the d_{z^2} orbitals and the p orbitals of the bridging hydroxide is small, it is the overlap of the $d_{x^2-y^2}$ orbitals via the μ -hydroxy p orbital that carries the large antiferromagnetic exchange interaction of Fe^{3+} jarosites. The observed properties of this exchange pathway concur with long-standing predictions of Goodenough and Kanamori,^{6,7} and accounts for the high degree of spin frustration observed in the d^5 ($S = 5/2$) spin jarosite system.

We hypothesize that an early metal in an $S = 1/2$ kagomé lattice, such as Ti^{3+} , would behave in a manner similar to V^{3+} and show nearest-neighbor ferromagnetism since the parentage of the exchange pathway is the same. Not to mention, there are synthetic challenges

associated with stabilizing Ti^{3+} in an aqueous environment. The trend shown in Figure 4.1 supports the notion that, as is the case of Fe^{3+} , strongest antiferromagnetism results from strong σ -overlap of the $d_{x^2-y^2}$ orbitals with the bridging hydroxy group. Therefore, an $S = \frac{1}{2}$ spin system in this electronic structure framework may be achieved if Cu^{2+} is the magnetic ion. A copper kagomé lattice is fitting since the high T_c superconductors are comprised of doped cupric oxide layers. Moreover, a DM interaction for an $S = \frac{1}{2}$ system, if present, will be much smaller ($25 \times$) since the interaction energy is proportional to S^2 (equation 3.1).

Spin frustration in Cu^{2+} triangles has been explored in molecules, which can be thought of as 0-D materials. However these compounds undergo a magnetic Jahn-Teller distortion to give a 2 (antiferromagnetically coupled) + 1 (uncoupled) spin ground state, illustrated in Figure 4.2.⁸⁻¹⁹ Recent magnetic circular dichroism and EPR work by Solomon shows that the zero-field splitting in a hydroxy-bridged Cu^{2+} triangle is controlled by the opposing effects of antisymmetric exchange and symmetry lowering, resulting in partial spin delocalization.¹⁹ Although the molecule has perfect D_3 symmetry with a 2E ground state at high temperature, distortions at low temperature eradicate the magnetic properties associated with spin frustration (a suppressed ordering temperature relative to Θ). Thus, an extended array is essential for bridging the connection of spin frustrated magnetism to the predictions of RVB theory.

In the mineralogy literature, we find that the compound, lindgrenite, $\text{Cu}_3(\text{OH})_2(\text{MoO}_4)_2$ is made up of 1-D chains of copper triangles,²⁰⁻²² in which the triangles alternate between corner-

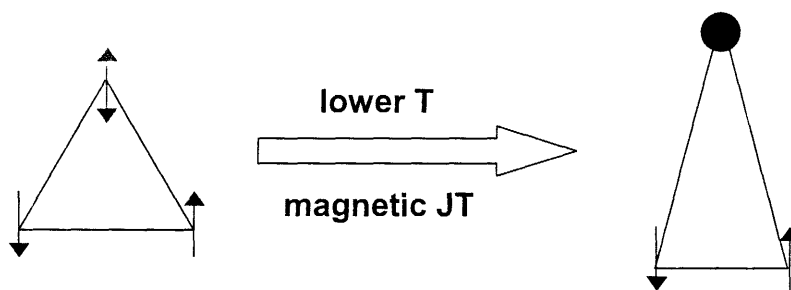


Figure 4.2. Magnetic Jahn-Teller distortions prevalent in molecular triangles relieve spin frustration by providing a 2 (coupled) + 1 (uncoupled) ground state.

and edge-sharing. In the lindgrenite structure, the molybdate dianion, MoO_4^{2-} , forms bridges to coppers within a layer through the its pyramidal base, and also connects adjacent layers via the apical oxygen. Extended copper molybdates have been well-studied by Zubieta, although, the structures obtained are dictated by reaction conditions,²³⁻²⁹ due to the rich chemistry of polyoxometallates which often results in large clusters of molybdate rather than tetrahedral MoO_4^{2-} .³⁰ This Chapter will start with the preparation and magnetic characterization of expanded lindgrenite structures with piperazine and biphenyl spacers to magnetically isolate layers of triangular chains. From here, we go on toward layered 2-D kagomé layered materials.

Although no stoichiometrically pure $S = \frac{1}{2}$ kagomé systems have been prepared to date,³¹ there are Cu^{2+} -containing kagomé compounds in the mineralogy literature. The atacamite family of minerals is comprised of monoclinic, orthorhombic, and rhombohedral polymorphs of $\text{Cu}_2(\text{OH})_3\text{Cl}$, where the corner sharing triangles are $\text{Cu}^{\text{II}}_3-(\mu\text{-OH})_3$ units, similar to the fundamental magnetic unit of the jarosites.³²⁻³⁵ These units make up 2-D sheets, but also form $\text{Cu}-\text{O}-\text{Cu}$ chains perpendicular to the sheets. The monoclinic polymorph, clinoatacamite, has been studied as a pyrochlore model, for example.³⁶ Original studies of the magnetism and heat capacity in synthetic orthorhombic atacamite show spin-glass behavior.³⁷ This leaves open the prospect of preparing a frustrated lattice consisting completely of Cu^{2+} kagomé layers if the interlayer Cu^{2+} (resulting in the pyrochlore structure) were replaced with a diamagnetic ion. Substitution of Zn^{2+} on the interlayer Cu^{2+} sites occurs in natural samples of clinoatacamite to give the compound zinc paratacamite, $\text{Zn}_x\text{Cu}_{1-x}\text{Cu}_3(\text{OH})_6\text{Cl}_2$.³⁴ For $x > 0.3$, the compound adopts perfect rhombohedral symmetry.³⁸ A range of compositions has been prepared, but the magnetism has yet to be reported in the literature. Moreover, mineralogical and synthetic samples prepared to date are not magnetically pure, leading to the same magnetostructural characterization problems that plagued the jarosites that we saw in § 2.1. This Chapter describes the synthesis and magnetic properties of clinoatacamite and zinc paratacamite, and provides a magnetic model for understanding a magnetochemical correlation in copper kagomé systems.

4.2 Experimental

4.2.1 General Procedures

All chemicals of reagent or analytical grade were obtained from Aldrich or Strem, and they were used without purification. Hydrothermal reactions were carried out in Teflon-lined pressure vessels, which were purchased from Parr Instruments. A Fisher Isotemp programmable oven with forced-air circulation was used to obtain the desired temperature profiles for hydrothermal reactions. Chemical analyses were conducted by the H. Kolbe Mikroanalytisches Laboratorium.

4.2.2 Synthesis of $(\text{pip})\text{Cu}_3(\text{OH})_2(\text{MoO}_4)_2$

A 23 mL Teflon liner was charged with 0.148 g of copper(II) hydroxide (1.52 mmol), 0.216 g of molybdenum(VI) oxide (1.50 mmol), 0.194 g of piperazine (1.00 mmol), and 5 mL of deionized water. The liner was capped and placed into a steel hydrothermal bomb under ambient room atmosphere. The tightened bomb was heated in the oven at a rate of 1 °C/min. to 140 °C, which was maintained for 12 h. The oven was then cooled to room temperature at a rate of 0.1 °C/min. A mixture of white precipitate, yellow-green, blue, and green microcrystals was isolated from the walls and bottom of the liner, and was washed with deionized water and dried in air. The yellow-green crystals are the title compound and green crystals are $(\text{pip})\text{Cu}_2(\text{MoO}_4)_2$, as identified by single crystal structures. Attempts to isolate the title compound in pure form have been unsuccessful.

4.2.3 Synthesis of $(4,4'\text{-bipy})\text{Cu}_3(\text{OH})_2(\text{MoO}_4)_2$

A 23 mL Teflon liner was charged with 0.100 g of copper(II) hydroxide (1.03 mmol), 0.220 g of basic copper carbonate (1.04 mmol), 0.153 g of 4,4'-dipyridyl (0.98 mmol), 0.341 g of ammonium dimolybdate (1.00 mmol), and 10 mL of deionized water. The liner was capped and placed into a steel hydrothermal bomb under ambient room atmosphere. The tightened bomb was

heated in the oven at a rate of 1 °C/min. to 180 °C, which was maintained for 36 h. The oven was then cooled to room temperature at a rate of 0.1 °C/min. A blue-green microcrystalline powder was isolated from the walls and bottom of the liner, and was washed with deionized water and dried in air. The bulk product was identified as (4,4'-bipy)Cu₃(OH)₂(MoO₄)₂ by powder X-ray diffraction. A solved single crystal structure was obtained, and comparison of the bulk sample to the simulated powder pattern shows no additional crystalline products. Yield: 0.555 g (79.2 % based on starting Cu²⁺). Anal. calcd. for C₁₀H₈N₂Cu₃Mo₂O₁₀: C, 17.14; H, 1.44; N, 4.00; Cu, 27.21; Mo, 27.31. Found: C, 17.06; H, 1.43; N, 3.94; Cu, 27.26; Mo, 27.31.

4.2.4 Synthesis of Clinoatacamite, Cu₂(OH)₃Cl

Method 1. A 23 mL TeflonTM liner was charged with 0.448 g of basic copper carbonate (2.03 mmol), 0.3 mL of conc. HCl (3.7 mmol), and 10 mL of deionized water. The liner was capped and placed into a steel hydrothermal bomb under ambient room atmosphere. The tightened bomb was heated in the oven at a rate of 5 °C/min. to 210 °C, which was maintained for 60 h. The oven was then cooled to room temperature at a rate of 0.1 °C/min. A blue-green microcrystalline powder was isolated from the walls and bottom of the liner, and was washed with deionized water and dried in air. The product was identified as clinoatacamite by powder X-ray diffraction. Yield: 0.139 g (32.0% based on starting Cu₂(OH)₂CO₃).

Method 2. An 800 mL TeflonTM liner was charged with 11.9 g of copper (I) chloride (0.120 mol) and 390 mL of deionized water. Into this mixture, 2.33 g of sodium chloride (0.040 mol) and 6.8 mL of hydrochloric acid (0.08 mol) were added. The liner was capped and placed into a steel hydrothermal bomb under an atmosphere of oxygen using an Aldrich AtmosbagTM. The tightened bomb was heated in the oven at a rate of 5 °C/min. to 210 °C, which was maintained for 9 d. The oven was then cooled to room temperature at a rate of 0.1 °C/min. Crystals were isolated as green plates from the walls of the liner. More green plates and a microcrystalline blue-green powder were isolated from the bottom of the liner. Sieves were employed to physically separate the plates and powder. The green crystals were washed with

deionized water and dried in air. The product was identified as clinoatacamite by powder X-ray diffraction. Yield: 0.905 g (7.05% based on starting CuCl).

Method 3. A 23 mL Teflon liner was charged with 0.294 g of copper (I) chloride (2.97 mmol) and 10 mL of deionized water. Into this mixture, 0.09 mL of perchloric acid (1.0 mmol) was added via Mohr pipet. The liner was capped and placed into a steel hydrothermal bomb under ambient room atmosphere. The tightened bomb was heated in the oven at a rate of 5 °C/min to 210 °C, which was maintained for 72 h. The oven was then cooled to room temperature at a rate of 0.1 °C/min. Crystals were isolated as green plates from the walls and base of the liner. The green crystals were washed with deionized water and dried in air. The product was identified as clinoatacamite by powder X-ray diffraction. Yield: 0.089 g (28.1% based on starting CuCl).

Anal. calcd. for $\text{H}_3\text{Cu}_2\text{ClO}_3$: H, 1.41; Cu, 59.51; Cl, 16.60. Found: H, 1.39; Cu, 59.48; Cl, 16.63.

4.2.5 Synthesis of Zinc Paratacamite, $\text{ZnCu}_3(\text{OH})_6\text{Cl}_2$

An 800 mL TeflonTM liner was charged with 16.7 g of basic copper carbonate (0.076 mol) and 350 mL of deionized water. Into this mixture, 12.2 g of zinc chloride (0.090 mol) was added. The liner was capped and placed into a steel hydrothermal bomb under ambient room atmosphere. The tightened bomb was heated in the oven at a rate of 5 °C/min. to 210 °C, which was maintained for 48 h. The oven was then cooled to room temperature at a rate of 0.1 °C/min. A blue-green microcrystalline powder was isolated from the walls and bottom of the liner, and was washed with deionized water and dried in air. The product was identified as zinc paratacamite by powder X-ray diffraction. Yield: 21.024 g (96.7 % based on starting $\text{Cu}_2(\text{OH})_2\text{CO}_3$).

Anal. calcd. For $\text{H}_6\text{ZnCu}_3\text{Cl}_2\text{O}_6$: H, 1.41; Zn, 15.24; Cu, 44.44; Cl, 16.53. Found: H, 1.46; Zn, 15.11; Cu, 44.50; Cl, 15.50.

4.2.6 X-ray Diffraction

Powder X-ray diffraction patterns were measured using a Rigaku RU300 rotating anode X-ray diffractometer with Cu K α radiation ($\lambda = 1.5405 \text{ \AA}$), which was wavelength-selected with a single-crystal graphite monochromator. Samples were spread onto a glass slide fixed with double-sided Scotch tape. Samples were rotated through $2\theta/\theta$ space and intensity was recorded as a function of 2θ from $10 - 60^\circ$. Patterns were indexed with MDI Jade software version 7.0 and references using the JCPDS powder diffraction database.

X-ray diffraction data were collected using a Brüker three-circle single crystal diffractometer on a SMART platform equipped with a CCD APEX detector. For all of the compounds, data were acquired at 150 K using Mo K α radiation ($\lambda = 0.71073 \text{ \AA}$), which was wavelength-selected with a single-crystal graphite monochromator. For each crystal, four sets of 40-s frames were collected over a hemisphere of reciprocal space using ω scans and a -0.3° scan width. The data frames were integrated to hkl /intensity, and final unit cells were calculated using the SAINT program. Space group assignments were based on systematic absences, E statistics, and successful refinement of the structures. Structures were solved by the Patterson methods with the aid of successive difference Fourier maps and were refined against all data using version 6.1 of the Brüker SHELXTL suite of programs. Thermal parameters for all heavy atoms were refined anisotropically. Details regarding the refined data and cell parameters are provided in Table A.3.

4.2.7 Physical Methods

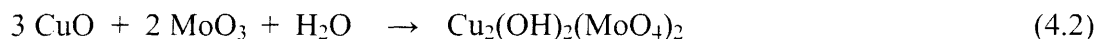
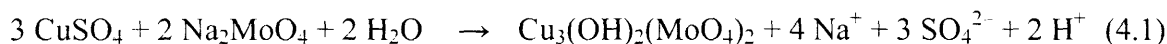
Magnetic susceptibilities were determined on powdered samples contained in gelatin capsules using a Quantum Design MPMSR2 Susceptometer over a $2 - 300 \text{ K}$ temperature range at field strengths varying from $0 - 50 \text{ kOe}$. For each dc susceptibility data point, the average of three measurements of 32 scans over a 4 cm scan length was acquired. Data were corrected for core diamagnetism using Pascal's constants. Ac susceptibilities were recorded for each compound under an ac field, $H_{ac} = H_0 \sin(2\pi ft)$ for $H_0 = 3 \text{ Oe}$ and $f = 2, 20, \text{ and } 200 \text{ Hz}$.

Zero-field cooled (ZFC) susceptibilities were measured by first cooling the samples from 300 K to 2 K under zero field. Dc susceptibility was then measured in a field $H_m = 100$ Oe as a function of temperature as the sample was warmed from 2 – 300 K. Field-cooled (FC) susceptibilities were measured in a similar fashion, except the cooling and measuring fields were both 100 Oe. Curie-Weiss analysis was done on the inverse susceptibility of ZFC over the temperature range 150 – 300 K. Curie-Weiss plots are included in Appendix B.

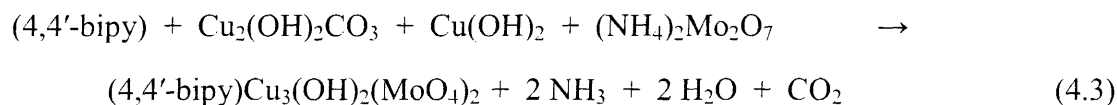
4.3 Results

4.3.1 Synthetic Methodology

The mineral lindgrenite can be prepared either under refluxing conditions (eq. 4.1) or hydrothermally (eq. 4.2) by published literature methods³⁹



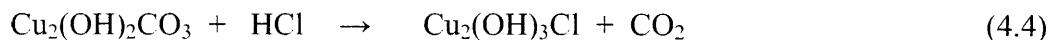
Extending this chemistry to expand the layers proceeds by using an amine donor to replace the apical oxygen of the MoO_4^{2-} moiety bound to Cu^{2+} . Reactions proceed hydrothermally as



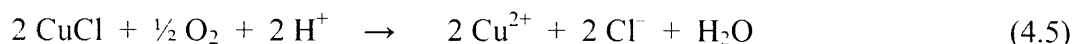
This reaction is run under basic conditions, with the pH increasing from 8.1 to 9.0 over the course of the reaction. Thus, the products of equation 4.3 seem reasonable. Most important, the structure shows that the materials is a hybrid inorganic-organic material, and the use of amine donors for pillaring or separating inorganic metal oxide layers is well precedented.⁴⁰

Synthetic clinoatacamite has been prepared in the literature by a precipitation route in an alkaline aqueous solution under ambient conditions.³⁴ We sought to extend this chemistry from the benchtop reaction to a hydrothermal-based route in order to improve the crystallinity of the mineral product. Noting that the pH of dissolved Cu^{2+} in water is approximately 5.5, we moved

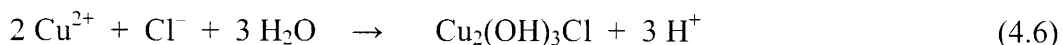
from basic to acidic condition, starting from Cu^{2+} salts in an acidic aqueous solution that results in an overall reaction



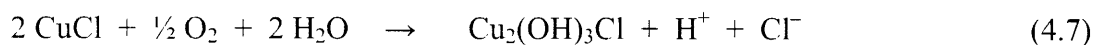
Reactions executed in this manner yield the desired product, clinoatacamite, in 32 % yield. However, only microcrystalline powders result from this reaction method. From our jarosite work in Chapter 2, we know that adding redox steps slows seed nucleation relative to the crystal growth process, allowing us to obtain large crystals. A similar kinetic control for Cu^{2+} chemistry can be achieved starting from copper(I) chloride with elemental oxygen as an oxidant (eq. 4.5). Reaction 4.5 is thermodynamically favored under standard conditions, with a driving force, E° , of 1.07 V. Additionally, dissociation of CuCl is necessarily slow as K_{sp} is on the order of 10^{-6} .



Precipitation of the Cu^{2+} as it appears in solution,

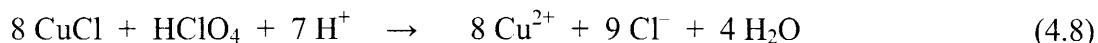


will yield clinoatacamite according to the overall balanced equation,

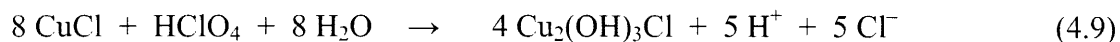


A separate source of chloride is added in the form of NaCl in order to assemble the lattice in eq. 4.6 since the chloride concentration is otherwise limited by the low solubility of CuCl . Reactions performed in this manner give single crystals ranging in size from 0.1 – 0.5 mm. We note that the yield is very low, and it takes 9 days to complete the reaction owing to the two slow steps, dissolution of both solid CuCl and gaseous O_2 in water, inserted in equation 4.5. This may be the reason why crystals, albeit small, are obtained and provides a hint into strategies to obtain larger crystals. If reactions are run for less than 9 days, unreacted CuCl starting material can be identified in the product mixture by powder XRD.

Faster reaction times and higher yields may be achieved with solution-based oxidants, which removes the heterogenous oxygen dissolving step. Again, the introduction of Cl^- into solution is limited by the insolubility of CuCl . Since Cl^- is required in the reaction, perchlorate, ClO_4^- , makes for an obvious choice of oxidant. The redox step is

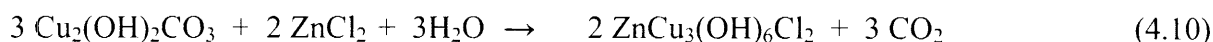


which when combined with eq. 4.6 gives an overall reaction of



With perchlorate as an oxidant, the driving force for eq. 4.8 is slightly larger ($E^\circ = 1.13 \text{ V}$) than the Cu^{2+} -generating reaction of eq. 4.2. Moreover, the reaction depicted in equation. 4.9 proceeds in half the time of equation 4.7 (4 d cf. 9 d). The overall balanced reaction (eq. 4.9) reveals that pH control is key to crystal growth. Experimentally, the pH is observed to increase from 0.6 to 1.4 during the course of the hydrothermal reactions.

Zinc paratacamite is prepared directly from the starting compounds malachite (basic copper carbonate) and zinc chloride



In this reaction, there is no redox chemistry employed, and again only microcrystalline powders result. Attempts to add redox steps results only in the formation of clinoatacamite, and we find that reacting clinoatacamite with zinc chloride under harsh, forcing conditions (hydrothermal reaction at 240 °C for several days both with and without added HCl) results in no incorporation of zinc into the lattice. Introducing clinoatacamite to basic solutions immediately results in decomposition of the material to the thermodynamically more stable tenorite (CuO) phase.

4.3.2 Structural Chemistry

Lindgrenite crystallizes in the space group $P2_1/n$, and is made up of alternating corner- and edge-sharing triangular chains, illustrated in Figure 4.3. The structure contains complex chains of $\text{CuO}_4(\text{OH})_2$ octahedra with two crystallographically distinct Cu atoms in the structure. The average Mo—O distance is 1.75 Å with Jahn Teller distorted Cu—O distances of 1.95 Å and 2.42 Å. The Cu—O distances are not significantly perturbed by the addition of the amine donor ligands, and the Cu—N distance is 2.02 Å, all within expected values. We do note that addition of the organic component lowers the overall symmetry of the structure to $P\bar{1}$, although the structure of the inorganic layers is conserved. Of course, the interlayer separation increases from

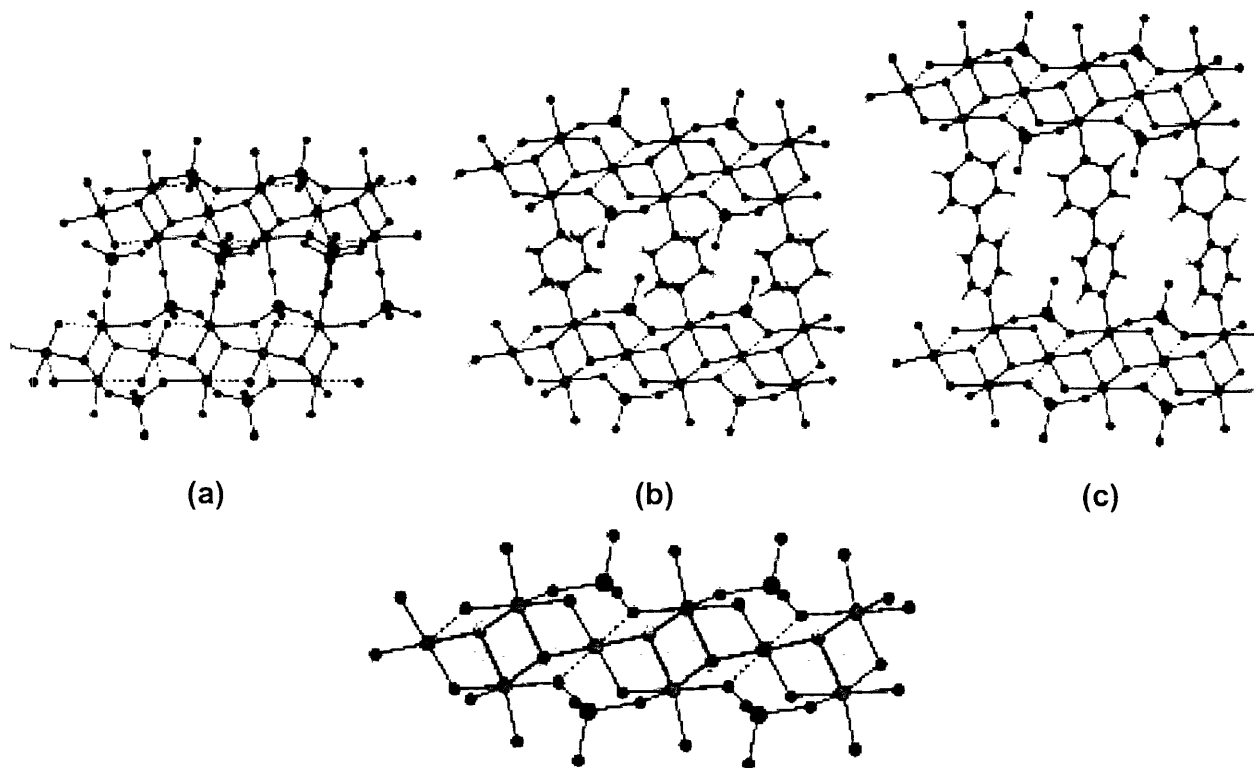


Figure 4.3. Structure of a) lindgrenite, $\text{Cu}_3(\text{OH})_2(\text{MoO}_4)_2$, and the layer-expanded versions b) $(\text{pip})\text{Cu}_3(\text{OH})_2(\text{MoO}_4)_2$ and c) $(4,4'\text{-bipy})\text{Cu}_3(\text{OH})_2(\text{MoO}_4)_2$. Light blue spheres are Cu, green spheres are Mo, red spheres are O, dark blue spheres are N, gray spheres are C, and white spheres are H. The bottom panel shows the alternating corner- and edge-sharing connectivity of the triangles within 1-D chains.

7.012(3) Å to 9.447(2) Å in the case of piperazine, and to 13.456(2) Å for 4,4'-bipyridyl. Full crystallographic data, including tables of bond distances and angles for the amine-expanded structures are provided in Appendix A.

The compounds clinoatacamite and zinc paratacamite are structurally related, and both can be generally represented by the formula $\text{MCu}_3(\text{OH})_6\text{Cl}_2$, where $\text{M} = \text{Cu}$ or Zn respectively. Figure 4.4 shows the X-ray powder diffraction pattern for the kagomé-containing compounds used in this study; the assigned indices of the diffraction patterns are given in Appendix A. As in jarosites, the kagomé layer is formed with $\text{Cu}_3-(\mu\text{-OH})_3$ triangles as the fundamental magnetic subunit. A Cl^- anion resides alternately above and below adjacent triangles with an interlayer M^{2+} ion opposite the Cl^- anion, also similar to the general structural motif of jarosites.

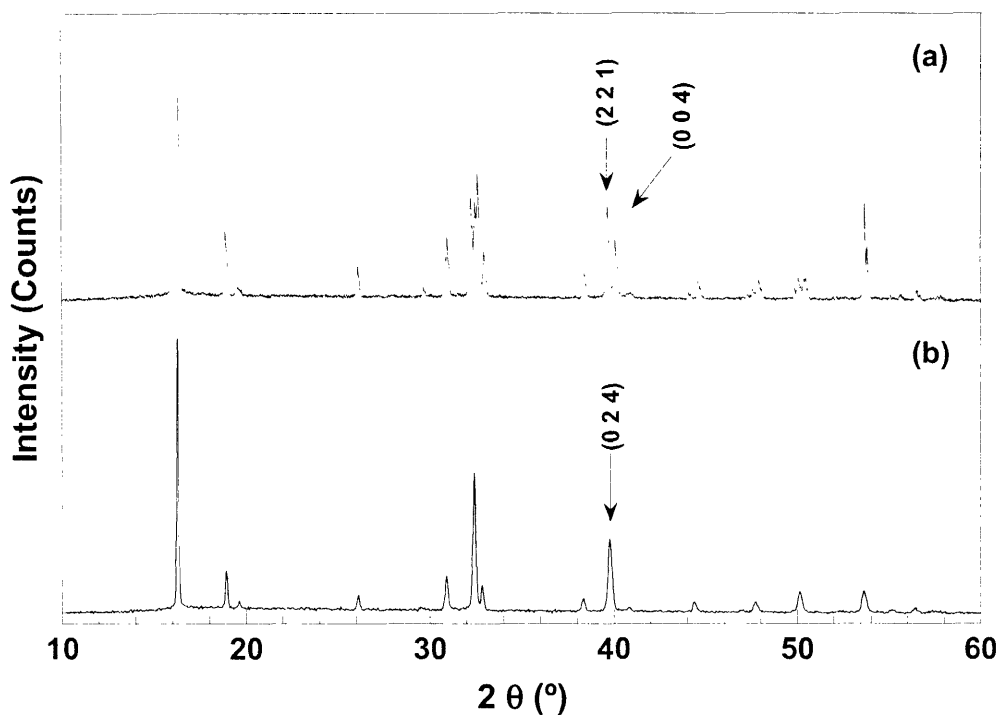


Figure 4.4. Powder X-ray diffraction patterns of a) clinoatacamite and b) zinc paratacamite. Although the structures are similar, the most distinguishing feature is found at $\approx 40^\circ 2\theta$, which occurs as two peaks in a), but a single peak in b) due to the difference in symmetry.

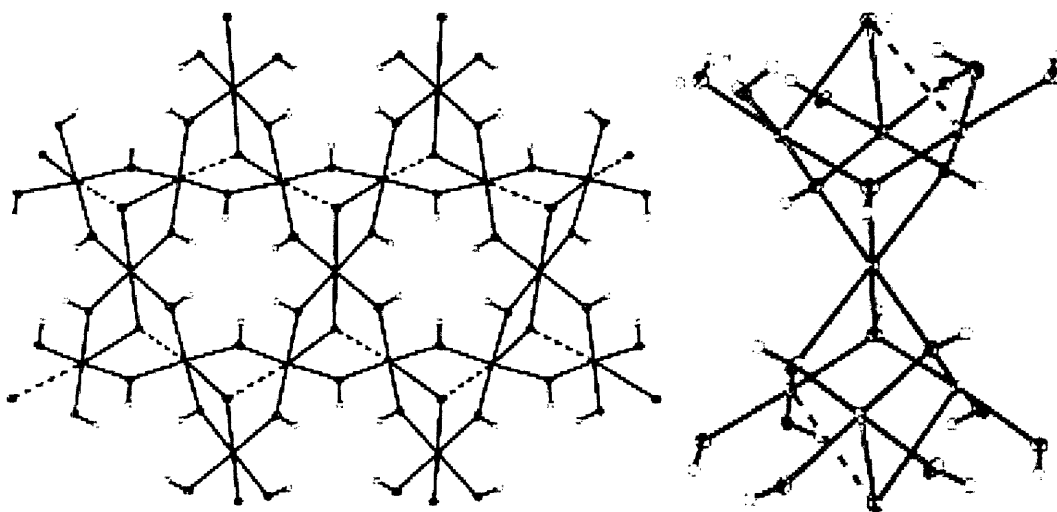


Figure 4.5. X-ray crystal structure of clinoatacamite, $\text{Cu}_2(\text{OH})_3\text{Cl}$, showing distorted kagomé layers (left) that come about due to Jahn-Teller distorted Cu^{2+} ions between the layers (right).

Climoatacamite crystallizes in the monoclinic space group $P2_1/n$, with three crystallographically distinct Cu^{2+} ions, as shown in Figure 4.5. The intralayer Cu—O distance ranges from 1.932(3) to 2.006(3) Å, with an average distance of 1.983 Å. The triangles are skewed from perfect equilateral triangles with two Cu··Cu in-plane distances of 3.410 and 3.423 Å. As a result, the Cl^- anion that resides above and below the layers then forms two short and one long contact to a given triangle. This deviation from rhombohedral symmetry can be understood by examining the coordination geometry of the interlayer copper cation, labeled Cu(3). Cu^{2+} in the interlayer also undergoes Jahn-Teller distortion to give three distinct Cu(3)—O distances of 1.980, 2.022, and 2.356 Å. In the triangular plane, the Cu—O—Cu bridging angle ranges from 117.0 – 124.1°, whereas the interlayer Cu—O—Cu(3) angle is much more acute, 90.9 – 101.5°.

Zinc paratacamite, on the other hand, shows perfect rhombohedral symmetry, and crystallizes in the $R\bar{3}m$ space group. The closed-shell Zn^{2+} ion in the interlayer space does not Jahn-Teller distort, and sits on the $\bar{3}$ axis above and below each triangle, alternating with the Cl^- anion. Figure 4.6 shows that the asymmetric unit is composed of unique Cu, O, Zn, and Cl atoms, with a Cu—O distance of 1.979(16) Å. The Cu··Cu distance is 3.415 Å with a Cu—O—

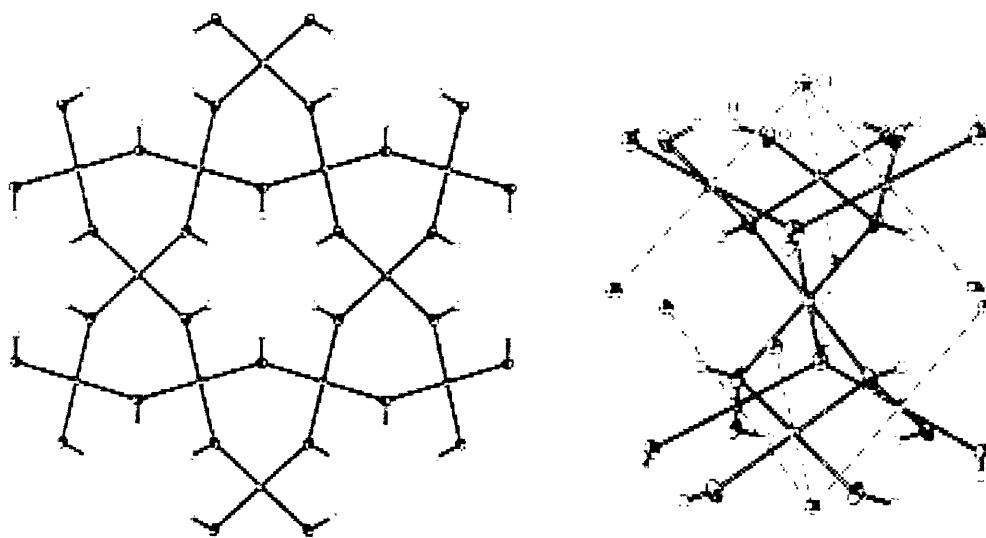


Figure 4.6. X-ray crystal structure of zinc paratacamite, $\text{ZnCu}_3(\text{OH})_6\text{Cl}_2$, showing perfect rhombohedral symmetry with no kagomé lattice distortions.

Cu bond angle of 119.2° . In zinc paratacamite, the Cu—O—Zn angle is 96.9° . Comparing the structures, we see that ignoring the Jahn-Teller distortion present in clinoatacamite, both the in-plane and out-of-plane structures of the two species are similar. Key structural features of the two compounds are compared in Table 4.1 with the atom labeling scheme provided in Figure 4.7.

Table 4.1. Structural comparison of clinoatacamite and zinc paratacamite.

Bond	Clinoatacamite				Zn-Paratacamite
	Bond distances (Å)				
Cu—O	1.932(3)	Cu(1)—O(1)	1.943(3)	Cu(2)—O(1)	1.9791(16)
	1.991(3)	Cu(1)—O(2)	2.006(3)	Cu(2)—O(2)	
	1.998(3)	Cu(1)—O(3)			
Cu—Cl		2.7685(11)	Cu(1)—Cl		2.772
		2.7514(10)	Cu(2)—Cl		
M—O		2.356(3)	Cu(3)—O(1)		2.105(3)
		1.980(3)	Cu(3)—O(2)		
		2.022(3)	Cu(3)—O(3)		
Angle	Bond angles ($^\circ$)				
Cu—O—Cu		124.15(14)	Cu(1)—O(1)—Cu(2)		119.24(16)
		116.96(14)	Cu(1)—O(3)—Cu(1)		
		117.14(13)	Cu(1)—O(2)—Cu(2)		
Cu—O—M	92.65(11)	Cu(1)—O(1)—Cu(3)	90.94(11)	Cu(2)—O(1)—Cu(3)	96.91(11)
	97.19(11)	Cu(1)—O(2)—Cu(3)	101.11(12)	Cu(2)—O(2)—Cu(3)	
	95.62(12)	Cu(1)—O(3)—Cu(3)			
	101.48(12)	Cu(1)—O(3)—Cu(3)			

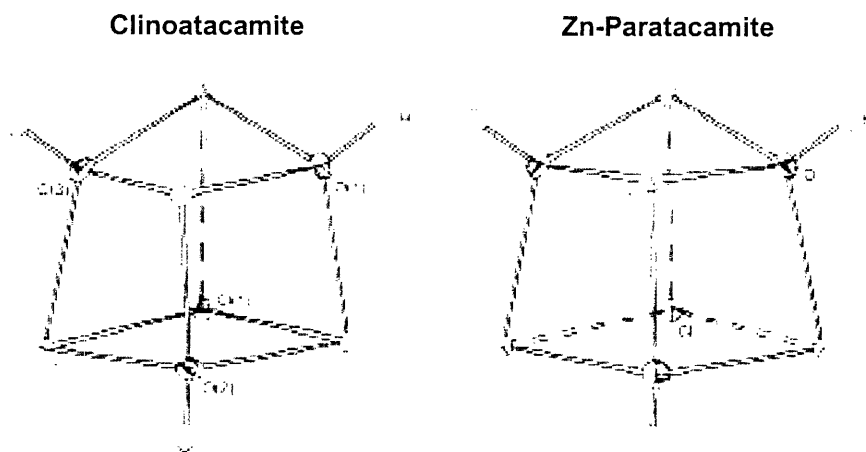


Figure 4.7. Atom labeling scheme for triangles of clinoatacamite and Zn-paratacamite.

4.3.3 Magnetic Properties

The d.c. susceptibility of lindgrenite, $\text{Cu}_3(\text{OH})_2(\text{MoO}_4)_2$, shown in Figure 4.8(a) exhibits a ferromagnetic ordering at $T_c = 13$ K. Magnetization versus field at 2 K shows hysteresis with a coercive field of $H_{\text{coercive}} = 0.4$ T (Figure 4.8(b)), supporting ferromagnetism below T_c . Curie-Weiss analysis of $\chi^{-1}(T)$ at high temperatures reveals weak antiferromagnetic nearest-neighbor exchange ($\Theta = -18$ K). Upon increasing the interlayer spacing in $(4,4'\text{-bipy})\text{Cu}_3(\text{OH})_2(\text{MoO}_4)_2$, we find that the ordering event is suppressed to 3.1 K (Figure 4.9(a)) and is now antiferromagnetic in origin, as the susceptibility reaches a cusp at 3.1 K. Antiferromagnetic LRO is further supported by the lack of hysteresis in the magnetization (Figure 4.9(b)), although the magnetization profile is unusual. Magnetization versus field is linear at low applied fields (below 1000 Oe), but follows an “S” shape above 1000 Oe. The nearest-neighbor exchange interaction in the bipy-expanded lindgrenite is more strongly antiferromagnetic than in lindgrenite alone ($\Theta = -63$ K).

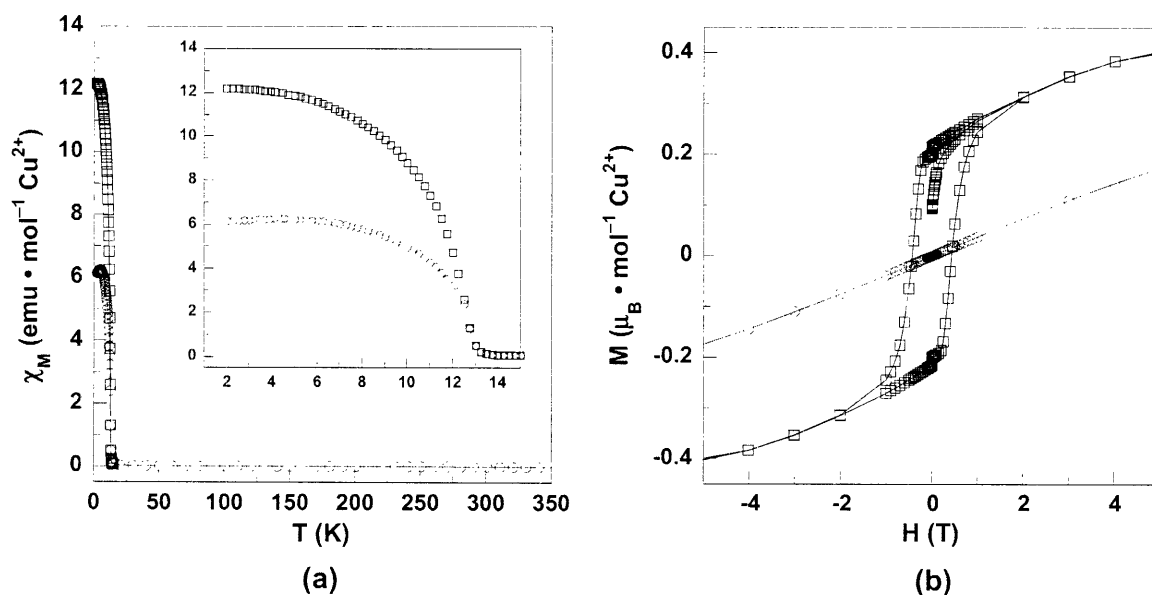


Figure 4.8. (a) ZFC (○) and FC (□) susceptibility of $\text{Cu}_3(\text{OH})_2(\text{MoO}_4)_2$. (b) Magnetization of $\text{Cu}_3(\text{OH})_2(\text{MoO}_4)_2$ showing hysteresis at 5 K (○), but not above the ordering temperature at 20 K (□).

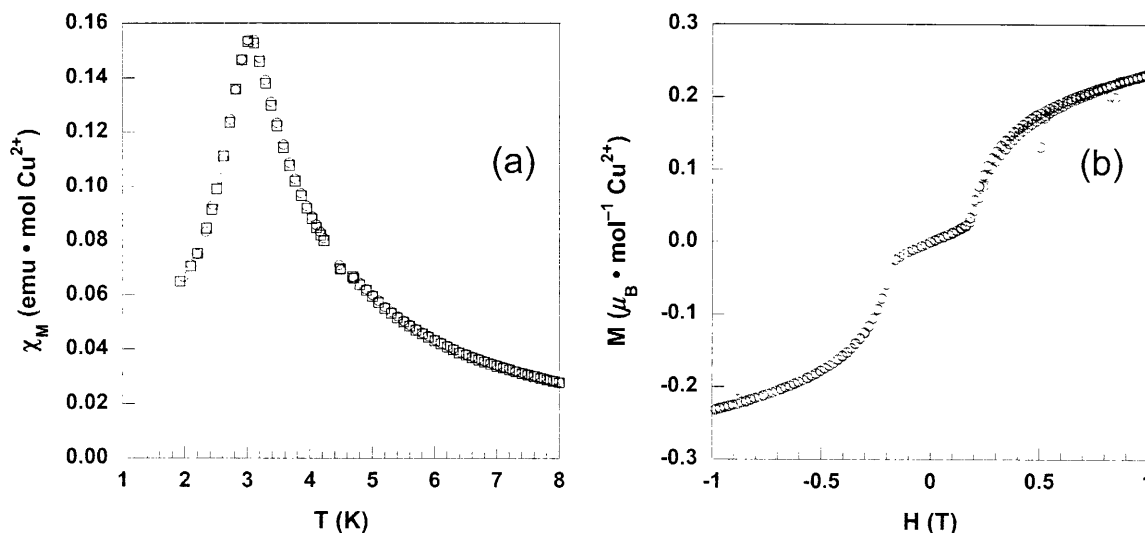


Figure 4.9. (a) ZFC (○) and FC (□) susceptibility and (b) magnetization versus field of (4,4'-bipy) $\text{Cu}_3(\text{OH})_2(\text{MoO}_4)_2$.

Looking at the kagomé lattice containing compounds, the d.c. susceptibility plot shown in figure 4.10 for clinoatacamite, $\text{Cu}_2(\text{OH})_3\text{Cl}$, exhibits a transition to a long-range ordered state at $T_c = 6.5$ K. This transition is ferromagnetic in nature, noted by the increase in $\chi(T)$ below the transition temperature, although Curie-Weiss analysis of $\chi^{-1}(T)$ reveals that on average, the nearest-neighbor exchange is strongly antiferromagnetic ($\Theta = -200$ K). Ferromagnetic long-range order is further supported by hysteresis in the magnetization below T_c with a coercive field, $H_{\text{coercive}} \approx 0.1$ T, and the a.c. susceptibility shows as single maximum at 6.5 K that is frequency independent, which precludes the presence of spin glass behavior. The evidence for ferromagnetism is shown in Figure 4.11.

Zinc paratacamite, $\text{ZnCu}_3(\text{OH})_6\text{Cl}_2$ shows no transition to LRO to temperatures down to 2 K (Figure 4.12), despite an exceptionally strong antiferromagnetic nearest-neighbor exchange interaction of $\Theta = -314$ K. Although no LRO is observed, $\chi(T)$ differs from what we would expect for non-interacting spins following a simple Curie law, also illustrated in Figure 4.12. That is, we can distinguish between spin frustration and paramagnetism in the SQUID magnetometer. Then, the absence of hysteresis in the field-dependent magnetization to applied

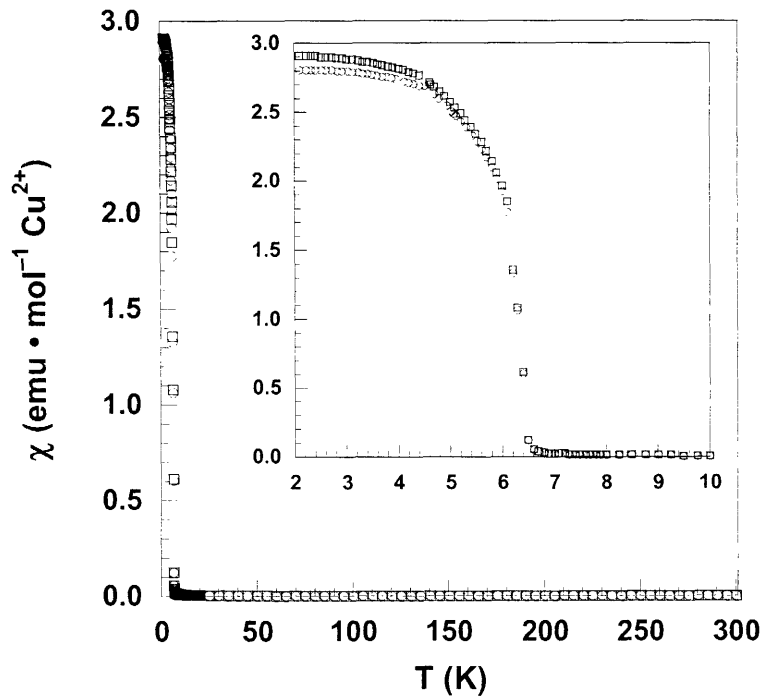


Figure 4.10. ZFC (\circ) and FC (\square) molar susceptibility in clinoatacamite, showing a sharp transition to a ferromagnetically ordered state at 6.5 K.

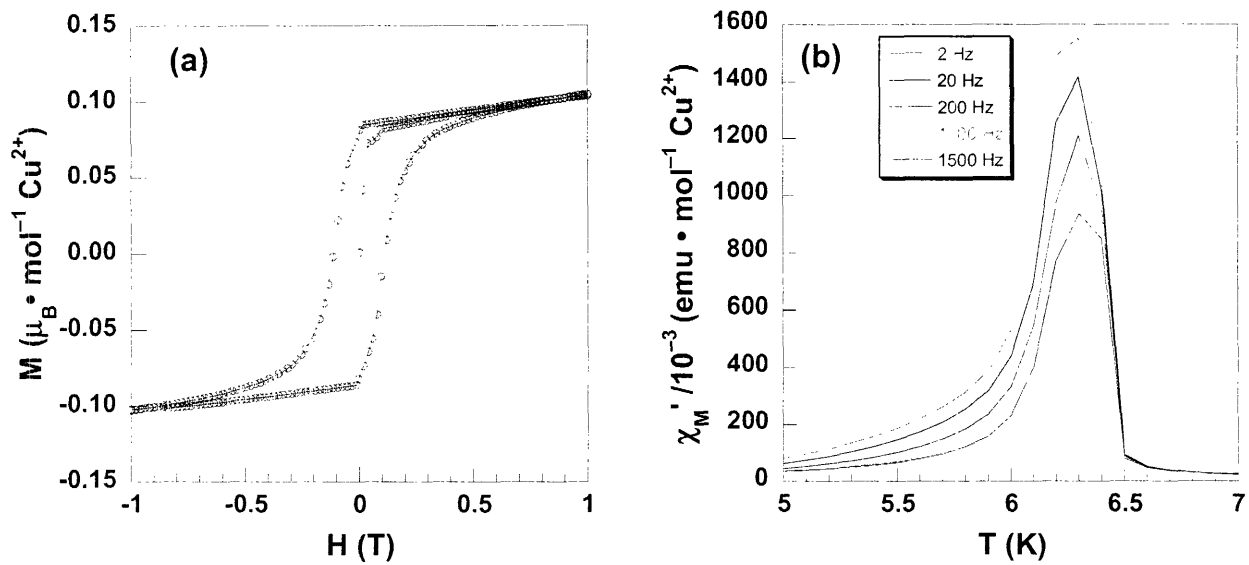


Figure 4.11. Evidence for ferromagnetic ordering in $\text{Cu}_2(\text{OH})_3\text{Cl}$ given by (a) hysteresis in the magnetization with a coercive field of $H_{\text{coercive}} \approx 0.1$ T, and b) a frequency independent maximum in the ac susceptibility.

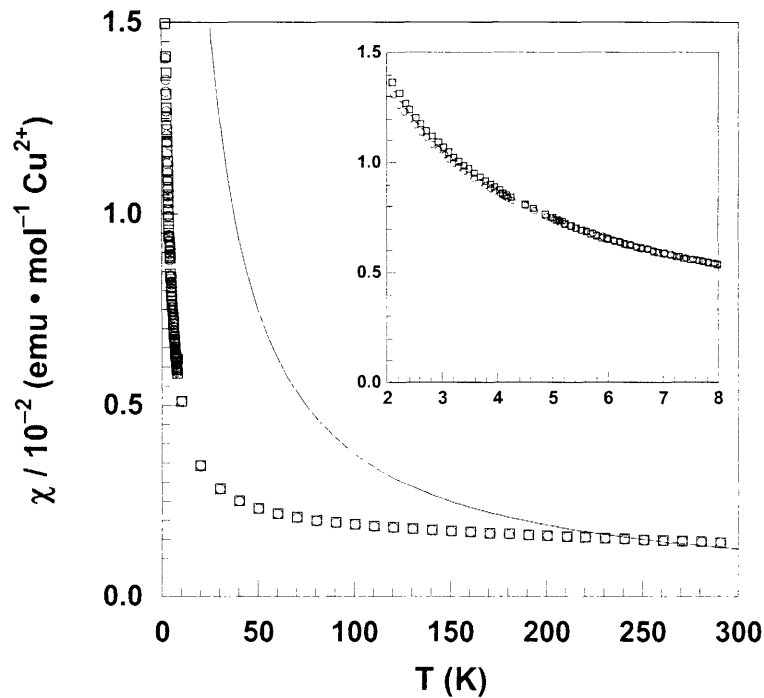


Figure 4.12. ZFC (\circ) and FC (\square) molar susceptibility in zinc paratacamite, showing no transition to LRO. The black line on the plot is the expected molar susceptibility of a simple $S = \frac{1}{2}$ paramagnet, following the Curie law. The inset shows blows up the region from 2 – 8 K.

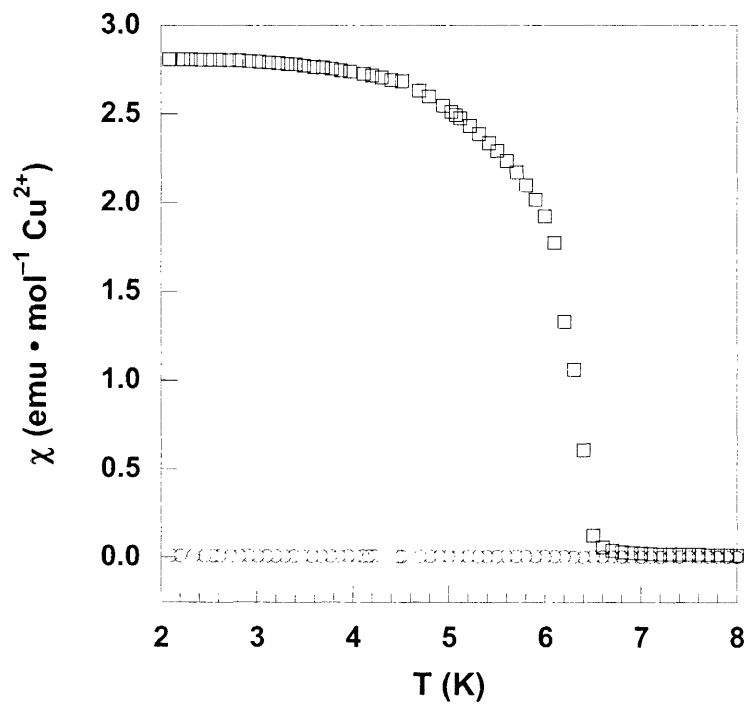


Figure 4.13. Comparison of the ZFC susceptibility measured for clinoatacamite (\square) which orders ferromagnetically at 6.5 K, and zinc paratacamite (\circ) which shows no ordering transition to temperatures down to 2 K.

fields of 5 T indicates that there is no ferromagnetic component of the magnetism of pure phases of Zn paratacamite. Figure 4.13 highlights the profound effect of having interlayer magnetic Cu^{2+} cations by plotting the susceptibilities of clinoatacamite and zinc paratacamite on the same scale.

4.4 Discussion

Starting with the molybdate chemistry introduced in this Chapter, we demonstrate that Cu^{2+} triangles can be prepared in extended solids (1-D), and not just in isolated molecules (0-D). Lindgrenite and its layer expanded congeners provide an entry point into exploratory chemistry with studies of spin frustrated magnetism on a Cu^{2+} lattice. Of note, we see evidence for ferromagnetism in lindgrenite, but not in the 4,4'-bipy expanded version, which hints that ferromagnetism is due to interchain coupling through the MoO_4^{2-} anion, which is destroyed with the large interlayer separation of over 13 Å in the hybrid material. In both cases, nearest-neighbor antiferromagnetism is observed, although the coupling is weak compared to the magnetism observed in the fully 2-D frustrated materials, clinoatacamite and Zn paratacamite.

The isolated 2-D layers of Zn paratacamite show strong nearest-neighbor antiferromagnetic exchange within the kagomé planes, which arises from the strong σ -symmetry superexchange pathway involving $\text{Cu}(d_{x^2-y^2})\text{—O}(sp^3)\text{—Cu}(d_{x^2-y^2})$. The bridging angle, 119.2°, falls within the expected range for antiferromagnetic coupling, as predicted by the Goodenough-Kanamori rules.⁴¹ The magnetic consequence of additional Cu^{2+} ions between the layers in clinoatacamite may be understood by comparison to zinc paratacamite, which provides a reference with only diamagnetic Zn^{2+} ions between the layers. We start by using the mean-field theory analysis of the Curie-Weiss law introduced in § 1.2, noting that since we can measure the susceptibility at temperatures on the order of Θ , and thus do not require the correction factors as we did for iron jarosites. The mean-field isotropic J values are found to be -93 cm^{-1} and -218 cm^{-1} for clinoatacamite and zinc paratacamite respectively. In using equation 1.3, we note that the number of nearest-neighbor magnetic ions, z , is six for clinoatacamite, and four for zinc

paratacamite. From the perspective of the Cu^{2+} ions in the kagomé plane of clinoatacamite, labeled Cu(1) and Cu(2) in Figure 4.5, there are four in-plane nearest neighbors, one interlayer Cu^{2+} above, and one interlayer Cu^{2+} below the plane. Similarly, each interlayer Cu(3) has six nearest-neighbors—three from the triangle above it, and three from the triangle below. In zinc paratacamite, there are no interlayer magnetic ions to consider. If we assume that the contributions from interlayer versus intralayer coupling are the same, we find that all of the interactions are described by looking at one Cu^{2+} ion in the kagomé plane. Since there are four in-plane nearest-neighbors and two out-of-plane nearest neighbors, the interlayer exchange constant (J_{inter}) and the intralayer exchange constant (J_{intra}) are given by,

$$J = \frac{2}{3} J_{\text{intra}} + \frac{1}{3} J_{\text{inter}} \quad (4.11)$$

The structural similarity of clinoatacamite and zinc paratacamite should result in the same intralayer coupling for the two compounds. That is, we assume that J_{intra} , -218 cm^{-1} in clinoatacamite. Thus, from equation 4.11, we estimate J_{inter} to be $+157 \text{ cm}^{-1}$. This strong ferromagnetic coupling between kagomé layers is what we would expect for a Cu—O—Cu angle of $\approx 95^\circ$ in a Goodenough-Kanamori treatment. These coupling constants are also consistent with observed magnetostructural relationships originally studied in μ -hydroxy copper (II) dimers.⁴² Taken together, these results account for the observation of ferromagnetic ordering below $T_c = 6.5 \text{ K}$ in clinoatacamite. Heat capacity studies to determine the spin entropy of ordering due to the interlayer Cu^{2+} cation are currently underway.

With the interlayer Cu^{2+} ion responsible for the 3-D transition in clinoatacamite, the absence of LRO in pure zinc paratacamite is satisfying since there is no paramagnetic cation in the interlayer spacing to make a ferromagnetic exchange pathway. Moreover, second order effects, such as the DM interaction also do not prevail, to $T > 2 \text{ K}$. In conjunction with the observation that Zn paratacamite represents the most geometrically frustrated system to date, with an empirical frustration parameter, $f > 157$ (see equation 1.4), Zn paratacamite appears to be an ideal venue for observing the RVB state in a spin frustrated system. Current efforts consist of inelastic neutron scattering studies on deuterated powdered samples to determine the low

temperature magnetic structure. Although the absolute spin configuration requires single crystals, powders will show the singlet-to-triplet spin-gap (see § 1.4) that is a hallmark of a possible RVB state if present.

4.5 Conclusions

Copper materials containing the model kagomé lattice have been prepared and fully characterized structurally and magnetically. Most important to this Chapter, we have prepared pure Zn paratacamite, the first $S = \frac{1}{2}$ 2-D kagomé system, and provide initial structural and magnetic characterization of such a material. We find that pure Zn paratacamite is the most frustrated kagomé system prepared to date and at the same time find no evidence for structural distortion at low temperature and no transition to LRO is observed to temperatures down to 2 K, despite strong nearest-neighbor antiferromagnetic coupling. The confluence of these observations suggest that Zn paratacamite poised to reveal the ground state physics of a quantum spin liquid in a Heisenberg antiferromagnet. But before this occurs, single crystals will have to be grown. Studies along these lines are currently under investigation.

4.6 References

1. Shender, E. F.; Holdsworth, P. C. W., Order by Disorder and Topology in Frustrated Magnetic Systems. In *Fluctuations and Order*, Millionas, M., Ed. Springer-Verlag: Berlin, 1995; p 259.
2. Sachdev, S. *Phys. Rev. B* **1992**, *45*, 12377-12396.
3. Moessner, R.; Sondhi, S. L. *Phys. Rev. B* **2001**, *63*, 224401/1-19.
4. Lin, Y.-L.; Nori, F. *Phys. Rev. B* **2002**, *65*, 214504/1-21.
5. Wen, X.-G. *Phys. Rev. B* **2002**, *65*, 165113/1-37.
6. Goodenough, J. B. *J. Phys. Chem. Solids* **1958**, *6*, 287-297.
7. Kanamori, J. *J. Phys. Chem. Solids* **1959**, *10*, 87-98.
8. Beckett, R.; Colton, R.; Hoskins, B. F.; Martin, R. L.; Vince, D. G. *Aust. J. Chem.* **1969**, *22*, 2527-2533.

Chapter 4

9. Butcher, R. J.; O'Connor, C. J.; Sinn, E. *Inorg. Chem.* **1981**, *20*, 537-545.
10. Kwiatkowski, M.; Kwiatkowski, E.; Olechnowicz, A.; Ho, D. M.; Deutsch, E. *Inorg. Chim. Acta* **1988**, *150*, 65-73.
11. Chaudhuri, P.; Karpenstein, I.; Winter, M.; Butzlaff, C.; Bill, E.; Trautwein, A. X.; Floerke, U.; Haupt, H. J. *J. Chem. Soc., Chem. Commun.* **1992**, 321-322.
12. Colacio, E.; Dominguez-Vera, J. M.; Escuer, A.; Klinga, M.; Kivekas, R.; Romerosa, A. *J. Chem. Soc., Dalton Trans.* **1995**, 343-348.
13. Padilla, J.; Gatteschi, D.; Chaudhuri, P. *Inorg. Chim. Acta* **1997**, *260*, 217-220.
14. Ferrer, S.; Haasnoot, J. G.; Reedijk, J.; Mueller, E.; Cingi, M. B.; Lanfranchi, M.; Lanfredi, A. M. M.; Ribas, J. *Inorg. Chem.* **2000**, *39*, 1859-1867.
15. Clerac, R.; Cotton, F. A.; Dunbar, K. R.; Hillard, E. A.; Petrukhina, M. A.; Smucker, B. W. *Comptes Rendus Ser. IIc* **2001**, *4*, 315-319.
16. Ferrer, S.; Lloret, F.; Bertomeu, I.; Alzuet, G.; Borrás, J.; Garcia-Granda, S.; Liu-Gonzalez, M.; Haasnoot, J. G. *Inorg. Chem.* **2002**, *41*, 5821-5830.
17. Cage, B.; Cotton, F. A.; Dalal, N. S.; Hillard, E. A.; Rakvin, B.; Ramsey, C. M. *J. Am. Chem. Soc.* **2003**, *125*, 5270-5271.
18. Liu, X.; de Miranda Marcelo, P.; McInnes Eric, J. L.; Kilner Colin, A.; Halcrow Malcolm, A. *Dalton Trans* **2004**, 59-64.
19. Yoon, J.; Mirica, L. M.; Stack, T. D. P.; Solomon, E. I. *J. Am. Chem. Soc.* **2004**, *126*, 12586-12595.
20. Palache, C. *Am. Mineral.* **1935**, *20*, 484-491.
21. Calvert, L. D.; Barnes, W. H. *Can. Mineral.* **1957**, *6*, 31-51.
22. Hawthorne, F. C.; Eby, R. K. *Neues Jahrb. Mineral., Monatsh.* **1985**, 234-40.
23. Hagrman, D.; Warren, C. J.; Haushalter, R. C.; Seip, C.; O'Connor, C. J.; Rarig, R. S., Jr.; Johnson, K. M., III; LaDuca, R. L., Jr.; Zubieta, J. *Chem. Mater.* **1998**, *10*, 3294-3297.
24. Hagrman, D.; Haushalter, R. C.; Zubieta, J. *Chem. Mater.* **1998**, *10*, 361-365.
25. Hagrman, P. J.; Zubieta, J. *Inorg. Chem.* **1999**, *38*, 4480-4485.
26. Hagrman, P. J.; Zubieta, J. *Inorg. Chem.* **2000**, *39*, 5218-5224.
27. Hagrman, D. E.; Zubieta, J. *J. Solid State Chem.* **2000**, *152*, 141-151.
28. Koo, B.-K.; Bewley, L.; Golub, V.; Rarig, R. S.; Burkholder, E.; O'Connor, C. J.; Zubieta, J. *Inorg. Chim. Acta* **2003**, *351*, 167-176.

Chapter 4

29. Rarig, R. S., Jr.; Lam, R.; Zavalij, P. Y.; Ngala, J. K.; LaDuca, R. L., Jr.; Greedan, J. E.; Zubieta, J. *Inorg. Chem.* **2002**, *41*, 2124-2133.
30. Mueller, A.; Peters, F.; Pope, M. T.; Gatteschi, D. *Chem. Rev.* **1998**, *98*, 239-271.
31. Lhuillier, C.; Misguich, G. *Lect. Notes Phys.* **2001**, *595*, 161-190.
32. Oswald, H. R.; Guenter, J. R. *J. Appl. Crystallogr.* **1971**, *4*, 530-531.
33. Parise, J. B.; Hyde, B. G. *Acta Crystallogr., Sect. C* **1986**, *C42*, 1277-1280.
34. Jambor, J. L.; Dutrizac, J. E.; Roberts, A. C.; Grice, J. D.; Szymanski, J. T. *Can. Mineral.* **1996**, *34*, 61-72.
35. Grice, J. D.; Szymanski, J. T.; Jambor, J. L. *Can. Mineral.* **1996**, *34*, 73-78.
36. Wills, A. S.; Raymond, S.; Henry, J. Y. *J. Magn. Magn. Mater.* **2004**, *272-276*, 850-851.
37. Kawaji, H.; Atake, T.; Chihara, H.; Mori, W.; Kishita, M. *Thermochim. Acta* **1985**, *88*, 195-198.
38. Braithwaite, R. S. W.; Mereiter, K.; Paar, W. H.; Clark, A. M. *Mineral. Mag.* **2004**, *68*, 527-539.
39. Moini, A.; Peascoe, R.; Rudolf, P. R.; Clearfield, A. *Inorg. Chem.* **1986**, *25*, 3782-3785.
40. Hagrman, P. J.; Hagrman, D.; Zubieta, J. *Angew. Chem., Int. Ed. Engl.* **1999**, *38*, 2639-2684.
41. Kahn, O. *Molecular Magnetism*; VCH: New York, 1993; pp 190-191.
42. Crawford, V. H.; Richardson, H. W.; Wasson, J. R.; Hodgson, D. J.; Hatfield, W. E. *Inorg. Chem.* **1976**, *15*, 2107-10.

Chapter 5. Searching for the Resonating Valence Bond (RVB) State

5.1 Introduction

The research presented in Chapters 2 – 4 was directed at preparing pure materials with which we could characterize the magnetic ground states of geometrically frustrated spin systems. Preparing the $S = 1/2$ zinc paratacamite is a triumph in that the resonating valence bond (RVB) picture is predicated on strong quantum fluctuations favoring singlet bond formation as opposed to a classical Néel ordered state.¹ The pure zinc paratacamite material may reveal evidence for the quantum spin liquid state since magnetic ordering is suppressed to at least 2 K. Neutron scattering is now the technique that will answer this question. Nevertheless, we note that our work as chemists is far from complete because most real materials that have one unpaired spin at each lattice point do order antiferromagnetically, rendering them electrically insulating. These materials, referred to as Mott insulators, undergo a superconducting transition upon doping, with La_2CuO_4 again being a prime example introduced in § 1.4. In the superconducting phase, there must be no magnetic order, as it destroys the purported spin liquid phase.² Therefore, we note that although zinc paratacamite shows no ordering, it remains an electrical insulator to temperatures down to 2 K.

In cuprates, the parent compound La_2CuO_4 crystallizes with the tetragonal K_2NiF_4 structure,³ shown in Figure 5.1, but undergoes a crystallographic phase change to a lower symmetry orthorhombic structure at 530 K which serves to elongate the CuO_6 octahedron and to tilt the CuO_6 octahedra 2.8° . Oxygen nonstoichiometry affects this phase transition,⁴ although both crystallographic phases show superconductivity.^{5,6} In the RVB liquid model, superconductivity in the cuprate oxide square lattice still involves a spin frustration problem for doped charge carriers within singlet pairs although there is no LRO, as shown in Figure 5.2. Doping in the solid-state superconducting materials is generally achieved either at the synthesis level by substituting ions of differing charge onto regular lattice points and/ or by annealing under various partial pressures of oxygen.⁷⁻¹⁹ Nevertheless, there are reports of simple “one-step” procedures after synthesis such as electrochemical treatment,²⁰⁻²⁶ and there are a few examples of

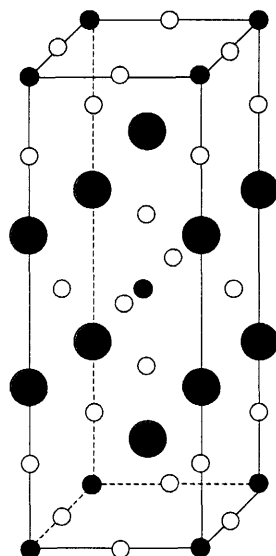


Figure 5.1. Tetragonal unit cell of La_2CuO_4 . Green circles are La, black circles are Cu, and white circles are O.

chemical oxidation with NaClO ²⁷⁻³⁰ and KMnO_4 .³¹⁻³⁴ However, these chemical reactions can take days to run, depending on the porosity of the material, thus, it generally remains routine to empirically prepare potential superconducting materials by introducing various cations during the synthesis.

In turning attention to our copper hydroxide chlorides, one key consideration is the relative instability of Cu^{3+} in a hydroxy environment. Cyclic voltammetry studies on periodate and pertellurate complexes of copper in basic media show that the $\text{Cu}^{2+}/\text{Cu}^{3+}$ potential is ≈ 610 mV (vs NHE) uphill.³⁵⁻³⁷ However, at high basicity, $\text{Cu}(\text{OH})_2$ precipitates out of solution.

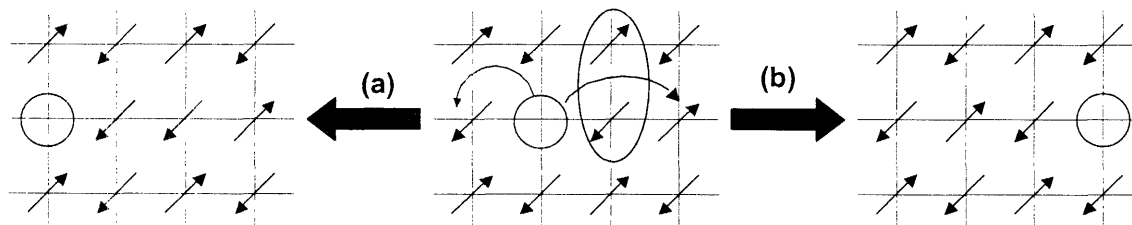


Figure 5.2. Spin frustration in transport of a hole in a square lattice. Nearest-neighbor exchange results in frustration in mechanism (a), but transport through a singlet pair of spins in the RVB liquid state shown in (b) does not create frustration.

Additionally, adding hydroxide or amine bases to the materials prepared in Chapter 4 immediately results in the precipitation of CuO. Therefore, we must find oxidants with sufficient potential that do not require added base.

The work presented in this Chapter describes current efforts to prepare mixed valent materials containing a kagomé lattice in an effort to explore their transport properties. While little success has been made to date, we describe experiments that provide insight into the reactivity of zinc paratacamite such that future work may produce an $S = \frac{1}{2}$ kagomé lattice with charge carriers doped therein.

5.2 Experimental

5.2.1 General Procedures

All chemicals of reagent or analytical grade were obtained from Aldrich or Strem, and they were used without purification. THF and acetonitrile solvents were first dried on a Braun MB-SPS solvent purification system. Hydrothermal reactions were carried out in Teflon-lined pressure vessels, which were purchased from Parr Instruments. A Fisher Isotemp programmable oven with forced-air circulation was used to obtain the desired temperature profiles for hydrothermal reactions. Reactions run under refluxing conditions were carried out in a 25 mL round-bottom flask fitted with a water-cooled reflux condenser. Additionally, some reactions were run under an argon atmosphere. Chemical analyses were conducted by the H. Kolbe Mikroanalytisches Laboratorium.

5.2.2 Synthesis of $\text{KFe}_{3-x}\text{V}_x(\text{OH})_6(\text{SO}_4)_2$ ($x \approx 0.8$)

A 23 mL Teflon liner was charged with 0.171 g of Fe wire (3.06 mmol) and 0.230 g of VO_2SO_4 (0.98 mmol). To this liner, 1.044 g of K_2SO_4 (5.98 mmol) was dissolved in 10 mL of deionized water, and 0.33 mL of H_2SO_4 (6.0 mmol) was added via Mohr pipet. The Teflon liner was capped under an oxygen atmosphere using an Aldrich Atmosbag, placed into a steel hydrothermal bomb. The tightened bomb was heated to at a rate of 5 °C/min to 210 °C, which

was maintained for 72 h. The oven was then cooled to room temperature at a rate of 0.1 °C/min. A red-brown crystalline powder was isolated from the walls and the bottom of the Teflon liner, and the product was washed with deionized water and dried in air. The powder was found to have a structure consistent with jarosite by powder X-ray diffraction. Yield: 0.382 g. Anal. Calcd. for $\text{KFe}_{2.2}\text{V}_{0.8}(\text{OH})_6(\text{SO}_4)_2$: H, 1.22; K, 7.89; Fe, 24.73; V, 8.20; S, 12.91. Found: H, 1.16; K, 7.85; Fe, 24.66; V, 7.98; S, 12.22.

5.2.3 Synthesis of barbosalite, $\text{Fe}^{2+}\text{Fe}_2^{3+}(\text{PO}_4)_2(\text{OH})_2$

0.157 g (2.81 mmol) iron wire was weighed out in an argon drybox and placed into a 23 mL Teflon cup. 0.55 mL (8.0 mmol) phosphoric acid and 10 mL distilled water were added to the Teflon liner, which was then capped and placed into a steel Parr hydrothermal reaction vessel. The sealed vessel was heated in a Fisher Isotemp™ programmable oven at 5 °C/min to a final temperature of 210 °C, which was maintained for 72 h. The oven was then cooled to 40 °C at a rate of 0.1 °C/min. A black crystalline solid was filtered, washed with distilled water, and dried in air. Yield: 0.271 g (73.8 %, based on starting iron metal). Powder x-ray diffraction identified the material as barbosalite, $\text{Fe}^{2+}\text{Fe}_2^{3+}(\text{PO}_4)_2(\text{OH})_2$. Anal. Calcd. for $\text{Fe}_3\text{P}_2\text{O}_{10}\text{H}_2$: Fe, 42.80; P, 15.82; H, 0.51. Found: Fe, 42.83; P, 15.87; H, 0.48.

5.2.4 Physical methods

IR spectra were recorded in KBr pellets on a Nicolet Magna-IR 860 spectrometer equipped with a KBr beam splitter and a DTGS detector. For each spectrum, 32 scans were acquired with 4 cm^{-1} resolution over a wavelength range of 4000 – 400 cm^{-1} .

Magnetic susceptibilities were determined on powdered samples contained in gelatin capsules using a Quantum Design MPMSR2 Susceptometer over a 5 – 300 K temperature range at field strengths varying from 0 – 50 kOe. For each dc susceptibility data point, the average of three measurements of 32 scans over a 4 cm scan length was acquired. Data were corrected for core diamagnetism using Pascal's constants. Ac susceptibilities were recorded for each

compound under an ac field, $H_{ac} = H_0 \sin(2\pi ft)$ for $H_0 = 3$ Oe and $f = 2, 20,$ and 200 Hz.

Zero-field cooled (ZFC) susceptibilities were measured by first cooling the samples from 300 K to 5 K under zero field. Dc susceptibility was then measured in a field $H_m = 100$ Oe as a function of temperature as the sample was warmed from 5 – 300 K. Field-cooled (FC) susceptibilities were measured in a similar fashion, except the cooling and measuring fields were both 100 Oe. Curie-Weiss analysis was done on the inverse susceptibility of ZFC samples under $H_m = 2000$ Oe over the temperature range 150 – 300 K.

The Mössbauer spectrum of barbosalite was recorded on a MS1 spectrometer (WEB Research Co. Model W200 instrument) with a ^{57}Co source in a Rh matrix kept at room temperature. Data were acquired at room temperature over 3 d. The spectrum was fit to Lorentzian line shapes by using the WMOSS software package, and isomer shifts were referenced to a room temperature iron foil calibration. The solid samples was prepared by suspending powdered material (≈ 20 mg) in Apiezon N grease and placing the mixture into a nylon sample holder.

^{60}Co γ -irradiation (incident photon energy = 1.2 MeV) was performed at the MIT research reactor. Samples were irradiated at room temperature as powders suspended in water in glass scintillation vials sealed under ambient room atmosphere at an average radiation dose rate of 0.1 Mrad/h for 1 – 96 h.

5.3 Results and Discussion

5.3.1 Mixed-metal Jarosite, $\text{KFe}_{3-x}\text{V}_x(\text{OH})_6(\text{SO}_4)_2$

Although still electrically insulating, one means of introducing different exchange interactions through the diamagnetic bridging OH group into the jarosite structure is to use metals with unlike d -electron counts within the kagomé framework. From the redox synthesis described in Chapter 2, we know that both Fe^{3+} (d^5) and V^{3+} (d^2) can be incorporated into the jarosite structure, and both compounds can be made under strongly oxidizing acidic conditions.

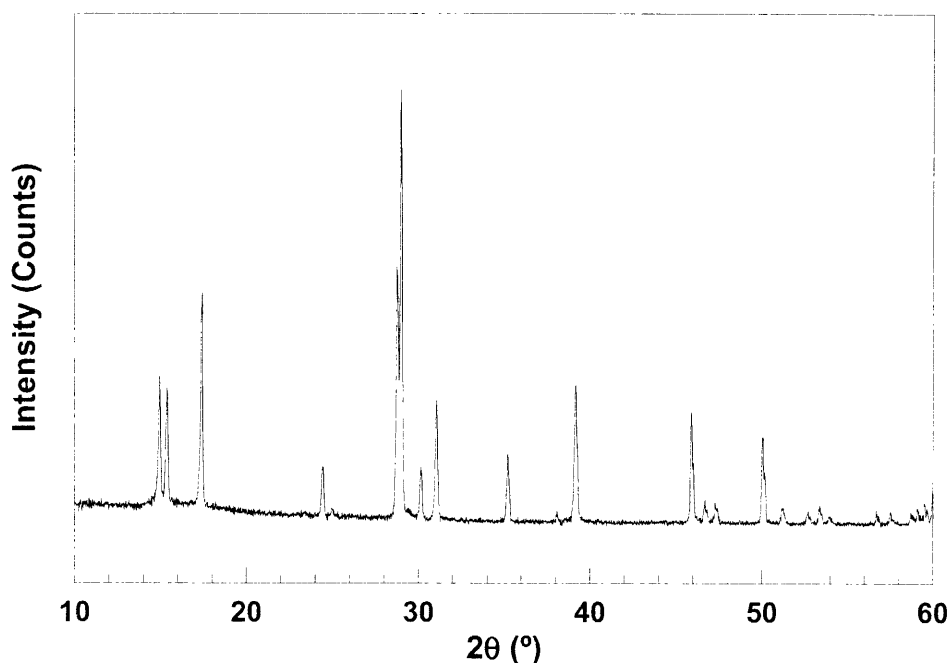


Figure 5.3. X-ray powder pattern of $\text{KFe}_{3-x}\text{V}_x(\text{OH})_6(\text{SO}_4)_2$.

Therefore, a reaction starting with both Fe and V could conceivably produce a mixed-metal compound, provided the two reactions are kinetically competitive. We find that indeed a mixed-metal system can be prepared, relying on the synthetic chemistry outlined in § 2.3.1. Figure 5.3 shows the X-ray powder diffraction pattern for the mixed-metal material, and the peaks match those of jarosite. A table of Miller indices is given in Appendix A.

The magnetism of this species provides evidence that the compound is actually mixed-metal and not a physical mixture of the two independent species. As Figure 5.4 shows, the d.c. susceptibility shows a sharp rise at 22 K, and a subtle drop at 8 K. Most important, there are no discernable features at 65 K, expected for pure $\text{KFe}_3(\text{OH})_6(\text{SO}_4)_2$, or at 35 K, expected for pure $\text{KV}_3(\text{OH})_6(\text{SO}_4)_2$. The a.c. susceptibility (Figure B.21) supports phase transitions at 22 K and at 8 K with no spin glass behavior, as there is no frequency-dependence on the observed magnetic ordering temperature. Curie-Weiss analysis of the inverse susceptibility reveals that the average nearest-neighbor exchange interaction is antiferromagnetic with $\Theta = -628$ K, although the Weiss constant is much smaller than that of the pure Fe^{3+} jarosites. Thus, the material prepared has

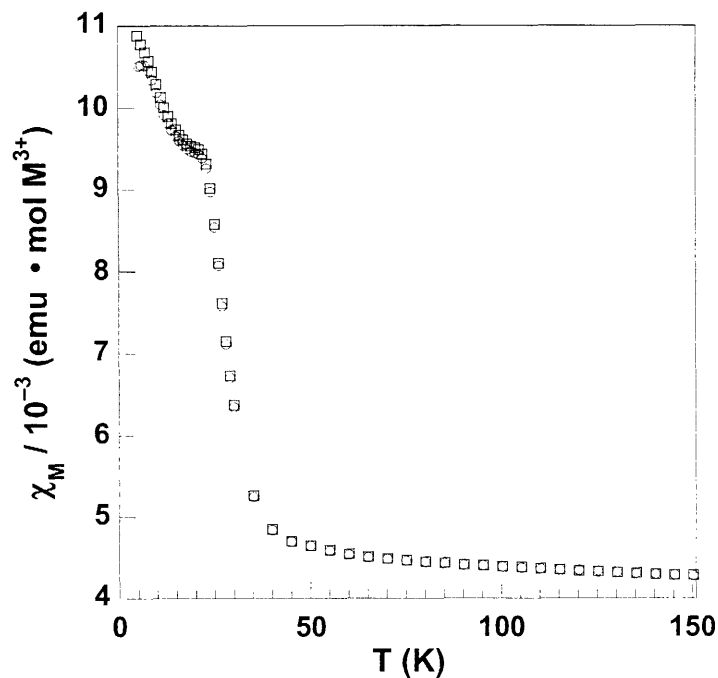


Figure 5.4. ZFC (\circ) and FC (\square) susceptibility of mixed-metal $\text{KFe}_{3-x}\text{V}_x(\text{OH})_6(\text{SO}_4)_2$, showing no features of pure $\text{KFe}_3(\text{OH})_6(\text{SO}_4)_2$ or $\text{KV}_3(\text{OH})_6(\text{SO}_4)_2$.

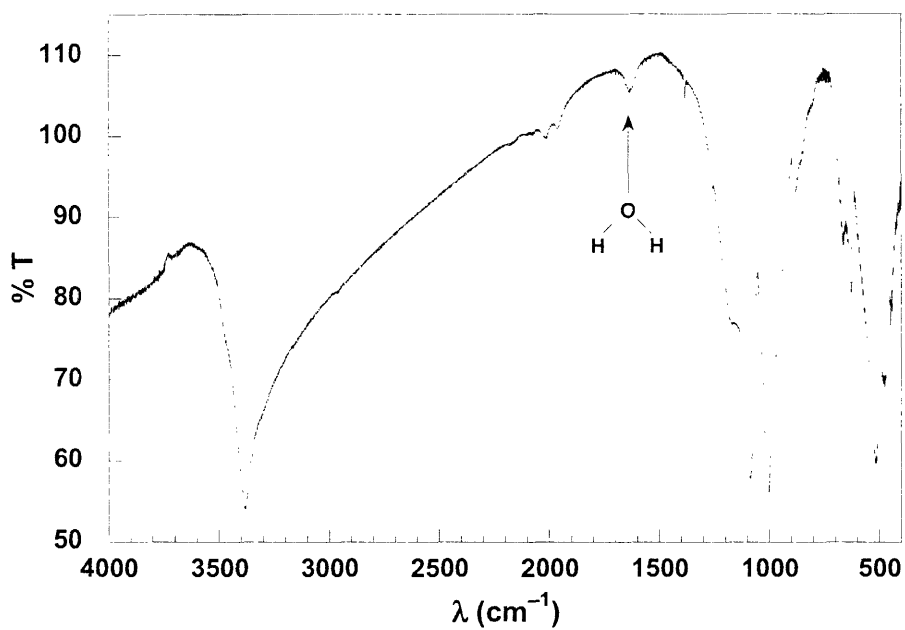


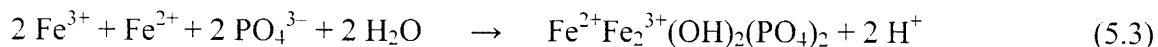
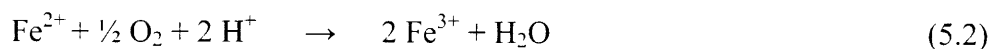
Figure 5.5. IR spectrum of $\text{KFe}_{3-x}\text{V}_x(\text{OH})_6(\text{SO}_4)_2$, emphasizing the presence of an H—O—H bending mode at 1630 cm^{-1} .

properties distinctly different from either pure parent compound.

Despite our efforts to use redox chemistry to prepare a mixed-metal material with no other site defects, the IR spectrum presented in Figure 5.5 shows that the material prepared has H—O—H moieties present, noted by the bending mode at 1630 cm^{-1} . Therefore, this material is not ideal in studying the magnetic exchange interactions between metals with different *d*-electron counts since there may be two different superexchange pathways (aquo and hydroxy). However, preparing this compound does reveal that the kinetics of crystal growth must be similar for Fe^{3+} and V^{3+} jarosites since we can isolate a mixed-metal material.

5.3.2 Mixed-valency in Barbosalite, $\text{Fe}^{2+}\text{Fe}_2^{3+}(\text{OH})_2(\text{PO}_4)_2$

The attempts to prepare phosphate-capped jarosite analogs described in § 2.3.1 unsuspectingly led us to the mineral barbosalite, a mixed-valent $\text{Fe}^{2+}/\text{Fe}^{3+}$ linear chain material. Barbosalite is a known mineral whose magnetic properties have been examined on a cursory level, although the preparation of pure samples has remained elusive. Here, as in our work in making pure jarosites in presented in Chapter 2, we take advantage of redox chemistry to provide the kinetic steps necessary to prepare pure materials.



The dissolution of iron wire by protons in step 1 of the reaction scheme is slow because the proton concentration is limited by the $\text{p}K_a$ of phosphoric acid ($\text{p}K_1$ is 2.12). Then, oxidation of Fe^{2+} must also be slow since Fe^{2+} is found in the resulting barbosalite species. We find that barbosalite is the only product of the reaction whether run under an oxygen atmosphere or ambient room atmosphere, with no significant difference in crystal size, shape, or morphology.

While the reaction gives highly crystalline material, attempts to mount a single crystal were unsuccessful. Severe twinning prevents us from obtaining a reasonable unit cell. However, the X-ray diffraction pattern of barbosalite presented in Figure 5.6 is consistent with the known

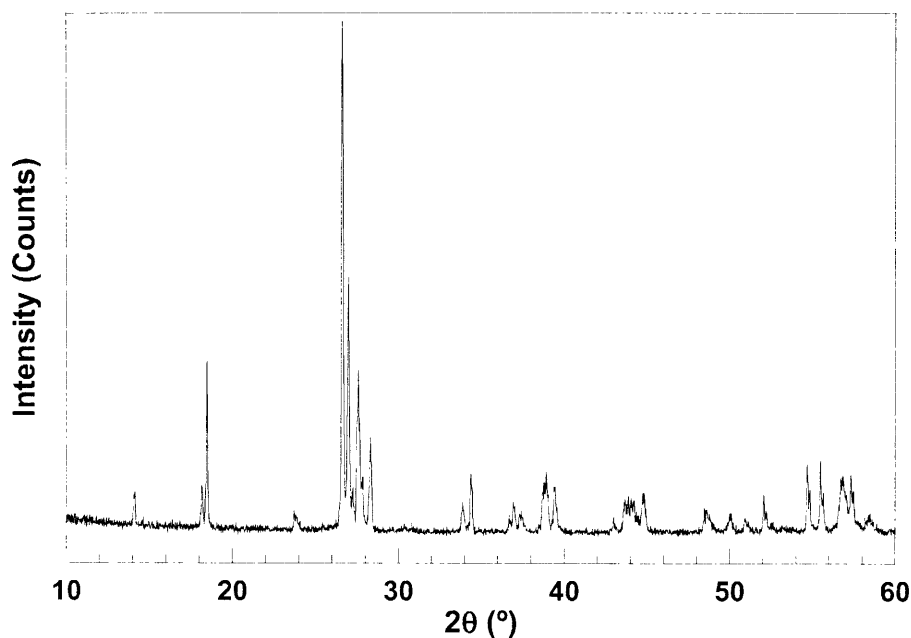


Figure 5.6. pXRD pattern of $\text{Fe}^{2+}\text{Fe}_2^{3+}(\text{OH})_2(\text{PO}_4)_2$.

mineralogical species.³⁸ A full table of Miller indices is given in Appendix A.

The zero-field-cooled (ZFC) and field-cooled (FC) d.c. susceptibility displayed in Figure 5.7 shows a sharp rise in the magnetic susceptibility for $T < 164$ K. The magnetic behavior below this ordering temperature appears to be ferromagnetic in origin. Further evidence for ferromagnetism is given by the divergence in ZFC and FC susceptibility, with $\chi(0)$ following an $H_{\text{cooling}}^{0.04}$ -dependence upon fitting the ordered-regime to a power function. Additionally, the compound displays low-temperature hysteresis shown in Figure 5.8(a), with a large coercive field of $H_{\text{coercive}} \approx 0.6$ T and remanent magnetization (Figure 5.8(b)). Despite strong ferromagnetic ordering, a Curie-Weiss fit of the inverse susceptibility gives evidence of nearest-neighbor antiferromagnetism, with a Weiss constant of $\Theta = -400$ K.

The Mössbauer spectrum of barbosalite supports a mixed valent $\text{Fe}^{2+}/\text{Fe}^{3+}$ compound. As shown in Figure 5.9, there are two quadrupole doublets, one with an isomer shift and quadrupole splitting of $\delta = 0.43$ $\text{mm}\cdot\text{s}^{-1}$ and $\Delta E_Q = 0.40$ $\text{mm}\cdot\text{s}^{-1}$ respectively, which are indicative of high spin Fe^{3+} . The other doublet has $\delta = 1.09$ $\text{mm}\cdot\text{s}^{-1}$ and $\Delta E_Q = 3.52$ $\text{mm}\cdot\text{s}^{-1}$, consistent with high spin Fe^{2+} . These values are spot-on with the room temperature Mössbauer parameters reported

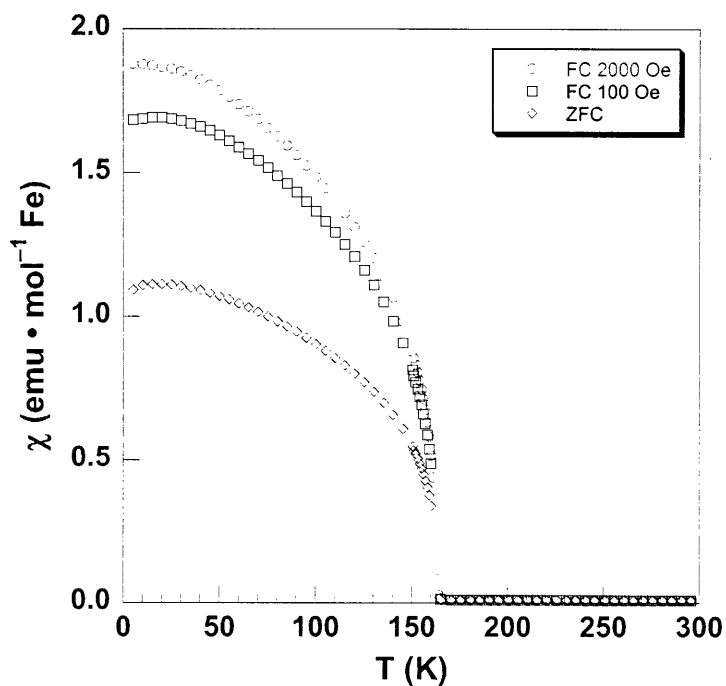


Figure 5.7. ZFC (\diamond) and FC (100 Oe, \square ; 2000 Oe, \circ) d.c. susceptibility of $\text{Fe}^{2+}\text{Fe}_2^{3+}(\text{OH})_2(\text{PO}_4)_2$. The susceptibility at 0 T follows an $H_{\text{cooling}}^{0.04}$ -power dependence.

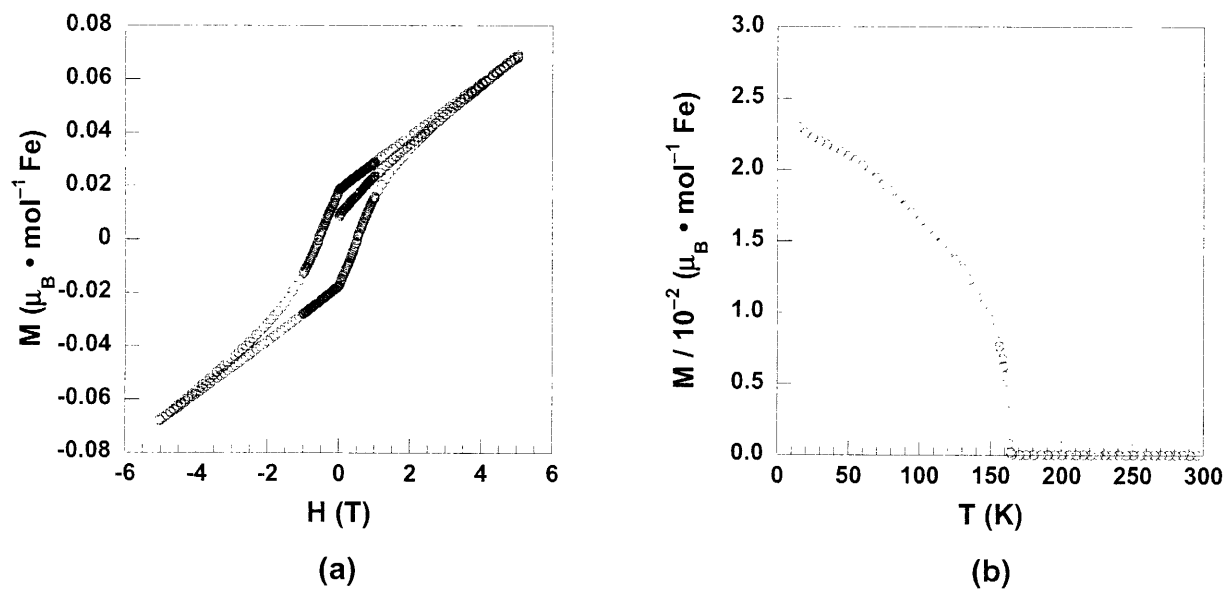


Figure 5.8. (a) Hysteresis loop for $\text{Fe}^{2+}\text{Fe}_2^{3+}(\text{OH})_2(\text{PO}_4)_2$, with $H_{\text{coercive}} \approx 0.6$ T. (b) Remanent magnetization at $H_{\text{cooling}} = 2000$ Oe, measured in zero field.

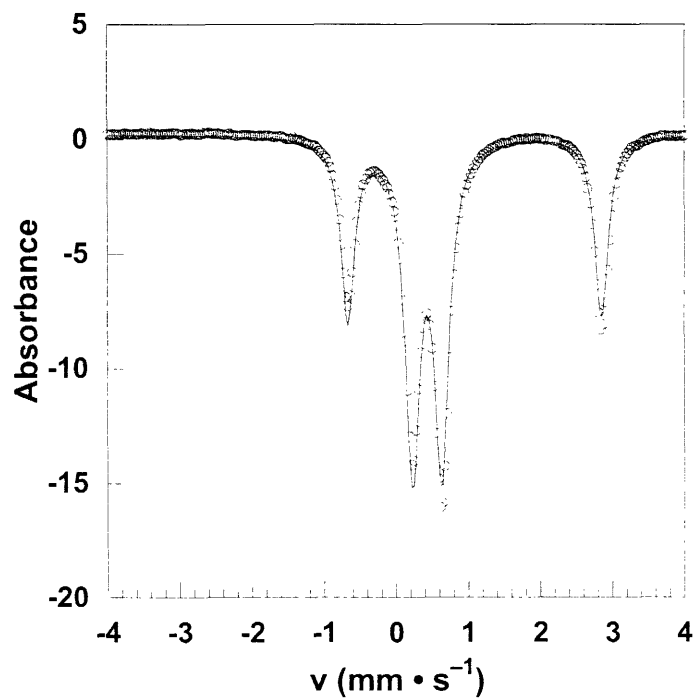


Figure 5.9. Mössbauer spectrum of $\text{Fe}^{2+}\text{Fe}_2^{3+}(\text{OH})_2(\text{PO}_4)_2$, providing evidence for mixed-valency.

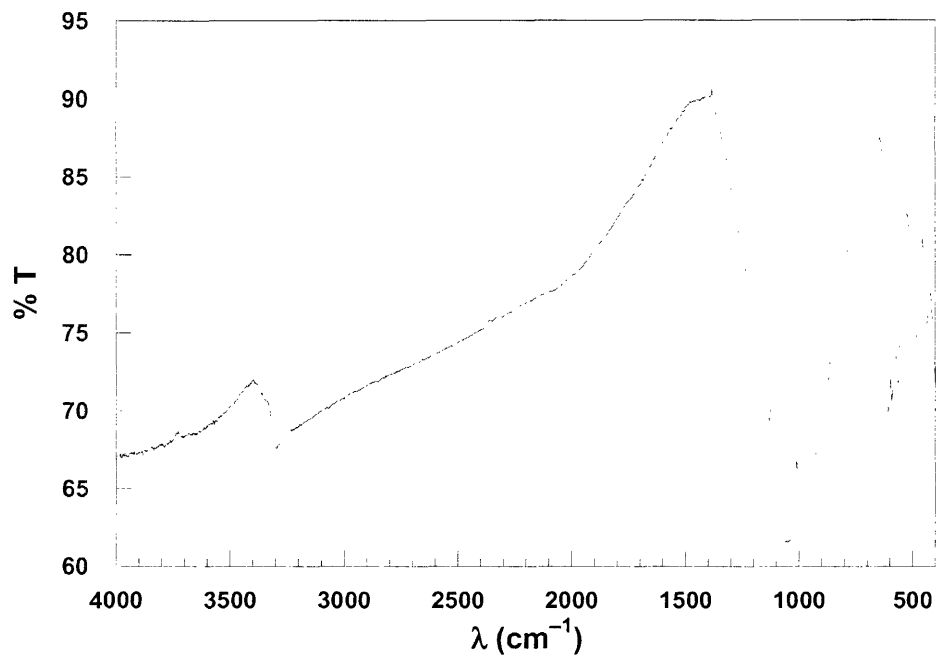


Figure 5.10. IR spectrum of $\text{Fe}^{2+}\text{Fe}_2^{3+}(\text{OH})_6(\text{PO}_4)_2$ showing no H—O—H bending mode.

for mineral samples in the literature.³⁹ Moreover, the IR spectrum shows only OH⁻ structural units to be present, with no evidence of an H—O—H bending mode present. This is again consistent with the formula obtained from elemental analysis and the powder X-ray data, and the mixed valency supported by the Mössbauer spectrum. That is, mixed valency in the mineral barbosolite arises due to crystallographically distinct Fe²⁺ and Fe³⁺ sites within the compound, and not from an incomplete reaction with substitution of aquo for hydroxy bridges in the compound.

The two different magnetic interactions can be understood by examining the crystal structure of barbosolite.⁴⁰ Trimeric Fe₂³⁺Fe²⁺O₈(OH)₄ groups run along the [1 1 0] direction, and the Fe²⁺—O—Fe³⁺ angles which range from 83 to 86°, which should give ferromagnetic exchange between the *d*⁶ and *d*⁵ centers. Additionally, there are Fe³⁺O₄(OH)₂ chains which are oriented [101] that give rise to antiferromagnetic exchange.

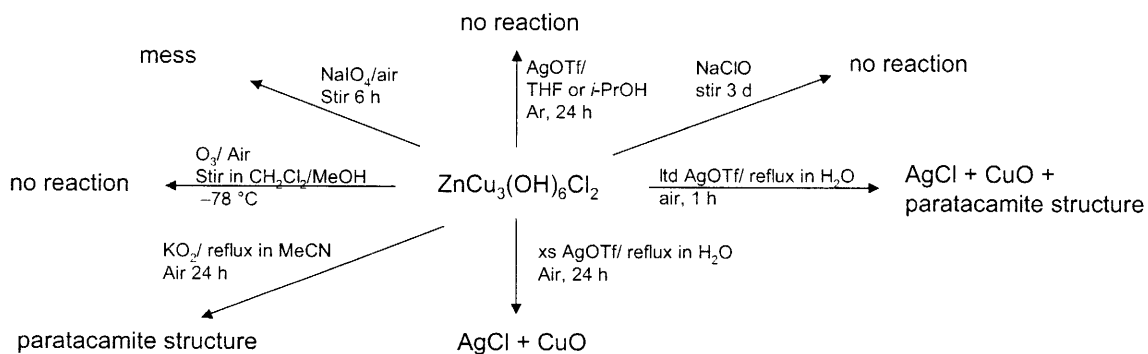
Despite the abundance of basic iron phosphate minerals in nature, chemical and physical properties for many materials remain uncharted due to the difficulty of obtaining pure materials. These difficulties arise from the presence of various oxidation states of iron due to chemical impurity, variable water content within the crystal lattice, and transition-metal ion impurities such as Mn²⁺ or Mn³⁺. Often, fibrous microcrystals result in which several closely related phases of similar chemical composition form together. The phases have nearly identical physical properties such as hardness, density, and color, making it difficult to characterize mined samples or synthetic powders.³⁸

Nonetheless, mixed-valent iron phosphates are gaining attention because of their catalytic properties. Hydroxyphosphates, such as barbosolite, lipscombite, and Fe₄(OH)₃(PO₄)₃ catalyze the esterification of methacrylic acid to methylmethacrylate.⁴¹ These mixed-valent materials function as redox centers by forming solid solutions of Fe_{4-x}Fe_{3x}(PO₄)₃(OH)_{3-3x}O_{3x} (0 ≤ *x* ≤ 1). Thus, recent studies focus on compositional change of the mineral species during catalysis and on solid-state phase relationships.^{42,43}

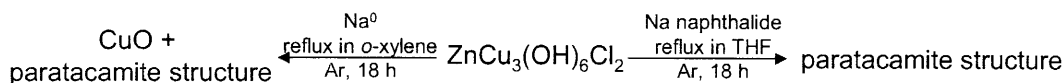
5.3.3 Reaction Chemistry of $\text{ZnCu}_3(\text{OH})_6\text{Cl}_2$

Taking clues from the chemistry of oxo-bridged cuprates introduced in § 5.1, chemical oxidations of zinc paratacamite were attempted by using a variety of reagents, as shown in Scheme 5.1. We note that oxidation does not occur—neither in reactions done in air nor under an inert argon atmosphere. In addition, for those reactions done in water, the products identified by powder X-ray diffraction reveal that only acid-base chemistry occurs, leading to decomposition of the starting zinc paratacamite to make tenorite (cupric oxide). In order to balance the charge of a potential zinc paratacamite oxidation, either interlayer zinc cations must be lost or monoanionic bridging hydroxy groups must be deprotonated. Both of these reactions seem problematic at first glance because Zn^{2+} is necessary to electrostatically hold the kagomé layers together, and addition of hydroxide or amine bases to zinc paratacamite in water immediately results in the formation of black copper oxide solid or deep blue soluble aminocopper species. Thus, decomposition by acid-base chemistry does not seem surprising.

For reactions carried out in non-aqueous solution, no new products are observed by either pXRD or SQUID, although the starting zinc paratacamite powder turns from blue-green to gray-black in a reaction with KO_2 in refluxing acetonitrile. This could be due to surface decomposition, noting that $< 5\%$ impurity can go undetected by pXRD. Additionally, CuO orders antiferromagnetically below 230 K, which can be shown unequivocally by neutron



Scheme 5.1.



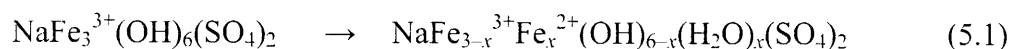
Scheme 5.2

studies. However, the transition in the SQUID is very broad, centered about 550 K,⁴⁴ thus no difference would be observed in the susceptibility of zinc paratacamite.

In addition to oxidations, we tried reducing some of the intralayer Cu^{2+} to Cu^+ , noting that the $\text{Cu}^{2+}/\text{Cu}^+$ standard reduction potential is 0.16 V. The reactions employed used strong reductants both sodium metal and sodium naphthalide as reducing agents, as shown in Scheme 5.2. Again, these reactions show no redox products, rather acid-base chemistry occurs even in non-aqueous solution under harsh reducing conditions.

5.3.4 ^{60}Co γ -irradiation

As a last-ditch effort, γ rays can invoke redox chemistry for Fe^{3+} in aqueous suspensions, and finds ample precedence in the mineralogical literature.⁴⁵⁻⁴⁸ Thus, we irradiated natrojarosite at the MIT reactor for 1 – 96 h with the overall goal of achieving the following reaction



which would proceed by known radiation processes involving water,⁴⁹



After 96 h however, the magnetic susceptibility of $\text{NaFe}_3(\text{OH})_6(\text{SO}_4)_2$ remains unchanged, as shown in Figure 5.11. That is, even under extreme doses of irradiation, we see that photochemical reduction of jarosites does not occur.

Focusing then on zinc paratacamite, we irradiated a sample in the presence of the $\text{S}_2\text{O}_8^{2-}$ anion, which is known to liberate the hot oxidant $\text{SO}_4^{\bullet -}$ upon photolysis according to the reaction⁵⁰⁻⁵⁴

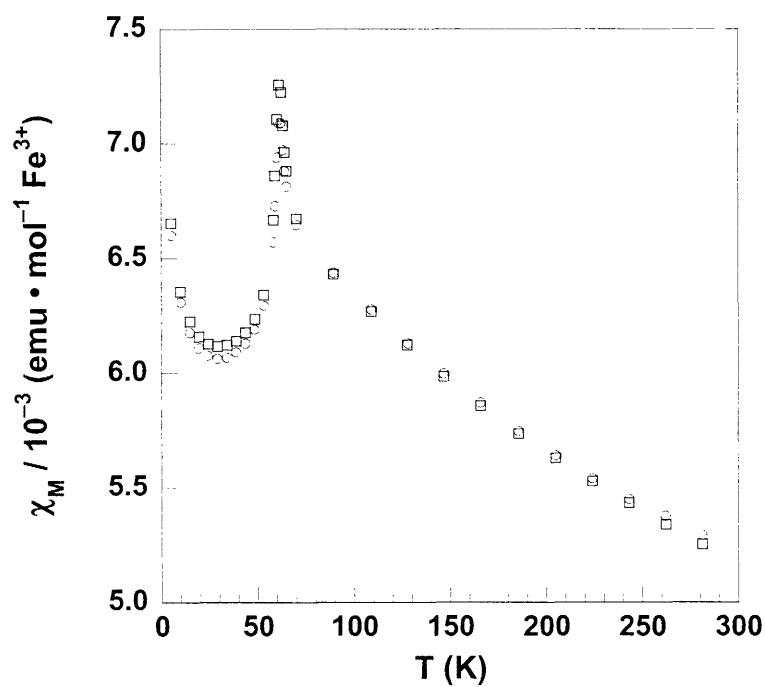


Figure 5.11. ZFC dc susceptibility of NaFe₃(OH)₆(SO₄)₂ recorded before γ -irradiation (\circ) and after 96 h of irradiation (\square).

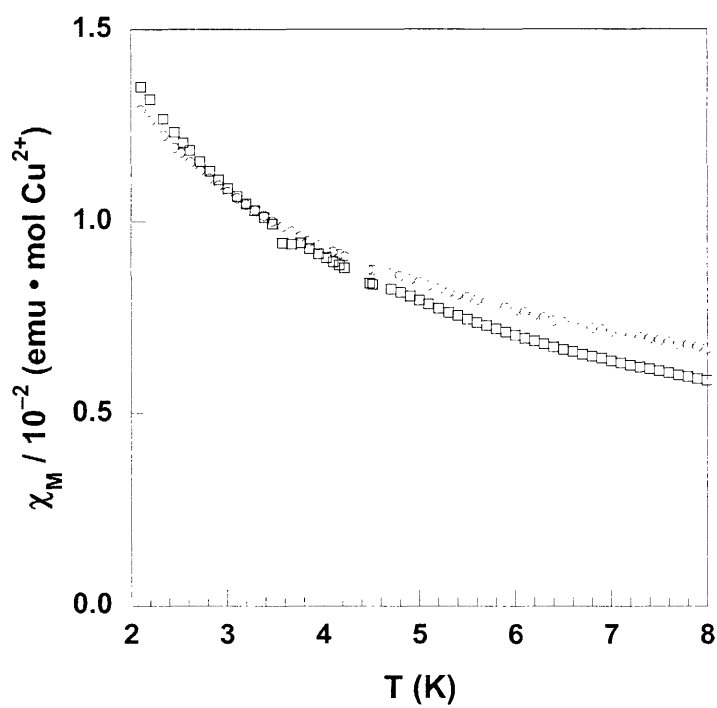
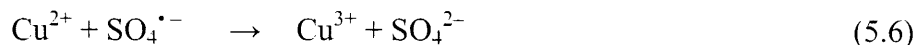


Figure 5.12. Comparison of ZnCu₃(OH)₆Cl₂ before (\circ) and after (\square) γ -irradiation.



$\text{SO}_4^{\bullet -}$ has a standard reduction potential of 2.4 V, and is certainly strong enough to oxidize Cu^{2+} to Cu^{3+} .⁵⁵



However, after 96 h of irradiation, we find that zinc paratacamite is also unchanged, shown in Figure 5.12.

5.4 Conclusions

In our efforts to explore mixed-valency in iron systems, we have prepared and fully characterized the mineralogical species barbosalite, which shows evidence of both ferro- and antiferromagnetic behavior. In copper chemistry, there are still synthetic challenges that lie ahead. Future work is geared towards the redox chemistry of $S = \frac{1}{2}$ zinc paratacamite. Reactions done to date reveal that acid/base processes dominate in aqueous solution to give thermodynamically stable CuO. Therefore, controlling the acid/base chemistry of the bridging hydroxy group in the presence of redox reagents will be key to realizing charge carrier doping. Further, the mineral species prepared in this thesis are not soluble, thus in order to achieve solution-based chemistry, the porosity of the material and the kinetics of surface passivation for a given redox reagent must also be considered.

5.5 References

1. Anderson, P. W.; Lee, P. A.; Randeria, M.; Rice, T. M.; Trivedi, N.; Zhang, F. C. *J. Phys.: Condens. Matter* **2004**, *16*, R755-R769.
2. Lee, P. A.; Nagaosa, N.; Wen, X.-G., In *Los Alamos National Laboratory, Preprint Archive, Condensed Matter* **2004**, arXiv:cond-mat/0410445/1-69.
3. Grande, B.; Mueller-Buschbaum, H.; Schweizer, M. Z. *Allorg. Allg. Chem.* **1977**, *428*, 120-124.
4. Johnston, D. C.; Stokes, J. P.; Goshorn, D. P.; Lewandowski, J. T. *Phys. Rev. B* **1987**, *36*, 4007-4010.
5. Fleming, R. M.; Batlogg, B.; Cava, R. J.; Rietman, E. A. *Phys. Rev. B* **1987**, *35*, 7191-

- 7194.
6. Cheong, S. W.; Thompson, J. D.; Fisk, Z. *Physica C* **1989**, *158*, 109-126.
 7. Maric, M. *Key Engineering Materials* **1991**, *53-55*, 647-52.
 8. Araki, T.; Hirabayashi, I. *Supercond. Sci. Technol.* **2003**, *16*, R71-R94.
 9. McMillan, P. F. *Curr. Opin. Solid State Mater. Sci.* **1999**, *4*, 171-178.
 10. Marezio, M.; Chenavas, J. *J. Solid State Chem.* **1996**, *121*, 24-32.
 11. Hervieu, M. *Curr. Opin. Solid State Mater. Sci.* **1996**, *1*, 29-36.
 12. Hiroi, Z.; Takano, M. *Physica C* **1994**, *235-240*, 29-32.
 13. Zhao, Z.-X.; Zhou, X.-J. *Prog. Nat. Sci.* **1994**, *4*, 385-97.
 14. Wong-Ng, W.; Freiman, S. W. *Appl. Supercond.* **1994**, *2*, 163-180.
 15. Dabrowski, B.; Zhang-MacCoy, V.; Wang, Z.; Hannon, R.; Jorgensen, J. D.; Hunter, B. A.; Hinks, D. G.; Wagner, J. L.; Hitterman, R. L. *J. Supercond.* **1994**, *7*, 45-48.
 16. Cava, R. J. In *Synthesis and crystal chemistry of high-Tc oxide superconductors* 1993; pp 1-44.
 17. Freiman, S. W.; Ritter, J. J.; Cline, J. P. In *Molecular-chemical approach to high-Tc superconductors*, 1992; pp 297-313.
 18. Li, Z. G.; Feng, H. H.; Yang, Z. Y.; Hamed, A.; Ting, S. T.; Hor, P. H.; Bhavaraju, S.; DiCarlo, J. F.; Jacobson, A. J. *Phys. Rev. Lett.* **1996**, *77*, 5413-5416.
 19. Weller, M. T.; Knee, C. S. *J. Mater. Chem.* **2001**, *11*, 701-712.
 20. Casan-Pastor, N.; Gomez-Romero, P.; Fuertes, A.; Navarro, J. M.; Sanchis, M. J.; Ondoño, S. *Physica C* **1993**, *216*, 478-490.
 21. Chou, F. C.; Johnston, D. C.; Cheong, S. W.; Canfield, P. C. *Physica C* **1993**, *216*, 66-76.
 22. Grenier, J. C.; Wattiaux, A.; Monroux, C.; Pouchard, M.; Locquet, J. P. *Physica C* **1994**, *235-240*, 79-82.
 23. Feng, H. H.; Li, Z. G.; Hor, P. H.; Bhavaraju, S.; DiCarlo, J. F.; Jacobson, A. J. *Phys. Rev. B* **1995**, *51*, 16499-16502.
 24. Blakeslee, P.; Birgeneau, R. J.; Chou, F. C.; Christianson, R.; Kastner, M. A.; Lee, Y. S.; Wells, B. O. *Phys. Rev. B* **1998**, *57*, 13915-13921.
 25. Magnone, E.; Cerisola, G.; Ferretti, M.; Barbucci, A. *J. Solid State Chem.* **1999**, *144*, 8-15.

Chapter 5

26. Scarfe, D. P.; Xiong, X.; Zhu, W. J.; Hor, P. H.; Moss, S. C.; Jacobson, A. J. *J. Mater. Res.* **1999**, *14*, 1221-1226.
27. Tu, Q. Y.; Chen, X. L.; Ma, B. K.; Zhao, Z. X.; Li, J. Q.; Liang, J. K. *Physica C* **2002**, *370*, 94-100.
28. Jacob, A.; Barbut, D.; Wattiaux, A.; Delville, M.-H.; Grenier, J.-C.; Pouchard, M.; Etourneau, J. *J. Mater. Chem.* **2000**, *10*, 829-831.
29. Michel, C. R.; Casan-Pastor, N. *Physica C* **1997**, *278*, 149-159.
30. Wang, C. C.; Cui, M. L.; Zheng, X.; Zhu, J. *Appl. Phys. A* **2004**, *A78*, 1193-1196.
31. Tu, Q. Y.; Ma, B. K.; Chen, X. L.; Lan, Y. C.; Xu, Y. X.; Liang, J. K.; Zhao, Z. X.; Li, J. Q. *Mod. Phys. Lett. B* **2001**, *15*, 1171-1179.
32. Lan, Y. C.; Chen, X. L.; Cao, Y. G.; Huang, J. K.; Che, G. C.; Liu, G. D.; Xu, Y. P.; Xu, T.; Li, J. Y. *Physica C* **2000**, *336*, 151-156.
33. Rapp, R. P.; Mehta, A.; DiCarlo, J.; Navrotsky, A. *J. Mater. Res.* **1994**, *9*, 8-12.
34. Takayama-Muromachi, E.; Sasaki, T.; Matsui, Y. *Physica C* **1993**, *207*, 97-101.
35. Raspi, G.; Zanello, P.; Cinquantini, A.; Corti, P. *Anal. Chim. Acta* **1973**, *66*, 435-442.
36. Wu, Z.; Zhang, Z.; Liu, L. *Electrochim. Acta* **1997**, *42*, 2719-2723.
37. Ogorevc, B.; Tavcar, G.; Hudnik, V.; Pejovnik, S. *J. Electroanal. Chem.* **1993**, *351*, 81-90.
38. Moore, P. B. *Am. Mineral.* **1970**, *55*, 135-169.
39. Rouzies, D.; Millet, J. M. M. *Hyperfine Interactions* **1993**, *77*, 11-18.
40. Redhammer, G. J.; Tippelt, G.; Roth, G.; Lottermoser, W.; Amthauer, G. *Phys. Chem. Miner.* **2000**, *27*, 419-429.
41. Rouzies, D.; Millet, J. M. M.; Siew Hew Sam, D.; Vedrine, J. C. *Appl. Catal., A* **1995**, *124*, 189-203.
42. Schmid-Beurmann, P. *J. Mater. Chem.* **2001**, *11*, 660-667.
43. Schmid-Beurmann, P. *J. Solid State Chem.* **2000**, *153*, 237-247.
44. Forsyth, J. B.; Brown, P. J.; Wanklyn, B. M. *J. Phys. C* **1988**, *21*, 2917-2929.
45. Amphlett, C. B. *Nature* **1950**, *165*, 977-978.
46. Wang, S.; Xin, H. *Radiat. Phys. Chem.* **1999**, *56*, 567-572.

Chapter 5

47. Gournis, D.; Mantaka-Marketou, A. E.; Karakassides, M. A.; Petridis, D. *Phys. Chem. Minerals* **2000**, *27*, 514-521.
48. Plotze, M.; Kahr, G.; Stengele, R. H. *Applied Clay Science* **2003**, *23*, 195-202.
49. Allen, A. O. *Actions Chim. et Biol. Radiations* **1961**, 11-30.
50. Symons, M. C. R.; Barnes, S. B. *J. Chem. Soc., Sect. A* **1970**, 2000-2002.
51. Caregnato, P.; Mora, V. C.; Le Roux, G. C.; Martire, D. O.; Gonzalez, M. C. *J. Phys. Chem. B* **2003**, *107*, 6131-6138.
52. Chitose, N.; Katsumura, Y.; Domae, M.; Zuo, Z.; Murakami, T. *Radiat. Phys. Chem.* **1999**, *54*, 385-391.
53. Buxton, G. V.; Djouider, F.; Alan Lynch, D.; Malone, T. N. *J. Chem. Soc., Faraday Trans.* **1997**, *93*, 4265-4268.
54. O'Neill, P.; Steenken, S.; Schulte-Frohlinde, D. *J. Phys. Chem.* **1975**, *79*, 2773-2779.
55. Wardman, P. *J. Phys. Chem. Ref. Data* **1989**, *18*, 1637-1755.

Appendix A. Crystallographic Data

Appendix A

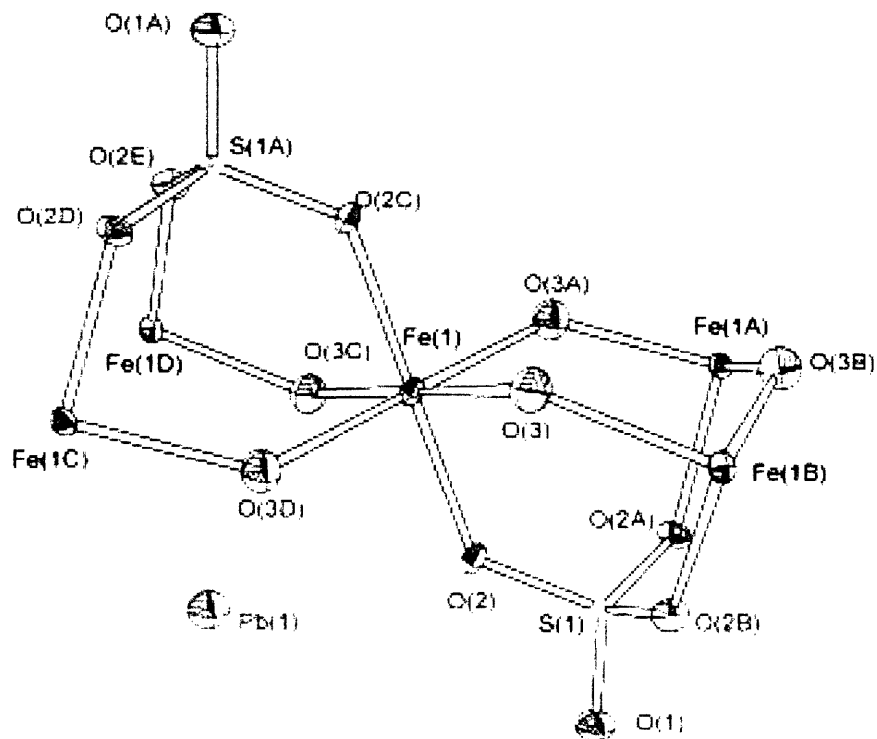


Figure A.1. Thermal ellipsoid plot for $\text{Pb}_{0.5}\text{Fe}_3(\text{OH})_6(\text{SO}_4)_2$. Ellipsoids shown at 50% probability.

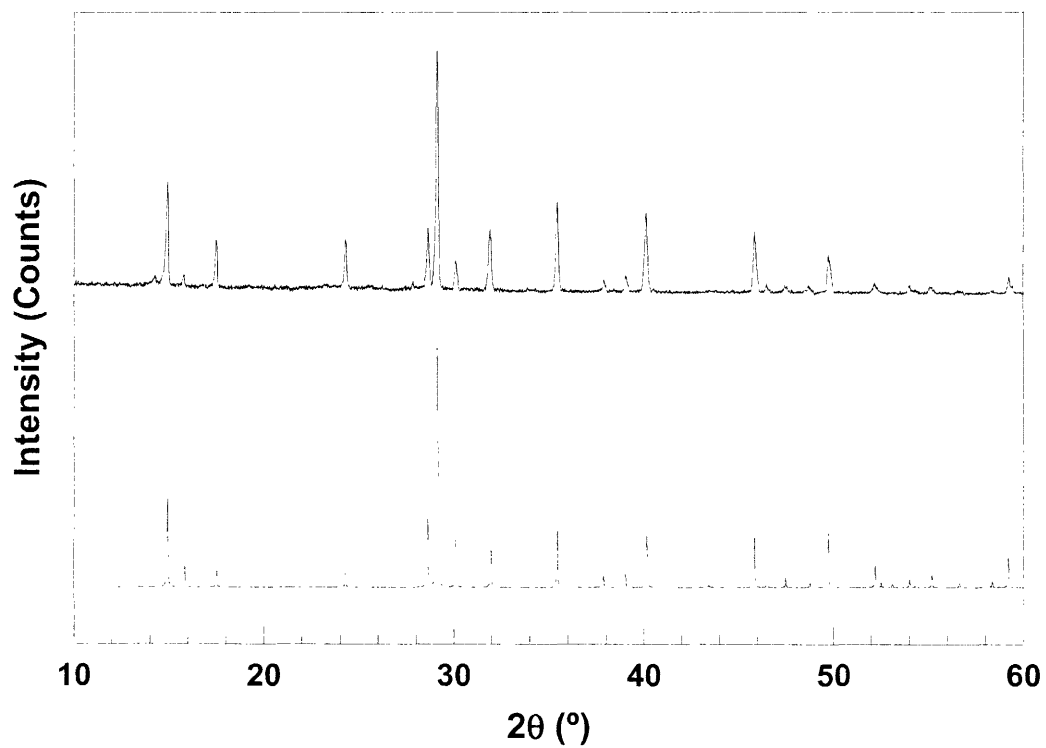


Figure A.2. Recorded (top) and simulated (bottom) pXRD pattern of $\text{Pb}_{0.5}\text{Fe}_3(\text{OH})_6(\text{SO}_4)_2$.

Appendix A

Table A.1. Crystal data and structure refinement for $\text{Pb}_{0.5}\text{Fe}_3(\text{OH})_6(\text{SO}_4)_2$.

Identification code	001206m	
Empirical formula	$\text{H}_6\text{Fe}_3\text{O}_{14}\text{Pb}_{0.5}\text{S}_2$	
Formula weight	565.31	
Temperature	183(2) K	
Wavelength	0.71073 Å	
Crystal system	Rhombohedral	
Space group	$R\bar{3}m$	
Unit cell dimensions	$a = 7.328(2)$ Å	$\alpha = 90^\circ$
	$b = 7.328(2)$ Å	$\beta = 90^\circ$
	$c = 16.795(6)$ Å	$\gamma = 120^\circ$
Volume	$781.1(4)$ Å ³	
Z	3	
Density (calculated)	3.606 Mg/m ³	
Absorption coefficient	15.334 mm ⁻¹	
F(000)	848	
Crystal size	$0.04 \times 0.04 \times 0.04$ mm ³	
Theta range for data collection	3.43 to 23.22°.	
Index ranges	$-4 \leq h \leq 8$	
	$-8 \leq k \leq 5$	
	$-18 \leq l \leq 17$	
Reflections collected	937	
Independent reflections	164 [$R_{\text{int}} = 0.0833$]	
Completeness to theta = 23.22°	100.0 %	
Absorption correction	None	
Refinement method	Full-matrix least-squares on F^2	
Data / restraints / parameters	164 / 1 / 34	
Goodness-of-fit on F^2	1.190	
Final R indices [$I > 2\sigma(I)$]	$R1 = 0.0268$	$wR2 = 0.0538$
R indices (all data)	$R1 = 0.0297$	$wR2 = 0.0552$
Largest diff. peak and hole	0.736 eÅ ⁻³	-0.593 eÅ ⁻³

Appendix A

Table A.2. Atomic coordinates ($\times 10^4$) and equivalent isotropic displacement parameters ($\text{\AA}^2 \times 10^3$) for $\text{Pb}_{0.5}\text{Fe}_3(\text{OH})_6(\text{SO}_4)_2$. $U(\text{eq})$ is defined as one third of the trace of the orthogonalized U_{ij} tensor.

Atom	x	y	z	$U(\text{eq})$
Pb(1)	0	0	0	21(1)
S(1)	0	0	3109(2)	7(1)
Fe(1)	3333	1667	1667	8(1)
O(1)	0	0	3973(4)	20(3)
O(2)	2200(7)	1100(3)	2810(2)	15(2)
O(3)	1266(3)	2532(7)	1343(2)	18(2)

Table A.3. Anisotropic displacement parameters ($\text{\AA}^2 \times 10^3$) for $\text{Pb}_{0.5}\text{Fe}_3(\text{OH})_6(\text{SO}_4)_2$. The anisotropic displacement factor exponent takes the form: $-2\pi^2 [h^2a^{*2}U_{11} + \dots + 2hka^*b^*U_{12}]$.

	U_{11}	U_{22}	U_{33}	U_{23}	U_{13}	U_{12}
Pb(1)	22(1)	22(1)	20(1)	0	0	11(1)
S(1)	8(1)	8(1)	5(1)	0	0	4(1)
Fe(1)	7(1)	8(1)	10(1)	1(1)	2(1)	4(1)
O(1)	22(4)	22(4)	14(4)	0	0	11(2)
O(3)	16(2)	16(3)	22(2)	3(2)	1(1)	8(1)
O(2)	10(3)	19(2)	13(2)	1(1)	3(2)	5(1)

Table A.4. Hydrogen coordinates ($\times 10^4$) and isotropic displacement parameters ($\text{\AA}^2 \times 10^3$) for $\text{Pb}_{0.5}\text{Fe}_3(\text{OH})_6(\text{SO}_4)_2$.

	x	y	z	$U(\text{eq})$
H(1)	1920(40)	3840(70)	1050(40)	60(50)

Appendix A

Table A.5. Bragg reflections and Miller indices of pXRD pattern for $\text{Pb}_{0.5}\text{Fe}_3(\text{OH})_6(\text{SO}_4)_2$.

2θ	d_{obs}	% I_{obs}	d_{calcd}	% I_{calcd}	Δd	hkl
14.920	5.9331	42.9	5.9367	37.54	-0.0036	1 0 1
15.780	5.6113	4.9	5.5985	8.88	0.0128	0 0 3
17.484	5.0683	20.3	5.0631	7.79	0.0052	0 1 2
24.285	3.6621	20.1	3.6641	6.13	-0.002	1 1 0
25.548	3.4838	1.9	3.5018	0.0	-0.018	1 0 4
28.637	3.1146	25.5	3.1180	29.76	-0.0034	0 2 1
29.119	3.0643	100.0	3.0659	100.0	-0.0016	1 1 3
30.101	2.9664	11.8	2.9689	20.03	-0.0025	2 0 2
31.901	2.8030	25.6	2.7993	16.36	0.0037	0 0 6
35.439	2.5309	37.6	2.5316	23.26	-0.0007	0 2 4
37.900	2.3720	4.9	2.3746	4.67	-0.0026	2 1 1
39.060	2.3042	6.9	2.3067	0.26	-0.0025	1 2 2
40.119	2.2458	33.5	2.2443	21.24	0.0015	1 0 7
40.537	2.2236	1.5	2.2244	0.0	-0.0008	1 1 6
45.841	1.9779	25.9	1.9789	19.08	-0.001	0 3 3
46.481	1.9521	3.7	1.9521	2.83	0	1 2 5
47.441	1.9148	2.9	1.9138	3.91	0.001	0 2 7
48.683	1.8689	2.7	1.8662	1.87	0.0027	0 0 9
49.742	1.8315	15.9	1.8321	24.09	-0.0006	2 2 0
52.181	1.7515	4.3	1.7509	6.48	0.0006	2 0 8
54.037	1.6957	3.5	1.6964	3.15	-0.0007	2 1 7
54.318	1.6875	2.1	1.6877	0.30	-0.0002	0 3 6
55.102	1.6654	3.0	1.6629	5.27	0.0025	1 1 9
56.576	1.6254	1.7	1.6237	1.29	0.0017	1 0 10
58.431	1.5782	1.0	1.5796	1.58	-0.0014	4 0 1
59.262	1.5580	6.9	1.5590	6.42	-0.001	0 4 2

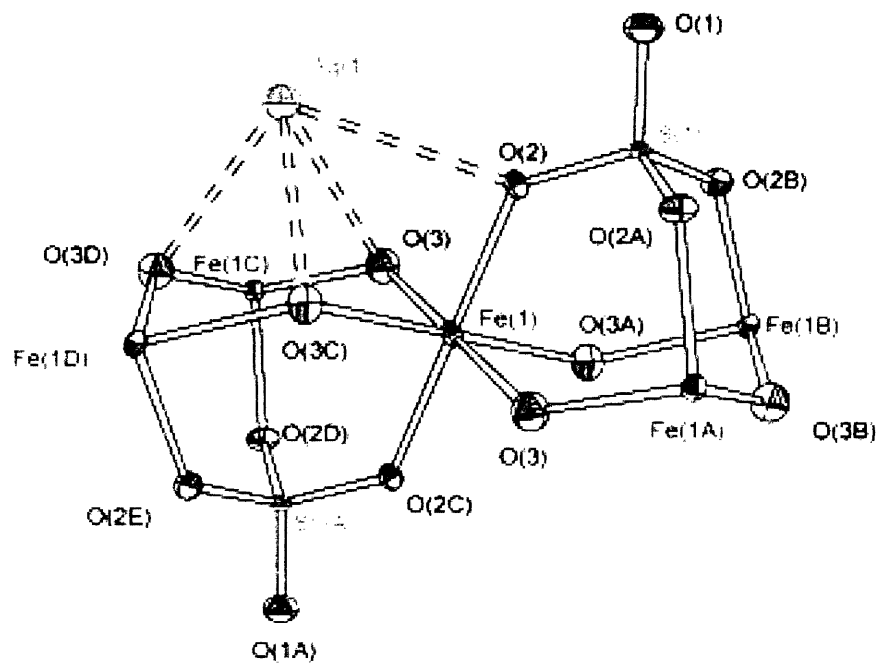


Figure A.3. Thermal ellipsoid plot for $\text{AgFe}_3(\text{OH})_6(\text{SO}_4)_2$. Ellipsoids shown at 50% probability.

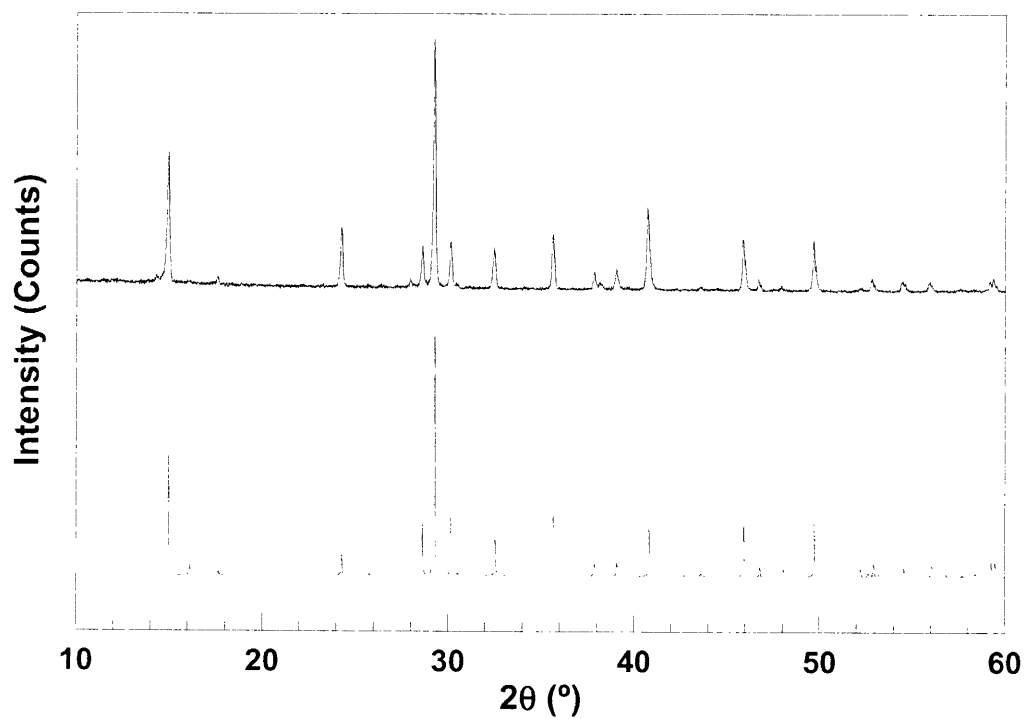


Figure A.4. Recorded (top) and simulated (bottom) pXRD pattern of $\text{AgFe}_3(\text{OH})_6(\text{SO}_4)_2$.

Table A.6. Crystal data and structure refinement for $\text{AgFe}_3(\text{OH})_6(\text{SO}_4)_2$.

Identification code	002032m	
Empirical formula	$\text{H}_6\text{Fe}_3\text{O}_{14}\text{AgS}_2$	
Formula weight	569.59	
Temperature	183(2) K	
Wavelength	0.71073 Å	
Crystal system	Rhombohedral	
Space group	$R\bar{3}m$	
Unit cell dimensions	$a = 7.3300(9)$ Å	$\alpha = 90^\circ$
	$b = 7.3300(9)$ Å	$\beta = 90^\circ$
	$c = 16.497(3)$ Å	$\gamma = 120^\circ$
Volume	$767.62(19)$ Å ³	
Z	3	
Density (calculated)	3.696 Mg/m ³	
Absorption coefficient	6.547 mm ⁻¹	
F(000)	825	
Crystal size	$0.04 \times 0.04 \times 0.04$ mm ³	
Theta range for data collection	3.44 to 23.27° .	
Index ranges	$-8 \leq h \leq 8$	
	$-8 \leq k \leq 8$	
	$-7 \leq l \leq 18$	
Reflections collected	1039	
Independent reflections	161 [$R_{\text{int}} = 0.0459$]	
Completeness to theta = 23.27°	100.0 %	
Absorption correction	None	
Refinement method	Full-matrix least-squares on F^2	
Data / restraints / parameters	161 / 1 / 29	
Goodness-of-fit on F^2	1.224	
Final R indices [$I > 2\sigma(I)$]	$R1 = 0.0255$	$wR2 = 0.0642$
R indices (all data)	$R1 = 0.0259$	$wR2 = 0.0644$
Largest diff. peak and hole	0.508 eÅ ⁻³	-0.906 eÅ ⁻³

Appendix A

Table A.7. Atomic coordinates ($\times 10^4$) and equivalent isotropic displacement parameters ($\text{\AA}^2 \times 10^3$) for $\text{AgFe}_3(\text{OH})_6(\text{SO}_4)_2$. $U(\text{eq})$ is defined as one third of the trace of the orthogonalized U_{ij} tensor.

Atom	x	y	z	$U(\text{eq})$
Ag(1)	0	0	0	27(1)
S(1)	0	0	3123(2)	7(1)
Fe(1)	3333	1667	1667	7(1)
O(1)	0	0	4009(5)	8(2)
O(2)	2194(8)	1097(4)	2823(3)	10(1)
O(3)	1256(4)	2512(8)	1331(3)	8(1)

Table A.8. Anisotropic displacement parameters ($\text{\AA}^2 \times 10^3$) for $\text{AgFe}_3(\text{OH})_6(\text{SO}_4)_2$. The anisotropic displacement factor exponent takes the form: $-2\pi^2 [h^2 a^{*2} U_{11} + \dots + 2hka^* b^* U_{12}]$.

	U_{11}	U_{22}	U_{33}	U_{23}	U_{13}	U_{12}
Ag(1)	34(1)	34(1)	13(1)	0	0	17(1)
S(1)	8(1)	8(1)	5(2)	0	0	4(1)
Fe(1)	5(1)	7(1)	8(1)	0(1)	1(1)	3(1)
O(1)	12(3)	12(3)	1(4)	0	0	6(2)
O(2)	6(3)	13(2)	7(2)	0(1)	0(2)	3(1)
O(3)	7(2)	7(3)	11(2)	1(2)	1(1)	4(2)

Table A.9. Hydrogen coordinates ($\times 10^4$) and isotropic displacement parameters ($\text{\AA}^2 \times 10^3$) for $\text{AgFe}_3(\text{OH})_6(\text{SO}_4)_2$.

	x	y	z	$U(\text{eq})$
H(1)	2000(20)	3990(50)	1180(70)	120(70)

Table A.10. Bragg reflections and Miller indices of pXRD pattern for $\text{AgFe}_3(\text{OH})_6(\text{SO}_4)_2$.

2θ	d_{obs}	% I_{obs}	d_{calcd}	% I_{calcd}	Δd	hkl
14.922	5.9321	4.9	5.9245	49.98	0.0076	1 0 1
16.019	5.5280	1.9	5.4990	4.02	0.0290	0 0 3
17.597	5.0361	3.2	5.0307	1.69	0.0054	0 1 2
24.242	3.6685	24.3	3.6650	9.09	0.0035	1 1 0
26.350	3.3796	1.4	3.4585	0.47	-0.0789	1 0 4
28.616	3.1170	16.4	3.1168	21.51	0.0002	0 2 1
29.222	3.0537	100.0	3.0497	100.0	0.004	1 1 3
30.136	2.9631	18.3	2.9623	23.87	0.0008	2 0 2
30.417	2.9363	1.6	2.9276	0.96	0.0087	0 1 5
32.443	2.7575	16.3	2.7495	16.35	0.008	0 0 6
35.618	2.5186	21.9	2.5153	24.24	0.0033	0 2 4
37.837	2.3758	7.0	2.3743	6.40	0.0015	2 1 1
39.020	2.3065	8.4	2.3038	5.73	0.0027	1 2 2
40.701	2.2150	33.3	2.2094	19.94	0.0056	1 0 7
43.559	2.0761	1.5	2.0739	1.27	0.0022	2 1 4
45.844	1.9778	20.4	1.9748	17.84	0.003	0 3 3
46.700	1.9435	4.0	1.9405	3.67	0.003	1 2 5
47.922	1.8967	2.0	1.8922	2.96	0.0045	0 2 7
49.622	1.8343	20.2	1.8325	22.66	0.0018	2 2 0
52.141	1.7528	1.7	1.7509	6.48	0.0019	2 0 8
52.800	1.7324	4.8	1.7218	0.89	0.0106	3 1 2
54.458	1.6835	4.1	1.6813	3.57	0.0022	2 1 7
55.920	1.6429	3.9	1.6394	5.57	0.0035	1 1 9
57.552	1.6001	1.4	1.5967	1.29	0.0034	1 0 10
59.179	1.5600	4.0	1.5639	0.56	-0.0039	1 2 8
59.375	1.5553	5.0	1.5584	6.45	-0.0031	0 4 2

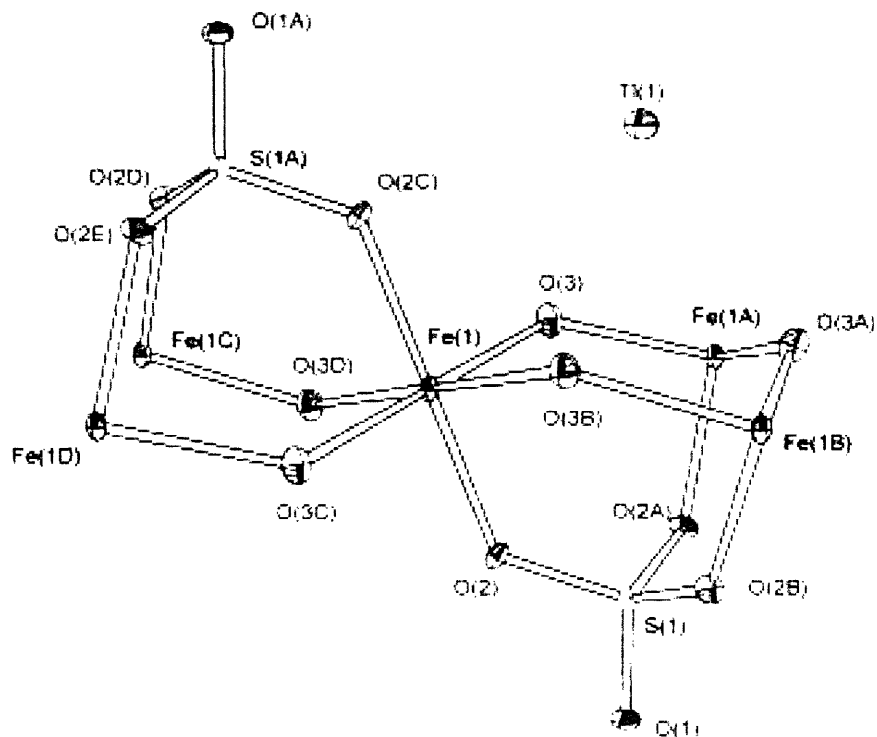


Figure A.5. Thermal ellipsoid plot for $\text{TlFe}_3(\text{OH})_6(\text{SO}_4)_2$. Ellipsoids shown at 50% probability.

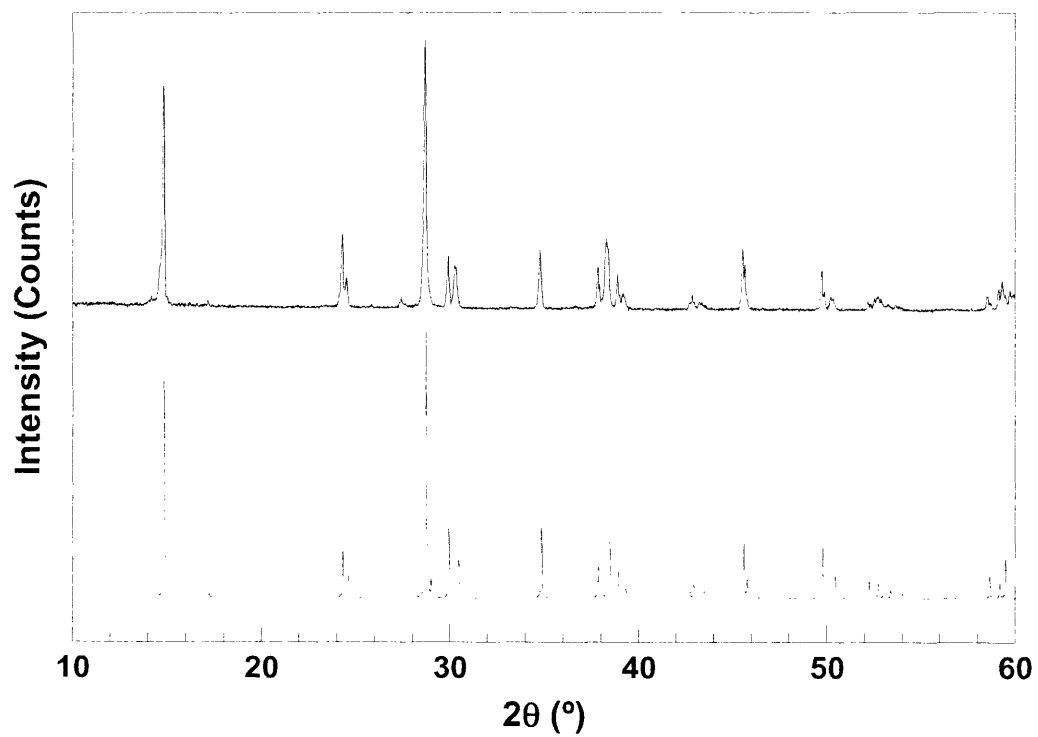


Figure A.6. Recorded (top) and simulated (bottom) pXRD pattern of $\text{TlFe}_3(\text{OH})_6(\text{SO}_4)_2$.

Table A.11. Crystal data and structure refinement for $\text{TlFe}_3(\text{OH})_6(\text{SO}_4)_2$.

Identification code	002124m	
Empirical formula	$\text{H}_6\text{Fe}_3\text{O}_{14}\text{TlS}_2$	
Formula weight	666.09	
Temperature	183(2) K	
Wavelength	0.71073 Å	
Crystal system	Rhombohedral	
Space group	$R\bar{3}m$	
Unit cell dimensions	$a = 7.3226(7)$ Å	$\alpha = 90^\circ$
	$b = 7.3226(7)$ Å	$\beta = 90^\circ$
	$c = 17.610(2)$ Å	$\gamma = 120^\circ$
Volume	$817.74(15)$ Å ³	
Z	3	
Density (calculated)	4.058 Mg/m ³	
Absorption coefficient	19.111 mm ⁻¹	
F(000)	927	
Crystal size	$0.04 \times 0.04 \times 0.04$ mm ³	
Theta range for data collection	3.41 to 23.22°.	
Index ranges	$-6 \leq h \leq 8$	
	$-7 \leq k \leq 8$	
	$-18 \leq l \leq 19$	
Reflections collected	1080	
Independent reflections	169 [$R_{\text{int}} = 0.0589$]	
Completeness to theta = 23.22°	100.0 %	
Absorption correction	None	
Refinement method	Full-matrix least-squares on F^2	
Data / restraints / parameters	169 / 1 / 29	
Goodness-of-fit on F^2	1.292	
Final R indices [$I > 2\sigma(I)$]	$R_I = 0.0207$	$wR_2 = 0.0546$
R indices (all data)	$R_I = 0.0207$	$wR_2 = 0.0546$
Largest diff. peak and hole	0.754 eÅ ⁻³	-0.649 eÅ ⁻³

Appendix A

Table A.12. Atomic coordinates ($\times 10^4$) and equivalent isotropic displacement parameters ($\text{\AA}^2 \times 10^3$) for $\text{TlFe}_3(\text{OH})_6(\text{SO}_4)_2$. $U(\text{eq})$ is defined as one third of the trace of the orthogonalized U_{ij} tensor.

Atom	x	y	z	$U(\text{eq})$
Tl(1)	0	0	0	12(1)
S(1)	0	0	3050(2)	6(1)
Fe(1)	3333	1667	1667	5(1)
O(1)	0	0	3873(6)	9(2)
O(2)	2202(10)	1101(5)	2762(3)	9(1)
O(3)	1283(5)	2565(10)	1374(3)	12(2)

Table A.13. Anisotropic displacement parameters ($\text{\AA}^2 \times 10^3$) for $\text{TlFe}_3(\text{OH})_6(\text{SO}_4)_2$. The anisotropic displacement factor exponent takes the form: $-2\pi^2 [h^2 a^{*2} U_{11} + \dots + 2hka^* b^* U_{12}]$.

	U_{11}	U_{22}	U_{33}	U_{23}	U_{13}	U_{12}
Tl(1)	13(1)	13(1)	11(1)	0	0	7(1)
S(1)	5(1)	5(1)	7(2)	0	0	3(1)
Fe(1)	3(1)	4(1)	9(1)	0(1)	0(1)	2(1)
O(1)	11(4)	11(4)	5(5)	0	0	6(2)
O(2)	6(3)	11(2)	9(3)	2(1)	3(3)	3(2)
O(3)	9(3)	10(4)	16(4)	-2(3)	-1(1)	5(2)

Table A.14. Hydrogen coordinates ($\times 10^4$) and isotropic displacement parameters ($\text{\AA}^2 \times 10^3$) for $\text{TlFe}_3(\text{OH})_6(\text{SO}_4)_2$.

	x	y	z	$U(\text{eq})$
H(1)	1300(300)	2700(500)	824(15)	230(160)

Appendix A

Table A.15. Bragg reflections and Miller indices of pXRD pattern for $\text{TlFe}_3(\text{OH})_6(\text{SO}_4)_2$.

2θ	d_{obs}	% I_{obs}	d_{calcd}	% I_{calcd}	Δd	hkl
14.181	5.9730	83.0	5.9665	83.82	0.0065	1 0 1
17.164	5.1619	2.3	5.1458	1.84	0.0161	0 1 2
24.280	3.6629	27.3	3.6613	17.02	0.0016	1 1 0
24.484	3.6327	10.8	3.6164	7.79	0.0163	1 0 4
28.661	3.1121	100.0	3.1065	100.0	0.0056	1 1 3
29.900	2.9860	18.9	2.9832	26.07	0.0028	2 0 2
30.243	2.9528	15.7	2.9350	16.48	0.0178	0 0 6
34.780	2.5773	21.7	2.5729	26.04	0.0044	0 2 4
37.835	2.3759	14.6	2.3750	12.35	0.0009	2 1 1
38.262	2.3504	25.3	2.3384	21.62	0.012	1 0 7
38.879	2.3145	11.9	2.3127	10.49	0.0018	1 2 2
39.161	2.2985	5.3	2.1994	0.13	0.0991	1 1 6
42.860	2.1083	5.2	2.1139	2.17	-0.0056	3 0 0
43.256	2.0899	2.7	2.1051	5.43	-0.0152	2 1 4
45.522	1.9910	22.8	1.9888	17.63	0.0022	0 3 3
49.737	1.8317	14.7	1.8307	19.22	0.001	2 2 0
50.200	1.8159	4.9	1.8082	8.11	0.0077	2 0 8
52.701	1.7354	4.7	1.7353	5.88	1×10^{-4}	2 1 7
52.822	1.7299	3.7	1.7257	7.45	0.0042	1 1 9
53.258	1.7186	1.5	1.7153	1.45	0.0033	0 3 6
53.648	1.7070	1.4	1.6968	1.62	0.0102	1 0 10
57.695	1.5965	0.9	1.5790	0.02	0.0175	4 0 1
58.539	1.5755	4.5	1.5735	7.81	0.002	3 1 5
59.138	1.5610	7.9	1.5603	6.01	0.0007	0 4 2
59.320	1.5566	10.5	1.5533	14.40	0.0033	2 2 6

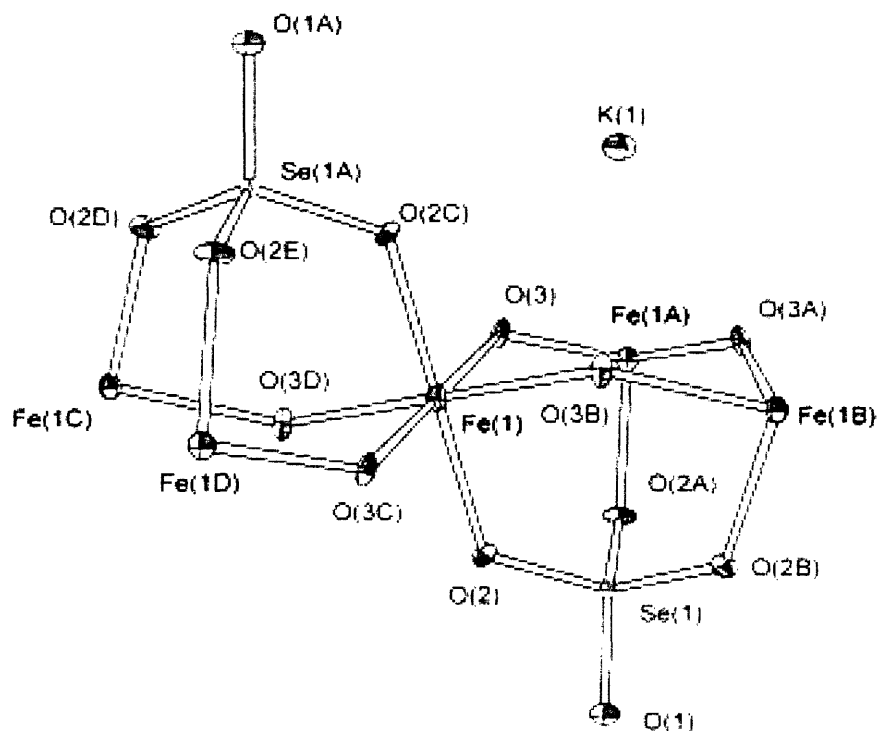


Figure A.7. Thermal ellipsoid plot for $\text{KFe}_3(\text{OH})_6(\text{SeO}_4)_2$. Ellipsoids shown at 50% probability.

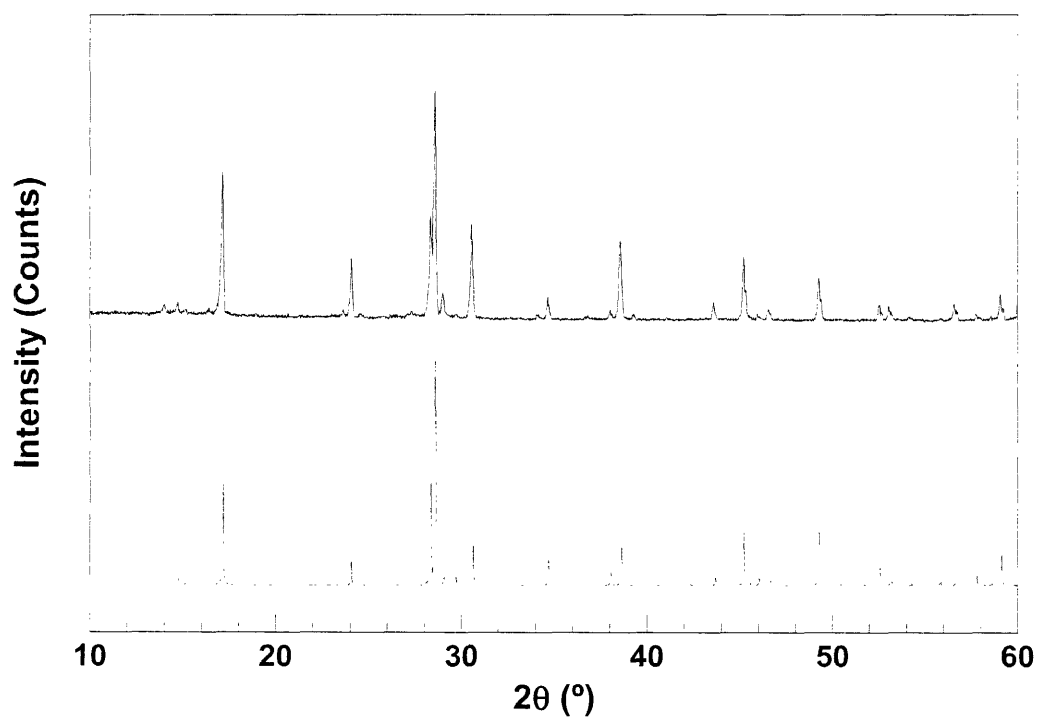


Figure A.8. Recorded (top) and simulated (bottom) pXRD pattern of $\text{KFe}_3(\text{OH})_6(\text{SeO}_4)_2$.

Table A.16. Crystal data and structure refinement for $\text{KFe}_3(\text{OH})_6(\text{SeO}_4)_2$.

Identification code	002127m	
Empirical formula	$\text{H}_6\text{Fe}_3\text{O}_{14}\text{KSe}_2$	
Formula weight	594.62	
Temperature	183(2) K	
Wavelength	0.71073 Å	
Crystal system	Rhombohedral	
Space group	$R\bar{3}m$	
Unit cell dimensions	$a = 7.3902(9)$ Å	$\alpha = 90^\circ$
	$b = 7.3902(9)$ Å	$\beta = 90^\circ$
	$c = 17.498(3)$ Å	$\gamma = 120^\circ$
Volume	$827.6(2)$ Å ³	
Z	3	
Density (calculated)	3.579 Mg/m ³	
Absorption coefficient	10.947 mm ⁻¹	
F(000)	849	
Crystal size	$0.04 \times 0.04 \times 0.02$ mm ³	
Theta range for data collection	3.39 to 23.27°.	
Index ranges	$-7 \leq h \leq 8$	
	$-7 \leq k \leq 8$	
	$-19 \leq l \leq 19$	
Reflections collected	1130	
Independent reflections	171 [$R_{\text{int}} = 0.0706$]	
Completeness to theta = 23.27°	100.0 %	
Absorption correction	None	
Refinement method	Full-matrix least-squares on F^2	
Data / restraints / parameters	171 / 1 / 29	
Goodness-of-fit on F^2	1.245	
Final R indices [$I > 2\sigma(I)$]	$R_I = 0.0367$	$wR_2 = 0.0781$
R indices (all data)	$R_I = 0.0374$	$wR_2 = 0.0786$
Largest diff. peak and hole	0.913 eÅ ⁻³	-0.690 eÅ ⁻³

Appendix A

Table A.17. Atomic coordinates ($\times 10^4$) and equivalent isotropic displacement parameters ($\text{\AA}^2 \times 10^3$) for $\text{KFe}_3(\text{OH})_6(\text{SeO}_4)_2$. $U(\text{eq})$ is defined as one third of the trace of the orthogonalized U_{ij} tensor.

Atom	x	y	z	$U(\text{eq})$
K(1)	0	0	0	13(1)
Se(1)	0	0	3115(1)	5(1)
Fe(1)	3333	1667	1667	7(1)
O(1)	0	0	4036(7)	11(3)
O(2)	2410(11)	1205(6)	2792(3)	10(2)
O(3)	1258(6)	2516(12)	1387(4)	9(2)

Table A.18. Anisotropic displacement parameters ($\text{\AA}^2 \times 10^3$) for $\text{KFe}_3(\text{OH})_6(\text{SeO}_4)_2$. The anisotropic displacement factor exponent takes the form: $-2\pi^2 [h^2a^{*2}U_{11} + \dots + 2hka^*b^*U_{12}]$.

	U_{11}	U_{22}	U_{33}	U_{23}	U_{13}	U_{12}
K(1)	15(2)	15(2)	10(3)	0	0	7(1)
Se(1)	5(1)	5(1)	5(1)	0	0	3(1)
Fe(1)	5(1)	7(1)	10(1)	0(1)	1(1)	3(1)
O(1)	12(5)	12(5)	7(6)	0	0	6(2)
O(2)	6(4)	6(4)	7(3)	2(1)	4(3)	3(2)
O(3)	5(3)	6(4)	16(4)	4(3)	2(2)	3(2)

Table A.19. Hydrogen coordinates ($\times 10^4$) and isotropic displacement parameters ($\text{\AA}^2 \times 10^3$) for $\text{KFe}_3(\text{OH})_6(\text{SeO}_4)_2$.

	x	y	z	$U(\text{eq})$
H(1)	1930(40)	3860(80)	1130(50)	40(50)

Appendix A

Table A.20. Bragg reflections and Miller indices of pXRD pattern for $\text{KFe}_3(\text{OH})_6(\text{SeO}_4)_2$.

2θ	d_{obs}	% I_{obs}	d_{calcd}	% I_{calcd}	Δd	hkl
14.739	6.0053	5.2	6.0107	3.06	-0.0054	1 0 1
15.108	5.8596	2.1	5.8327	3.93	0.0269	0 0 3
17.140	5.1692	63.5	5.1655	46.27	0.0037	0 1 2
24.062	3.6954	26.3	3.6951	10.00	0.0003	1 1 0
28.339	3.1468	44.4	3.1478	47.30	-0.001	0 2 1
28.558	3.1231	100.0	3.1214	100.0	0.0017	1 1 3
28.997	3.0768	10.3	3.0706	4.83	0.0062	0 1 5
29.717	3.0039	1.6	3.0053	3.97	-0.0014	2 0 2
30.557	2.9232	41.4	2.9164	16.99	0.0068	0 0 6
34.676	2.5848	10.0	2.5828	11.04	0.002	0 2 4
38.032	2.3641	3.8	2.3616	5.93	0.0025	2 0 5
38.540	2.3341	34.7	2.3284	0.17	0.0057	1 0 7
39.243	2.2939	2.6	2.2892	1.08	0.0047	1 1 6
43.563	2.0759	7.4	2.0697	3.27	0.0062	0 1 8
45.184	2.0051	28.3	2.0035	19.04	0.0016	0 3 3
45.935	1.9740	2.4	1.9699	3.10	0.0041	0 2 7
46.542	1.9504	4.6	1.9442	2.21	0.0062	0 0 9
49.245	1.8488	18.9	1.8476	26.55	0.0012	2 2 0
52.521	1.7410	6.5	1.7396	7.09	0.0014	3 1 2
53.041	1.7251	6.3	1.7206	5.12	0.0045	1 1 9
54.141	1.6926	1.7	1.6879	0.61	0.0047	1 0 10
56.577	1.6254	7.1	1.6224	6.41	0.003	1 2 8
57.765	1.5948	2.5	1.5934	4.21	0.0014	4 0 1
57.919	1.5909	1.1	1.5831	0.35	0.0078	3 1 5
59.075	1.5625	10.5	1.5607	13.52	0.0018	2 2 6

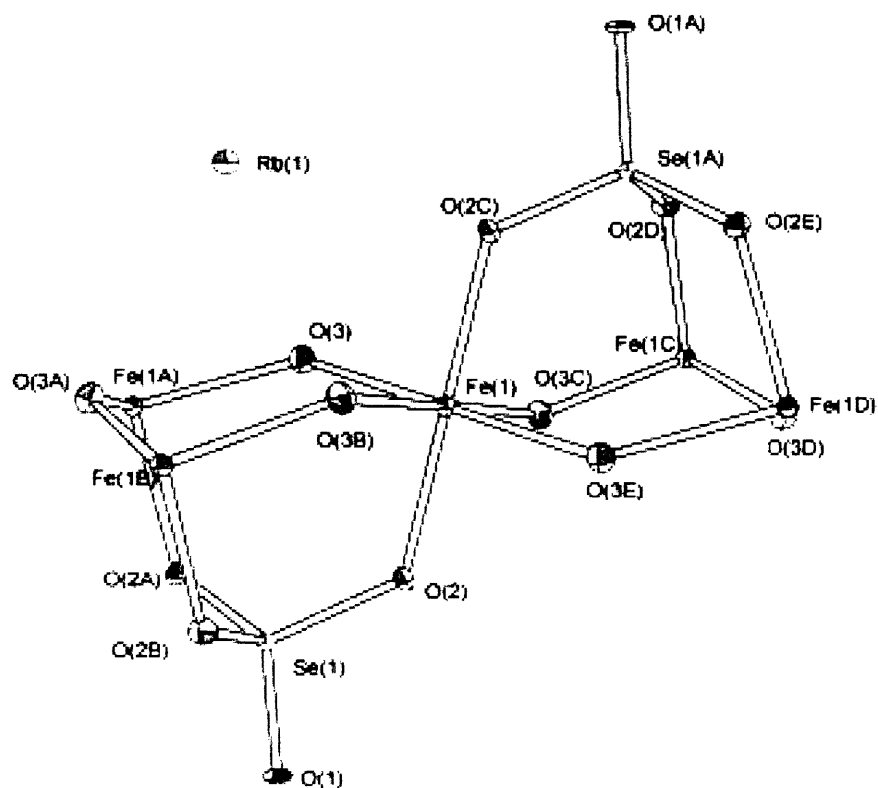


Figure A.9. Thermal ellipsoid plot for $\text{RbFe}_3(\text{OH})_6(\text{SeO}_4)_2$. Ellipsoids shown at 50% probability.

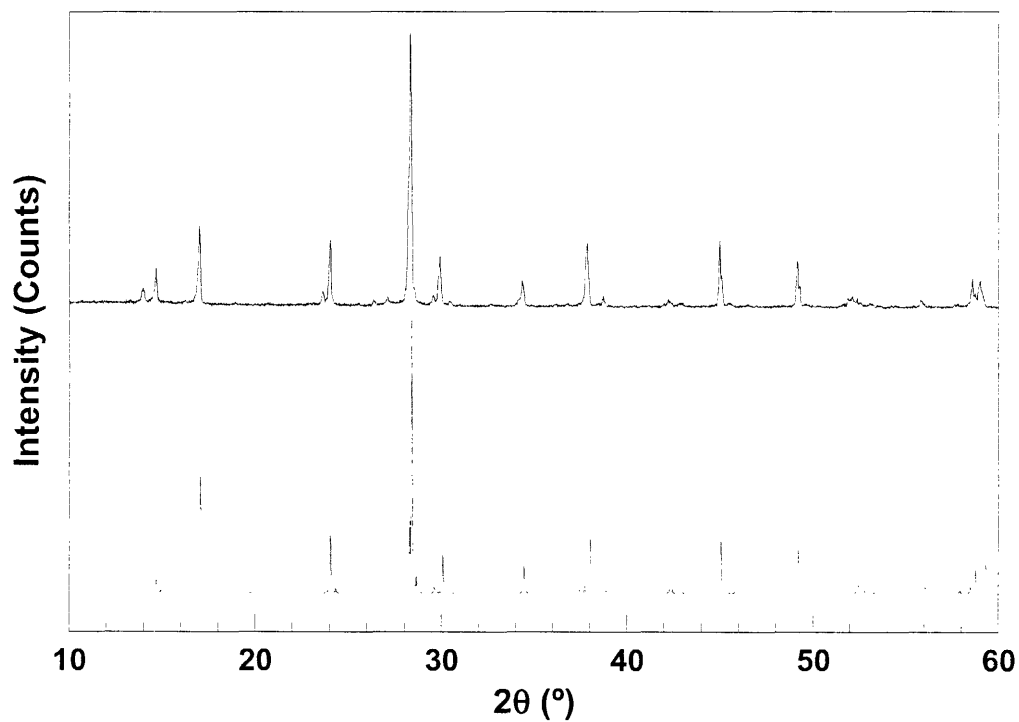


Figure A.10. Recorded (top) and simulated (bottom) pXRD pattern of $\text{RbFe}_3(\text{OH})_6(\text{SeO}_4)_2$.

Table A.21. Crystal data and structure refinement for $\text{RbFe}_3(\text{OH})_6(\text{SeO}_4)_2$.

Identification code	003096m	
Empirical formula	$\text{H}_6\text{Fe}_3\text{O}_{14}\text{RbSe}_2$	
Formula weight	640.99	
Temperature	100(2) K	
Wavelength	0.71073 Å	
Crystal system	Rhombohedral	
Space group	$R\bar{3}m$	
Unit cell dimensions	$a = 7.4022(16)$ Å	$\alpha = 90^\circ$
	$b = 7.4022(16)$ Å	$\beta = 90^\circ$
	$c = 17.816(5)$ Å	$\gamma = 120^\circ$
Volume	$845.4(4)$ Å ³	
Z	3	
Density (calculated)	3.777 Mg/m ³	
Absorption coefficient	4.879 mm ⁻¹	
F(000)	301	
Crystal size	$0.04 \times 0.04 \times 0.03$ mm ³	
Theta range for data collection	3.38 to 28.47°	
Index ranges	$-9 \leq h \leq 9$	
	$-9 \leq k \leq 9$	
	$-23 \leq l \leq 23$	
Reflections collected	5356	
Independent reflections	293 [$R_{\text{(int)}} = 0.0323$]	
Completeness to theta = 28.47°	100.0 %	
Absorption correction	None	
Refinement method	Full-matrix least-squares on F^2	
Data / restraints / parameters	293 / 1 / 29	
Goodness-of-fit on F^2	1.116	
Final R indices [$I > 2\sigma(I)$]	$R1 = 0.0156$	$wR2 = 0.0433$
R indices (all data)	$R1 = 0.0162$	$wR2 = 0.0436$
Largest diff. peak and hole	0.617 eÅ ⁻³	-0.812 eÅ ⁻³

Appendix A

Table A.22. Atomic coordinates ($\times 10^4$) and equivalent isotropic displacement parameters ($\text{\AA}^2 \times 10^3$) for $\text{RbFe}_3(\text{OH})_6(\text{SeO}_4)_2$. $U(\text{eq})$ is defined as one third of the trace of the orthogonalized U_{ij} tensor.

Atom	x	y	z	$U(\text{eq})$
Rb(1)	0	0	0	8(1)
Se(1)	0	0	3093(1)	5(1)
Fe(1)	3333	1667	1667	5(1)
O(1)	0	0	4002(2)	8(1)
O(2)	2409(3)	1204(2)	2774(1)	8(1)
O(3)	1264(2)	2527(3)	1408(1)	10(1)

Table A.23. Anisotropic displacement parameters ($\text{\AA}^2 \times 10^3$) for $\text{RbFe}_3(\text{OH})_6(\text{SeO}_4)_2$. The anisotropic displacement factor exponent takes the form: $-2\pi^2 [h^2 a^{*2} U_{11} + \dots + 2hka^* b^* U_{12}]$.

	U_{11}	U_{22}	U_{33}	U_{23}	U_{13}	U_{12}
Rb(1)	8(1)	8(1)	7(1)	0	0	4(1)
Se(1)	5(1)	5(1)	5(1)	0	0	3(1)
Fe(1)	5(1)	5(1)	6(1)	0(1)	1(1)	2(1)
O(1)	10(1)	10(10)	2(2)	0	0	5(1)
O(2)	5(1)	10(1)	8(1)	1(1)	1(1)	2(1)
O(3)	9(1)	10(1)	12(1)	1(1)	1(1)	5(1)

Table A.24. Hydrogen coordinates ($\times 10^4$) and isotropic displacement parameters ($\text{\AA}^2 \times 10^3$) for $\text{RbFe}_3(\text{OH})_6(\text{SeO}_4)_2$.

	x	y	z	$U(\text{eq})$
H(1)	1959(14)	3920(30)	1210(20)	19(10)

Appendix A

Table A.25. Bragg reflections and Miller indices of pXRD pattern for $\text{RbFe}_3(\text{OH})_6(\text{SeO}_4)_2$.

2θ	d_{obs}	% I_{obs}	d_{calcd}	% I_{calcd}	Δd	hkl
14.658	6.0383	12.3	6.0319	16.41	0.0064	1 0 1
16.983	5.2167	29.5	5.2033	25.29	0.0134	0 1 2
24.019	3.7021	23.6	3.7011	29.34	0.001	1 1 0
28.338	3.1468	100.0	3.1411	100.0	0.0057	1 1 3
29.560	3.0194	3.2	3.0160	3.90	0.0034	2 0 2
29.917	2.9842	17.8	2.9694	17.25	0.0148	0 0 6
34.344	2.6090	9.3	2.6016	11.92	0.0074	0 2 4
36.797	2.4405	1.0	2.4008	1.48	0.0397	2 1 1
37.839	2.3757	23.0	2.3656	24.80	0.0101	1 0 7
38.717	2.3238	3.6	2.3161	3.90	0.0077	1 1 6
42.219	2.1388	2.5	2.1368	2.53	0.002	3 0 0
43.001	2.1017	1.1	2.1037	1.11	-0.002	0 1 8
44.981	2.0137	24.0	2.0106	23.66	0.0031	0 3 3
45.557	1.9895	1.2	1.9932	0.31	-0.0037	0 2 7
46.482	1.9521	1.1	1.9796	1.36	-0.0275	0 0 9
49.157	1.8519	16.6	1.8506	26.64	0.0013	2 2 0
49.616	1.8359	1.1	1.8289	0.83	0.007	2 0 8
51.897	1.7604	3.2	1.7667	0.31	-0.0063	2 2 3
52.099	1.7541	3.5	1.7549	4.89	-0.0008	2 1 7
52.375	1.7455	2.9	1.7456	4.48	-1×10^{-4}	1 1 9
52.575	1.7393	1.4	1.7344	0.96	0.0049	0 3 6
53.444	1.7131	0.8	1.7166	1.62	-0.0035	1 0 10
55.822	1.6456	2.6	1.6396	3.31	0.006	1 2 8
57.831	1.5931	0.9	1.5909	0.51	0.0022	3 1 5
58.598	1.5741	10.1	1.5705	13.66	0.0036	2 2 6
59.037	1.5634	9.5	1.5572	15.38	0.0062	0 2 10

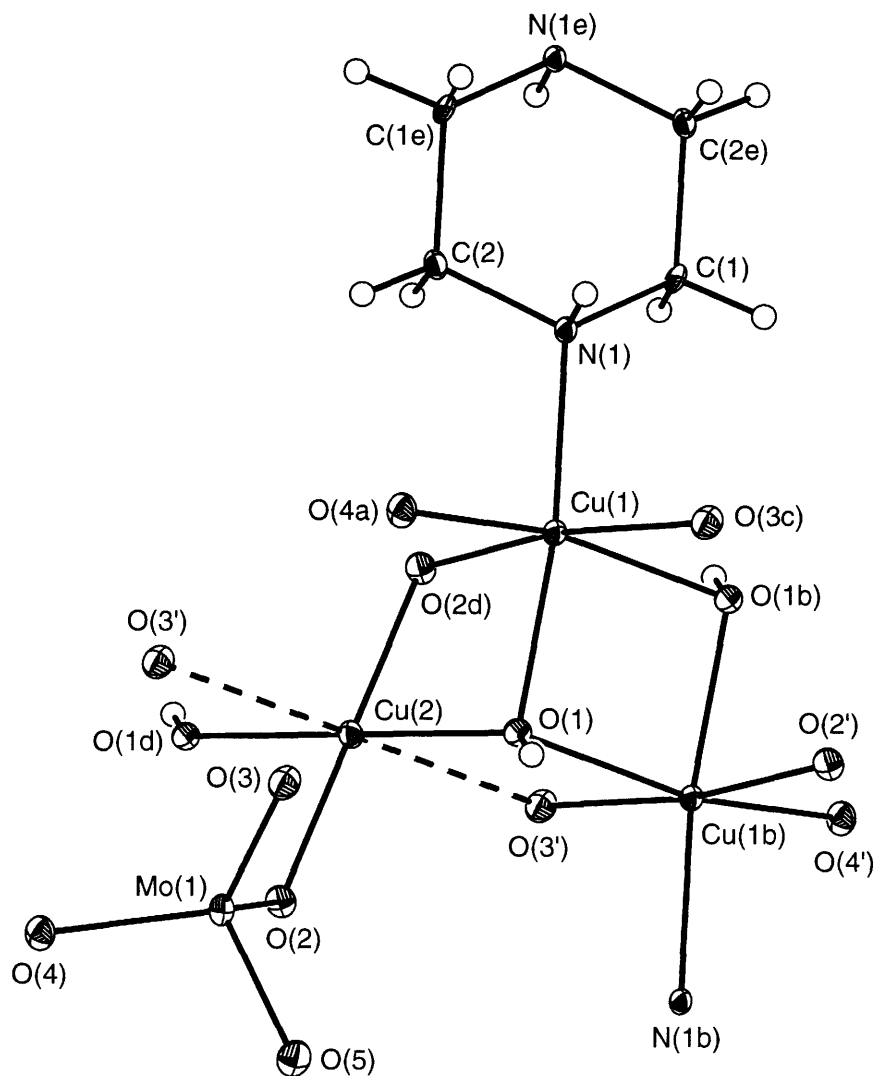


Figure A.11. A portion of the crystal structure of $(\text{pip})\text{Cu}_3(\text{OH})_2(\text{MoO}_4)_2$, rendered with 40% thermal ellipsoids. One inversion center is located at the center of the piperazine ring, the other is located on Cu(2). Atoms labeled with letters correspond to symmetry equivalent atoms as found in Tables A.28 and A.29. Hydrogen atoms are not labeled.

Table A.26. Crystal data and structure refinement for (pip)Cu₃(OH)₂(MoO₄)₂.

Identification code	c04046a	
Empirical formula	C ₄ H ₁₂ Cu ₃ Mo ₂ N ₂ O ₁₀	
Formula weight	630.66	
Temperature	150(2) K	
Wavelength	0.71073 Å	
Crystal system	Triclinic	
Space group	<i>P</i> $\bar{1}$	
Unit cell dimensions	$a = 5.6757(15)$ Å	$\alpha = 95.284(5)^\circ$
	$b = 5.7121(15)$ Å	$\beta = 91.557(5)^\circ$
	$c = 9.447(2)$ Å	$\gamma = 100.248(5)^\circ$
Volume, <i>Z</i>	299.82(14) Å ³	1
Density (calculated)	3.493 g/cm ³	
Absorption coefficient	7.324 mm ⁻¹	
F(000)	301	
Crystal size	0.10 × 0.05 × 0.05 mm	
θ range for data collection	2.17 to 28.33°	
Limiting indices	$-4 \leq h \leq 7$ $-7 \leq k \leq 7$ $-12 \leq l \leq 12$	
Reflections collected	2494	
Independent reflections	1459 ($R_{\text{int}} = 0.0296$)	
Completeness to $\theta = 25.00^\circ$	99.3 %	
Absorption correction	Semi-empirical from equivalents	
Max. and min. transmission	0.7109	0.5279
Refinement method	Full-matrix least-squares on F^2	
Data / restraints / parameters	1459 / 1 / 100	
Goodness-of-fit on F^2	1.076	
Final <i>R</i> indices [$I > 2\sigma(I)$]	$R_1 = 0.0337$	$wR_2 = 0.0814$
<i>R</i> indices (all data)	$R_1 = 0.0394$	$wR_2 = 0.0836$
Largest diff. peak and hole	1.350 eÅ ⁻³	-1.077 eÅ ⁻³

Appendix A

Table A.27. Atomic coordinates ($\times 10^4$) and equivalent isotropic displacement parameters ($\text{\AA}^2 \times 10^3$) for $(\text{pip})\text{Cu}_3(\text{OH})_2(\text{MoO}_4)_2$. $U(\text{eq})$ is defined as one third of the trace of the orthogonalized U_{ij} tensor.

	x	y	z	$U(\text{eq})$
Cu(1)	-1229(1)	355(1)	1423(1)	9(1)
Cu(2)	0	5000	0	10(1)
Mo(1)	-4705(1)	5565(1)	-1886(1)	10(1)
O(1)	-1244(6)	1481(6)	-525(4)	9(1)
O(2)	-1469(6)	5978(6)	-1663(4)	12(1)
O(3)	-6396(6)	3389(6)	-906(4)	14(1)
O(4)	-5757(6)	8335(6)	-1752(4)	13(1)
O(5)	-5318(6)	4358(6)	-3618(4)	14(1)
N(1)	-925(7)	-183(7)	3500(4)	9(1)
C(1)	1049(8)	-1392(9)	3934(5)	11(1)
C(2)	-900(9)	1975(8)	4510(5)	12(1)

Table A.28. Bond lengths (\AA) for $(\text{pip})\text{Cu}_3(\text{OH})_2(\text{MoO}_4)_2$.

Cu(1)–O(1)	2.005(3)	O(1)–Cu(1) ^b	2.053(3)
Cu(1)–O(4) ^a	2.006(3)	O(1)–H(1)	0.835(10)
Cu(1)–N(1)	2.022(4)	O(2)–Cu(1) ^d	2.353(3)
Cu(1)–O(1) ^b	2.053(3)	O(3)–Cu(1) ^c	2.319(3)
Cu(1)–O(3) ^c	2.319(3)	O(4)–Cu(1) ^a	2.006(3)
Cu(1)–O(2) ^d	2.353(3)	N(1)–C(1)	1.484(6)
Cu(2)–O(2) ^d	1.932(3)	N(1)–C(2)	1.486(6)
Cu(2)–O(2)	1.932(3)	N(1)–H(1A)	0.9300
Cu(2)–O(1) ^d	2.019(3)	C(1)–C(2) ^e	1.538(7)
Cu(2)–O(1)	2.019(3)	C(1)–H(1B)	0.9900
Mo(1)–O(5)	1.718(4)	C(1)–H(1C)	0.9900
Mo(1)–O(3)	1.777(3)	C(2)–C(1) ^e	1.538(7)
Mo(1)–O(4)	1.783(3)	C(2)–H(2A)	0.9900
Mo(1)–O(2)	1.813(3)	C(2)–H(2B)	0.9900

Symmetry transformations used to generate equivalent atoms:

^a $-x - 1, -y + 1, -z$ ^b $-x, -y, -z$ ^c $-x - 1, -y, -z$ ^d $-x, -y + 1, -z$ ^e $-x, -y, -z + 1$

Appendix A

Table A.29. Bond angles (°) for (pip)Cu₃(OH)₂(MoO₄)₂.

O(1)–Cu(1)–O(4) ^a	87.97(14)	Cu(1)–O(1)–Cu(1) ^b	99.16(14)
O(1)–Cu(1)–N(1)	169.89(15)	Cu(2)–O(1)–Cu(1) ^b	114.31(15)
O(4) ^a –Cu(1)–N(1)	90.94(15)	Cu(1)–O(1)–H(1)	103(4)
O(1)–Cu(1)–O(1) ^b	80.84(14)	Cu(2)–O(1)–H(1)	133(4)
O(4) ^a –Cu(1)–O(1) ^b	162.08(14)	Cu(1) ^b –O(1)–H(1)	102(4)
N(1)–Cu(1)–O(1) ^b	102.48(14)	Mo(1)–O(2)–Cu(2)	120.36(18)
O(1)–Cu(1)–O(3) ^c	98.85(13)	Mo(1)–O(2)–Cu(1) ^d	126.52(17)
O(4) ^a –Cu(1)–O(3) ^c	87.94(13)	Cu(2)–O(2)–Cu(1) ^d	90.71(12)
N(1)–Cu(1)–O(3) ^c	91.15(15)	Mo(1)–O(3)–Cu(1) ^c	136.41(19)
O(1) ^b –Cu(1)–O(3) ^c	80.07(12)	Mo(1)–O(4)–Cu(1) ^a	140.6(2)
O(1)–Cu(1)–O(2) ^d	75.74(13)	C(1)–N(1)–C(2)	108.6(4)
O(4) ^a –Cu(1)–O(2) ^d	97.62(13)	C(1)–N(1)–Cu(1)	117.1(3)
N(1)–Cu(1)–O(2) ^d	94.46(14)	C(2)–N(1)–Cu(1)	114.8(3)
O(1) ^b –Cu(1)–O(2) ^d	93.16(13)	C(1)–N(1)–H(1A)	105.0
O(3) ^c –Cu(1)–O(2) ^d	172.02(12)	C(2)–N(1)–H(1A)	105.0
O(2) ^d –Cu(2)–O(2)	180.0	Cu(1)–N(1)–H(1A)	105.0
O(2) ^d –Cu(2)–O(1) ^d	94.25(14)	N(1)–C(1)–C(2) ^e	112.0(4)
O(2)–Cu(2)–O(1) ^d	85.75(14)	N(1)–C(1)–H(1B)	109.2
O(2) ^d –Cu(2)–O(1)	85.75(14)	C(2) ^e –C(1)–H(1B)	109.2
O(2)–Cu(2)–O(1)	94.25(14)	N(1)–C(1)–H(1C)	109.2
O(1) ^d –Cu(2)–O(1)	180.00(19)	C(2) ^e –C(1)–H(1C)	109.2
O(5)–Mo(1)–O(3)	102.89(16)	H(1B)–C(1)–H(1C)	107.9
O(5)–Mo(1)–O(4)	105.99(16)	N(1)–C(2)–C(1) ^e	112.5(4)
O(3)–Mo(1)–O(4)	113.06(16)	N(1)–C(2)–H(2A)	109.1
O(5)–Mo(1)–O(2)	104.36(16)	C(1) ^e –C(2)–H(2A)	109.1
O(3)–Mo(1)–O(2)	116.77(15)	N(1)–C(2)–H(2B)	109.1
O(4)–Mo(1)–O(2)	112.27(15)	C(1) ^e –C(2)–H(2B)	109.1
Cu(1)–O(1)–Cu(2)	99.13(15)	H(2A)–C(2)–H(2B)	107.8

Symmetry transformations used to generate equivalent atoms:

^a –x – 1, –y + 1, –z ^b –x, –y, –z ^c –x – 1, –y, –z ^d –x, –y + 1, –z ^e –x, –y, –z + 1

Appendix A

Table A.30. Anisotropic displacement parameters ($\text{\AA}^2 \times 10^3$) for (pip)Cu₃(OH)₂(MoO₄)₂. The anisotropic displacement factor exponent takes the form: $-2\pi^2[(ha^*)^2U_{11} + \dots + 2hka^*b^*U_{12}]$.

	U ₁₁	U ₂₂	U ₃₃	U ₂₃	U ₁₃	U ₁₂
Cu(1)	10(1)	9(1)	8(1)	0(1)	0(1)	4(1)
Cu(2)	13(1)	8(1)	9(1)	0(1)	-2(1)	3(1)
Mo(1)	9(1)	9(1)	12(1)	0(1)	0(1)	3(1)
O(1)	9(1)	9(2)	9(2)	0(1)	-1(1)	1(1)
O(2)	11(2)	11(2)	13(2)	0(1)	-2(1)	2(1)
O(3)	14(2)	12(2)	14(2)	0(1)	2(1)	2(1)
O(4)	12(2)	14(2)	14(2)	0(1)	-2(1)	5(1)
O(5)	13(2)	15(2)	14(2)	-2(1)	-3(1)	3(1)
N(1)	10(2)	9(2)	8(2)	0(2)	-1(2)	5(2)
C(1)	14(2)	13(2)	10(2)	-1(2)	4(2)	9(2)
C(2)	18(2)	8(2)	10(2)	0(2)	-4(2)	6(2)

Table A.31. Hydrogen coordinates ($\times 10^4$) and isotropic displacement parameters ($\text{\AA}^2 \times 10^3$) for (pip)Cu₃(OH)₂(MoO₄)₂.

	<i>x</i>	<i>y</i>	<i>z</i>	U(eq)
H(1)	-2530(60)	710(90)	-900(50)	11
H(1A)	-2325	-1220	3670	10
H(1B)	2605	-347	3813	14
H(1C)	980	-2891	3306	14
H(2A)	-2272	2738	4263	14
H(2B)	590	3135	4409	14

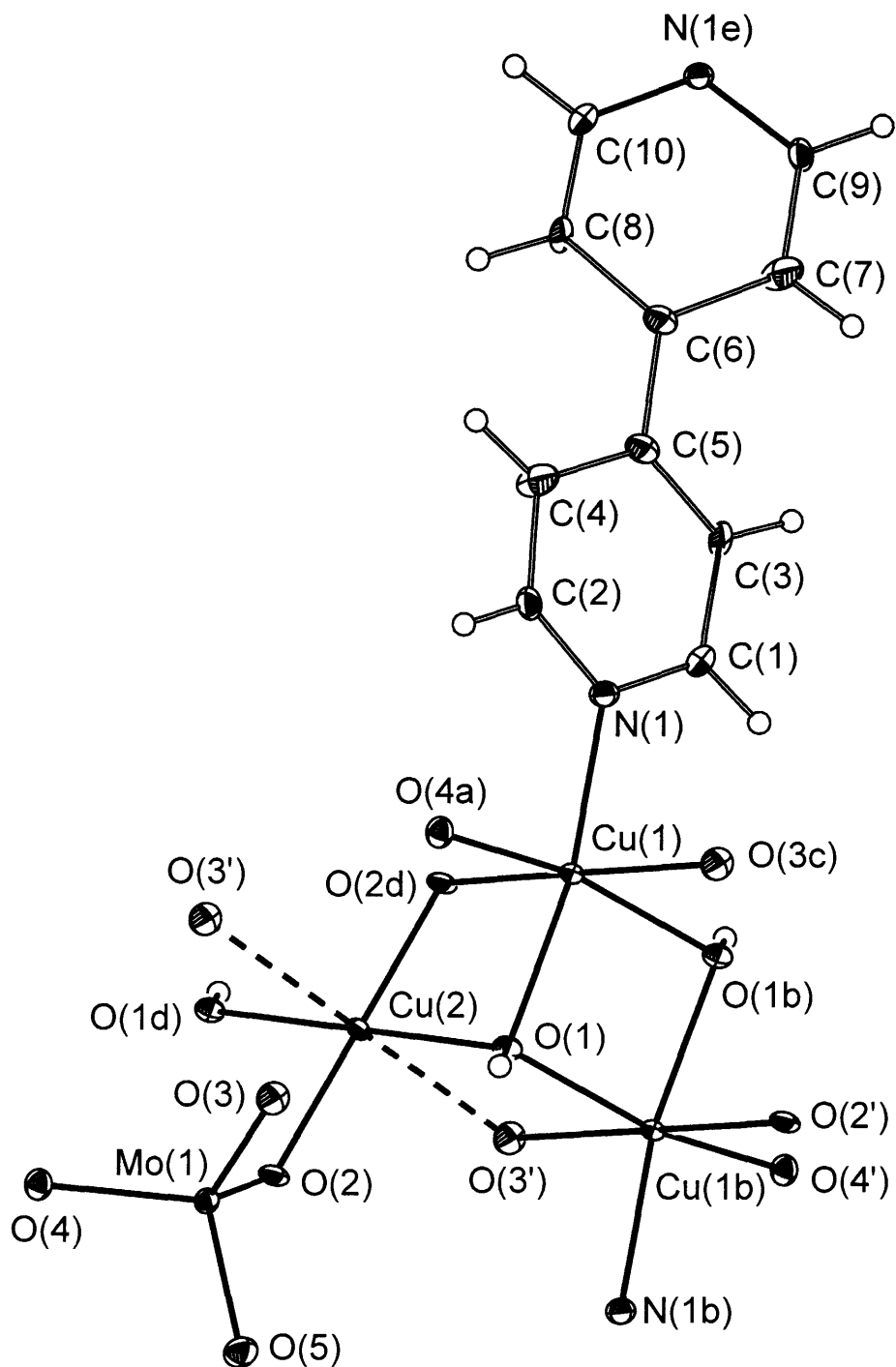


Figure A.12. A portion of the crystal structure of $(\text{bipy})\text{Cu}_3(\text{OH})_2(\text{MoO}_4)_2$, rendered with 40% thermal ellipsoids. Inversion centers are located between C(5) and C(6) (symmetry equivalent atoms) and on Cu(2). Only one orientation of the bipyridine ligand is shown for clarity. Atoms labeled with letters correspond to symmetry equivalent atoms as found in Tables A.34 and A.35. Hydrogen atoms are not labeled.

Table A.32. Crystal data and structure refinement for (bipy)Cu₃(OH)₂(MoO₄)₂.

Identification code	c04077a	
Empirical formula	C ₁₀ H ₁₀ Cu ₃ Mo ₂ N ₂ O ₁₀	
Formula weight	700.70	
Temperature	150(2) K	
Wavelength	0.71073 Å	
Crystal system	Triclinic	
Space group	<i>P</i> $\bar{1}$	
Unit cell dimensions	<i>a</i> = 5.5199(9) Å	α = 83.015(3)°
	<i>b</i> = 5.6912(10) Å	β = 85.442(3)°
	<i>c</i> = 13.456(2) Å	γ = 79.488(3)°
Volume, <i>Z</i>	411.82(12) Å ³	1
Density (calculated)	2.825 g/cm ³	
Absorption coefficient	5.348 mm ⁻¹	
F(000)	335	
Crystal size	0.09 × 0.04 × 0.04 mm	
θ range for data collection	1.53 to 24.75°	
Limiting indices	-6 ≤ <i>h</i> ≤ 6	
	-6 ≤ <i>k</i> ≤ 6	
	-15 ≤ <i>l</i> ≤ 15	
Reflections collected	2670	
Independent reflections	1413 (<i>R</i> _{int} = 0.0277)	
Completeness to θ = 24.75°	99.5 %	
Absorption correction	Semi-empirical from equivalents	
Refinement method	Full-matrix least-squares on <i>F</i> ²	
Data / restraints / parameters	1413 / 1 / 142	
Goodness-of-fit on <i>F</i> ²	1.085	
Final <i>R</i> indices [<i>I</i> > 2σ(<i>I</i>)]	<i>R</i> ₁ = 0.0292	<i>wR</i> ₂ = 0.0711
<i>R</i> indices (all data)	<i>R</i> ₁ = 0.0322	<i>wR</i> ₂ = 0.0726
Largest diff. peak and hole	1.140 eÅ ⁻³	-0.799 eÅ ⁻³

Appendix A

Table A.33. Atomic coordinates ($\times 10^4$) and equivalent isotropic displacement parameters ($\text{\AA}^2 \times 10^3$) for $(\text{bipy})\text{Cu}_3(\text{OH})_2(\text{MoO}_4)_2$. U(eq) is defined as one third of the trace of the orthogonalized U_{ij} tensor.

	<i>x</i>	<i>y</i>	<i>z</i>	U(eq)
Cu(1)	1511(1)	-4744(1)	-993(1)	9(1)
Cu(2)	0	0	0	9(1)
Mo(1)	4368(1)	686(1)	1489(1)	9(1)
O(1)	1204(6)	-3547(6)	349(2)	10(1)
O(2)	1210(6)	903(6)	1180(2)	11(1)
O(3)	6354(6)	-1432(6)	828(2)	14(1)
O(4)	5362(6)	3543(6)	1267(2)	12(1)
O(5)	4543(6)	-261(6)	2741(2)	16(1)
N(1)	1052(7)	-4945(7)	-2448(3)	12(1)
C(1)	-640(40)	-6010(30)	-2731(19)	18(3)
C(2)	2450(30)	-4010(20)	-3169(12)	20(3)
C(3)	-1090(40)	-6060(30)	-3740(20)	20(4)
C(4)	2100(30)	-3850(40)	-4187(17)	27(4)
C(5)	200(700)	-5000(700)	-4500(300)	16(1)
C(6)	-200(700)	-5000(700)	-5500(300)	16(1)
C(7)	-1140(30)	-6920(40)	-5858(17)	27(4)
C(8)	360(40)	-3190(40)	-6290(20)	20(4)
C(9)	-1570(30)	-6940(20)	-6844(12)	20(3)
C(10)	-140(40)	-3250(40)	-7242(18)	18(3)

Appendix A

Table A.34. Bond lengths (Å) for (bipy)Cu₃(OH)₂(MoO₄)₂.

Cu(1)–O(4) ^a	1.962(3)	N(1)–C(2)	1.316(17)
Cu(1)–O(1)	1.991(3)	C(1)–C(3)	1.40(4)
Cu(1)–N(1)	2.013(4)	C(1)–H(1A)	0.9500
Cu(1)–O(1) ^b	2.016(3)	C(2)–C(4)	1.39(3)
Cu(1)–O(3) ^c	2.272(3)	C(2)–H(2)	0.9500
Cu(1)–O(2) ^d	2.413(3)	C(3)–C(5)	1.3(4)
Cu(1)–Cu(1) ^b	3.0487(11)	C(3)–H(3)	0.9500
Cu(2)–O(2)	1.929(3)	C(4)–C(5)	1.4(4)
Cu(2)–O(2) ^d	1.929(3)	C(4)–H(4)	0.9500
Cu(2)–O(1) ^d	2.017(3)	C(5)–C(6)	1.468(10)
Cu(2)–O(1)	2.017(3)	C(6)–C(7)	1.4(4)
Mo(1)–O(5)	1.710(3)	C(6)–C(8)	1.4(4)
Mo(1)–O(3)	1.752(3)	C(7)–C(9)	1.37(3)
Mo(1)–O(4)	1.793(3)	C(7)–H(7)	0.9500
Mo(1)–O(2)	1.803(3)	C(8)–C(10)	1.34(4)
O(1)–Cu(1) ^b	2.016(3)	C(8)–H(8)	0.9500
O(1)–H(1)	0.834(10)	C(9)–N(1) ^e	1.398(16)
O(2)–Cu(1) ^d	2.413(3)	C(9)–H(9)	0.9500
O(3)–Cu(1) ^c	2.272(3)	C(10)–N(1) ^e	1.34(2)
O(4)–Cu(1) ^a	1.962(3)	C(10)–H(10)	0.9500
N(1)–C(1)	1.31(3)		

Symmetry transformations used to generate equivalent atoms:

^a $-x + 1, -y, -z$ ^b $-x, -y - 1, -z$ ^c $-x + 1, -y - 1, -z$ ^d $-x, -y, -z$ ^e $-x, -y - 1, -z - 1$

Table A.35. Bond angles (°) for (bipy)Cu₃(OH)₂(MoO₄)₂.

O(4) ^a –Cu(1)–O(1)	88.94(13)	Cu(2)–O(2)–Cu(1) ^d	90.63(12)
O(4) ^a –Cu(1)–N(1)	94.07(15)	Mo(1)–O(3)–Cu(1) ^c	142.56(18)
O(1)–Cu(1)–N(1)	161.28(15)	Mo(1)–O(4)–Cu(1) ^a	137.48(18)
O(4) ^a –Cu(1)–O(1) ^b	163.14(13)	C(1)–N(1)–C(2)	116.2(13)
O(1)–Cu(1)–O(1) ^b	80.94(14)	C(2)–N(1)–C(10) ^e	110.5(12)
N(1)–Cu(1)–O(1) ^b	99.85(14)	C(1)–N(1)–C(9) ^e	112.2(13)
O(4) ^a –Cu(1)–O(3) ^c	89.50(13)	C(10) ^e –N(1)–C(9) ^e	118.8(13)
O(1)–Cu(1)–O(3) ^c	107.48(12)	C(1)–N(1)–Cu(1)	122.2(11)
N(1)–Cu(1)–O(3) ^c	91.04(14)	C(2)–N(1)–Cu(1)	121.6(7)
O(1) ^b –Cu(1)–O(3) ^c	80.83(12)	C(10) ^e –N(1)–Cu(1)	122.6(11)
O(4) ^a –Cu(1)–O(2) ^d	97.46(12)	C(9) ^e –N(1)–Cu(1)	118.5(7)
O(1)–Cu(1)–O(2) ^d	74.51(12)	N(1)–C(1)–C(3)	123(2)
N(1)–Cu(1)–O(2) ^d	86.78(13)	N(1)–C(1)–H(1A)	118.3
O(1) ^b –Cu(1)–O(2) ^d	92.80(12)	C(3)–C(1)–H(1A)	118.3
O(3) ^c –Cu(1)–O(2) ^d	172.83(12)	N(1)–C(2)–C(4)	125.1(15)
O(4) ^a –Cu(1)–Cu(1) ^b	128.37(10)	N(1)–C(2)–H(2)	117.4
O(1)–Cu(1)–Cu(1) ^b	40.77(9)	C(4)–C(2)–H(2)	117.4
N(1)–Cu(1)–Cu(1) ^b	137.03(12)	C(5)–C(3)–C(1)	121(10)
O(1) ^b –Cu(1)–Cu(1) ^b	40.17(9)	C(5)–C(3)–H(3)	119.5
O(3) ^c –Cu(1)–Cu(1) ^b	95.21(9)	C(1)–C(3)–H(3)	119.5
O(2) ^d –Cu(1)–Cu(1) ^b	81.83(8)	C(2)–C(4)–C(5)	117(10)
O(2)–Cu(2)–O(2) ^d	180.00(9)	C(2)–C(4)–H(4)	121.6
O(2)–Cu(2)–O(1) ^d	85.83(13)	C(5)–C(4)–H(4)	121.6
O(2) ^d –Cu(2)–O(1) ^d	94.17(13)	C(3)–C(5)–C(4)	117(10)
O(2)–Cu(2)–O(1)	94.17(13)	C(3)–C(5)–C(6)	123(10)
O(2) ^d –Cu(2)–O(1)	85.83(13)	C(4)–C(5)–C(6)	120(10)
O(1) ^d –Cu(2)–O(1)	180.0(2)	C(7)–C(6)–C(8)	116(10)
O(5)–Mo(1)–O(3)	107.88(16)	C(7)–C(6)–C(5)	120(10)
O(5)–Mo(1)–O(4)	107.59(16)	C(8)–C(6)–C(5)	123(10)
O(3)–Mo(1)–O(4)	110.22(15)	C(9)–C(7)–C(6)	121(10)
O(5)–Mo(1)–O(2)	107.86(15)	C(9)–C(7)–H(7)	119.4
O(3)–Mo(1)–O(2)	111.32(15)	C(6)–C(7)–H(7)	119.4
O(4)–Mo(1)–O(2)	111.78(15)	C(10)–C(8)–C(6)	120(10)
Cu(1)–O(1)–Cu(1) ^b	99.06(14)	C(10)–C(8)–H(8)	119.8
Cu(1)–O(1)–Cu(2)	101.62(14)	C(6)–C(8)–H(8)	119.8
Cu(1) ^b –O(1)–Cu(2)	112.12(15)	C(7)–C(9)–N(1) ^e	119.8(15)
Cu(1)–O(1)–H(1)	102(4)	C(7)–C(9)–H(9)	120.1
Cu(1) ^b –O(1)–H(1)	115(4)	N(1) ^e –C(9)–H(9)	120.1
Cu(2)–O(1)–H(1)	122(4)	N(1) ^e –C(10)–C(8)	123(2)
Mo(1)–O(2)–Cu(2)	128.22(17)	N(1) ^e –C(10)–H(10)	118.4
Mo(1)–O(2)–Cu(1) ^d	120.88(16)	C(8)–C(10)–H(10)	118.4

Symmetry transformations used to generate equivalent atoms:

^a –x + 1, –y, –z ^b –x, –y – 1, –z ^c –x + 1, –y – 1, –z ^d –x, –y, –z ^e –x, –y – 1, –z – 1

Table A.36. Anisotropic displacement parameters ($\text{\AA}^2 \times 10^3$) for $(\text{bipy})\text{Cu}_3(\text{OH})_2(\text{MoO}_4)_2$. The anisotropic displacement factor exponent takes the form: $-2\pi^2[(\text{ha}^*)^2U_{11} + \dots + 2\text{hka}^*\text{b}^*U_{12}]$.

	U_{11}	U_{22}	U_{33}	U_{23}	U_{13}	U_{12}
Cu(1)	11(1)	9(1)	6(1)	-2(1)	-1(1)	-3(1)
Cu(2)	12(1)	7(1)	7(1)	-2(1)	-3(1)	-2(1)
Mo(1)	10(1)	9(1)	9(1)	0(1)	-2(1)	-2(1)
O(1)	9(2)	12(2)	8(2)	-1(1)	-4(1)	0(1)
O(2)	15(2)	12(2)	6(2)	-2(1)	-3(1)	0(1)
O(3)	14(2)	12(2)	16(2)	-1(1)	0(1)	1(1)
O(4)	12(2)	12(2)	14(2)	-1(1)	-2(1)	-4(1)
O(5)	18(2)	18(2)	12(2)	1(1)	-4(1)	-5(2)
N(1)	13(2)	12(2)	10(2)	-1(2)	0(2)	-2(2)
C(1)	25(11)	16(11)	14(3)	2(7)	1(7)	-9(6)
C(2)	38(9)	11(8)	14(3)	2(6)	-9(6)	-10(5)
C(3)	39(13)	12(11)	13(3)	9(8)	-17(8)	-13(7)
C(4)	26(11)	48(12)	14(4)	1(7)	-2(8)	-28(8)
C(5)	19(3)	19(3)	12(3)	-4(2)	-3(2)	-5(2)
C(6)	19(3)	19(3)	12(3)	-4(2)	-3(2)	-5(2)
C(7)	26(11)	48(12)	14(4)	1(7)	-2(8)	-28(8)
C(8)	39(13)	12(11)	13(3)	9(8)	-17(8)	-13(7)
C(9)	38(9)	11(8)	14(3)	2(6)	-9(6)	-10(5)
C(10)	25(11)	16(11)	14(3)	2(7)	1(7)	-9(6)

Appendix A

Table A.37. Hydrogen coordinates ($\times 10^4$) and isotropic displacement parameters ($\text{\AA}^2 \times 10^3$) for $(\text{bipy})\text{Cu}_3(\text{OH})_2(\text{MoO}_4)_2$.

	x	y	z	U(eq)
H(1)	2600(40)	-4070(90)	560(40)	12
H(1A)	-1606	-6806	-2229	22
H(2)	3811	-3383	-2978	24
H(3)	-2361	-6849	-3897	24
H(4)	3078	-3019	-4673	33
H(7)	-1458	-8219	-5384	33
H(8)	1097	-1921	-6115	24
H(9)	-2229	-8221	-7048	24
H(10)	159	-1956	-7723	22

Appendix A

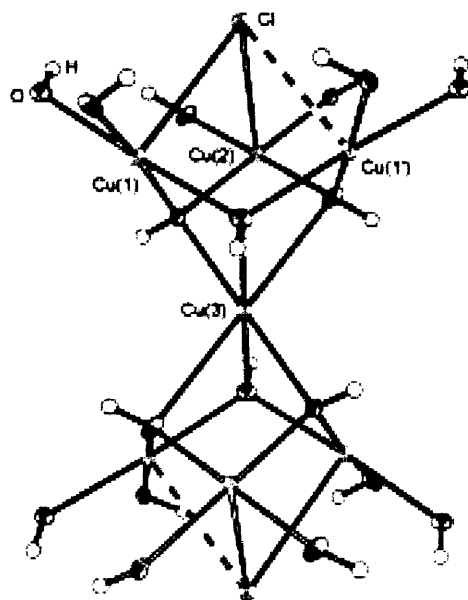


Figure A.13. Thermal ellipsoid plot for $\text{Cu}_2(\text{OH})_3\text{Cl}$. Ellipsoids shown at 50% probability.

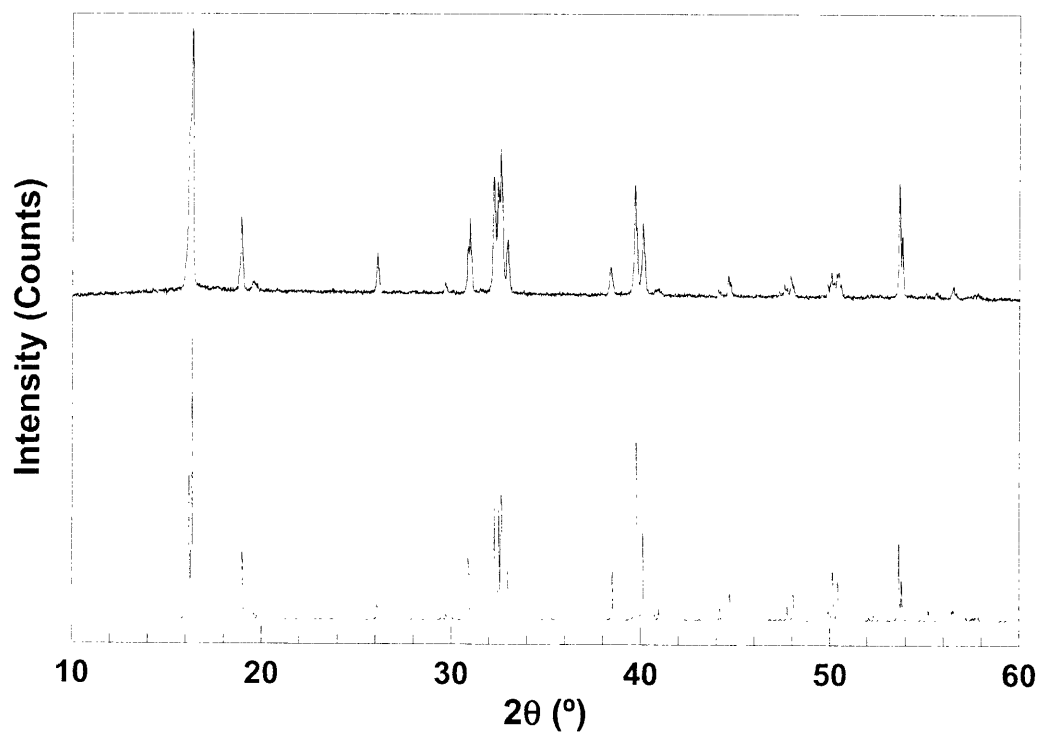


Figure A.14. Recorded (top) and simulated (bottom) pXRD pattern of $\text{Cu}_2(\text{OH})_3\text{Cl}$.

Table A.38. Crystal data and structure refinement for $\text{Cu}_2(\text{OH})_3\text{Cl}$.

Identification code	c0402a	
Empirical formula	$\text{H}_3\text{ClCu}_2\text{O}_3$	
Formula weight	213.55	
Temperature	150(2) K	
Wavelength	0.71073 Å	
Crystal system	Monoclinic	
Space group	$P2_1/n$	
Unit cell dimensions	$a = 6.1565(9)$ Å	$\alpha = 90^\circ$
	$b = 6.8128(11)$ Å	$\beta = 99.800(4)^\circ$
	$c = 9.1188(14)$ Å	$\gamma = 90^\circ$
Volume	376.94 Å ³	
Z	4	
Density (calculated)	3.763 Mg/m ³	
Absorption coefficient	11.819 mm ⁻¹	
F(000)	408	
Crystal size	$0.04 \times 0.02 \times 0.02$ mm ³	
Theta range for data collection	3.72 to 26.43° .	
Index ranges	$-7 \leq h \leq 7$	
	$-8 \leq k \leq 7$	
	$-11 \leq l \leq 10$	
Reflections collected	3798	
Independent reflections	784 [$R_{\text{int}} = 0.0493$]	
Completeness to theta = 26.43°	100.0 %	
Absorption correction	None	
Refinement method	Full-matrix least-squares on F^2	
Data / restraints / parameters	784 / 0 / 70	
Goodness-of-fit on F^2	1.123	
Final R indices [$I > 2\sigma(I)$]	$R_I = 0.0290$	$wR_2 = 0.0731$
R indices (all data)	$R_I = 0.0312$	$wR_2 = 0.0745$
Largest diff. peak and hole	1.068 eÅ ⁻³	-0.948 eÅ ⁻³

Appendix A

Table A.39. Atomic coordinates ($\times 10^4$) and equivalent isotropic displacement parameters ($\text{\AA}^2 \times 10^3$) for $\text{Cu}_2(\text{OH})_3\text{Cl}$. $U(\text{eq})$ is defined as one third of the trace of the orthogonalized U_{ij} tensor.

Atom	x	y	z	$U(\text{eq})$
Cu(1)	2406(1)	2354(1)	7516(1)	6(1)
Cu(2)	0	5000	10000	6(1)
Cu(3)	0	0	5000	6(1)
O(1)	1908(4)	2917(4)	9508(3)	10(1)
O(2)	2573(4)	1784(4)	5396(3)	7(2)
O(3)	780(5)	-194(4)	7240(3)	8(1)
Cl(1)	-1121(2)	5045(1)	6928(1)	8(1)

Table A.40. Anisotropic displacement parameters ($\text{\AA}^2 \times 10^3$) for $\text{Cu}_2(\text{OH})_3\text{Cl}$. The anisotropic displacement factor exponent takes the form: $-2\pi^2 [h^2 a^{*2} U_{11} + \dots + 2hka^* b^* U_{12}]$.

	U_{11}	U_{22}	U_{33}	U_{23}	U_{13}	U_{12}
Cu(1)	8(1)	6(1)	4(1)	-1(1)	3(1)	-1(1)
Cu(2)	7(1)	6(1)	6(1)	0(2)	3(1)	0(1)
Cu(3)	7(1)	7(1)	4(1)	0(1)	2(1)	-1(1)
O(1)	13(1)	10(1)	6(1)	4(1)	2(1)	4(1)
O(2)	10(1)	6(1)	6(1)	0(1)	1(1)	-1(1)
O(3)	6(1)	10(1)	9(1)	2(1)	4(1)	0(1)
Cl(1)	9(1)	9(1)	6(1)	0(1)	2(1)	-1(1)

Table A.41. Hydrogen coordinates ($\times 10^4$) and isotropic displacement parameters ($\text{\AA}^2 \times 10^3$) for $\text{Cu}_2(\text{OH})_3\text{Cl}$.

	x	y	z	$U(\text{eq})$
H(1)	2090(90)	1990(90)	100090(60)	31(16)
H(2)	2420(80)	2770(80)	4870(60)	15(13)
H(3)	-410(110)	-230(70)	7610(70)	27(16)

Appendix A

Table A.42. Bragg peaks and Miller indices for $\text{Cu}_2(\text{OH})_3\text{Cl}$.

2θ	d_{obs}	% I_{obs}	d_{calcd}	% I_{calcd}	Δd	hkl
16.192	5.4695	63.5	5.4791	49.11	-0.0096	-1 0 1
16.321	5.4265	100.0	5.4294	100.0	-0.0029	0 1 1
18.904	4.6907	27.9	4.6727	24.4	0.018	1 0 1
19.559	4.5349	3.8	4.5310	2.26	0.0039	1 1 0
26.081	3.4138	15.0	3.4148	5.15	-0.001	-1 1 2
29.662	3.0093	4.5	3.0050	2.07	0.0043	1 1 2
30.859	2.8953	16.0	2.8932	21.73	0.0021	-1 2 1
30.961	2.8860	28.7	2.8880	12.46	-0.002	-1 0 3
32.223	2.7758	43.6	2.7723	41.82	0.0035	-2 1 1
32.443	2.7574	41.9	2.7429	42.22	0.0145	1 2 1
32.601	2.7445	54.8	2.7420	37.23	0.0025	0 1 3
32.959	2.7154	19.8	2.7147	17.63	0.0007	0 2 2
35.702	2.5129	1.4	2.5208	0.08	-0.0079	2 1 1
37.864	2.3742	1.4	2.3642	0.09	0.01	1 1 3
38.399	2.3423	10.5	2.3363	17.49	0.006	2 0 2
39.680	2.2696	42.1	2.2655	63.13	0.0041	2 2 0
40.100	2.2468	26.6	2.2464	30.37	0.0004	0 0 4
40.922	2.2036	2.1	2.2020	2.45	0.0016	0 3 1
42.263	2.1367	1.7	2.1334	0.31	0.0033	2 2 1
44.075	2.0530	2.6	2.0490	4.44	0.004	-3 0 1
44.605	2.0298	7.8	2.0264	9.73	0.0034	1 2 3
47.301	1.9202	2.2	1.9268	0.43	-0.0066	2 2 2
47.579	1.9096	4.6	1.9047	5.44	0.0049	3 0 1
47.906	1.8973	8.2	1.8927	10.06	0.0046	2 1 3
49.858	1.8275	5.1	1.8264	3.16	0.0011	-3 0 3
50.197	1.8160	5.6	1.8184	16.94	-0.0024	-2 3 1
50.346	1.8110	9.2	1.8097	5.72	0.0013	0 3 3
50.455	1.8073	9.2	1.8090	9.41	-0.0017	-1 0 5
52.175	1.7517	1.5	1.7559	1.40	-0.0042	-3 2 1
53.663	1.7066	43.6	1.7074	27.88	-0.0008	-2 2 4
53.815	1.7021	23.2	1.7035	13.52	-0.0014	0 4 0
55.082	1.6659	1.9	1.6625	4.06	0.0034	3 2 1
57.268	1.6074	1.3	1.6097	1.49	-0.0023	-3 2 3
57.441	1.6030	1.9	1.6027	0.95	0.0003	-3 1 4
57.818	1.5934	2.1	1.5978	1.24	-0.0044	-1 2 5

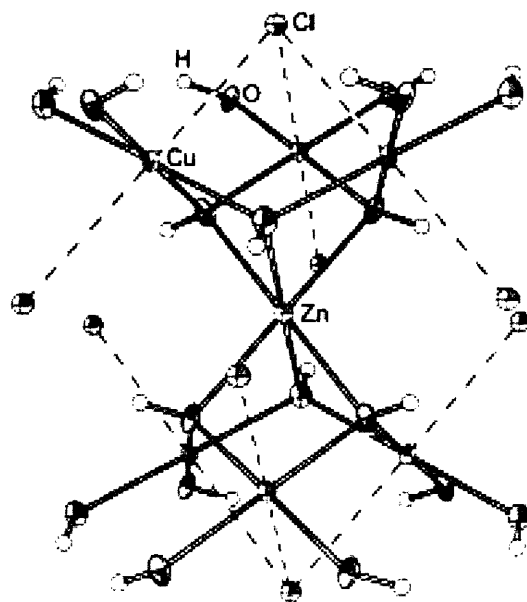


Figure A.15. Thermal ellipsoid plot for $\text{ZnCu}_3(\text{OH})_6\text{Cl}_2$. Ellipsoids shown at 50% probability.

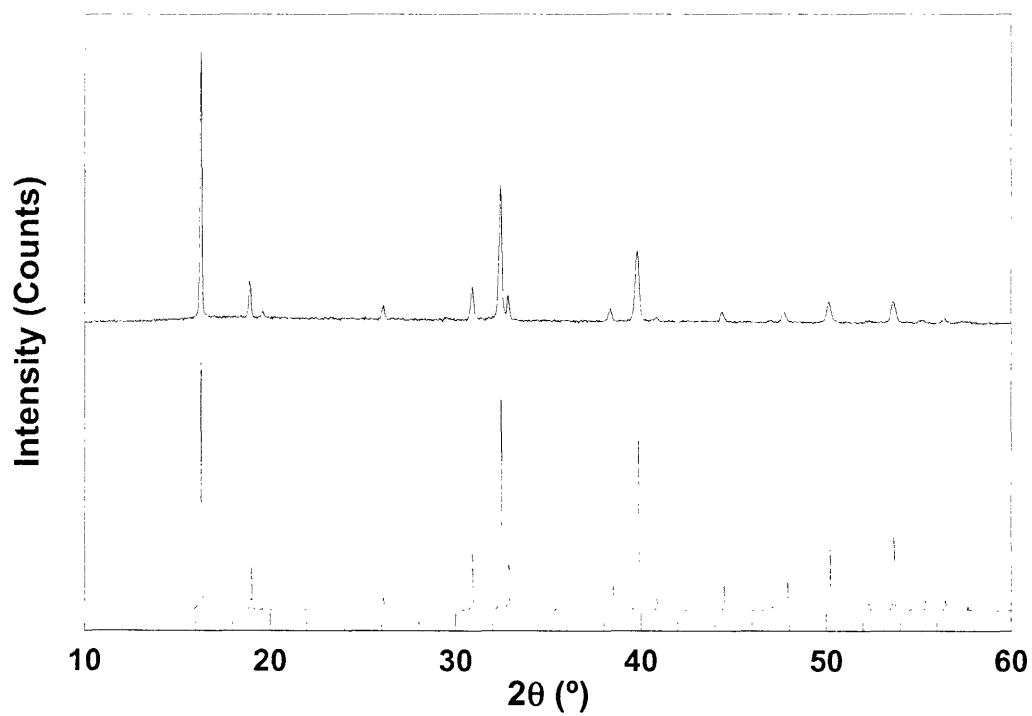


Figure A.16. Recorded (top) and simulated (bottom) pXRD pattern of $\text{ZnCu}_3(\text{OH})_6\text{Cl}_2$.

Table A.43. Crystal data and structure refinement for $\text{ZnCu}_3(\text{OH})_6\text{Cl}_2$.

Identification code	mps3a	
Empirical formula	$\text{H}_6\text{Cl}_2\text{Cu}_3\text{O}_6\text{Zn}$	
Formula weight	428.94	
Temperature	150(2) K	
Wavelength	0.71073 Å	
Crystal system	Rhombohedral	
Space group	$P2_1/n$	
Unit cell dimensions	$a = 6.8293(6)$ Å	$\alpha = 90^\circ$
	$b = 6.8293(6)$ Å	$\beta = 90^\circ$
	$c = 14.024(2)$ Å	$\gamma = 120^\circ$
Volume	$566.46(12)$ Å ³	
Z	3	
Density (calculated)	3.772 Mg/m ³	
Absorption coefficient	12.157 mm ⁻¹	
F(000)	615	
Crystal size	$0.04 \times 0.02 \times 0.02$ mm ³	
Theta range for data collection	3.74 to 24.70° .	
Index ranges	$-7 \leq h \leq 8$	
	$-7 \leq k \leq 7$	
	$-16 \leq l \leq 16$	
Reflections collected	1161	
Independent reflections	138 [$R_{\text{int}} = 0.0404$]	
Completeness to theta = 24.70°	100.0 %	
Refinement method	Full-matrix least-squares on F^2	
Data / restraints / parameters	138 / 1 / 19	
Goodness-of-fit on F^2	1.245	
Final R indices [$I > 2\sigma(I)$]	$R1 = 0.0205$	$wR2 = 0.0551$
R indices (all data)	$R1 = 0.0205$	$wR2 = 0.0551$
Largest diff. peak and hole	0.377 eÅ ⁻³	-0.775 eÅ ⁻³

Appendix A

Table A.44. Atomic coordinates ($\times 10^4$) and equivalent isotropic displacement parameters ($\text{\AA}^2 \times 10^3$) for $\text{ZnCu}_3(\text{OH})_6\text{Cl}_2$. $U(\text{eq})$ is defined as one third of the trace of the orthogonalized U_{ij} tensor.

Atom	x	y	z	$U(\text{eq})$
Cu(1)	8333	11667	1667	8(1)
O(1)	7466(6)	8733(3)	1054(2)	13(1)
Zn(1)	10000	10000	0	9(1)
Cl(1)	6667	3333	277(1)	10(1)

Table A.45. Anisotropic displacement parameters ($\text{\AA}^2 \times 10^3$) for $\text{ZnCu}_3(\text{OH})_6\text{Cl}_2$. The anisotropic displacement factor exponent takes the form: $-2\pi^2 [h^2 a^{*2} U_{11} + \dots + 2hka^* b^* U_{12}]$.

	U_{11}	U_{22}	U_{33}	U_{23}	U_{13}	U_{12}
Cu(1)	8(1)	8(1)	10(1)	0(1)	0(1)	4(1)
O(1)	8(2)	11(1)	18(2)	-3(1)	-5(2)	4(1)
Zn(1)	9(1)	9(1)	9(1)	0	0	4(1)
Cl(1)	10(1)	10(1)	9(1)	0	0	5(1)

Table A.46. Hydrogen coordinates ($\times 10^4$) and isotropic displacement parameters ($\text{\AA}^2 \times 10^3$) for $\text{ZnCu}_3(\text{OH})_3\text{Cl}_2$.

	x	y	z	$U(\text{eq})$
H(1)	6150(40)	8080(20)	850(40)	40(20)

Appendix A

Table A.47. Bragg peaks and Miller indices for $\text{ZnCu}_3(\text{OH})_6\text{Cl}_2$.

2θ	d_{obs}	% I_{obs}	d_{calcd}	% I_{calcd}	Δd	hkl
16.269	5.4439	100.0	5.4496	100.00	-0.0057	1 0 1
18.915	4.6879	13.4	4.6748	15.12	0.0131	0 0 3
19.609	4.5235	2.4	4.5210	2.06	0.0025	0 1 2
26.091	3.4125	4.7	3.4147	5.25	-0.0022	1 1 0
29.494	3.0261	0.9	3.0160	1.58	0.0101	1 0 4
30.899	2.8916	12.4	2.8936	21.77	-0.002	0 2 1
32.412	2.7600	50.6	2.7574	76.94	0.0026	1 1 3
32.846	2.7245	8.6	2.7248	17.24	-0.0003	2 0 2
38.346	2.3454	4.6	2.3374	10.55	0.008	0 0 6
39.800	2.2630	26.4	2.2605	61.42	0.0025	0 2 4
40.845	2.2075	1.2	2.2076	4.26	-1×10^{-4}	2 1 1
44.400	2.0387	2.7	2.0351	8.89	0.0036	2 0 5
47.705	1.9048	3.6	1.8976	10.12	0.0072	1 0 7
50.148	1.8176	7.6	1.8165	17.19	0.0011	0 3 3
52.156	1.7523	0.9	1.7482	3.55	0.0041	1 2 5
53.608	1.7082	7.8	1.7073	25.36	0.0009	2 2 0
55.150	1.6640	1.1	1.6587	3.57	0.0053	0 2 7
56.432	1.6292	1.6	1.6292	5.52	0	1 3 1
57.345	1.6054	0.9	1.6037	2.40	0.0017	2 2 3

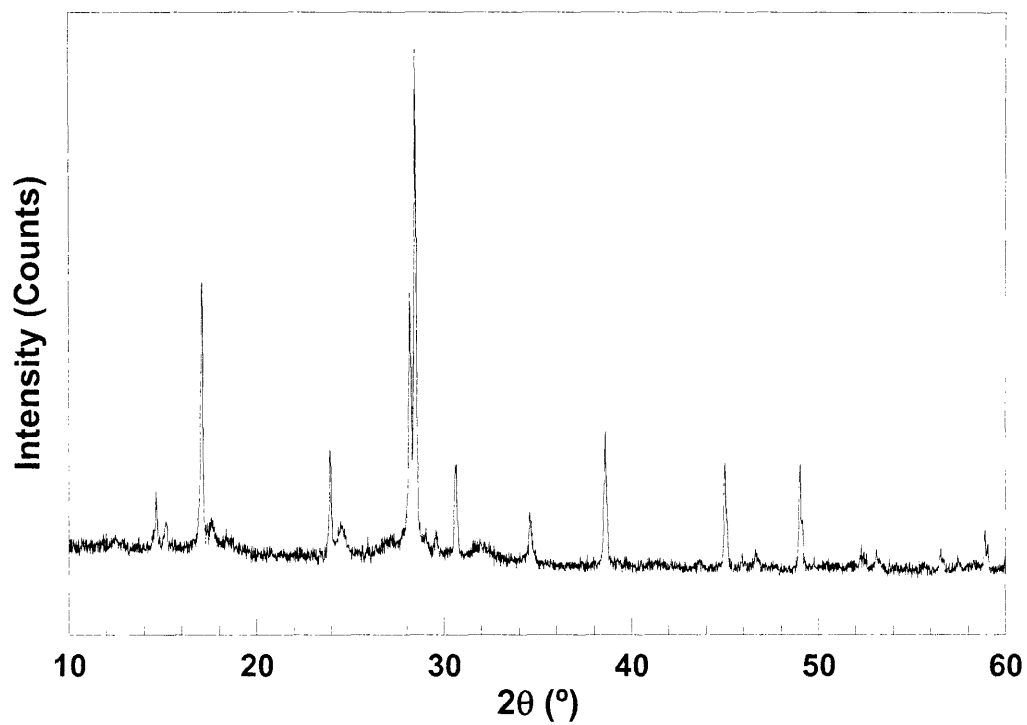


Figure A.17. X-ray powder pattern of $\text{KFe}_3(\text{OH})_6(\text{CrO}_4)_2$.

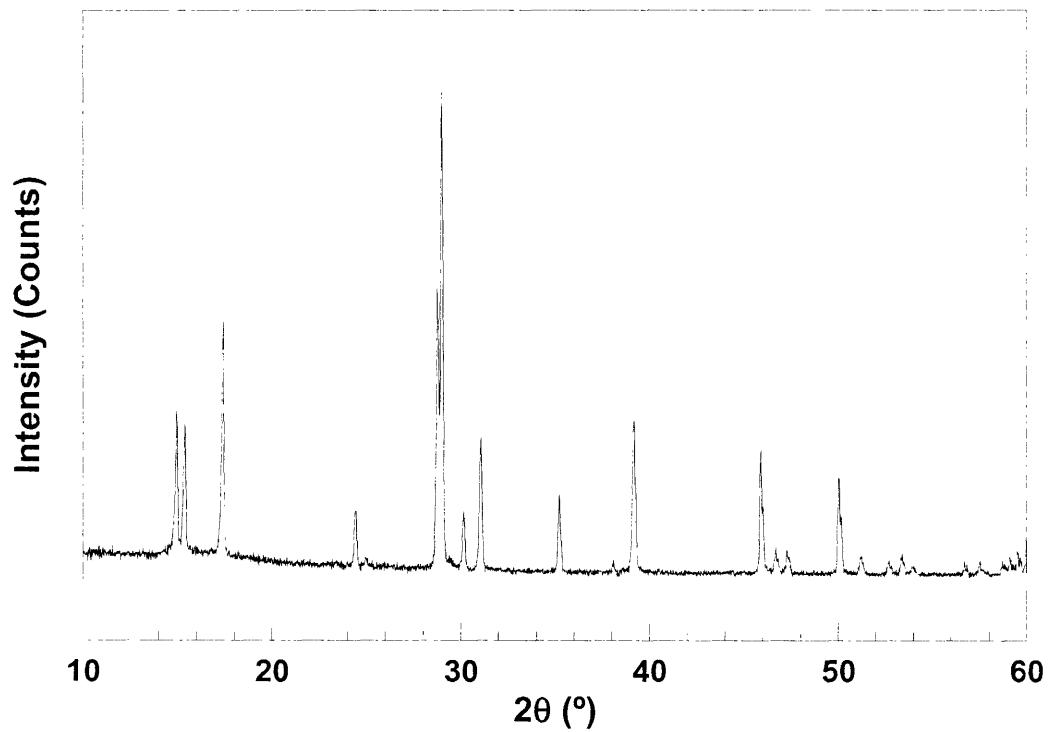


Figure A.18. X-ray powder pattern of $\text{KFe}_{3-x}\text{V}_x(\text{OH})_6(\text{SO}_4)_2$.

Appendix A

Table A.48. Bragg peaks and Miller indices for $\text{KFe}_3(\text{OH})_6(\text{CrO}_4)_2$.^a

2θ	d_{obs}	% I_{obs}	d_{calcd}	% I_{calcd}	Δd	hkl
14.639	6.0463	11.0	6.0318	12.0	0.0145	1 0 1
15.141	5.8470	5.1	5.8124	8.0	0.0346	0 0 3
17.080	5.1872	52.7	5.1740	35.0	0.0132	1 0 2
23.924	3.7166	21.6	3.7169	10.0	-0.0003	1 1 0
24.463	3.6359	6.6	3.6171	2.0	0.0188	1 0 4
28.164	3.1659	51.5	3.1678	100.0	-0.0019	2 0 1
28.444	3.1354	100.0	3.1279	100.0	0.0075	1 1 3
29.562	3.0193	4.7	3.0180	8.0	0.0013	2 0 2
30.585	2.9206	18.1	2.9062	16.0	0.0144	0 0 6
34.563	2.5930	10.5	2.5866	8.0	0.0064	2 0 4
38.598	2.3307	27.0	2.3238	20.0	0.0069	1 0 7
44.982	2.0137	21.3	2.0122	25.0	0.0015	3 0 3
45.918	1.9747	2.9	1.9702	4.0	0.0045	2 0 7
46.678	1.9444	2.9	1.9372	4.0	0.0072	0 0 9
48.998	1.8576	21.1	1.8573	25.0	0.0003	2 2 0
52.273	1.7486	4.8	1.7494	6.0	-0.0008	3 1 2
53.083	1.7239	4.2	1.7194	4.0	0.0045	1 1 9
56.536	1.6265	4.2	1.6235	4.0	0.003	2 1 8

^a Peak assignments based on PDF #00-020-0894 (Potassium Iron Chromium Oxide Hydroxide) in $R\bar{3}m$ symmetry.

Appendix A

Table A.49. Bragg peaks and Miller indices for $\text{KFe}_{3-x}\text{V}_x(\text{OH})_6(\text{CrO}_4)_2$.^a

2θ	d_{obs}	% I_{obs}	d_{calcd}	% I_{calcd}	Δd	hkl
14.942	5.9242	29.7	5.9379	45.0	-0.0137	1 0 1
15.380	5.7565	26.7	5.7274	25.0	0.0291	0 0 3
17.415	5.0882	49.9	5.0958	70.0	-0.0076	0 1 2
24.422	3.6418	11.5	3.6530	40.0	-0.0112	1 1 0
24.949	3.5662	1.8	3.5528	4.0	0.0134	1 0 4
28.761	3.1015	58.5	3.1121	75.0	-0.0106	0 1 2
28.982	3.0783	100.0	3.0821	100.0	-0.0038	1 1 3
29.381	3.0375	2.3	3.0220	6.0	0.0155	0 1 5
30.143	2.9624	11.8	2.9669	15.0	-0.0045	2 0 2
31.042	2.8787	27.3	2.8628	30.0	0.0159	0 0 6
35.202	2.5474	16.6	2.5434	30.0	0.004	0 2 4
38.077	2.3614	2.7	2.3692	4.0	-0.0078	2 1 1
39.159	2.2986	32.0	2.3031	12.0	-0.0045	1 2 2
45.899	1.9755	25.9	1.9778	45.0	-0.0023	3 0 3
46.681	1.9442	5.0	1.9378	10.0	0.0064	0 2 7
47.296	1.9204	4.6	1.9098	8.0	0.0106	0 0 9
50.040	1.8213	20.2	1.8257	45.0	-0.0044	2 2 0
51.219	1.7821	3.7	1.7766	6.0	0.0055	2 0 8
52.695	1.7356	2.8	1.7386	6.0	-0.003	2 2 3
53.379	1.7150	4.1	1.7176	6.0	-0.0026	3 1 2
53.921	1.6990	1.7	1.6906	2.0	0.0084	1 1 9
56.691	1.6224	3.1	1.6215	6.0	0.0009	1 3 4
57.522	1.6009	3.0	1.5955	6.0	0.0054	1 2 8
59.116	1.5615	3.2	1.5605	6.0	0.001	3 1 5
59.502	1.5523	4.1	1.5525	6.0	-0.0002	0 4 2

^a Peak assignments based on PDF #00-022-0827 (Jarosite, syn) in $R\bar{3}m$ symmetry.

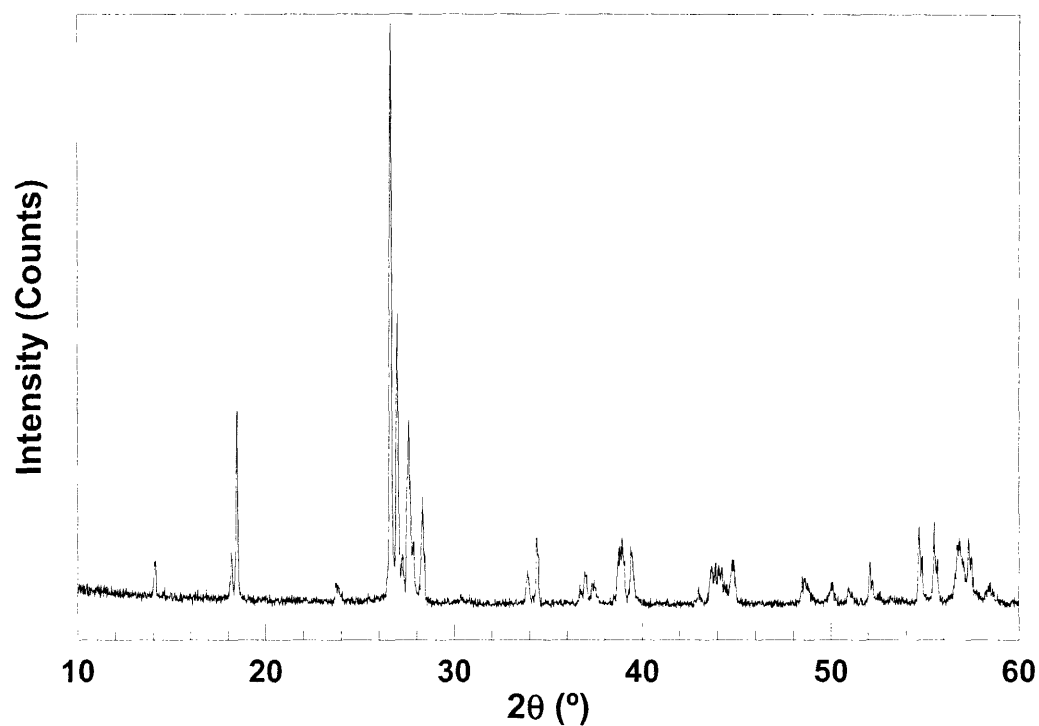


Figure A.19. X-ray powder pattern of $\text{Fe}^{2+}\text{Fe}_2^{3+}(\text{OH})_2(\text{PO}_4)_2$.

Appendix A

Table A.50. Bragg peaks and Miller indices for $\text{Fe}^{2+}\text{Fe}_2^{3+}(\text{OH})_2(\text{PO}_4)_2$.^a

2θ	d_{obs}	% I_{obs}	d_{calcd}	% I_{calcd}	Δd	hkl
14.037	6.3040	5.6	6.2926	12.6	0.0114	1 0 0
18.137	4.8873	10.9	4.9054	13.5	-0.0181	0 1 1
18.392	4.8199	27.1	4.8135	37.1	0.0064	1 1 0
23.709	3.7497	7.4	3.7539	2.9	-0.0042	-1 0 2
26.550	3.3546	100.0	3.3540	100.0	0.0006	-1 1 2
26.907	3.3108	57.9	3.3022	47.4	0.0086	1 1 1
27.180	3.2783	9.1	3.2668	14.6	0.0115	-2 1 1
27.490	3.2420	31.3	3.2388	31.5	0.0032	0 0 2
27.749	3.2123	11.7	3.2119	12.3	0.0004	1 2 0
28.255	3.1559	21.7	3.1395	28.4	0.0164	2 0 0
33.825	2.6479	8.7	2.6472	6.0	0.0007	-1 2 2
34.342	2.6091	12.8	2.6037	12.7	0.0054	-2 2 1
36.636	2.4509	3.0	2.4485	1.3	0.0024	0 2 2
36.900	2.4339	6.8	2.4292	7.6	0.0047	-2 2 2
37.274	2.4104	4.6	2.4027	2.4	0.0077	2 2 0
38.710	2.3242	22.1	2.3248	13.0	-0.0006	0 3 1
38.851	2.3161	13.6	2.3147	13.9	0.0014	1 3 0
39.371	2.2867	11.9	2.2747	7.3	0.012	2 1 1
42.947	2.1042	2.7	2.0914	3.4	0.0128	3 0 0
43.592	2.0648	9.0	2.0618	5.0	0.003	1 3 1
44.192	2.0478	9.2	2.0492	4.5	-0.0014	-3 1 3
44.722	2.0247	13.3	2.0337	2.8	-0.009	1 2 2
48.478	1.8763	6.9	1.8744	6.2	0.0019	-2 0 4
48.704	1.8681	3.6	1.8672	8.4	0.0009	0 4 0
49.026	1.8566	3.2	1.8506	0.4	0.006	-3 2 3
49.980	1.8234	7.8	1.8244	0.2	-0.001	3 2 0
50.877	1.7933	4.7	1.7922	1.2	0.0011	-1 4 1
51.552	1.7714	2.7	1.7628	1.2	0.0086	-4 1 2
52.021	1.7565	8.6	1.7532	3.3	0.0033	-1 4 1
54.648	1.6781	19.2	1.6750	11.8	0.0031	-2 2 4
55.455	1.6556	19.7	1.6600	0.6	-0.0044	-2 4 1
56.642	1.6237	16.9	1.6239	2.0	-0.0002	-1 2 4
57.302	1.6065	11.3	1.6119	10.0	-0.0054	-3 2 4
58.377	1.5795	5.7	1.5747	2.2	0.0048	-4 2 1
58.846	1.5680	2.2	1.5680	7.9	0	4 0 0

^a Peak assignments based on PDF #01-085-1728 (Barbosalite) in $P2_1/n$ symmetry.

Appendix B. Magnetic Data

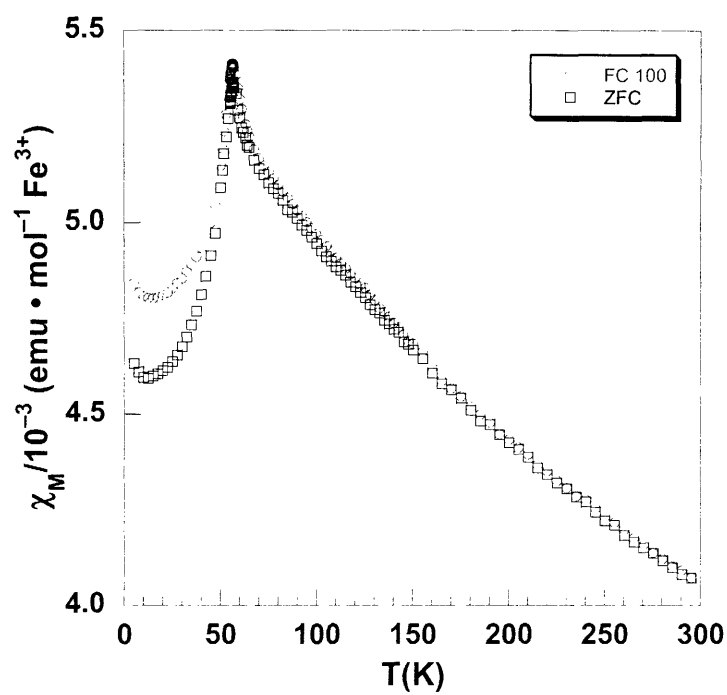


Figure B.1. ZFC and FC molar susceptibility for Pb_{0.5}Fe₃(OH)₆(SO₄)₂.

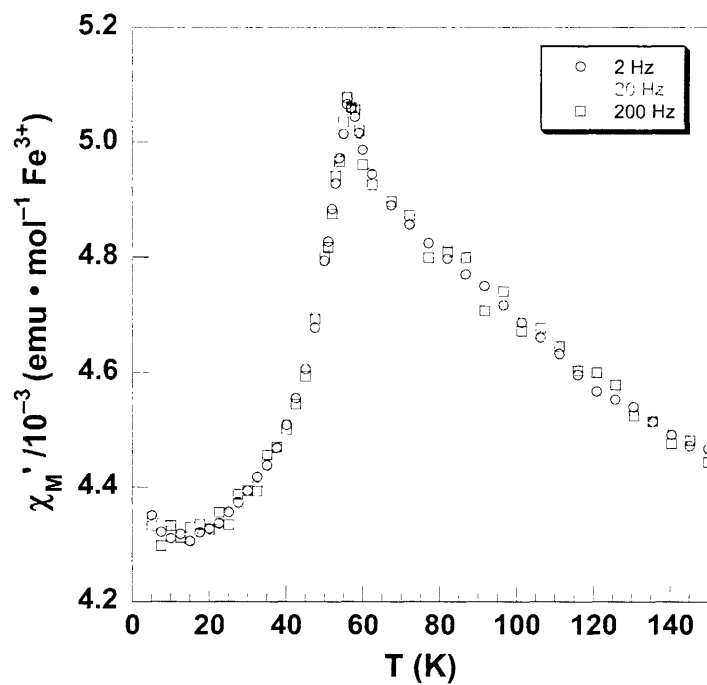


Figure B.2. AC Susceptibility of PbFe₃(OH)₆(SO₄)₂ measured under various frequencies.

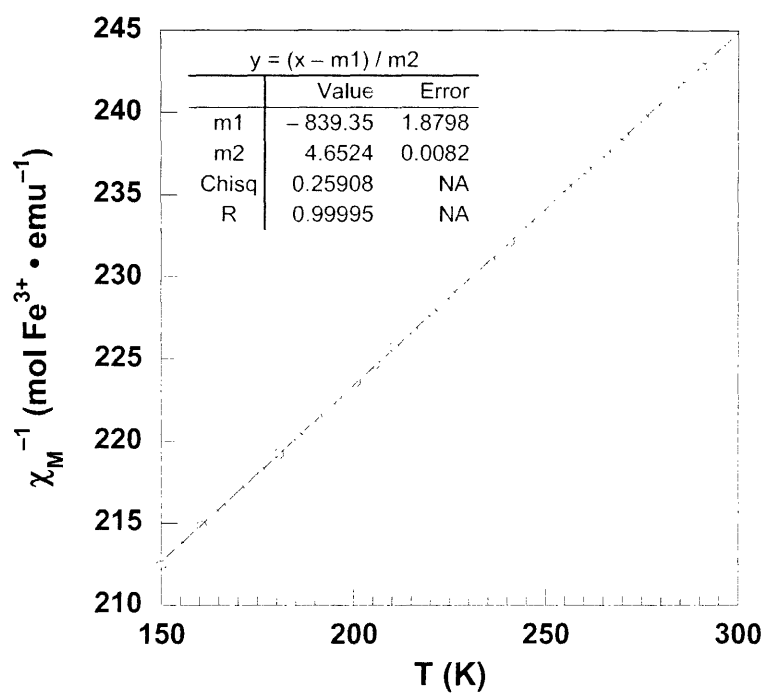


Figure B.3. Curie-Weiss plot for $\text{Pb}_{0.5}\text{Fe}_3(\text{OH})_6(\text{SO}_4)_2$.

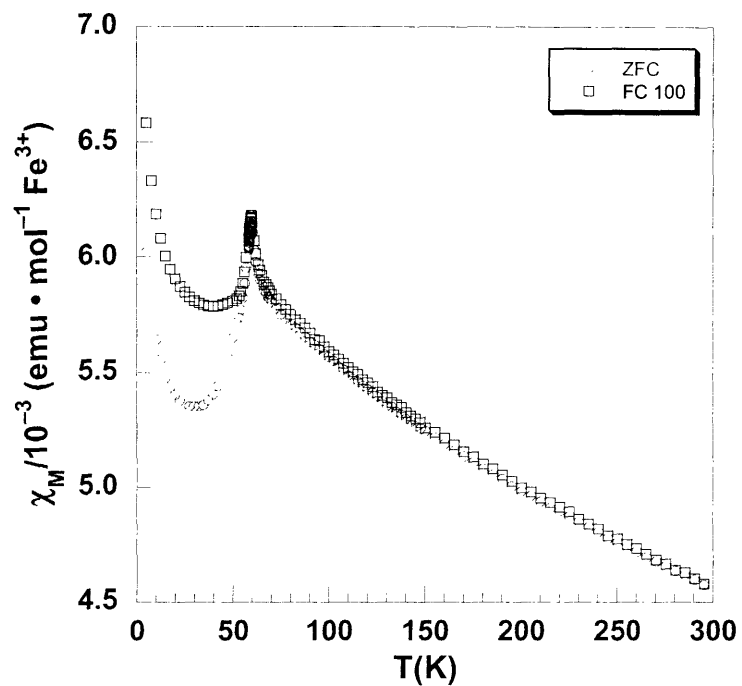


Figure B.4. ZFC and FC molar susceptibility for $\text{AgFe}_3(\text{OH})_6(\text{SO}_4)_2$.

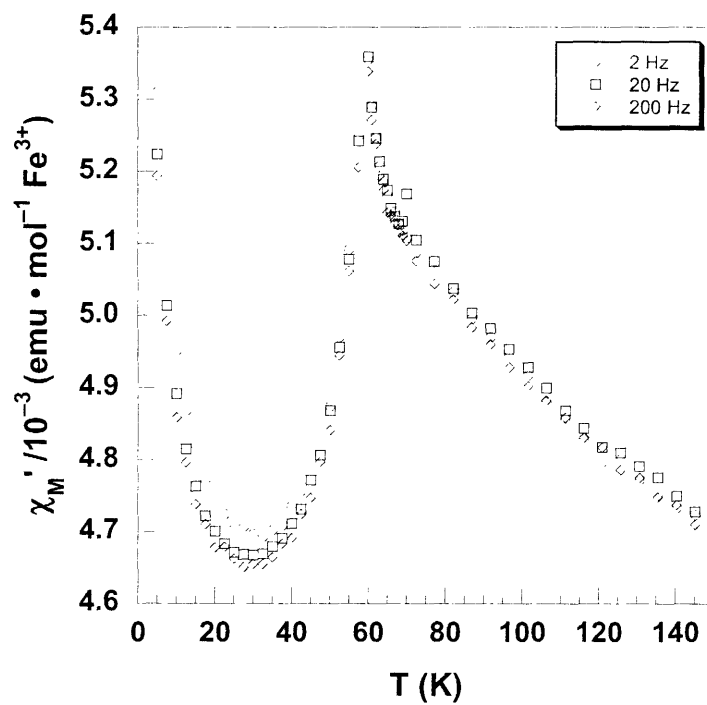


Figure B.5. AC Susceptibility of $\text{AgFe}_3(\text{OH})_6(\text{SO}_4)_2$ measured under various frequencies.

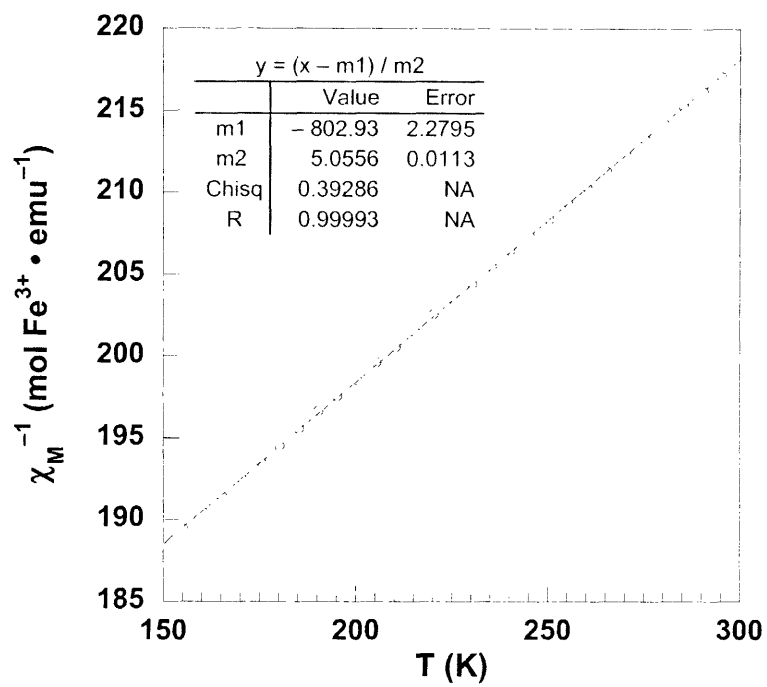


Figure B.6. Curie-Weiss plot for $\text{AgFe}_3(\text{OH})_6(\text{SO}_4)_2$.

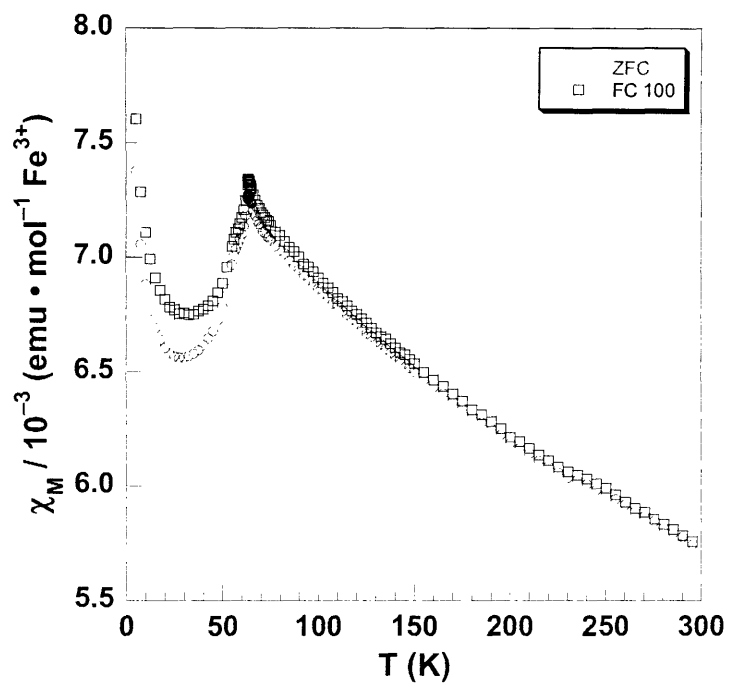


Figure B.7. ZFC and FC molar susceptibility for $\text{TiFe}_3(\text{OH})_6(\text{SO}_4)_2$.

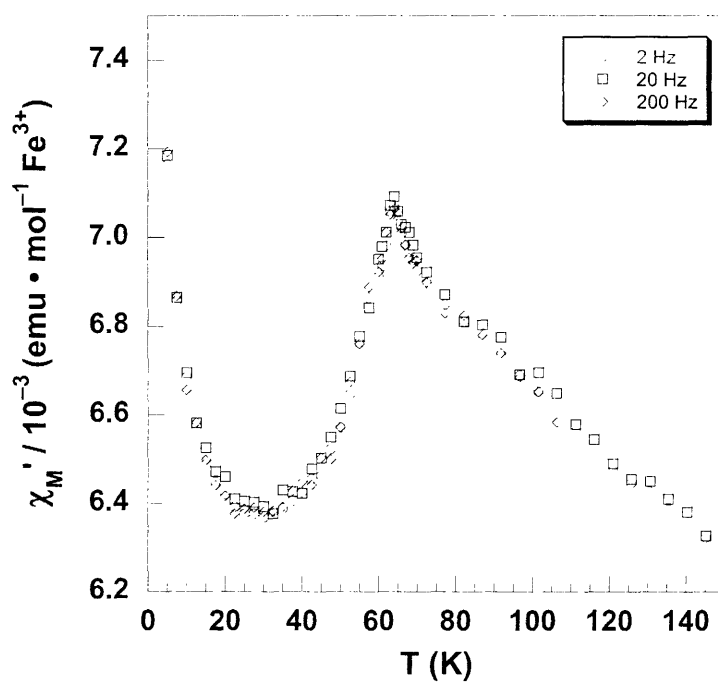


Figure B.8. AC Susceptibility of $\text{TiFe}_3(\text{OH})_6(\text{SO}_4)_2$ measured under various frequencies.

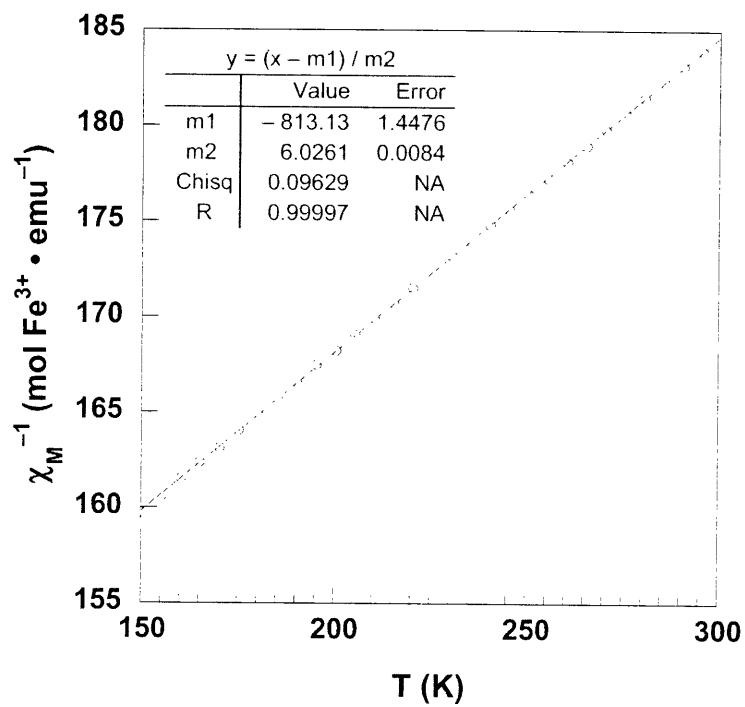


Figure B.9. Curie-Weiss plot for $\text{TlFe}_3(\text{OH})_6(\text{SO}_4)_2$.

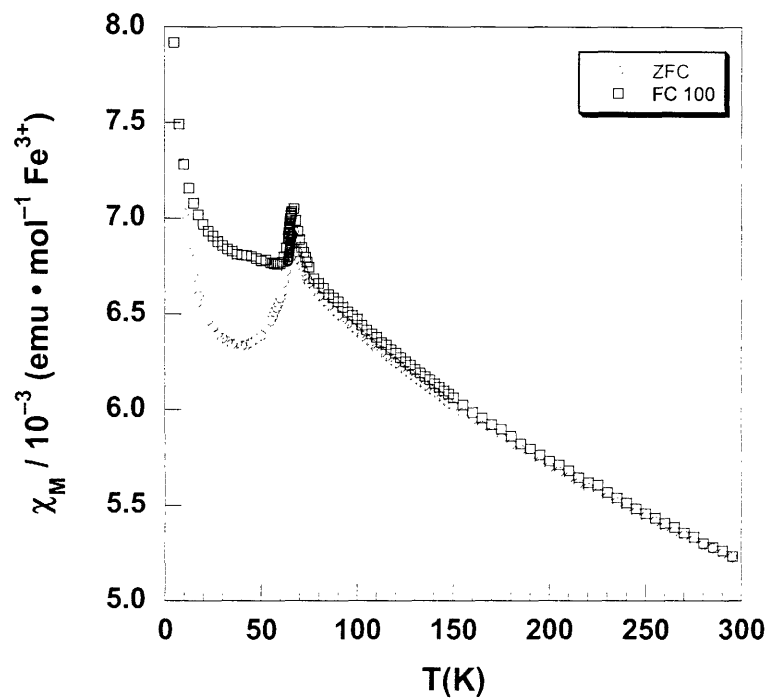


Figure B.10. ZFC and FC molar susceptibility for $\text{KFe}_3(\text{OH})_6(\text{SeO}_4)_2$.

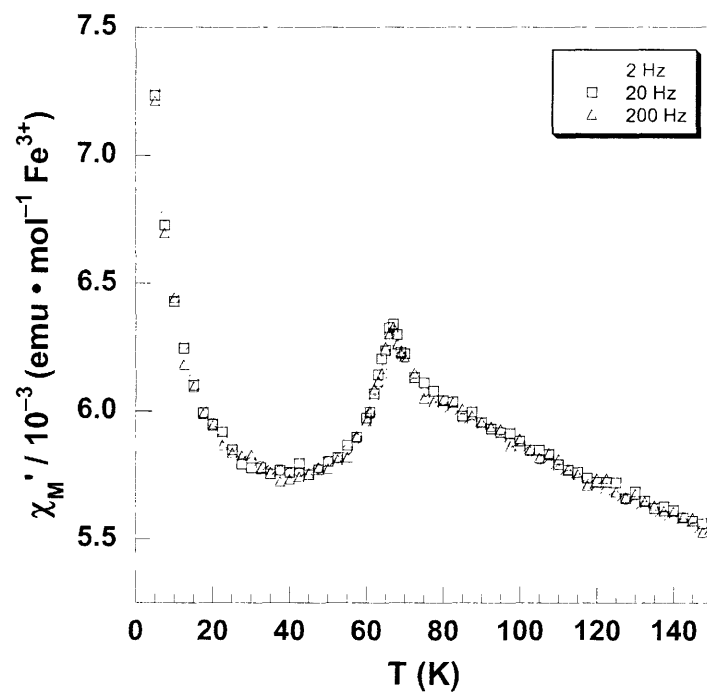


Figure B.11. AC Susceptibility of $\text{KFe}_3(\text{OH})_6(\text{SeO}_4)_2$ measured under various frequencies.

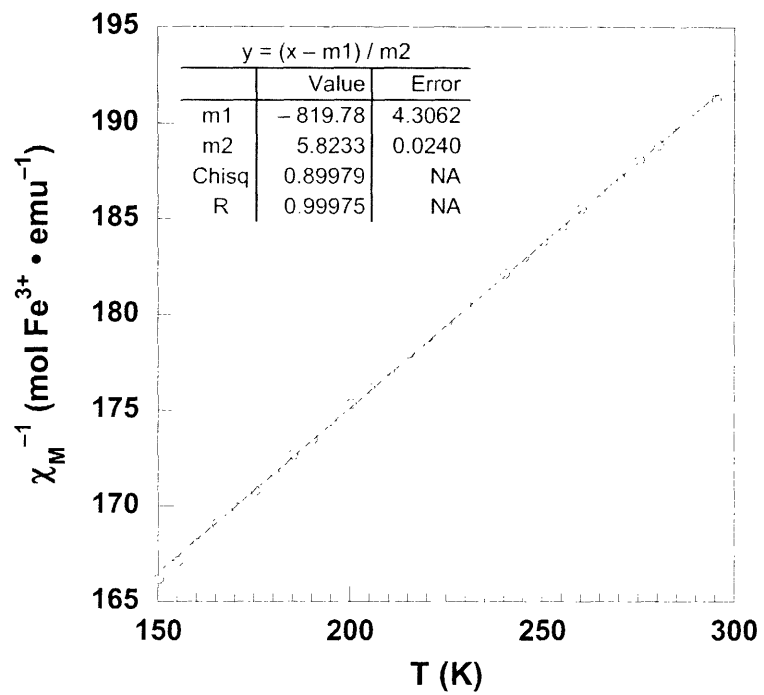


Figure B.12. Curie-Weiss plot for $\text{KFe}_3(\text{OH})_6(\text{SeO}_4)_2$.

Appendix B

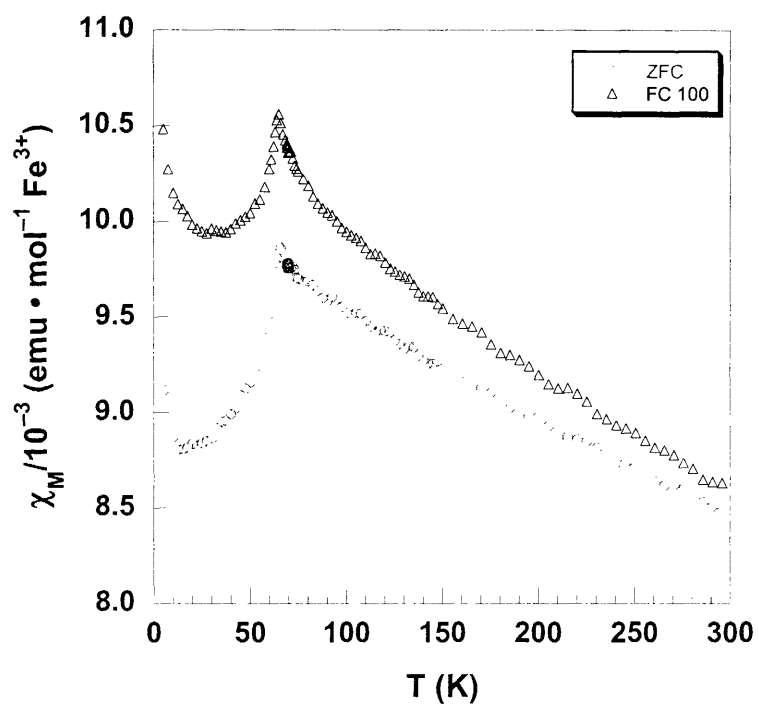


Figure B.13. ZFC and FC molar susceptibility for $\text{RbFe}_3(\text{OH})_6(\text{SeO}_4)_2$.

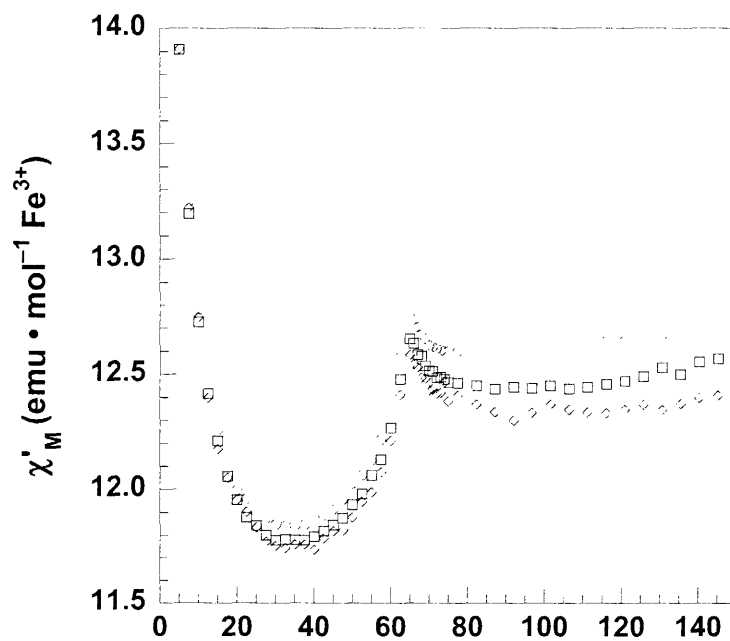


Figure B.14. AC Susceptibility of $\text{RbFe}_3(\text{OH})_6(\text{SeO}_4)_2$ measured under various frequencies.

Appendix B

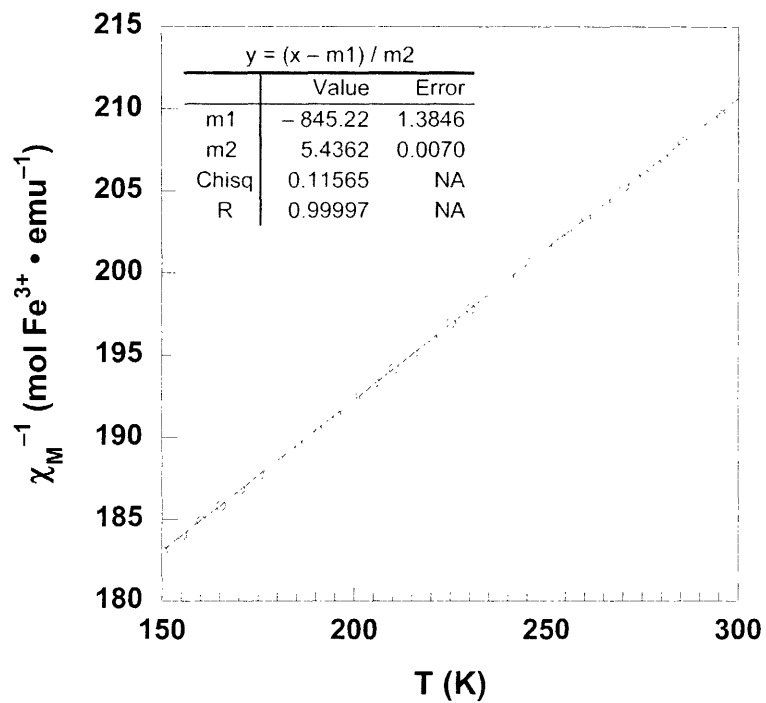


Figure B.15. Curie-Weiss plot for $\text{RbFe}_3(\text{OH})_6(\text{SeO}_4)_2$.

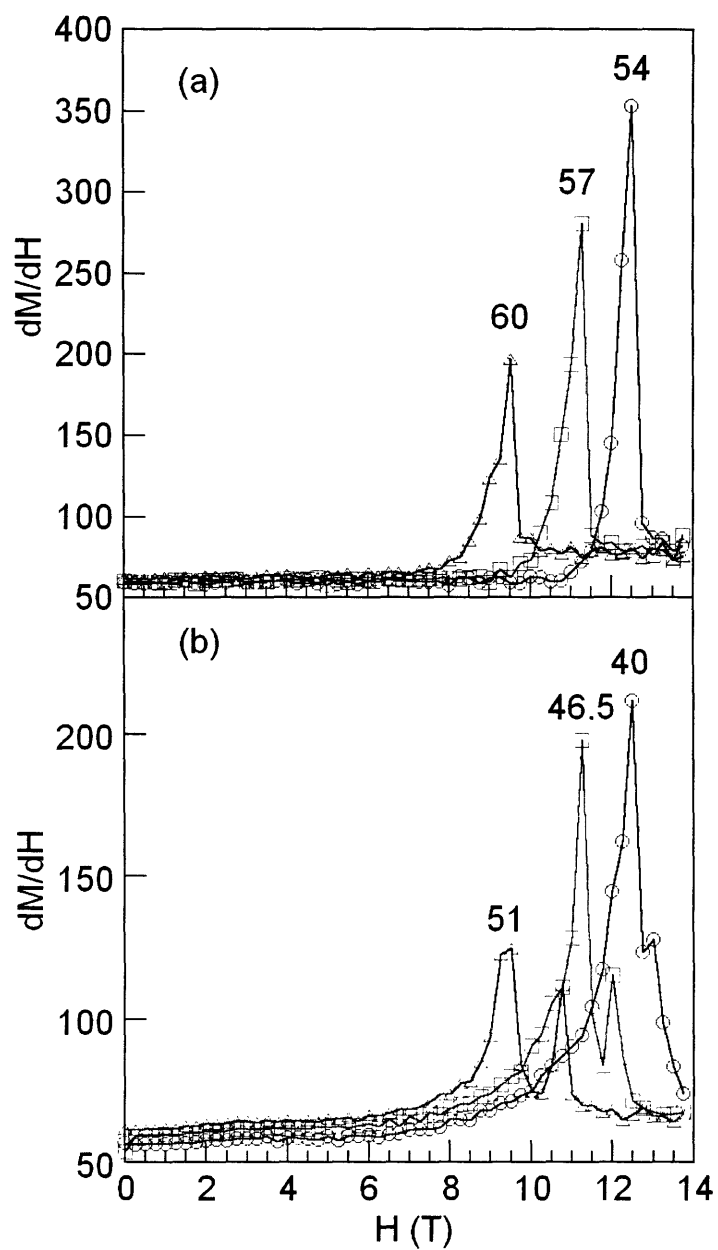
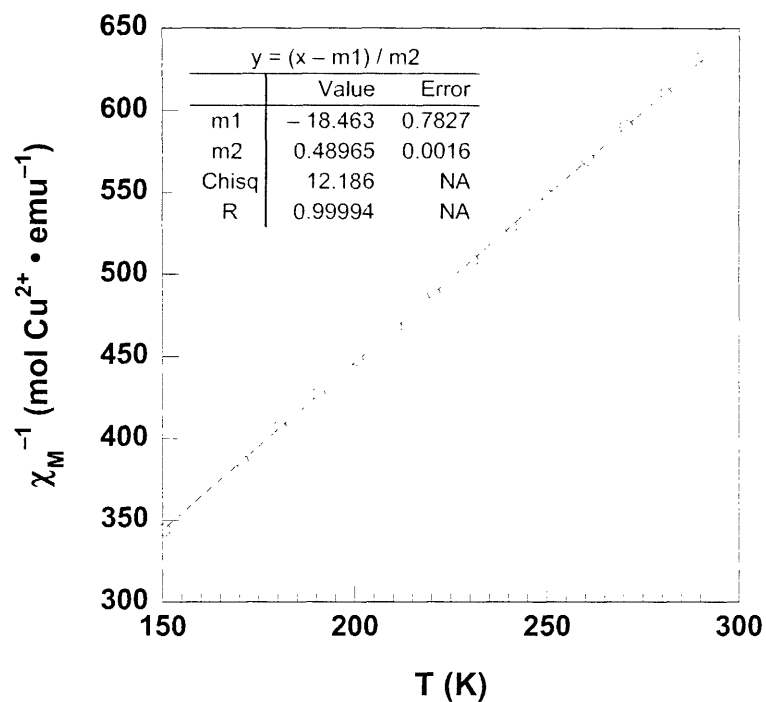
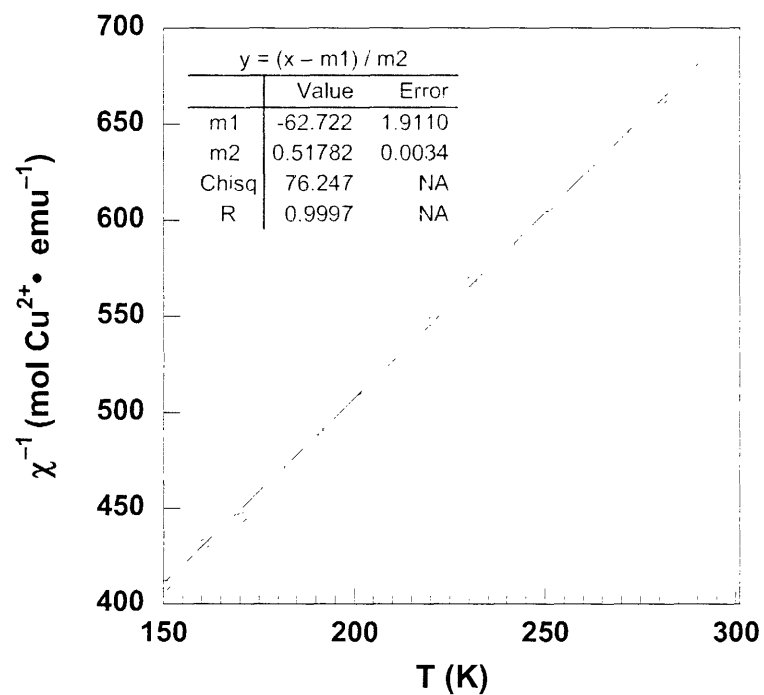


Figure B.16. First derivative plots of the magnetization with applied field at a given temperature for (a) $\text{RbFe}_3(\text{OH})_6(\text{SO}_4)_2$ and (b) $\text{Pb}_{0.5}\text{Fe}_3(\text{OH})_6(\text{SO}_4)_2$. The maximum gives the critical field for the ferromagnetic alignment of canted spins between layers.

Figure B.17. Curie-Weiss plot for $\text{Cu}_3(\text{OH})_2(\text{MoO}_4)_2$.Figure B.18. Curie-Weiss plot for $(4,4'\text{-bipy})\text{Cu}_3(\text{OH})_2(\text{MoO}_4)_2$.

Appendix B

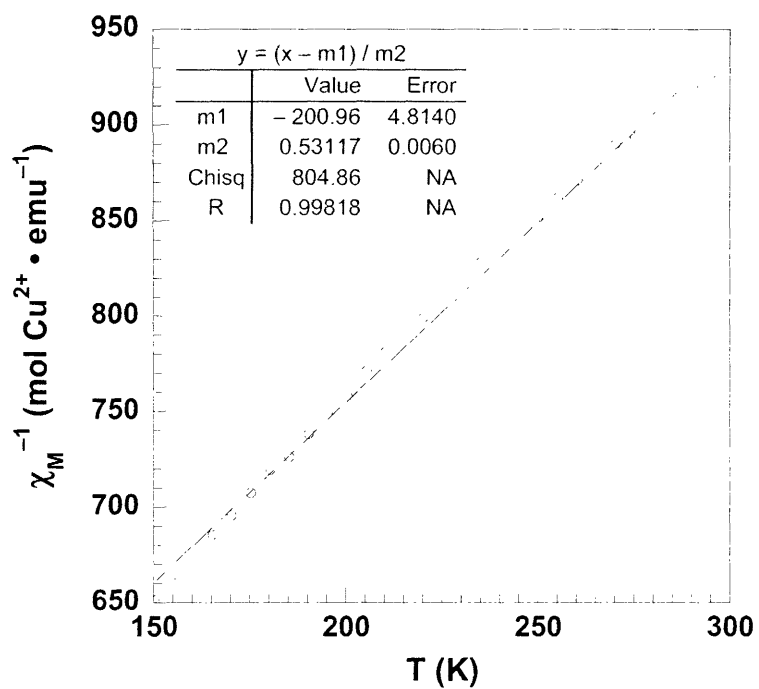


Figure B.19. Curie-Weiss plot for $\text{Cu}_2(\text{OH})_3\text{Cl}$.

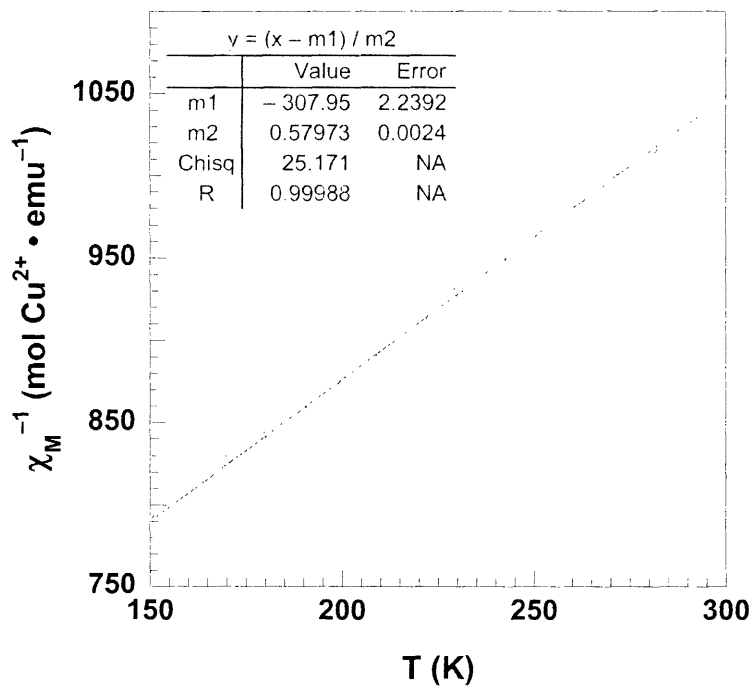


Figure B.20. Curie-Weiss plot for $\text{ZnCu}_3(\text{OH})_6\text{Cl}_2$.

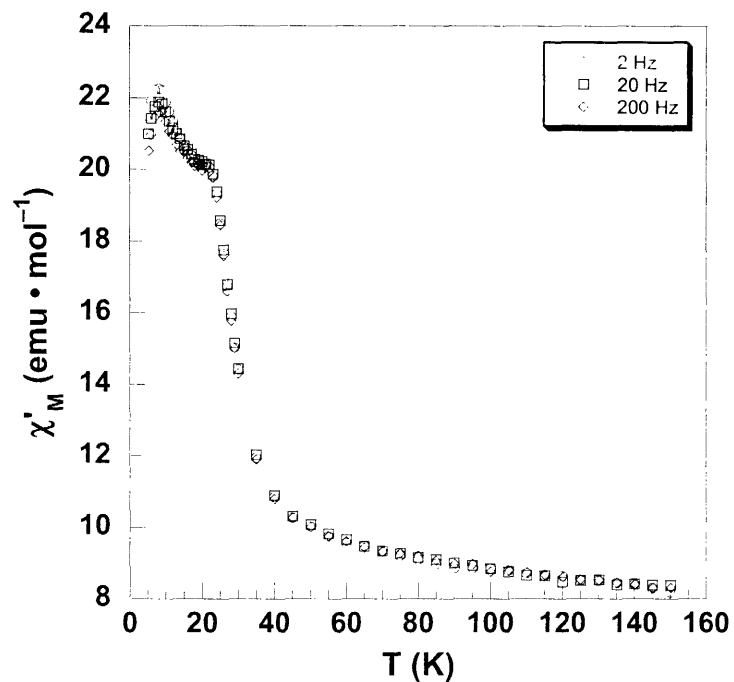


Figure B.21. AC Susceptibility of $\text{KFe}_{3-x}\text{V}_x(\text{OH})_6(\text{SO}_4)_2$ measured under various frequencies.

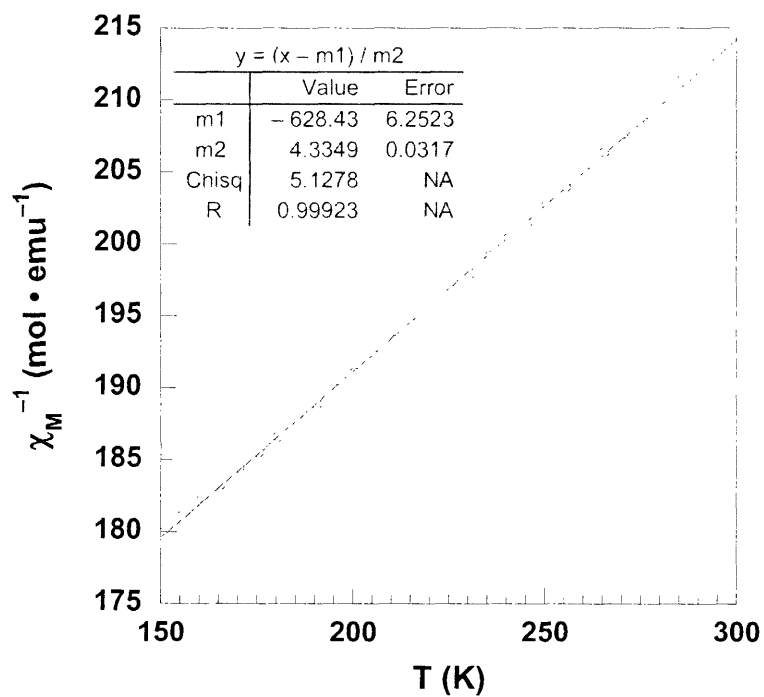


Figure B.22. Curie-Weiss plot for $\text{KFe}_{3-x}\text{V}_x(\text{OH})_6(\text{SO}_4)_2$.

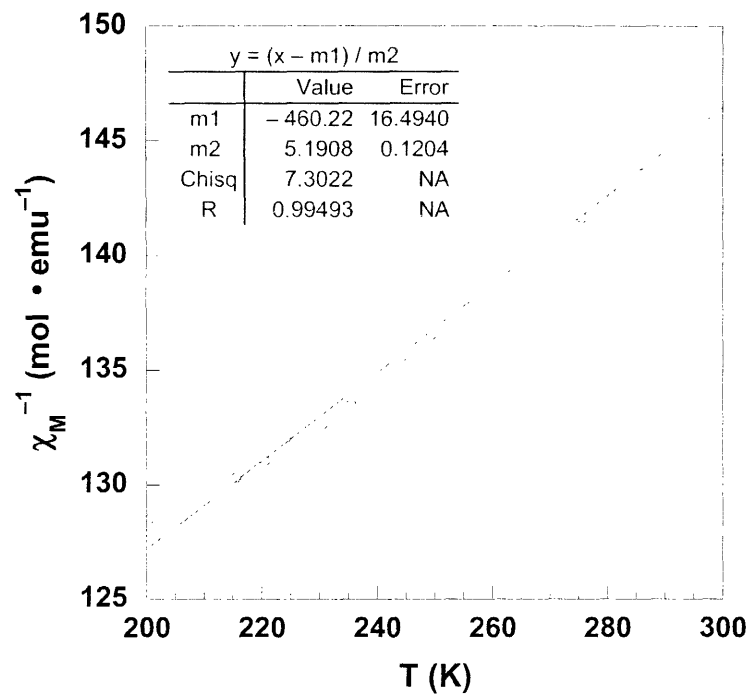


Figure B.23. Curie-Weiss plot for $\text{Fe}^{2+}\text{Fe}_3^{3+}(\text{OH})_2(\text{PO}_4)_2$.

Biographical Sketch

Bart Martel Bartlett, son of Charles Martel Bartlett and Joy Vernice Bartlett, was born on January 26, 1978 in St. Louis, MO. He was raised in St. Louis, where he attended Metro Academic and Classical High School. Interestingly, his first job was for the United States House of Representatives, working as a Congressional Page appointed by then Hon. William L. Clay, Sr. Then, his first experience as a research scientist started with summer research at the Washington University School of Medicine's *Young Scientist Program*, where he worked with graduate student James P. McCarter in Tim Schedl's lab, studying soma-germ cell interaction in the soil nematode *C. elegans*.

After graduating from Metro in 1996, Bart went on to attend Washington University in St. Louis as a John B. Ervin Scholar, where he did undergraduate research in chemistry with Professor William E. Buhro. His project focused on synthesizing III-V semiconductors for the study of quantum confinement effects in nanometer-based materials. While there, the American Chemical Society and the Monsanto Corporation awarded him scholarships. He graduated in May 2000 with a degree in chemistry and minors in French, physics, and hanging out with his peeps at the Wohl Info Desk.

Bart's was awarded a National Science Foundation Graduate Research Fellowship, and began studies in the fall of 2000 to work with Professor Daniel G. Nocera on spin frustrated magnetism. He won an outstanding teaching assistant award in 2000, and the 2004 DuPont Award from the National Organization of Black Chemists and Chemical Engineers. After completing his Ph.D. studies, Bart will join Professor Jeffrey R. Long at the University of California Berkeley as a University of California President's Postdoctoral Fellow.

Outside of his scientific endeavors, Bart enjoys sports—avidly supporting his hometown St. Louis Cardinals and Rams (who both had championship hopes dashed by the Red Sox and the Patriots while he was in graduate school), running, playing softball, listening to and singing along with his favorite artist, Stevie Wonder, and volunteering and serving at his local church.

Bart M. Bartlett

Massachusetts Institute of Technology
Department of Chemistry
77 Massachusetts Avenue Room 2-209
Cambridge, MA 02139-4370

Phone: 617.258.8120
Fax: 617.253.7670
E-mail: bartlett@mit.edu

EDUCATION

Massachusetts Institute of Technology, Cambridge, MA

Ph.D. Inorganic Chemistry, June 2005

Advisor: Professor Daniel G. Nocera

Thesis Title: Synthesis, Structure, and Magnetic Properties of Extended 2-D Triangular Lattices

Washington University in St. Louis, MO

A.B. *summa cum laude* Chemistry, 2000

Advisor: Professor William E. Buhro

RESEARCH EXPERIENCE

Ph.D. research, January 2001–present

Spin frustration gives rise to unusual magnetic properties on triangular-based lattices of exchanged-coupled moments. The kagomé lattice, made of corner-sharing triangles of magnetic ions, represents the ideal prototype in which to study spin frustration. For classical spins, spin frustration engenders an infinite number of degenerate ground states. For quantum spins, the theoretically predicted spin liquid phase in the kagomé lattice models the scatterless hole transport in resonance valence bond theory of high- T_c superconductors.

Jarosite, a mineral having the formula $AFe_3(OH)_6(SO_4)_2$ ($A = Na^+, K^+, Rb^+, NH_4^+, H_3O^+, Ag^+, Tl^+$, and $\frac{1}{2} Pb^{2+}$) shows 3-D long-range order (LRO) despite possessing the 2-D kagomé lattice of $S = 5/2$ Fe^{3+} ions. It has long been shown that purely 2-D magnetic systems cannot display LRO. Jarosites have escaped precise magnetic characterization over the past three decades due to the difficulty of preparing materials in pure and crystalline form. These materials suffer from having magnetic ion site vacancies and are prepared only as powders. A redox-based hydrothermal synthetic strategy allows us to eliminate ion vacancy and to prepare large single crystals. With pure materials in hand, we have fully characterized the magnetism of iron jarosites.

While jarosites show classical spin behavior, current aims in this project seek to prepare $S = \frac{1}{2}$ Cu^{2+} compounds possessing the kagomé lattice. These compounds should display quantum spin liquid behavior at low temperatures, although the lack of pure materials has thus far precluded systematic investigation.

Undergraduate research, February 1998–July 2000

Synthesized nickel and nickel boride nanoparticles for the growth of boron nitride nanotubes from *in situ* generated borazine precursors.

Mallinckrodt Chemical, St. Louis, MO. Laboratory assistant in the Central Stability Group, Summer 1997

Washington University School of Medicine. Laboratory assistant in genetics with the *Young Scientist Program*, 1995–1997

AWARDS AND HONORS

National Science Foundation Graduate Research Fellow, 2000–2003

E. I. DuPont Graduate Fellowship Award, 2003

Outstanding Teaching Assistant Award in Chemistry, 2000–2001

John B. Ervin Scholar, 1996–2000

Washington University Merit Scholar, 1996–2000

Scholar in Arts and Sciences, 1997–2000

American Chemical Society Scholar, 1998–2000

Monsanto Scholar, 1996–1998

International Science and Engineering Fair First-Place Grand Awards Winner, May 1996

TEACHING EXPERIENCE

MIT. Teaching assistant in Principles of Inorganic Chemistry I, Spring 2001

MIT. Teaching assistant in Principles of Chemical Science, Fall 2000

Washington University. Workshop tutor in General Chemistry II, Spring 2000

Washington University. Workshop tutor in General Chemistry I, Fall 1999

RESEARCH INTERESTS AND SKILLS

Solid state synthesis, semiconducting materials, magnetic materials, superconducting materials
SQUID magnetometry, powder X-ray diffraction, glove box and Schlenk techniques

ADDITIONAL EXPERIENCES

MIT. Underrepresented Minorities in Academic Chemistry Task Force Committee Member, 2002--present

MIT. Chemistry Department Mediator with thirty-six hours of basic training in mediation according to Massachusetts General Laws, c. 233, sec. 23C, 2001–present

MIT. Chemical Hygiene and Safety Committee Member, 2001–present

MIT. Nocera Group Environmental Health and Safety Representative, 2001–present

Washington University. Resident Advisor, 1998–2000

Washington University. French Summer Language Institute, Summer 1999

United States House of Representatives. Congressional Page, Fall 1994

SCIENTIFIC PUBLICATIONS AND PRESENTATIONS

Publications

Bartlett, B. M.; Matan, K.; Lee, Y. S.; Nocera, D. G. Direct measurement of the Dzyaloshinsky-Moriya interaction in iron jarosite. *Manuscript in preparation.*

Shores, M.P.; Nytko, E. A.; Bartlett, B. M.; Nocera, D. G. The First Structurally Perfect $S = \frac{1}{2}$ Kagomé Antiferromagnet. *Manuscript in preparation.*

Shores, M.P.; Bartlett, B. M.; Nocera, D. G. Expanding the Layers in Ferromagnetic Lindgrenite to Reveal Spin Frustrated Antiferromagnetism. *Manuscript in preparation.*

Bartlett, B. M.; Nocera, D. G. Long-Range Magnetic Ordering in Iron Jarosites Prepared by Redox-Based Hydrothermal Methods. *J. Am. Chem. Soc.* **2005**, *In press.*

Nocera, D. G.; Bartlett, B. M.; Grohol, D.; Papoutsakis, D.; Shores, M. P. Spin Frustration in 2D Kagomé Lattices: A Problem for Inorganic Synthetic Chemistry. *Chem. Eur. J.* **2004**, *10*, 3850-3859.

Lourie, O.; Jones, C. R.; Bartlett, B. M.; Gibbons, P. C.; Ruoff, R. S.; Buhro, W. E. CVD Growth of Boron Nitride Nanotubes. *Chem. Mater.* **2000**, *12*, 1808-1810.

McCarter, J.; Bartlett, B.; Dang, T.; Schedl, T. On the Control of Oocyte Maturation and Ovulation in *Caenorhabditis elegans*. *Dev. Biol.* **1999**, *205*, 111-128.

McCarter, J.; Bartlett, B.; Dang, T.; Schedl, T. Soma-Germ Cell Interaction in *C.elegans*. Multiple Events of Hermaphrodite Germline Development Require the Somatic Sheath and Spermathecal Lineages. *Dev. Biol.* **1997**, *181*, 121-143.

Talks

Bartlett, B. M.; Nocera, D. G. The Dzyaloshinsky-Moriya Interaction in Jarosites. Abstract of Papers, 229th ACS National Meeting, San Diego, CA, March 2005.

Bartlett, B. M.; Grohol, D.; Papoutsakis, D.; Nocera, D. G. Magnetic properties of new jarosite analogs prepared by redox-based hydrothermal synthesis. Abstract of Papers, 224th ACS National Meeting, Boston, MA, August 2002.

Posters

Bartlett, B. M.; Jones, C. R.; Lourie, O.; Ruoff, R. S.; Buhro, W. E. Chemical vapor deposition growth of boron nitride nanotubes. Semiconductor Research Corporation Annual Review, Madison, WI, July 1999.

Bartlett, B. M.; Buhro, W. E.. Chemical vapor deposition growth of boron nitride nanotubes. The PEW Undergraduate Research Symposium, Washington University, St. Louis, MO, November 1998.

Abstracts

Bartlett, B.; McCarter, J.; Schedl, T. Germline regulation of sheath contractile activity during the *C. elegans* ovulation motor program. Midwest Caenorhabditis elegans Meeting, Normal, IL, June 1996.

McCarter, J; Bartlett, B.; Dang, T.; Schedl, T. Germ cells may modulate the smooth muscle activity of the somatic gonad for ovulation in *C. elegans*. *The Worm Breeder's Gazette*, 14:2. 52-53. February 1, 1996.

GRANTS RECEIVED

Sigma Xi Scientific Research Society. Grant #42, awarded January 2001. \$1000 for the study entitled, "Spin-Frustration Effects on the Antiferromagnetic Coupling in Kagomé Lattice Systems."

REFERENCES

Professor Daniel G. Nocera
Department of Chemistry
Massachusetts Institute of Technology
77 Massachusetts Avenue, Room 6-333
Cambridge, MA 02139
nocera@mit.edu
(617) 253-5537

Professor Stephen J. Lippard
Department of Chemistry
Massachusetts Institute of Technology
77 Massachusetts Avenue, Room 18-498
Cambridge, MA 02139
lippard@mit.edu
(617) 253-1892

Professor William E. Buhro
Department of Chemistry
Washington University in St. Louis
One Brookings Drive
Campus Box 1134
St. Louis, MO 63130
buhro@wuchem.wustl.edu
(314) 935-4269

Professor Young S. Lee
Department of Physics
Massachusetts Institute of Technology
77 Massachusetts Avenue, Room 13-2153
Cambridge, MA 02139
younglee@mit.edu
(617) 253-7834